Creep and Shrinkage Behavior of Concrete in Segmental Bridge Construction

by

Daniel T. Richey

A thesis submitted to the Graduate Faculty of
Auburn University
in partial fulfillment of the
requirements for the Degree of
Master of Science

Auburn, Alabama
December 15, 2018

Keywords: elastic modulus, compressive strength, predictions,
field work, laboratory work, compliance

Approved by

Anton K. Schindler, Chair, Professor and Director of Highway Research Center
Robert W. Barnes, Associate Professor of Civil Engineering
J. Michael Stallings, Professor of Civil Engineering

ABSTRACT

This thesis is aimed at quantifying the shrinkage and creep behavior of the I-59/I-20 segmental bridge located in downtown Birmingham, Alabama. Also, two laboratory concrete mixtures of different coarse aggregate types were produced at Auburn University. These mixtures were used to evaluate the significance that coarse aggregate type plays in creep and shrinkage behavior when all other constituent materials are held constant and mixed under laboratory conditions. For the samples that were collected in the field, the creep behavior for the following four loading ages were investigated: 7 days, 28 days, 91 days, and 182 days. For the two laboratory mixtures, the creep behavior for the following loading ages were investigated: 7 days, 28 days, and 91 days. Both the field and laboratory mixtures were cured at elevated temperatures. The field specimens were cured in the same manner as the actual segment from which they were sampled from, and the laboratory specimens were match-cured at a temperature cycle similar to one that the field specimens were exposed too.

Also, the creep and shrinkage strains that were monitored for the duration of this project were then compared to predicted values using five different models that are common in design of many concrete structures of today. These models include the AASHTO LRFD 2017, ACI 209, CEB MC 2010, GL 2000, and the B3 Model. Also, after evaluating the accuracy of the each of the prediction methods previously mentioned, the method that produced the overall best results was subjected to a calibration process.

After careful evaluation of all collected creep and shrinkage data for the field-mixed concrete, it was noticed that the concrete that was sampled and tested on July 9, 2018 exhibited smaller creep and shrinkage strains as compared to the concrete that was sampled and tested on April 10,2018. The measured compressive strength and modulus of elasticity also improved for each loading age for the concrete that was sampled on July 9, 2018 as compared to concrete that was sampled on April 10, 2018. Also, it was discovered that the substitution of coarse aggregate type did not have a significant impact on creep and shrinkage behavior after evaluating all creep and shrinkage data for the laboratory-mixed concrete.

ACKNOWLEDGMENTS

I would first and foremost like to give a special thanks to my friends, family, and most of all my amazing wife-to-be, Peyton. All of your love and support during this adventure have not went unnoticed, and I am forever grateful for all that you have sacrificed so that this opportunity could be made possible for me. You all will never know the impact that you have made in my life, and you have always supported me in all decisions that I have made whether it be in my career or personal choices.

Second, I want to extend a thank you to Auburn University's lab technician, Rob Crosby. Rob sacrificed his time and effort as well during the duration of this project whether it be traveling with me to Birmingham to collect field samples for testing or collecting data on the test specimens when I was unavailable. Also, I want to thank Grant Cooper as well for his time and effort in preparing test specimens in the lab when I was in desperate need of concrete cylinders needing to be end grinded and DEMEC points needing to be epoxied. Not only were Rob and Grant a huge help to this project, but I also want to thank Preston Fittro, Anna Quinn, Elliot Burrow, and Kelsey Doan for all their time and laughter during our time at Auburn University.

This thesis would also not be possible without the support and continuing guidance from my advising professor, Dr. Anton Schindler. I greatly appreciate all the words of wisdom and providing me a sense of direction in our weekly meetings as to how to achieve the overall goal of my graduate work. I also want to thank Dr. Barnes for his time and guidance for all the times that he would drop by the office to assist his own research assistants, but also assist me with any concerns that I may have had as well. I know that you had many other tasks that you could have devoted your time too, but you always found a minute or two to spare to answer any questions I may have had. And to Dr. Stallings, thank you for all your time not only in the classroom for both my undergraduate and graduate studies but also for serving on my thesis committee.

This project would not have been possible without the cooperation of outside companies. First, I would like to thank the Highway Research Center for their financial contributions in funding this research effort and providing me with this opportunity. Second, I would like to

thank Johnson Brothers for their time and cooperation for each of our site visits, and meeting all of our requests as far as where and when we could collect samples and other important items of business. Also, Adam Dye was a huge help in being our contact in helping us schedule all site visits and always being eager to help whenever needed.

Lastly, I want to thank my Lord and Savior, Jesus Christ. None of this would have been possible without having His guidance along the way and putting my faith and trust in His ways.

TABLE OF CONTENTS

LIST OF TABLES

LIST OF FIGURES

CHAPTER 1: INTRODUCTION

1.1 BACKGROUND

Prestressed and post-tensioning segmental bridge construction is one of the greatest breakthroughs in bridge engineering in the past thirty years (Shushkewich 1986). This type of construction has brought new options to bridge engineers, by allowing concrete bridges to span farther than ever while still remaining adaptable to almost any type of site condition (Shushkewich 1986). In addition to the engineering advantages that concrete segmental bridges allow, these structures are also aesthetically pleasing as shown in Figure 1-1 below.

Figure 1-1: Completed Roosevelt Concrete Segmental Bridge located in Stuart, Florida (Cross 2012)

This research project is being conducted to collect data on creep and shrinkage behavior of concrete that is used in these types of structures. The I-59/I-20 interchange located in downtown Birmingham, Alabama is currently undergoing construction where a concrete segmental bridge is being implemented to replace the current concrete bridge. This bridge serves as a major commuter for traffic on a daily basis throughout the State of Alabama. As shown in

Figure 1-2 and Figure 1-3 below, the construction of the concrete segments being used for the erection of this segmental bridge requires an immense amount of space for casting and storage.

Figure 1-2: Concrete segments and formwork used in the construction of the I-59/I-20 segmental bridge replacement

Figure 1-3: Formwork used during casting of concrete segments

With any type of concrete structure, once load is applied elastic strains instantly occur, and with these strains comes the complex phenomena known as creep (Wang et al. 2014). According to Neville (2011), creep can be defined as the gradual increase in strain with time under a given load, or creep can also be defined as the increase in strain under a sustained stress. However, the significance of the creep strains that develop through the structure depends on many different variables, but one of the most crucial factors is the age of the concrete when the load is applied (Wang et al. 2014). According to the American Concrete Institute (ACI) Committee 209 (2008) creep strains can be assumed to be proportional to initial elastic strains when the elastic stress is less than 40 percent of the compressive strength of the concrete. Creep strains can affect a structure in two distinct ways: excessive structural displacements can occur and load redistributions, specifically the loss of prestressing and post-tensioning force in tendons caused by this redistribution (Wang et al. 2014). For structures that are built in multiple stages, creep analyses can be complicated due to the age and the loading of the concrete being complicated to dictate; therefore, this makes this time-dependent property crucial to the overall concrete bridge analysis and design (Wang et al. 2014).

Not only will concrete develop creep strains once loading is applied, but it will also undergo strains due to shrinkage as well. The driving force behind shrinkage strains is a much simpler concept due to shrinkage being elastic strain independent (Wang et al. 2014). Shrinkage strains can simply be described as the volumetric change in concrete due to the movement of moisture from the concrete to the surrounding environment and also due to the chemical reactions that take place during the hydration process of the cementitious materials (Neville 2011).

1.2 RESEARCH OBJECTIVES

This project is being conducted to gain valuable insight into how the time-dependent properties of concrete behave when being used in a segmental bridge construction application. This is the beginning phase of testing for creep and drying shrinkage of concrete used in the concrete segments of the I-59/I-20 segmental bridge replacement in downtown Birmingham, Alabama.

This thesis outlines the testing and analysis of creep and shrinkage behavior of three concrete mixtures that were obtained from the jobsite where concrete segments were cast and stored for erection. Also, two concrete mixtures were mixed in the laboratory at Auburn University using the same mixture design that was approved by ALDOT during the duration of this project. The primary objectives associated with this study include:

- Quantify the creep and shrinkage behavior of the concrete used in the precast segmental bridge of the I-59/I-20 project located in downtown Birmingham, AL.
- Comparing the creep and shrinkage behavior of concrete made with limestone coarse aggregate to the behavior of concrete made with quartzite coarse aggregate.
- Compare creep and shrinkage strains of the concrete mixtures sampled at the segmental bridge jobsite to the values predicted using the models below:
    - ACI 209 (ACI Committee 209 2008),
    - AASHTO (2017),
    - CEB-FIB MC 2010 (fib 2012),
    - GL 2000 (Gardner and Lockman 2001), and
    - B3 (Bazant and Baweja 2000).
- Calibrate the most accurate creep and shrinkage model to improve its prediction of the measured creep and shrinkage strains.

Also, a secondary objective associated with this study includes:

- Determining the most accurate process to effectively track the compressive load that is applied to each creep frame during testing in accordance with ASTM C 512 (2018).

1.3 RESEARCH SCOPE

As previously stated in Section 1.2, this study was conducted to determine the creep and shrinkage behavior of three different concrete mixtures that were used in the casting of concrete for the I-59/I-20 segmental bridge replacement in downtown Birmingham, Alabama. Also, the same testing was performed with two concrete mixtures that were mixed at Auburn University's Structural Engineering Laboratory using the approved ALDOT mixture design with the exception of replacing the coarse aggregate of one mixture with a No. 67 limestone rather than the No. 67 quartzite that was used for the duration of the construction project. All of the mixtures included the same cementitious materials: Type I/II portland cement and Class F Fly Ash.

Loading ages of 7 days, 28 days, 91 days, and 182 days were evaluated for the concrete samples obtained from the jobsite. Specimens that were mixed in the Auburn University laboratory were loaded at 7 days, 28 days, or 91 days. Jobsite specimens were subjected to an accelerated curing cycle based on the procedures performed by the contractor, while laboratory specimens were match-cured at a controlled elevated temperature.

Each of the creep specimens were loaded to 40 percent of their ultimate compressive strength that was determined immediately prior to load application. Once the desired load was applied to each of the creep specimens, strain readings were taken periodically to analyze the overall creep behavior. Once subjected to drying, strain readings were recorded for all companion shrinkage specimens at the same time as the corresponding creep specimens. Additionally, the collected data were then used with various creep and shrinkage prediction models to evaluate the accuracy of the measured versus predicted values. These models included: ACI 209, AASHTO 2017, CEB MC 2010, GL 2000, and B3.

1.4 ORGANIZATION OF THESIS

Chapter 2 outlines many characteristics of segmental bridge construction. This chapter includes the basic procedure of how segmental bridge construction is completed, the significance of time-dependent properties in segmental bridges, volumetric changes in concrete, creep and shrinkage

prediction methods, and previous studies related to these time-dependent properties in segmental bridge construction.

The experimental plan that was developed and utilized during this project is covered in Chapter 3. This includes specimen preparation and curing methods for both field and laboratory specimens, along with the quantities and types of materials used. Also, the details of how creep and drying shrinkage testing were completed.

The techniques and procedures that were used by the contractor to cast all concrete segments is presented in Chapter 4. This chapter includes an overview of how all steel reinforcement cages were constructed and placed in the proper formwork, the procedures followed during the placement of each concrete segment, and curing regimes used. Additionally, how each segment was properly transported and stored after curing was completed is discussed.

Chapter 5 includes a presentation of the collected data and the results of the data analysis. Here the creep and drying shrinkage response that was generated from the resulting data is discussed along with the fresh and hardened properties of each concrete mixture for both the field-mixed and laboratory-mixed test specimens.

Comparisons of recorded data versus each of the five creep and shrinkage prediction models are presented in Chapter 6. Also, the accuracy of each model is assessed with regards to estimating the creep and drying shrinkage behavior, and the most accurate method was calibrated to improve the overall predicted creep and shrinkage strains for the field-mixed concrete. Furthermore, conclusions on how each of the five methods perform are provided.

General conclusions from this research effort are presented in Chapter 7. Also, recommendations on how to improve creep and drying shrinkage testing are provided along with a summary of both the field and laboratory work that was completed.

CHAPTER 2: LITERATURE REVIEW

2.1 INTRODUCTION

The construction of segmental post-tensioning concrete box girder bridges is increasing in the United States, with the first bridge of its kind being constructed in the United States in 1973 near Corpus Christi, Texas (Roberts et al. 1993). These types of bridges offer many advantages to the construction industry when it comes to spanning great distances including large river crossings and where long spans are needed in metropolitan areas.

According to ACI Committee 209 (2008), creep is the time-dependent increase of strain in hardened concrete subjected to sustained stress, or in simpler terms it is the increase in deformation due to a sustained load over time. Shrinkage can be described as the decrease in concrete volume with time due to the hydration reactions taking place in the cement matrix, and when concrete is exposed to an atmosphere where drying can occur (ACI 209 2008). In order to successfully predict creep and drying shrinkage of concrete, the volumetric change of the concrete itself must be monitored. Simplified methods for analyzing service performance are justified because the prediction and control of time-dependent deformations and their effects on concrete structures are exceedingly complex when compared with the methods for analysis and design of strength performance (ACI 209 1992).

In Section 2.2 of this chapter, an overview of the development of segmental concrete bridges are covered along with common construction practices that are used when erecting segmental bridges. Section 2.3 of this chapter will provide information regarding volumetric changes in concrete and many of the factors that influence these changes in volume. In Section 2.4, an overview of the creep and shrinkage prediction models considered in this study are provided, and Section 2.5 will provide results of previous studies related to creep and shrinkage behavior that were conducted at Auburn University as well as results of case studies that were conducted on segmental bridges to analyze how creep and shrinkage behavior can effect segmental bridges.

2.2 DEVELOPMENT OF SEGMENTAL CONCRETE BRIDGES

Segmental post-tensioned concrete box girder bridges have many advantages as compared to more traditional systems. According to Roberts et al. (1993), not only are they more economical, versatile, and aesthetically pleasing, the list of advantages include

- They can be adapted to any reasonable horizontal and vertical curvature,
- They can be erected in ways which create minimal disruptions at ground level (Can be extremely important in urban and environmentally sensitive areas),
- External post-tensioning allows:
    - Thinner webs leading to smaller dead loads,
    - Easier installation of longitudinal tendons, and
    - Easier inspection of tendons and easier replacement of damaged tendons.

Segmental construction was first used in China for the construction of arch bridges in the seventh century but did not come back into effect until the twelfth century when various bridges throughout Europe were constructed using this technique (Roberts et al. 1993). Box shaped cross-sections were among the first types of segmental bridges that were constructed. These cross-sections were first utilized by Boussiron of France in 1899 and by Maillart of Switzerland in 1901, thus by the early 1900's, segmental bridge construction and new technologies had made their mark in the engineering world (Roberts et al. 1993).

Not long after segmental construction had been developed, modern prestressing of these concrete sructures shorly followed, which was applied to the three arch Le Veudre Bridge over the Allier River in France in 1912 (Roberts et al. 1993). Due to significant creep effects, jacks were positioned at the crown of the bridge to push the two halves back into their original positions, which proved to show the severity that creep can play in segmental conrete bridges. Another example includes the first modern prestressed bridge, the Saale-brucke bridge built in 1928, located in Germany. It consisted of a 200 foot span that was post-tensioned with large-diameter bars. However, these bars were of relatively low strength and as a result of creep, shrinkage, and relaxation introduced prestress losses equal to 75% of the original prestress level (Roberts et al. 1993).

2.2.1 Construction of Segmental Bridges

Segmental concrete box-girder bridges can be composed of two distinct types of segements: cast-in-place concrete segments or precast concrete segments. If cast-in-place segments are being used, the erection process is completed through a process known as the segmental, balanced cantilever method, but if precast segments are used, the erection of these segments can be done in different ways included the segmental, balanced cantilever method, the span-by-span method, or the progressive placement method. The segmental, balanced cantilever method procedure is done by cantilevering in two directions from a fixed pier location by successivley adding concrete units, and then post-tensioning each of these units to those that are already in place to form a continuous structure as illustrated in Figure 2-1 (Gallaway 1975).

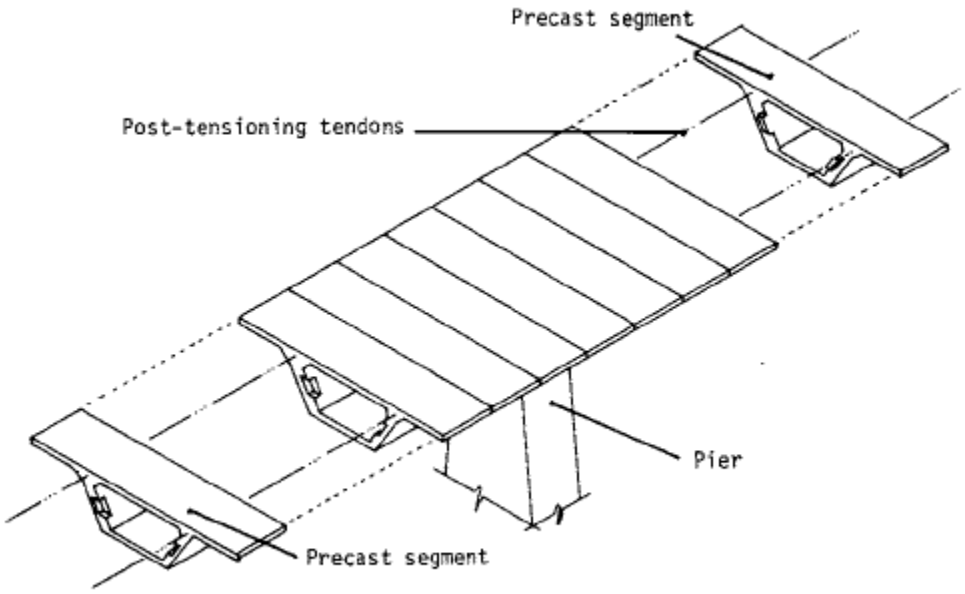

Figure 2-1: Precast segmental bridge construction by cantilever erection technique (Gallaway 1975)

In the span-by-span method, an entire span is assembled, post-tensioned, and erected so that it is self-supporting before the next span is erected; where as, with the progressive placement method, erection starts at one end of the bridge where segments are erected in sequential order (Podolny and Muller 1994). When precast concrete segments are being used, the tendons for

post-tensioning are typically passed completely through the structure from one end to the other as pairs of the segments are added to the structure (Gallaway 1975). An epoxy film is applied to the joining faces of each precast segement immediately prior to the post-tensioning of these tendons. If cast-in-place concrete segements are being utilized, prestressing takes place prior to the removal of the forms (Gallaway 1975).

The size of these segments can vary drastically. Their weight can range anywhere from 20 tons to over 600 tons depending on the overall geometrey of each segment and its functionallity in the structure. Each segment is usually cast in 8 to 10 feet lengths in the longitudinal direction and 30 to 60 feet in width (Gallaway 1975).

As stated earlier, there are two common types of segments that are used in segmental bridge construction: cast-in-place and precast. Precast units tend to be more beneficial, but they do not allow extreme amounts of error in dimensional areas. Due to the units being cast end-to-end, errors related to geometry of segments near the piers are greatly multiplied by the lever arm of the cantilever (Gallaway 1975). According to Gallaway (1975), a uniform error in the length of individually and independently cast segments produces wedge-shaped units, which leads to the formation of an arch-shaped double cantilever when erected. To eliminate these end deflections that are created due to the wedge effect are pratically impossible; however, the simplest solution to avoid this problem is by casting the segments end-to-end or also called “match-casting’.

Match-casting is accomplished by building an adjustable-height soffit form approximately one-half span long, which serves as the casting bed (Gallaway 1975). After the casting bed has been constructed, segments are cast and the forms are removed leaving the segment on the casting bed. Bond breaker is then applied to each end of the segment, and using two side forms, segments are cast against each side of the pier segment (Gallaway 1975). The above process is repeated unitl the casting bed is full, and once all segments have achieved their required strength, they are jacked apart and moved to a storage area for final curing (Gallaway 1975). Segments that are match-cast will always fit together in the completed structure with the exact orientation in which they were cast. An example of a casting bed is illustrated in Figure 2-2.

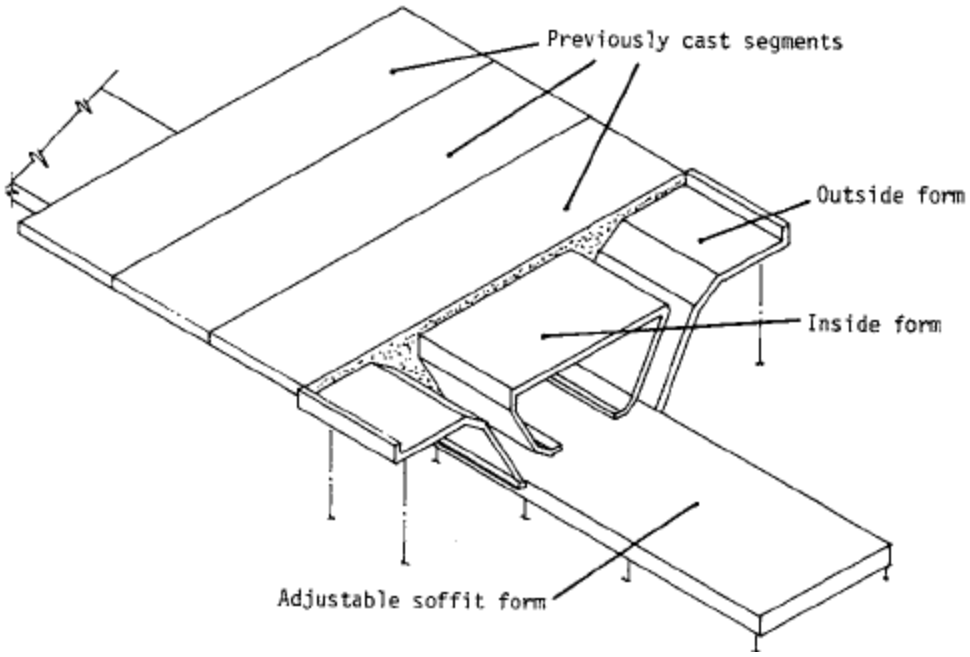

Figure 2-2: Casting bed used during match-casting of segments (Gallaway 1975)

Not only does match-casting help to eliminate dimensional errors of concrete segements, it also has proven to serve many other advantages. Since joining faces of each segment can be perfectly matched, stress concentrations that arise during post-tensioning can be greatly minimized (Gallaway 1975). Also, any irregularities on the face of one segment will be matched by the adjacent segment. However, when match-casting is used, all segments must be placed in the exact arrangement in which they were cast to avoid any stress concentrations (Gallaway 1975). Any stress concentrations could lead to excessive spalling of the concrete at the segment joints.

2.2.2 Creep and Shrinkage in Segmental Bridges

In the design of any concrete structure, volumetric changes such as shrinkage and creep of the concrete must be taken into consideration. This is extremely important in the design of concrete bridges due to these volumetric changes possibly causing major issues in calculated deflections and the specified camber along with moment distribution throughout the structure (Podolny and Muller 1994). However, these types of volumetric changes vary depending on the type of bridge that is being erected, and thus must be considered differently during the design phase.

In conventional, continuous, concrete box girder bridges, no creep and shrinkage-induced moment redistribution takes place at the time of prestressing due to the box girders being in their final structural configuration (Libby 1976). In contrast, segmentally constructed concrete bridges are prone to temporary unbalanced moments when certain types of construction are used, such as the cantilever method (Libby 1976). Early prestressed segmental bridges built using the cantilever method of construction formed hinges at mid-span. The creep and shrinkage behavior of the concrete would then lead to these hinges providing little to no restraint vertical and angular displacements of the cantilever, which resulted in significant strength losses of either the prestressed or post-tensioned steel (Podolny and Muller 1994).

The information in the following paragraph is from Libby (1976). Redistribution of moment due to concrete creep and shrinkage is critical when using the cantilever construction method for the erection of segmental bridges. This is due to the structure having a structural configuration that is different from its final one as is done in the construction of continuous structures with the cantilever erection technique. When using cast-in-place construction, redistribution of moment due to concrete creep and shrinkage does not have to be considered. This is characterized by a relatively small reduction in the effective negative moment at the supports and a large increase in the effective positive moment at midspan. When considering the two cantilever beams illustrated in Figure 2-3, these beams are considered continuous when the cast-in-place joint between them is constructed and the continuity tendons between the two cantilevers are installed. If they were not considered continuous, the effect of creep and shrinkage would lead to a deflection and rotation at the ends of the beams as time progressed. Due to this rotation being resisted by the provision of continuity, a creep and shrinkage-induced positive moment of considerable magnitude is created near midspan and is accompanied with a reduction of the negative moment at the supports. In early segmental construction, this type of moment redistribution lead to cracking in the tensile flanges near midspan, but was considered not critical to the overall strength of the structure. However, these cracks could lead to other issues, such as corrosion or alkali-silica reaction, which could adversely affect the durability of the concrete.

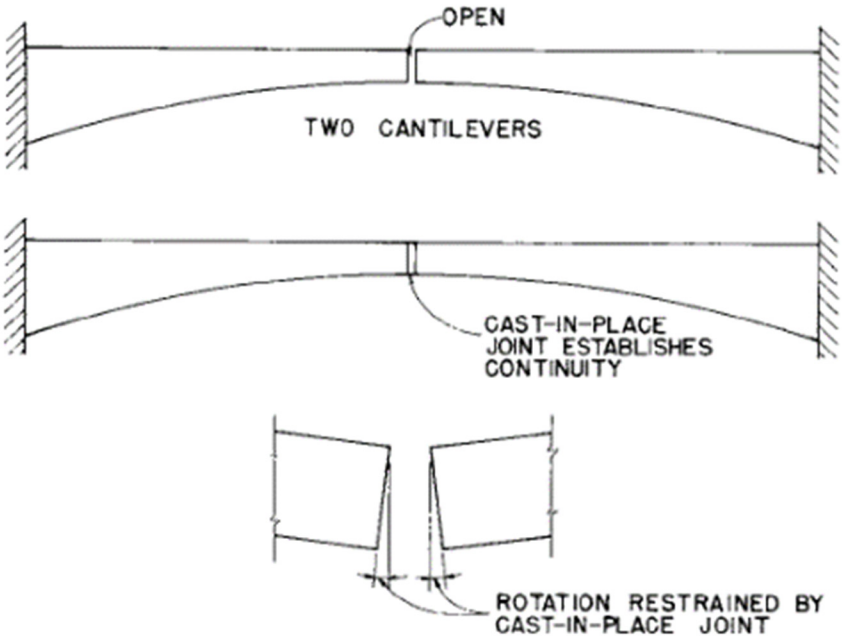

Figure 2-3: Two cantilever beams made continuous at their ends subsequent to construction (Libby 1976)

Muller (1969) published a paper that explained many of the previously mentioned topics related to creep and shrinkage-induced moment distribution. Muller provides calculations based on an example of a structure where it was estimated that the effect of creep would cause a three percent reduction in the effective negative moment and a twenty percent increase in the effective positive moment due to dead load

Later continuous bridges neglected the redistribution of moments due to creep and shrinkage and experienced joint openings and cracking in the positive moment area resulting in many having to be strengthened by the addition of external tendons (Roberts et al. 1993).

2.3 VOLUMETRIC CHANGES

Volumetric changes of concrete can be characterized by three distinct components: drying shrinkage, autogenous shrinkage, and basic creep. This section outlines these three basic components, and provides detail as to how each of these components contributes to volumetric changes in concrete based on many different parameters such as geometric properties, environmental conditions, and mixture proportions.

2.3.1 Drying Shrinkage

According to Mehta and Monteiro (2014), the driving force of drying shrinkage is due to the differential relative humidity between concrete and the environment. If the concrete is subjected to a saturated condition, no drying shrinkage will take place due to no water being lost from the hydrated cement paste. However, if the concrete is placed in any condition other than a saturated condition, shrinkage strains will develop in the concrete due to the loss of water. When concrete specimens are restrained, that is, not free to move, the strain will be zero, but tensile stresses develop on the exposed surface of the concrete which can lead to crack formation due to drying shrinkage (Kim and Lee 1998).

In practice, moisture movements in the hydrated paste, which essentially control the drying shrinkage strains in concrete, are influenced by many different factors acting simultaneously at the same time (Mehta and Monteiro 2014). These factors include: materials and mix-proportions, time and humidity, and also the geometry of the concrete element. To give a better understanding of how each of these factors directly effects the drying shrinkage of the concrete, each will be individually presented in the following sections.

2.3.1.1 Effects of Materials and Mixture Proportions on Drying Shrinkage

The hydrated cement paste in any concrete is the leading cause of moisture-related deformations. However, other contributing factors such as aggregate type and content, cement content, and water-cement ratio can greatly impact the shrinkage behavior of concrete (Mehta and Monteiro 2014). The following information in this section is from Mehta and Monteiro (2014).

The grading, maximum size, shape, and texture of aggregates are factors that can directly affect the drying shrinkage of concrete. The modulus of elasticity of the aggregate type is the most important factor due to this parameter primarily controlling the compactibility of the concrete. According to Mehta and Monteiro (2014), as the elastic modulus of the aggregate increases, the shrinkage of the concrete decreases, and vice versa.

In general, the influence of cement content and water-cement ratio of concrete on the drying shrinkage is not direct, because an increase in the cement paste volume means a decrease in the aggregate content and, consequently a corresponding increase in the moisture-dependent deformations in concrete (Mehta and Monteiro 2014). For a given cement content, if the water-

cement ratio is increased, the drying shrinkage of the concrete normally increases. This can be due to the decrease in strength and an increase in permeability of the system.

2.3.1.2 Effects of Time and Humidity on Drying Shrinkage

Time is a key factor in the overall measurement of drying shrinkage, and takes place over many years rather than a matter of weeks. For drying shrinkage tests lasting longer than 20 years, Mehta and Monteiro (2014) found that with a wide range of concrete mixture proportions, aggregate types, and environmental and loading conditions, only 20 to 25 percent of the 10-year drying shrinkage was realized in 2 weeks, 50 to 60 percent in 3 months, and 75 to 80 percent in 1 year. The relative humidity also is a crucial factor when dealing with drying shrinkage. In an area where there is a high relative humidity, drying shrinkage will develop at a much slower rate as compared to an area where the humidity is much lower. This is due to the moisture flow from the interior to the outer surfaces of the concrete being at a much slower rate (Mehta and Monteiro 2014).

2.3.2 Autogenous Shrinkage

According to Tazawa (1999), autogenous shrinkage is the macroscopic volume reduction of cementitious materials when cement hydrates after initial setting, but does not include volume changes due to loss or ingress of substances, temperature variations, or application of external forces or restraint. Autogenous shrinkage is usually a concern in high-strength or high-performance concrete (>40 MPa or 6000 psi) where there is a low water-to-cement ratio. Overall, early-age concrete shrinkage (autogenous and drying shrinkage) is of increasing concern, as it can be responsible for cracking when the concrete has not gained significant strength to withstand internal stresses (Holt 2005).

Autogenous shrinkage of concrete is influenced by mineral compositions within the cement and their hydration ratios (Tazawa 1999). However, before the mechanism behind how this phenomena can be fully comprehended, other important factors such as chemical shrinkage, microstructure, and self-desiccation need to be discussed.

2.3.2.1 Chemical Shrinkage, Microstructure, and Self-Desiccation

Cement materials produce various types of hydrates when they are subjected to water, which is known as hydration (Tazawa 1999). Once the hydration process has started, cementitious material volumes as well as liquid volumes decrease due to the reactions that take place. These volume changes are due to what is known as chemical shrinkage. In low water-to-cementitous ratio (w/cm) systems, further hydration is compensated by the formation of voids in the microstructure. At early ages of cement hydration, ettringite (needle like crystals) is formed on the surface of cement particles and in the pore solution, which lead to a large volume of fine pores in the hardened body (Tazawa 1999). Not only is ettringite formed during the hydration process, but also large amounts of Calcium Silicate Hydrate (C-S-H) are created over long periods of time also leading to the creation of more fine pores in the microstructure. Once these fine pores are created throughout the microstructure, self-desiccation is then able to take place based on the relative humidity of the surround environment. In hardened cement bodies, the amount of free water decreases and the water vapor pressure reduces and the relative humidity in fine pore decreases (Tazawa 1999). This phenomenon is known as self-desiccation, which in turn is highly relatable to the microstructure formation during the hydration process.

2.3.2.2 Factors Influencing Autogenous Shrinkage

Autogenous shrinkage is influenced by several different factors, but three distinct factors cause the largest impact on the phenomenon: mineral and chemical admixtures, mixture proportions, and curing conditions of the concrete (Tazawa 1999). Supplementary cementitious materials (SCM's) such as fly ash or silica fume greatly increase the autogenous shrinkage of concrete as compared to concrete that has been subjected to expansive additives, which will reduce the autogenous shrinkage (Tazawa 1999). Mixture proportions of the concrete can also decrease or increase the amount of autogenous shrinkage. Autogenous shrinkage increases with a decrease in water to cement ratio or with an increase in the amount of cement paste. This means that autogenous shrinkage is increased when the binder content is increased or when the volume of aggregate decreases (Tazawa 1999). Lastly, curing conditions of the concrete lead to impacts of the autogenous shrinkage as well. Concrete can be cured in many different ways such as moist curing or it can be subjected to a steam curing process to accelerate the strength and maturity. In the early stages of curing, the initial shrinkage becomes higher as compared to the shrinkage at

later stages and higher temperatures. However, the effect of the manufacturing process, or compaction on autogenous shrinkage is hardly studied, and would need to be researched more thoroughly before making final conclusions (Tazawa 1999). Sine autogenous shrinkage is caused due to the hydration reaction of cement, a way to mitigate autogenous shrinkage is to internally cure the concrete. This allows for more water during the hydration of the cement, which will lead to a decrease in autogenous shrinkage (Tazawa 1999).

2.3.3 Creep

One other important type of volumetric change that concrete undergoes is a phenomena known as creep. According to Neville (2011), creep can be defined as the gradual increase in strain with time under a given load, or it can further be defined as the increase in strain under a sustained stress. Many of the factors that affect shrinkage, also influence the behavior of creep with a few additional conditions that must be monitored.

First, both the drying shrinkage and creep originate from the same source, which is the hydrated cement paste; second, the strain-time curves are very similar; and third, the microstrain that is produced by both of these phenomenon can be significant and must be taken into account during the design process (Mehta and Monteiro 2014). In the case of many actual structures, however, creep and shrinkage occur simultaneously and the treatment of the two is, from a practical standpoint, often convenient (Neville 2011). These volumetric changes can be broken down into two basic categories: basic creep and drying creep (Neville 2011).

Basic creep is defined as the time-dependent strains resulting from the sustained loading only. However, as seen in Figure 2-4, the sum of the basic creep and free shrinkage time-dependent strains do not result in the total time-dependent deformation of the concrete. According to Neville (2011), to accurately predict the total deformation, a term known as drying creep is introduced. Drying creep is defined as the additional time-dependent strain due to drying of the concrete while sustained loading is applied (Neville 2011).

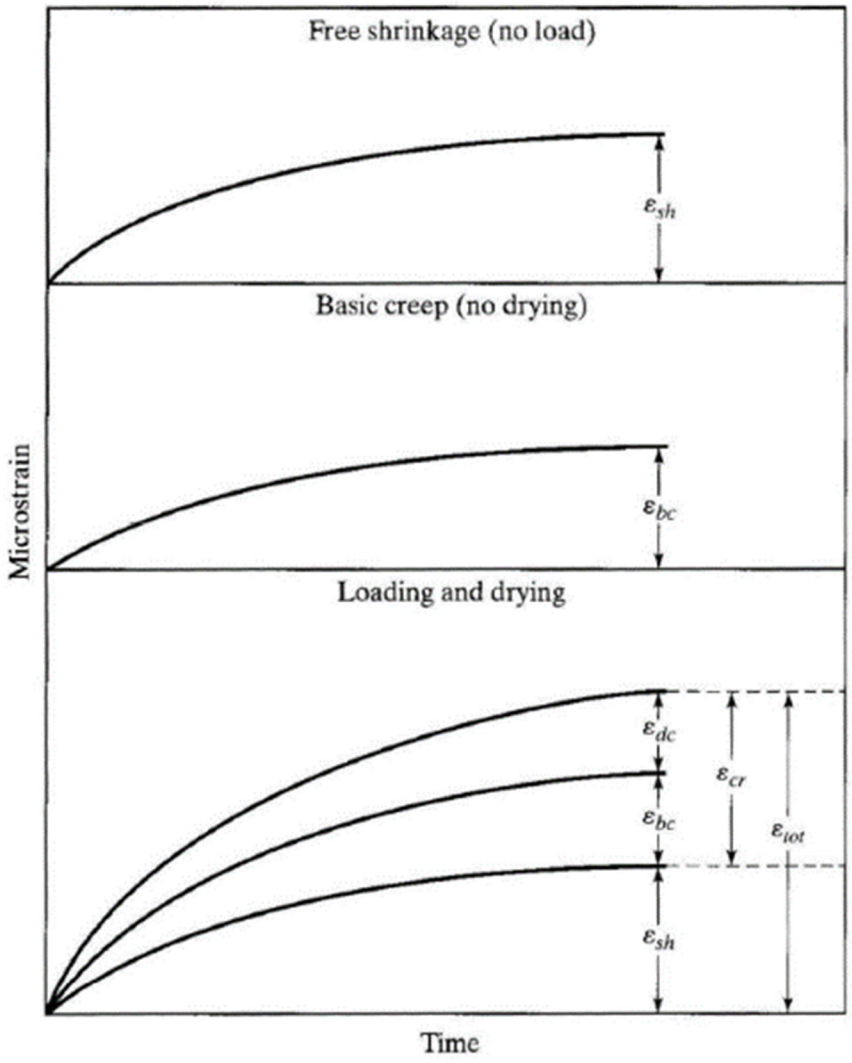

Figure 2-4: Creep behavior under simultaneous loading and drying (Neville 2011)

2.3.3.1 The Creep Mechanism

One of the most common theories for the driving mechanism of creep is related to the internal movement of adsorbed or intracrystalline water in the hydrated cement paste or also referred to as “internal seepage” (Neville 2011). Tests have proven that concrete that that has had all evaporable water removed practically exhibits no creep; however, the changes in creep behavior of concrete at high temperatures suggest that by the time all evaporable water has been removed, the water plays little to no role and the gel itself undergoes deformations due to creep (Neville 2011). Concrete deformations due to creep are not limited to small placements of concrete, but mass concrete structures can also be affected by this complex phenomena. According Neville

(2011), this proves that seepage of water to the outside of the concrete is not essential to the progress of basic creep, although such a process may take place in drying shrinkage.

Concrete can undergo creep deformations even when fully saturated. The capillary voids in the concrete do not remain full even when fully submerged in water; therefore, internal seepage is possible under any type of storage conditions (Neville 2011). This proves that creep of non-shrinking specimens is independent of the ambient relative humidity and that the fundamental cause of creep for both "in air" and "in water" is the same (Neville 2011).

2.3.3.2 Variables Affecting Creep

First, it should be noted that the hydrated cement paste in the concrete is what undergoes creep, not the aggregate that is used in the mixture. However, aggregate content does have a huge influence on how the hydrated cement paste will react when subjected to any type of loading. When the aggregate content of any given mixture is increased from 65 to 75 percent, there is a noticeable decrease in creep of approximately 10 percent; however, this correlation is far from a linear relationship (Neville 2011). It has been suggested that grading, maximum size, and the shape of the aggregate all effect creep behavior, but these parameters are only used to describe the aggregate content within the mixture providing that full consolidation has been achieved (Neville 2011). The physical properties of the aggregates also lead to variations in the creep behavior as well. For example, the higher the modulus of elasticity of the aggregate the higher the restraint, which results in a decrease in the creep strains in the hydrated cement paste (Neville 2011). Also, variations in the aggregate type can lead to changes in the total creep. Figure 2-5 illustrates the relationship between different aggregate types when subjected to a given loading over a certain length of time. Figure 2-5 shows that the creep behavior exhibited by sandstone is almost doubled as compared to quartzite.

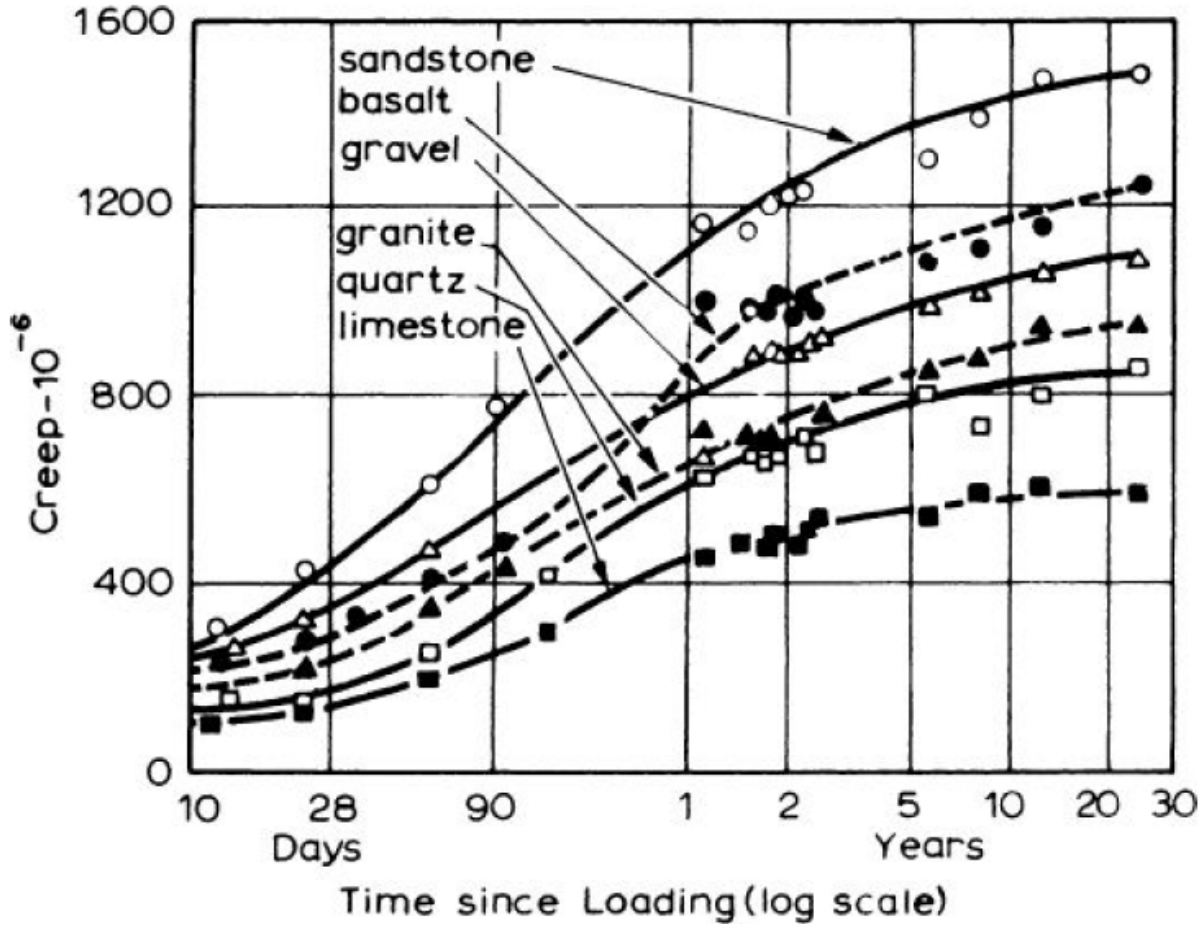

Figure 2-5: Creep behavior based on different aggregate types (Neville 2011)

Aggregate content and type have the largest impact on the creep strains that can develop throughout concrete, but it is not the only factor that can affect the total creep deformations. According to Neville (2011), the strength of concrete has a considerable influence on creep, and creep can be considered inversely proportional to the strength at the time of application of load for a wide range of values. As concrete matures, its compressive strength increases and as a result the creep deformations will decrease (Neville 2011). Another influencing factor on creep is the applied stress level that can result from loading. There is a direct proportionality between creep and the applied stress, but there are some exceptions that can be made for specimens that are loaded at a very early age (Neville 2011). The upper limit to this proportionality is approximately between 40 to 60 percent of the sustained loading. After 60 percent, severe microcracking may develop in the concrete, resulting in a highly nonlinear relationship between the applied stress levels and the total creep deformations (Neville 2011).

Some other important factors that can influence creep behavior include cement type, chemical admixtures, and also the ambient relative humidity. Cement type can affect the creep strains in concrete in the way that it affects the overall strength of the concrete. Different types of cement have different rates of hydration, which will result in differing strengths. Not only does the rate of hydration affect the strength gain of concrete, but the fineness of the cement will affect strength development at early ages and thus influence creep (Neville 2011).

According to Neville (2011), one of the most important external factors influencing creep is the relative humidity of the air surrounding the concrete. As mentioned earlier, drying creep is a volumetric change that must be considered in addition to basic creep. When the surrounding air around a specimen contains a high amount of moisture, the creep strains would be significantly lower as compared to a specimen whose surrounding ambient conditions are relatively dry. The specimen that is exposed to the lower relative humidity will exhibit higher creep strains due to the free moisture within the specimen being released to the environment as compared to the specimen that is exposed to a higher relative humidity (Neville 2011).

2.4 CREEP AND SHRINKAGE PREDICTION METHODS

This section covers the procedures for six different creep and shrinkage prediction models. The six models listed are most commonly used in today's research studies, and each section provides details on concrete properties and environmental conditions that are required to ensure accurate results are calculated. The six models that are being considered during this research study include:

- ACI 209 (ACI Committee 209 2008),
- AASHTO (2017),
- CEB MC 2010 (fib 2012),
- GL 2000 (Gardner and Lockman 2001), and
- B3 Model (Bazant and Baweja (2000).

2.4.1 ACI 209 Creep and Shrinkage Prediction Method

According to ACI 209 (2008), the overall shape of the creep and shrinkage development curve and the ultimate value are highly dependent on certain factors such as curing conditions, age at application of load, mixture proportions, ambient temperature, and relative humidity.

The creep model proposed by ACI 209 has two components that determine the asymptotic value and the time development of creep. The predicted parameter is not creep strain, but the creep coefficient $\varphi(t,t_o)$, which is defined as the ratio of creep strain to initial strain (ACI 209 2008).

For the standard conditions, in the absence of specific creep data for local aggregates and conditions, the average value proposed for the ultimate creep coefficient in Equation 2.1 is (ACI 209 (2008):

$$\Phi u = 2.35 \quad \text{Equation 2.1}$$

For the conditions other than the standard conditions, the value of the ultimate creep coefficient, Φu, needs to be modified by correction factors. As shown in Equations 2.2 through 2.9, ACI 209 (ACI 209 2008) suggests multiplying Φu by six factors, depending on particular conditions.

$$\Phi u = 2.35\gamma_{c,to}\gamma_{c,RH}\,\gamma_{c,vs}\,\gamma_{c,s}\gamma_{c,\psi}\gamma_{sh,\alpha} \quad \text{Equation 2.2}$$

With,

$\gamma_{c,to}$ being the loading age correction factor:

$$\gamma_{c,to} = 1.25t_o^{-0.118} \text{ (For moist curing)} \quad \text{Equation 2.3}$$

$$\gamma_{c,to} = 1.13t_o^{-0.094} \text{ (For steam curing)} \quad \text{Equation 2.4}$$

Where,

t_o= age of concrete when load is applied (days), only to be used for ages later than 7 days for non-accelerated-cured concrete and later than 1-3 days for steam-cured concrete.

$\gamma_{c,RH}$ being the ambient relative humidity correction factor:

$$\gamma_{c,to} = 1.27 - 0.67h \text{ (for h> 40\%)} \quad \text{Equation 2.5}$$

Where,

h= ambient relative humidity (%)

$\gamma_{c,vs}$ being the volume-to-surface area ratio correction factor:

$$\gamma_{c,vs} = \left(\frac{2}{3}\right)[1 + 1.13\exp(-0.54(V/S)] \quad \text{Equation 2.6}$$

Where,

V/S= volume-to-surface area ratio (in.)

$\gamma_{c,s}$ being the slump correction factor:

$$\gamma_{c,s} = 0.82 + 0.067s \quad \text{Equation 2.7}$$

Where,

s= observed slump (in.)

$\gamma_{c,\psi}$ being the fine aggregate percentage correction factor:

$$\gamma_{c,\psi} = 0.88 + 0.0024\psi \quad \text{Equation 2.8}$$

Where,

ψ= ratio of fine to total aggregate by weight (%)

$\gamma_{sh,\alpha}$ being the air content correction factor:

$$\gamma_{sh,\alpha} = 0.46 + 0.09\alpha \geq 1.0 \quad \text{Equation 2.9}$$

Where,

α= air content (%)

After applying all correction factors in order to adjust for conditions other than the standard, the ultimate creep coefficient, Φu, can then be multiplied by v_t, which is the parameter that accounts for the duration of loading:

$$\Phi(t, t_o) = v_t \Phi u \quad \text{Equation 2.10}$$

With,

$$v_t = \frac{(t - t_o)^{\psi}}{d + (t - t_o)^{\psi}} \quad \text{Equation 2.11}$$

Where,

$(t - t_o)$ = time since application of load (in days)

d *and* ψ = considered constants for a given member shape and size that define the time-ratio part, which can be taken as 10 and 0.6, respectively.

Equation 2.11 is only applicable to concretes with an age at loading of at least 7 days for non-accelerated-cured samples, and 1-3 days for steam-cured samples.

Once the creep coefficient is calculated, the predicted creep strain for the desired time step and associated loading is calculated by Equation 2.12.

$$predicted\ creep\ (t, t_i) = \Phi(t, t_o)\ \varepsilon_{initial-elastic} \qquad \text{Equation 2.12}$$

Where,

$\Phi(t, t_o)$ = Creep coefficient for a considered duration of loading, *t*

$\varepsilon_{initial-elastic}$ = Initial elastic strain upon loading

In addition to the predicted creep strains, another common method for describing the load-induced deformational behavior can be described using the compliance, $J(t,t_o)$. ACI 209 (2008) defines compliance as "the total load-induced strain (elastic strain plus creep strain) per unit stress caused by a unit uniaxial sustained load since loading age", which is shown in Equation 2.13. Equation 2.14 is the simplified form of how ACI 209 (2008) equates the compliance value.

$$J(t, t_o) = \frac{\varepsilon_{initial-elastic} + predicted\ creep(t, t_i)}{\sigma(t_o)} \qquad \text{Equation 2.13}$$

Where,

$\varepsilon_{initial-elastic}$= Initial elastic strain upon loading

$predicted\ creep(t, t_i)$= Predicted creep strain at desired time step, t_i

$\sigma(t_o)$ = Uniaxial stress resulting from loading (psi)

$$J(t, t_o) = \frac{1 + \Phi(t, t_o)}{E_{cmto}} \qquad \text{Equation 2.14}$$

Where,

$\Phi(t, t_o)$= creep coefficient for a considered duration of loading, *t*

E_{cmto}= Modulus of elasticity of concrete at time of loading (psi)

The shrinkage model proposed by ACI 209 (2008) shares many of the same correction factors that are associated with the prediction model for creep as previously discussed. The

shrinkage model also uses an ultimate value, which in the end are multiplied by a parameter that accounts for the concrete age.

For the standard conditions, in the absence of specific shrinkage data for local aggregates and conditions, the average value proposed for the ultimate shrinkage coefficient as shown in Equation 2.15 is (ACI 209 2008):

$$\varepsilon_{shu} = 780 \times 10^{-6} \qquad \text{Equation 2.15}$$

For the conditions other than the standard conditions, the value of the ultimate shrinkage coefficient ε_{shu} needs to be modified by correction factors. As shown in Equation 2.16, ACI 209 (2008) suggests multiplying ε_{shu} by seven factors, depending on particular conditions.

$$\varepsilon_{shu} = 780\gamma_{sh,tc}\gamma_{sh,RH}\,\gamma_{sh,vs}\,\gamma_{sh,s}\,\gamma_{sh,\psi}\,\gamma_{sh,c}\gamma_{sh,\alpha}\,\times 10^{-6} \qquad \text{Equation 2.16}$$

With,

$\gamma_{sh,tc}$ being the initial moist curing correction factor as shown in Table 2-1

Table 2-1: Shrinkage Correction Factors for Initial Moist Curing (ACI 209 2008)

Moist Curing Condition t_c, days	$\gamma_{sh,tc}$
1	1.20
3	1.10
7	1.00
14	0.93
28	0.86
90	0.75

$\gamma_{sh,RH}$ being the ambient relative humidity correction factor:

$$\gamma_{sh,RH} = \begin{cases} 1.40 - 1.02h \;\; for \; 0.40 \leq h \leq 0.80 \\ 3.00 - 3.0h \; for \; 0.80 \leq h \leq 1.00 \end{cases} \qquad \text{Equation 2.17}$$

Where,

h= ambient relative humidity (%)

$\gamma_{sh,vs}$ being the volume-to-surface area ratio correction factor:

$$\gamma_{sh,vs} = 1.2\exp(-0.12(V/S)] \quad \text{Equation 2.18}$$

Where,

V/S= volume-to-surface area ratio (in.)

$\gamma_{sh,s}$ being the slump correction factor:

$$\gamma_{sh,s} = 0.89 + 0.041s \quad \text{Equation 2.19}$$

Where,

s= observed slump (in.)

$\gamma_{sh,\psi}$ being the fine aggregate percentage correction factor:

$$\gamma_{sh,\psi} = \begin{cases} 0.30 + 0.014\psi \; for \; \psi \leq 50\% \\ 0.90 + 0.002\psi \; for \; \psi > 50\% \end{cases} \quad \text{Equation 2.20}$$

Where,

ψ= ratio of fine to total aggregate by weight (%)

$\gamma_{sh,c}$ being the air content correction factor:

$$\gamma_{sh,c} = 0.75 + 0.00036c \quad \text{Equation 2.21}$$

Where,

c= cement content (lb/yd^3)

$\gamma_{sh,\alpha}$ being the air content correction factor:

$$\gamma_{sh,\alpha} = 0.95 + 0.008\alpha \geq 1.0 \quad \text{Equation 2.22}$$

Where,

α= air content (%)

After applying all correction factors in order to adjust for conditions other than the standard, the ultimate shrinkage coefficient, ε_{shu}, can then be multiplied by v_t, which is the parameter that adjusts for the concrete age:

$$\varepsilon_{shu}(t, t_c) = v_t \varepsilon_{shu} \quad \text{Equation 2.23}$$

With,

$$v_t = \frac{(t-c)^\alpha}{f + (t - t_c)^\alpha} \quad \text{Equation 2.24}$$

Where,

$(t - t_c)$ = being the time since drying has started (in days)

f and α = considered constants for a given member shape and size that define the time-ratio part. ACI 209 (1992) recommends a value for *f* of 35 and 55 for 7 days of moist curing and 1 to 3 days of steam curing, respectively, while a value of 1 is suggested for α.

2.4.2 AASHTO 2017 Creep and Shrinkage Prediction Method

AASHTO LRFD 2017 is the governing set of requirements that ALDOT follows in all areas of design. Studies conducted by Tadros (2003) and Rizkalla et al. (2007) highly influenced the methods used by AASHTO 2017 in the prediction of creep and shrinkage. These references can be found in section C5.4.2.3.2 of the AASHTO LRFD Bridge Design Specifications (AASHTO 2017). The AASHTO 2017 method also uses an ultimate creep coefficient, which is then applied to the compressive strain caused by permanent loads to obtain the strain due to creep.

The governing equation used to predict the creep coefficient is given in Equation 2.25, along with the key environmental and mixture factors shown in Equation 2.26 through Equation 2.29, which account for:

- Volume-to-surface ratio,
- Humidity correction factor,
- Concrete strength factor, and
- Time development factor.

$$\psi\,(t, t_i) = 1.9 k_s k_{hc}\, k_f\, k_{td} t_i^{-0.118} \qquad \text{Equation 2.25}$$

With,

k_s being the volume-to-surface area ratio correction factor:

$$k_s = 1.45 - 0.13(V/S) \geq 1.0 \qquad \text{Equation 2.26}$$

Where,

V/S= volume-to-surface area ratio (in.)

k_{hc} being the ambient relative humidity correction factor:

$$k_{hc} = 1.56 - 0.008H \quad \text{Equation 2.27}$$

Where,

H= average annual ambient relative humidity (%)

k_f being the concrete strength factor:

$$k_f = \frac{5}{1 + f'_{ci}} \quad \text{Equation 2.28}$$

Where,

f'_{ci}= Design concrete compressive strength at time of initial loading. If concrete age at time of initial loading is unknown at design time, f'_{ci} may be taken as $0.80f'_c$ (ksi).

k_{td} being the time development factor:

$$k_{td} = \frac{t}{12\left(\frac{100 - 4f'_{ci}}{f'_{ci} + 20}\right) + t} \quad \text{Equation 2.29}$$

Where,

$t =$ Maturity of concrete (days), defined as age of concrete between time of loading for creep calculations, and time being considered for analysis of creep effects

t_i is the age of concrete at time of load application (days)

In the AASHTO LRFD 2017 model, the value of t_i is the chronological age of the concrete in days if accelerated curing is used. After the creep coefficient is calculated, the predicted creep strain for the desired time interval can be determined by using Equation 2.30.

$$predicted\ creep\ (t, t_i) = \psi\ (t, t_i) \times \varepsilon_{initial-elastic} \quad \text{Equation 2.30}$$

Where,

$\psi\ (t, t_i)$= Creep coefficient for a considered duration of loading, *t*

$\varepsilon_{initial-elastic}$ = Initial elastic strain upon loading

Many of the same parameters used in the AASHTO model used in creep prediction are also implemented into the shrinkage prediction model. The governing equation used in the prediction of shrinkage strains,ε_{sh} at time *t*, may is also shown in Equation 2.31:

$$\varepsilon_{sh} = k_s k_{hs}\, k_f\, k_{td}(0.48 \times 10^{-3}) \qquad \text{Equation 2.31}$$

All parameters that were used in the creep prediction model to account for volume-to-surface ratio and the effects of concrete strength remained constant for the shrinkage prediction model; however, the factor to adjust for the ambient relative humidity and the time development are shown in Equation 2.32 and Equation 2.33, respectively.

With,

k_{hs} being the ambient relative humidity correction factor:

$$k_{hs} = 2.00 - 0.014H \qquad \text{Equation 2.32}$$

Where,

H= average annual ambient relative humidity (%)

k_{td} being the time development factor:

$$k_{td} = \frac{t}{12\left(\frac{100 - 4f'_{ci}}{f'_{ci} + 20}\right) + t} \qquad \text{Equation 2.33}$$

Where,

t = Defined as age of concrete at end of curing for shrinkage calculations, and time being considered for analysis of shrinkage effects (days)

If the concrete is exposed to drying before 5 days of curing have elapsed, AASHTO 2017 states that all shrinkage strains should be increased by 20 percent to ensure accurate results.

2.4.3 CEB MC 2010 Creep and Shrinkage Prediction Method

The Model Code was developed to aid in providing an international harmonization of codes, and as a basis for the Eurocode for Concrete Structures, which is now introduced in most European countries (*fib* 2012). The first Model Code for concrete structures was a product between two committees known as the European International Concrete Committee (CEB) and the International Federation of Prestressing (FIP), but later the two committees combined to form

the International Federation for Structural Concrete (*fib*). The Model Code was first published in 1978, and has been revised over the years with the latest version being published in 2012, which is referred to as MC 2010 (*fib* 2012). The creep and shrinkage prediction models of MC 2010 relates very closely to its predecessor MC 1990 (1999). MC 1990 (1999) underwent changes to incorporate the effects of high-strength concretes, and those changes were carried over to MC 2010.

Much like the ACI 209 model, CEB MC 2010 uses a creep coefficient, $\varphi(t, t_o)$, which is calculated based on many different parameters. The creep coefficient is a relationship between the notional creep coefficient, φ_o, and the coefficient used to describe the development of creep with time after loading, $\beta_c(t,t_0)$.

The formula used to evaluate the notional creep coefficient is presented in Equation 2.34 along with all the parameters that must be taken into account to properly adjust for conditions other than the standard. Note that MC 2010 is in metric units; therefore, any data that is processed must be properly converted if other units are being used. Equation 2.34 represents the notional creep coefficient.

$$\varphi_o = \varphi_{RH}\beta(f_{cm})\beta(t_o) \qquad \text{Equation 2.34}$$

With,

φ_{RH} being a factor to allow for the effect of relative humidity:

$$\varphi_{RH} = 1 + \frac{1 - RH/100}{0.1\sqrt[3]{h_o}} \quad for\ f_{cm} \leq 35\ MPa \qquad \text{Equation 2.35}$$

$$\varphi_{RH} = \left[1 + \frac{1 - RH/100}{0.1\sqrt[3]{h_o}}\alpha_1\right]\alpha_2 \quad for\ f_{cm} > 35\ MPa \qquad \text{Equation 2.36}$$

Where,

RH= relative humidity of the ambient environment in %

h_o= notional size of the member in mm

$$h_o = \frac{2A_c}{u} \qquad \text{Equation 2.37}$$

With,

A_c= Cross-Sectional Area (mm^2)

u= Perimeter of the member in contact with the atmosphere (mm)

α_1, α_2, α_3= coefficients to consider the influence of concrete strength

$$\alpha_1 = [\frac{35}{f_{cm}}]^{0.7} \quad \text{Equation 2.38}$$

$$\alpha_2 = [\frac{35}{f_{cm}}]^{0.2} \quad \text{Equation 2.39}$$

$$\alpha_3 = [\frac{35}{f_{cm}}]^{0.5} \quad \text{Equation 2.40}$$

With,

f_{cm} = mean compressive strength of concrete at 28 days (MPa)

$\beta(f_{cm})$ being a factor to allow for the effect of concrete strength:

$$\beta(f_{cm}) = \frac{16.8}{\sqrt{f_{cm}}} \quad \text{Equation 2.41}$$

Where,

f_{cm} = mean compressive strength of concrete at 28 days (MPa)

$\beta(t_o)$ being a factor to allow for the effect of concrete age at loading:

$$\beta(t_o) = \frac{1}{(0.1 + t_o^{0.20})} \quad \text{Equation 2.42}$$

Where,

t_o = age of concrete at loading in days

Equation 2.43 represents the coefficient to describe the development of creep with time after loading.

$$\beta_c(t, t_o) = [\frac{(t - t_o)}{(\beta_H + t - t_o)}]^{0.3} \quad \text{Equation 2.43}$$

With,

β_H being a coefficient depending on the relative humidity and notional member size:

$$\beta_H = 1.5[1 + (0.012RH)^{18}]h_o + 250 \leq 1500$$
$$for\ f_{cm} \leq 35\ MPa \quad \text{Equation 2.44}$$

$$\beta_H = 1.5[1 + (0.012RH)^{18}]h_o + 250\alpha_3 \leq 1500\alpha_3$$
$$for\ f_{cm} > 35\ MPa \quad \text{Equation 2.45}$$

Where,

RH= relative humidity of the ambient environment in %

h_o= notional size of the member (mm)

α_3= coefficient to consider the influence of concrete strength

t_o being a coefficient to modify the age at loading:

$$t_o = t_{o,T}\left(\frac{9}{2 + t_{o,T}^{1.2}} + 1\right)^{\alpha} \geq 0.5 \qquad \text{Equation 2.46}$$

Where,

$t_{o,T}$ = temperature adjusted age of concrete at loading in days

$$t_T = \sum_{i=1}^{n} \exp\{-[(4000/(273 + T\Delta t_i)) - 13.65]\}\Delta t_i \qquad \text{Equation 2.47}$$

With,

t_T = temperature adjusted concrete age (replaces $t_{o,T}$)

$T(\Delta t_i)$= temperature in °C during time period Δt_i

Δt_i = number of days where temperature *T* prevails

α = power which depends on type of cement as shown in Table 2-2:

Table 2-2: Coefficients of α depending on type of cement for use in Equation 2.46 (fib 2012)

Strength Class of Concrete	α
32.5 N	800
32.5 R, 42.5 N	700
42.5 R, 52.5 N, 52.5 R	600

After all adjustments have been made to account for the different parameters that effect both the notional creep coefficient and the time dependent factor, the relationship between the two can be determined. Both of these factors are directly related to the creep coefficient as shown in Equation 2.48.

$$\varphi(t, t_o) = \varphi_o \beta_c(t, t_o) \qquad \text{Equation 2.48}$$

Once the creep coefficient has been determined, the predicted creep strain can be calculated by multiplying this coefficient by the elastic strain resulting from the applied load. Equation 2.49 below illustrates this relationship:

$$predicted\ creep\ (t, t_i) = \varphi(t, t_o) \times \varepsilon_{initial-elastic} \qquad \text{Equation 2.49}$$

Where,

$\varphi(t, t_o)$ = Creep coefficient for a considered duration of loading, *t*

$\varepsilon_{initial-elastic}$ = Initial elastic strain upon loading

In addition to the predicted creep strain, the compliance can also be calculated for a desired time step using the creep coefficient from Equation 2.48. The predicted compliance can be calculated using Equation 2.50.

$$J(t, t_o) = \frac{1}{E_{cmto}} + \frac{\varphi(t, t_o)}{E_{cm28}} \qquad \text{Equation 2.50}$$

Where,

$\varphi(t, t_o)$= creep coefficient for a considered duration of loading, *t*

E_{cmto}= Modulus of elasticity of concrete at time of loading (MPa or psi)

E_{cm28}= Modulus of elasticity of concrete at 28 days (MPa or psi)

As mentioned earlier, MC 2010 shares many of the same characteristics as MC 1990 in the calculation of total shrinkage due to the effects of high-strength concrete. The shrinkage prediction model is divided into two separate stages to accommodate both drying shrinkage and autogenous shrinkage of the concrete. This relationship is illustrated in Equation 2.51:

$$\varepsilon_{cs}(t, t_s) = \varepsilon_{cas}(t) + \varepsilon_{cds}(t, t_s) \qquad \text{Equation 2.51}$$

Where,

$\varepsilon_{cs}(t,t_s)$ = total shrinkage strain,

$\varepsilon_{cas}(t)$ = autogenous shrinkage strain,

$\varepsilon_{cds}(t,t_s)$ = drying shrinkage strain,

t = age of the concrete at the moment considered (days), and

t_s = age of the concrete when drying commences (days).

The autogenous component of the concrete can be calculated using Equation 2.52:

$$\varepsilon_{cas}(t) = \varepsilon_{cas0}(f_{cm})\beta_{as}(t) \quad \text{Equation 2.52}$$

With,

$\varepsilon_{cas0}(f_{cm})$ being the notional autogenous shrinkage coefficient:

$$\varepsilon_{cas0}(f_{cm}) = -\alpha_{as}\left(\frac{f_{cm}/10}{6 + f_{cm}/10}\right)^{2.5} \times 10^{-6} \quad \text{Equation 2.53}$$

Where,

f_{cm} is the mean compressive strength at 28 days (MPa)

α_{as} is the cement type coefficient defined in Table 2-3 below

Table 2-3: Coefficients of α_i used for total shrinkage calculations (fib 2012)

Strength Class of Concrete	α_{as}	α_{ds1}	α_{ds2}
32.5 N	800	3	0.013
32.5 R, 42.5 N	700	4	0.012
42.5 R, 52.5 N, 52.5 R	600	6	0.012

$\beta_{as}(t) =$ the time development function of autogenous shrinkage:

$$\beta_{as}(t) = 1 - \exp[-0.2\sqrt{t}] \quad \text{Equation 2.54}$$

The drying shrinkage strain can be calculated using Equation 2.55:

$$\varepsilon_{cds}(t, t_s) = \varepsilon_{cds0}(f_{cm})\beta_{RH}(RH)\beta_{ds}(t - t_s) \quad \text{Equation 2.55}$$

With,

$\varepsilon_{cds0}(f_{cm})$ is the notional drying shrinkage coefficient:

$$\varepsilon_{cds0}(f_{cm}) = [(220 + 110\alpha_{ds1})\exp(-\alpha_{ds2}f_{cm})] \times 10^{-6} \quad \text{Equation 2.56}$$

Where,

α_{ds1} and α_{ds2} = cement type coefficients defined in Table 2-3

$\beta_{RH}(RH)$ is the function to account for relative humidity

$$\beta_{RH}(RH) = \begin{cases} -1.55[1-(RH/100)^3] & for\ 40 \leq RH < 99\%\beta_{s1} \\ 0.25 & for\ RH \geq 99\%\beta_{s1} \end{cases}$$ Equation 2.57

Where,

RH = the relative humidity expressed as a percentage

β_{s1} = coefficient describing self-desiccation in high-performance concrete

With,

$$\beta_{s1} = (\frac{35}{f_{cm}})^{0.1} \leq 1.0$$ Equation 2.58

$\beta_{ds}(t-t_s)$ is the time development function for shrinkage

$$\beta_{ds}(t-t_s) = (\frac{(t-t_s)}{0.035h^2+(t-t_s)})^{0.5}$$ Equation 2.59

Where,

h = the notional member size described in Equation 2.37 (mm)

2.4.4 GL 2000 Creep and Shrinkage Prediction Method

The GL 2000 Model was developed by Gardner and Lockman (2001). The creep and shrinkage procedures within the GL 2000 Model were influenced by the Model Code 1990 (1999). According to Gardner and Lockman (2001), the method can be used regardless of the chemical admixture types or SCM's that are present in the concrete, casting temperature, or curing regimes. It uses the relative humidity, element size, and strength at loading. However, one key difference is the model requires the 28-day compressive strength in order to accurately predict the creep strains at varying time intervals.

To accurately predict the creep strains associated with the GL 2000 Model, Equation 2.60 is used to relate the creep coefficient and the modulus of elasticity at an age of 28 days. Due to the GL 2000 Model not having a term directly related to the relationship between the creep coefficient and modulus of elasticity, to simplify matters, it is referred to as "specific creep" (Gardner and Lockman 2001).

$$specific\ creep\ (t,t_o) = \frac{\Phi_{28}}{E_{cm28}} = \frac{\Phi(t,t_o)}{E_{cm28}}$$ Equation 2.60

With,

Φ_{28}= creep coefficient at 28 days,

$\Phi(t, t_o)$= creep coefficient at any time *t* (days) and for any loading age t_o (days), and

E_{cm28}= modulus of elasticity at 28 days (psi).

Once the specific creep has been calculated, the compliance can thus be determined by taking the initial elastic strain, which is the reciprocal of the modulus of elasticity at the age of loading, and adding it to the specific creep as shown in Equation 2.61:

$$J(t, t_o) = \frac{1}{E_{cmto}} + specific\ creep\ (t, t_o) \qquad \text{Equation 2.61}$$

With,

E_{cmto}= modulus of elasticity at time of loading (psi)

The creep coefficient for the GL 2000 Model consists of three individual terms. In Equation 2.62, the first two terms are used to account for basic creep strains in the concrete, and the third term is used to account for drying creep strains.

$$\Phi(t, t_o) = \Phi(t_c)[2\left(\frac{(t-t_o)^{0.3}}{(t-t_o)^{0.3}+14}\right) + \left(\frac{7}{t_o}\right)^{0.5}(\frac{t-t_o}{t-t_o+7})^{0.5} + 2.5(1-1.086h^2)(\frac{t-t_o}{t-t_o+77\left(\frac{v}{s}\right)^2})^{0.5} \qquad \text{Equation 2.62}$$

With,

t = the age of the concrete (days)

t_o = the age of concrete at loading (days)

h = the relative humidity expressed as a decimal

V/S = the volume-surface ratio (in.)

$\Phi(t_c)$= correction term for the effect of drying before loading

Where,

$$\Phi(t_c) = 1 \quad if\ t_o = t_c \qquad \text{Equation 2.63}$$

$$\Phi(t_c) = [1 - \left(\frac{t_o - t_c}{t_o - t_c + 77(V/S)^2}\right)^{0.5}]^{0.5} \quad if\ t_o > t_c \qquad \text{Equation 2.64}$$

With,

t_c = age when drying started (days)

After determining the compliance, $J(t, t_o)$, from Equation 2.61, the predicted creep strain can be calculated using Equation 2.65 below.

$$predicted\ creep\ (t, t_i) = J(t, t_o)\sigma(t_o) - \varepsilon_{initial-elastic} \qquad \text{Equation 2.65}$$

Where,

$J(t, t_o)$ = Compliance at any time *t* (days) and for any loading age t_o (days),

$\sigma(t_o)$ = Uniaxial stress resulting from loading (psi)

$\varepsilon_{initial-elastic}$ = Initial elastic strain upon loading.

Shrinkage strains for the GL 2000 Model can be calculated the using Equation 2.66. This equation uses an ultimate shrinkage strain that can be reduced based on the relative humidity of the surrounding environment and also a time correction factor for when drying starts.

$$\varepsilon_{sh}(t, t_c) = \varepsilon_{shu}\beta(h)\beta(t - t_c) \qquad \text{Equation 2.66}$$

With,

ε_{shu} = the ultimate shrinkage strain,

$\beta(h)$ = the correction term for the effects of humidity, and

$\beta(t - t_c)$ = the correction term for the effect of time on drying.

The ultimate shrinkage strain can be calculated using Equation 2.67:

$$\varepsilon_{shu} = 900k\left(\frac{4350}{f_{cm28}}\right)^{0.5} \quad (1 \times 10^{-6}\ in./in.) \qquad \text{Equation 2.67}$$

Where,

f_{cm28} = the mean compressive strength at 28 days (psi)

k = shrinkage constant based on cement type (Table 2-4)

Table 2-4: Values for *k* (Gardner and Lockman 2001)

Cement Type	***k***
Type I	1.00
Type II	0.75
Type III	1.15

The correction term for the effect of humidity can be calculated using Equation 2.68:

$$\beta(h) = 1 - 1.18h^4 \qquad \text{Equation 2.68}$$

Where,

h = the relative humidity expressed as a decimal.

The function to account for time development of shrinkage can be calculated using Equation 2.69:

$$\beta(t - t_c) = [\frac{(t - t_c)}{(t - t_c) + 77(V/S)^2}]^{0.5} \qquad \text{Equation 2.69}$$

Where,

t = the age of the concrete (days),

t_c = the age of concrete when drying starts (days), and

V/S = the volume-surface ratio (in.).

2.4.5 B3 Creep and Shrinkage Prediction Model

The B3 Model is intended to be an improvement over the ACI 209 model, but only applies to portland cement mixtures with the parameter ranges listed in Table 2-5 (Bazant and Baweja 2000). The formulae are valid for concretes cured for at least one day, and can also be applied to different portland cement mixtures given that proper interpolation of the parameters is applied to the mix design (Bazant and Baweja 2000).

Table 2-5: Material Parameters for B3 Model (Bazant and Baweja 2000)

Parameter	Range of Values
Water-Cement Ratio, w/c	$0.35 \leq w/c \leq 0.85$
Aggregate-Cement Ratio, a/c	$2.5 \leq a/c \leq 13.5$
Compressive Strength (psi)	$2500 \leq f_c' \leq 10{,}000$
Cement Content (pcf), c	$10 \leq c \leq 45$
Service Stress	Up to $0.45f_c'$

The Model B3 consists of many mathematical equations used to define the creep and drying shrinkage behavior of concrete. A compliance function is used, which describes the

relationship between an instantaneous strain due to a unit of stress, creep at a constant moisture content and no moisture movement through the material, and also drying shrinkage of the concrete. Equation 2.70 represents the compliance function for the B3 Model (Bazant and Baweja 2000):

$$J(t, t_0) = q_1 + C_0(t, t_0) + C_d(t, t_0, t_c) \qquad \text{Equation 2.70}$$

With,

q_1 = the instantaneous strain due to unit stress $(110^{-6}/\,psi)$,

$C_0\,(t,t_0)$ = the compliance function describing basic creep $(110^{-6}/\,psi)$,

$C_d\,(t,t_0,t_c)$ = compliance function to account for drying creep $(110^{-6}/\,psi)$,

t_0 = the loading age in days,

t = the age of concrete in days, and

t_c = the age when drying commenced in days.

The instantaneous strain due to unit stress can be calculated using Equation 2.71:

$$q_1 = 0.6 \times 10^6 / E_{cm28} \qquad \text{Equation 2.71}$$

With,

E_{cm28} = the elastic modulus of the concrete at 28 days (psi).

The basic creep compliance function is more conveniently defined by its time rate than its value, and can be altered to fit certain mixture designs. Equation 2.72 shows the different parameters that are used to define this function:

$$C_0(t, t_0) = q_2 Q(t, t_0) + q_3 \ln[1 + (t - t_0)^n] + q_4 \ln(t/t_0) \qquad \text{Equation 2.72}$$

With,

$q_2Q(t,t_0)$ = the aging viscoelastic compliance term $(1 \times 10^{-6}/psi)$,

q_3 = the non-aging viscoelastic aging parameter $(1 \times 10^{-6}/psi)$, and

q_4 = the aging flow compliance parameter $(1 \times 10^{-6}/psi)$.

Equations 2.73 through 2.77 are used to determine all terms associated with the aging viscoelastic term:

$$q_2 = 451.1\sqrt{c}{f_{cm28}}^{-0.9} \quad \text{Equation 2.73}$$

Where,

c = the cement content (lb/ft^3), and

f_{cm28} = the mean compressive strength at 28 days (psi).

The term $Q(t,t_0)$ is an approximate binomial integral that must be multiplied by the parameter q_2 to obtain the aging viscoelastic term. It is calculated using Equation 2.74:

$$Q(t,t_0) = Q_f(t_0)[1 + (\frac{Q_f(t_0)}{Z(t,t_0)})^{r(t_0)}]^{-1/r(t_0)} \quad \text{Equation 2.74}$$

With,

$$Q_f(t_o) = [0.086(t_o)^{2/9} + 1.21(t_o)^{4/9}]^{-1} \quad \text{Equation 2.75}$$

$$Z(t,t_o) = (t_o)^{-m}\ln[1 + (t - t_o)^n] \quad \text{Equation 2.76}$$

$$r(t_o) = 1.7(t_o)^{0.12} + 8 \quad \text{Equation 2.77}$$

Where,

m and n are empirical parameters whose values can be taken as 0.5 and 0.1, respectively

The nonaging viscoelastic term q_3 can be calculated using Equation 2.78:

$$q_3 = 0.29(w/c)^4 q_2 \quad \text{Equation 2.78}$$

Where,

w = the water content in (lb/ft^3)

c = the cement content (lb/ft^3)

The aging flow compliance parameter q_4 can be calculated using Equation 2.79:

$$q_4 = 0.14(a/c)^{-0.7} \quad \text{Equation 2.79}$$

Where,

a = the aggregate content (lb/ft^3)

c = the cement content (lb/ft^3)

When concrete is exposed to drying, additional creep can develop in addition to the creep that is developed due to loading. Equations 2.80 through 2.89 demonstrate how drying interacts with the basic creep function, and also show how environmental parameters affect basic creep within the concrete:

$$C_d(t, t_c) = q_5[\exp\{-8H(t)\} - \exp\{-8H(t_0)\}]^{1/2} \quad \text{Equation 2.80}$$

With,

q_5 = the drying creep compliance parameter $(1 \times 10^{-6}/psi)$

$H(t)$ and $H(t_0)$ = spatial averages or pore relative humidity

The drying creep compliance parameter can be calculated using the expression:

$$q_5 = 7.57 \times 10^5 {f_{cm28}}^{-1} |\varepsilon_{sh\infty}|^{-0.6} \quad \text{Equation 2.81}$$

With,

$\varepsilon_{sh\infty}$ is the ultimate shrinkage strain, which can be calculated using:

$$\varepsilon_{sh\infty} = -\varepsilon_{s\infty} \frac{E_{607}}{E_{cm(t_c+\tau_{sh})}} \quad \text{Equation 2.82}$$

Where,

$E_{607}/E_{cm(t_c+\tau_{sh})}$ = a time factor for ultimate shrinkage

$$E_{cmt} = E_{cm28}\left(\frac{t}{4 + 0.85t}\right)^{0.5} \quad \text{Equation 2.83}$$

$\varepsilon_{s\infty}$ = constant that is calculated using the equation below:

$$\varepsilon_{s\infty} = -\alpha_1\alpha_2\left[26w^{2.1}{f_{cm28}}^{-0.28} + 270\right]\ (1 \times 10^{-6}\ in./in.) \quad \text{Equation 2.84}$$

Where,

α_1 = the coefficient for cement type defined in Table 2-6

Table 2-6: Values of α_1 to account for cement type, B3 Model (Bazant and Baweja 2000)

Type of Cement	α_1
Type I	1.00
Type II	0.85
Type III	1.10

α_2 = the coefficient for curing condition defined in Table 2-7

Table 2-7: Values of α_2 to account for curing method, B3 Model (Bazant and Baweja 2000)

Curing Method	α_2
Steam Cured	0.75
Cured in Water or at 100% relative humidity	1.00
Sealed during curing or normal curing in air with initial protection against dying	1.20

The functions to account for spatial averages related to relative humidity can be calculated using Equations 2.85 and 2.86:

$$H(t) = 1 - (1 - h)S(t - t_c) \quad \text{Equation 2.85}$$

$$H(t_o) = 1 - (1 - h)S(t - t_0) \quad \text{Equation 2.86}$$

With,

h = the relative humidity expressed as a decimal

$S(t - t_c)$ = the time function for shrinkage of the concrete:

$$S(t - t_c) = \tanh[(\frac{t - t_c}{\tau_{sh}})^{0.5}] \quad \text{Equation 2.87}$$

$S(t_0 - t_c)$ = the time function for concrete at age of loading:

$$S(t_0 - t_c) = \tanh[(\frac{t_0 - t_c}{\tau_{sh}})^{0.5}] \quad \text{Equation 2.88}$$

Where,

τ_{sh} = the shrinkage half-time in days:

$$\tau_{sh} = 190.8 t_c^{-0.08} {f_{cm28}}^{-0.25} [2k_s(V/S)]^2 \quad \text{Equation 2.89}$$

Where,

k_s = the cross-section shape correction factor (Table 2-8)

Table 2-8: Values of k_s to account for cross section shape, B3 Model (Bazant and Baweja 2000)

Cross Section Shape	k_s
Infinite Slab	1.00
Infinite Cylinder	1.15
Infinite Square Prism	1.25
Sphere	1.30
Cube	1.55

In a similar manner to some of the previous models described, the B3 Model also takes into consideration if the concrete is cured at elevated temperatures by adjusting the age at loading, t_o. The equation that is affected by this parameter is the basic creep compliance, $C_0(t, t_0)$. The equivalent-age at loading when curing takes place at elevated temperatures is described in Equation 2.90.

$$t'_o = \sum_{i=1}^{n} \exp[\frac{U_h}{R}\left(\frac{1}{T_o} - \frac{1}{T}\right)]\Delta t_i \quad \text{Equation 2.90}$$

Where,

t'_o = Equivalent-age at loading (days),

U_h/R = 5000°K,

T_o = Reference absolute temperature (293°K),

T = Temperature in °K during time period Δt_i, and

Δt_i = Number of days where temperature T prevails.

After evaluating the equivalent-age at loading, the equivalent-age maturity of the concrete after loading can be described using Equation 2.91.

$$t'_T = \sum_{i=1}^{n} \exp[\frac{U_c}{R}\left(\frac{1}{T_o} - \frac{1}{T}\right)]\Delta t_i \quad \text{Equation 2.91}$$

Where,

t'_T= Equivalent-age of concrete after loading (days),

U_c/R= $110w^{-0.27}{f_{cm28}}^{0.54}$ (°K),

T_o= Reference absolute temperature (293°K),

T= Temperature in °K during time period Δt_i, and

Δt_i= Number of days where temperature T prevails.

One final parameter that must be equated before evaluating the basic creep compliance function is a parameter, R_T, which can be calculated using Equation 2.92:

$$R_T = \exp[\frac{U'_c}{R}\left(\frac{1}{T_o} - \frac{1}{T}\right)] \qquad \text{Equation 2.92}$$

Where,

R_T= Parameter to adjust the basic creep compliance for elevated temperatures,

U'_c= $0.18U_c$,

R= Universal gas constant,

T_o= Reference absolute temperature (293°K), and

T= Temperature in °K.

After determining all the parameters covered in Equations 2.90 through 2.92, they can then be inputted into the basic creep compliance function to evaluate a more accurate representation of the predicted compliance values when concrete is cured at elevated temperatures. The result of the basic creep compliance is presented in Equation 2.93.

$$C_0(t'_T, t'_o) = R_T[q_2 Q(t'_T, t'_o) + q_3 \ln[1 + (t'_T - t'_o)^n]$$

$$+q_4 \ln(t'_T/t'_o)] \quad (1 \times 10^{-6}/psi) \qquad \text{Equation 2.93}$$

After calculating the compliance using the parameters previously stated, the creep coefficient, $\phi(t, t')$, can be calculated using Equation 2.94. Once the creep coefficient is determined, the predicted creep strain at the desired time interval can be calculated using Equation 2.95.

$$\phi(t, t_o) = E(t_o)J(t, t_o) - 1 \qquad \text{Equation 2.94}$$

Where,

$E(t_o) =$ The modulus of elasticity at loading (psi), and

$J(t, t_o) =$ Compliance at time *t* $(1 \times 10^{-6}/psi)$

$$predicted\ creep\ (t, t_i) = \phi(t, t_o) \times \varepsilon_{initial-elastic} \qquad \text{Equation 2.95}$$

Where,

$\phi(t, t_o)$ = creep coefficient at any time *t* (days), and

$\varepsilon_{initial-elastic}$ = Initial elastic strain upon loading.

The B3 Model uses a relationship relating an ultimate shrinkage strain, a humidity dependence factor, and a time factor to account for when drying of the concrete begins. Both the ultimate shrinkage strain and the time factor associated with this relationship were discussed previously in the equations used to predict the creep and compliance values when using the B3 Model. Equation 2.96 represents the relationship between the ultimate shrinkage strain, the humidity dependence factor, and the time factor to account for when drying of the concrete begins:

$$\varepsilon_{sh}(t, t_c) = -\varepsilon_{sh\infty} k_h S(t - t_c) \qquad \text{Equation 2.96}$$

With,

$\varepsilon_{sh\infty}$ = the ultimate shrinkage strain

k_h = the humidity dependence factor

$S(t - t_c)$ = the time curve to account for drying

The humidity dependence factor k_h can be computed using Table 2-9:

Table 2-9: Humidity dependence factor k_h, B3 Model (Bazant and Baweja 2000)

Relative Humidity	$\boldsymbol{k_h}$
h ≤ 0.98	$k_h = 1 - h^3$
h = 1.00	$k_h = -0.2$
0.98 < h ≤ 1.00	$k_h = 12.74 - 12.94h$

2.5 PREVIOUS STUDIES RELATED TO CREEP OF CSC AND SEGMENTAL BRIDGES

Many different research projects have been conducted at Auburn University on creep and shrinkage behavior of both conventional slump concrete (CSC) and self-consolidating concrete (SCC). This section will outline two of the most recent studies conducted at Auburn University by Mante (2016) and Schindler et al. (2017) along with a quick overview of the experimental procedure that they followed during testing. Also, a case study covering the time-dependent effects of the Chevire bridge in France (Raphael et al. 2018). Also, a study by Malm et al. (2010) are covered to show how time-dependent properties can affect the tendency of cracking in segmental bridges.

2.5.1 Overview of Previous Studies Conducted at Auburn University

Mante (2016) and Schindler et al. (2017) both conducted research related to prestressed concrete applications and conducted testing to accurately predict volumetric changes that could be commonly associated with the concrete used in the prestressing industry. Mante (2016) focused primarily on field and laboratory for precast, prestressed concrete bridge girders, while Schindler et al. (2017) conducted laboratory testing related to comparing the compliance of CSC and SCC used in prestressed applications.

2.5.1.1 Experimental Plan used for Testing

In the studies conducted by Mante (2016) and Schindler et al. (2017), 6 in. × 12 in. cylinders were cast and cured by either an accelerated curing process to simulate techniques used in the prestressing industry or placed in a moist-cure room until the specimens were removed and placed in the creep room. After curing, the cylinders were then prepped and were loaded into creep frames that were designed and built in the structural laboratory at Auburn University in a previous study conducted by Bryan Kavanaugh (2008). To accurately determine the creep behavior of the concrete mixtures under consideration, these cylinders were loaded to 40% of their compressive strength specified by ASTM C 512 (2002), and the deformations associated with this sustained applied load were monitored for a period of approximately one year. Along with the creep specimens, drying shrinkage cylinders were cast and monitored to ensure that accurate creep results were calculated, which is also required by ASTM C 512 (2002).

In addition to monitoring the creep behavior, Mante (2016) also studied how shrinkage behavior is affected when different coarse aggregate types or the use of supplementary cementitious materials (SCMs) are used in CSC mixtures. This testing was completed in accordance with ASTM C 157 (2008), which is completed through the use of rectangular prisms. Also, the cylindrical shrinkage strains that were used in the creep testing (ASTM C 512 2002) were also recorded.

2.5.1.2 Evaluation of Volumetric Changes by Mante (2016)

The primary goal of this research study was to accurately predict the observed camber during the design phase of concrete bridge girders. One of the key areas of focus included time-dependent deformations of concrete mixtures containing materials that were regional specific.

The conventional-slump concrete mixtures that were prepared in this study were representative of typical ALDOT-approved mixtures that are generally used in the prestressing industry. All laboratory mixtures used constituent materials identical to those that are most commonly used by field producers (Mante 2016). These mixtures consisted of three regional coarse aggregates, such as dolomitic limestone and crush granite, and three combinations of supplementary cementing materials (SCMs) including Class F fly ash, silica fume, and slag cement along with a Type III cement only control mixture (Mante 2016). After mixing and casting of the 6 in. × 12 in. cylinders was completed, these samples were then subjected to accelerated curing practices mimicking those of accelerated curing methods used in precast, prestressed production.

The creep results that were estimated during testing were compared as compliance rather than a creep coefficient. ACI Committee 209 (2008) defines compliance as follows:

$$J(t, t_0) = \frac{Elastic\ Strain + Basic\ Creep + Drying\ Creep}{Stress} \quad \text{Equation 2.97}$$

With,

$J(t, t_0)$ =the creep compliance at age *t* per unit stress caused by a unit uniaxial sustained load applied since loading at age t_0

In the study conducted by Mante (2016), three creep and shrinkage prediction models were evaluated to see which one rendered the most accurate results when compared to the

measured values obtained through testing. The three models that were considered included the ACI 209 (2008), AASHTO (2014), and MC 2010.

Figure 2-6 shows a comparison between the predicted compliance of the three prediction models and the measured compliance of a typical dolomitic limestone mixture (Mante 2016). According to Mante (2016), for most dolomitic limestone mixtures, the MC 2010 prediction model most frequently tends to over-predict compliance for early ages, whereas, the AASHTO (2014) and ACI 209 models show relatively good agreement with experimental results at early ages. For later ages, the three prediction models yield highly similar results, approaching the precision of the measured collected data.

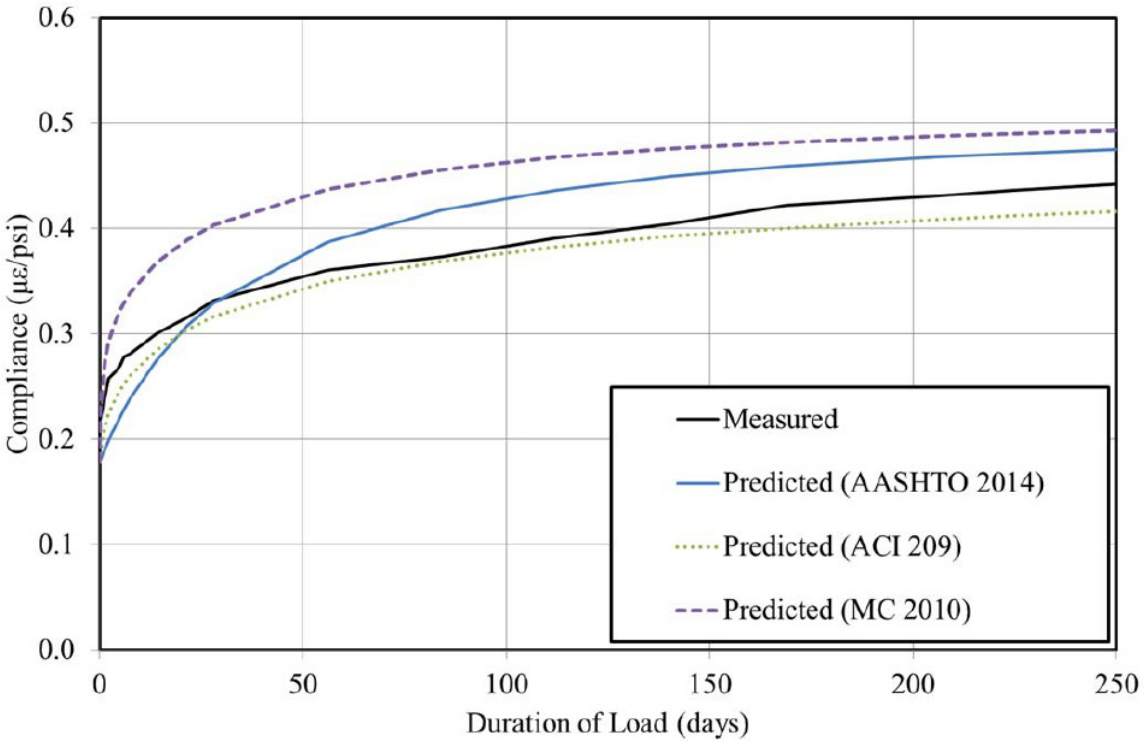

Figure 2-6: Comparison between experimental results and prediction models for compliance of a typical dolomitic limestone mixture (Mante 2016)

In order to determine which model performed the best in the prediction of compliance values, Mante (2016) used the computation of a time-weighted coefficient of variation, denoted as $\overline{\omega}_j$. In general, lower $\overline{\omega}_j$ values correspond to improved correlation between predicted and measured data. Table 2-10 shows the overall values for the coefficients of variation for the predicted compliance values for each of the prediction models that were considered in this study.

As shown in Table 2-10, overall the ACI 209 model performed the best in the predication of compliance values, while the MC 2010 performed the worse of the three prediction models.

Table 2-10: Overall relative goodness-of-fit of prediction models to experimental data for compliance (Mante 2016)

	Coefficient of Variation, $\overline{\omega}_j$ (%)		
	AASHTO 2014	**ACI 209**	**Model Code 2010**
Overall Coefficient of Variation, $\overline{\omega}_j$ (%)	12.9	10.3	19.2

The three prediction models considered in the prediction of creep behavior were also used in the prediction of shrinkage strains for both the rectangular prisms that were tested in accordance with ASTM C 157 (2008) and the cylindrical specimens used in creep testing as stated by ASTM C 512 (2002). Figure 2-7 and Figure 2-8 show the comparison of the predicted shrinkage strains to the measured shrinkage strains for the cylindrical and rectangular prism specimens, respectively. According to Mante (2016), even though each model tended to slightly overestimate the predicted shrinkage strains for both the cylindrical and prism test specimens, each of the three models were relatively accurate for dolomitic limestone mixtures.

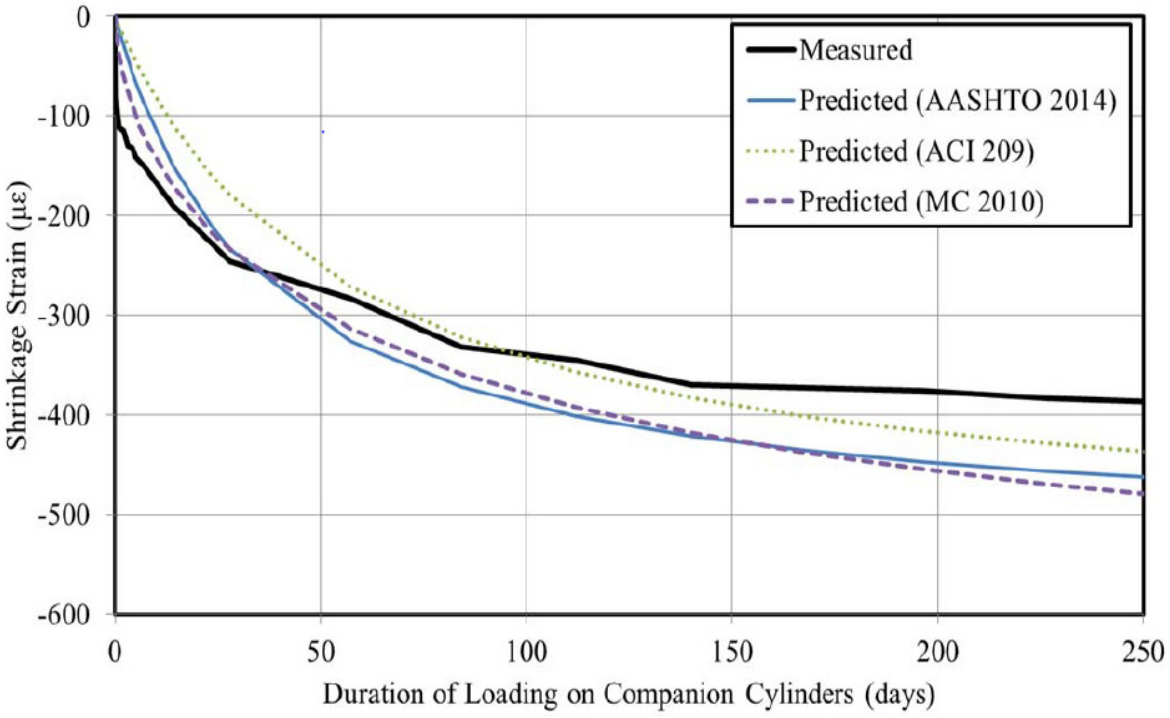

Figure 2-7: Comparison between experimental results and prediction models for cylinder shrinkage of typical dolomitic mixture (Mante 2016)

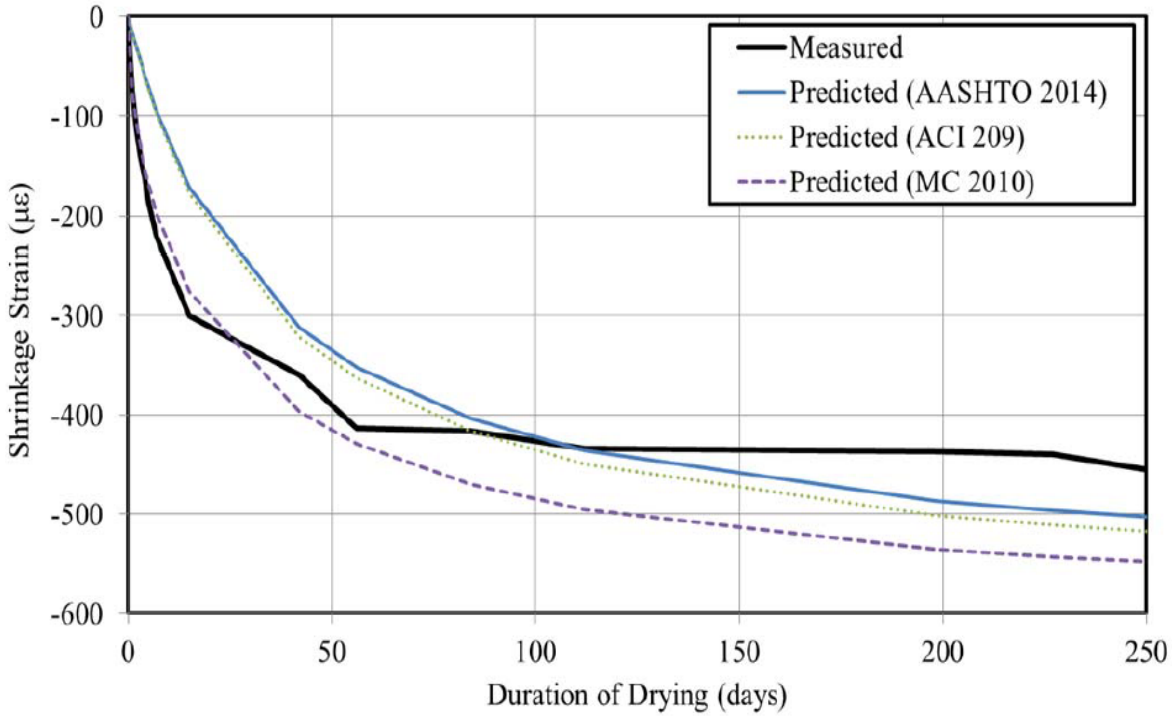

Figure 2-8: Comparison between experimental results and prediction models for rectangular prism shrinkage of typical dolomitic mixture (Mante 2016)

Similar to how the compliance values were evaluated based on the prediction model that was used, Mante (2016) uses the time-weighted coefficient of variation, $\overline{\omega}_j$, to evaluate goodness-of-fit. Table 2-10 shows the overall values for the coefficients of variation for the cylindrical and rectangular prism shrinkage specimens for each of the prediction models considered in the study conducted by Mante 2016. Table 2-11 shows that overall, the AASHTO 2014 method performed the best in the predictions of both the cylindrical and rectangular prism shrinkage strains, while ACI 209 performed the worst of the three models that were evaluated.

Table 2-11: Overall relative goodness-of-fit of prediction models to experimental data for cylindrical and rectangular prism shrinkage specimens (Mante 2016)

	Coefficient of Variation, $\overline{\omega}_j$ (%)					
	AASHTO 2014		**ACI 209**		**Model Code 2010**	
	Cylinder	**Prism**	**Cylinder**	**Prism**	**Cylinder**	**Prism**
Overall Coefficient of Variation, $\overline{\omega}_j$ (%)	38.4	37.3	41.2	42.0	38.4	47.9

2.5.1.3 Evaluation of Volumetric Changes by Schindler et al. (2017)

During this research study, four SCC mixtures and one CSC mixture were mixed under controlled laboratory conditions and were subjected to creep and drying shrinkage testing at five different loading ages including: 18 hours, 2 days, 7 days, 28 days, and 90 days. The compliance values associated with the SCC mixtures were compared to those of the CSC mixture to determine if SCC exhibits a similar behavior to that of CSC. Also, the accuracy of six compliance prediction models were investigated which include ACI 209, CEB 2010, GL 2000, B3, AASHTO 2012, and NCHRP 628. For simplicity purposes, only the predicted compliance results from ACI 209 and CEB 2010 are presented due to these models being the most accurate out of the six that were considered.

Each of the four SCC mixtures contained all the same materials with the exception of the water-cement ratio and SCMs used; two of the mixtures contained Class C fly ash and the other two contained Grade 120 slag cement. The CSC mixture contained no SCMs, and was composed entirely of Type III portland cement. Each of the loading ages were exposed to moist-curing conditions with the exception of the 18-hour loading age, which was subjected to an accelerated curing to provide an accurate representation of the techniques commonly used in the prestressing industry.

In the ACI 209 compliance prediction model, the calculated compliance as compared to the predicted compliance is much closer for all moist cured specimens rather than accelerated cured samples. Figure 2-9 provides a comparison of the predicted compliance values using the ACI 209 model to the compliance values that were measured through testing.

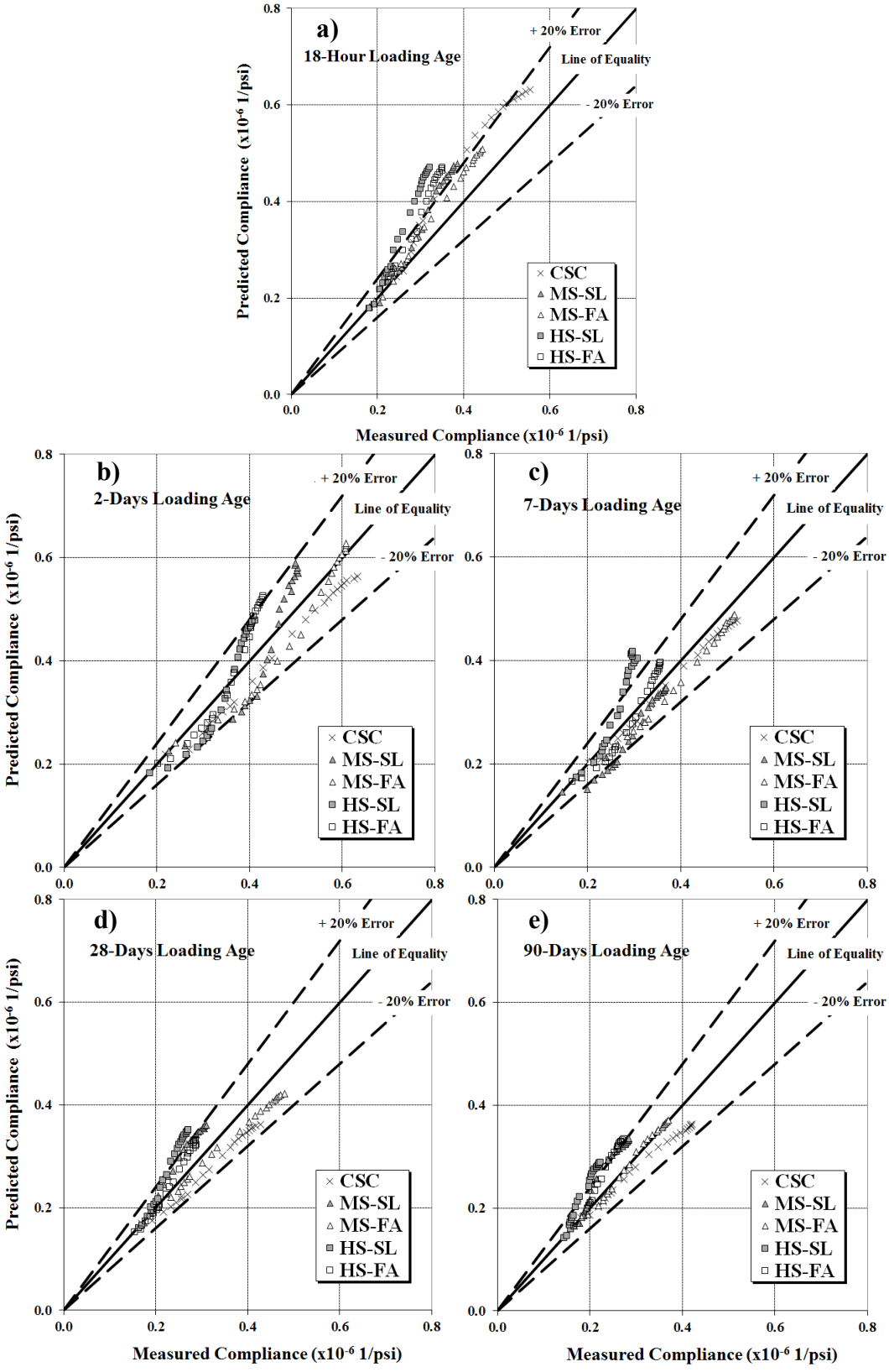

Figure 2-9: ACI 209 predicted compliance values for all loading ages (Schindler et al. 2017)

For each mixture shown in Figure 2-9, Schindler et al. (2017) concludes that the ACI 209 predicted compliance data are closer to the line of equality for moist-cured specimens than they are for accelerated-cured specimens. Also, from Figure 2-9 Schindler et al. (2017) concludes that for SCC mixtures with similar SCM and curing regime, the ACI 209 predicted data are closer to the line of equality for the moderate-strength mixtures than for high-strength mixtures. From Figure 2-9, for the same curing regime and similar strength level, the ACI 209 predicted data are closer to the line of equality for mixtures made with fly ash than for mixtures made with slag cement concluding that ACI 209 is more accurate in the predicted compliance for mixtures made with fly ash as compared to mixtures made with slag cement (Schindler et al. 2017).

As compared to the ACI 209 model, Schindler et al. (2017) concludes CEB 2010 is much better at predicting the compliance for later loading ages as compared to earlier loading ages as shown in Figure 2-10. In Figure 2-10, the compliance values that were predicted using the CEB 2010 model closely follow the line of equality for each of the SCC mixtures that were studied (Schindler et al. 2017). However, the CEB 2010 method did not predicted the compliance with great accuracy for the accelerated-cured CSC specimens, but the compliance predictions were equal or very close to the measured compliance for each of the other mixtures (Schindler et al. 2017).

As seen in Figure 2-10, the predicted compliance values for the moist-cured specimens that were composed of the fly ash mixture were more accurate as compared to the moist-cured specimens that were composed of the slag cement mixture. According to Schindler et al. (2017), it can be concluded that, for moist-cured specimens, CEB 2010 is more accurate for fly ash mixtures than it is for slag cement mixtures.

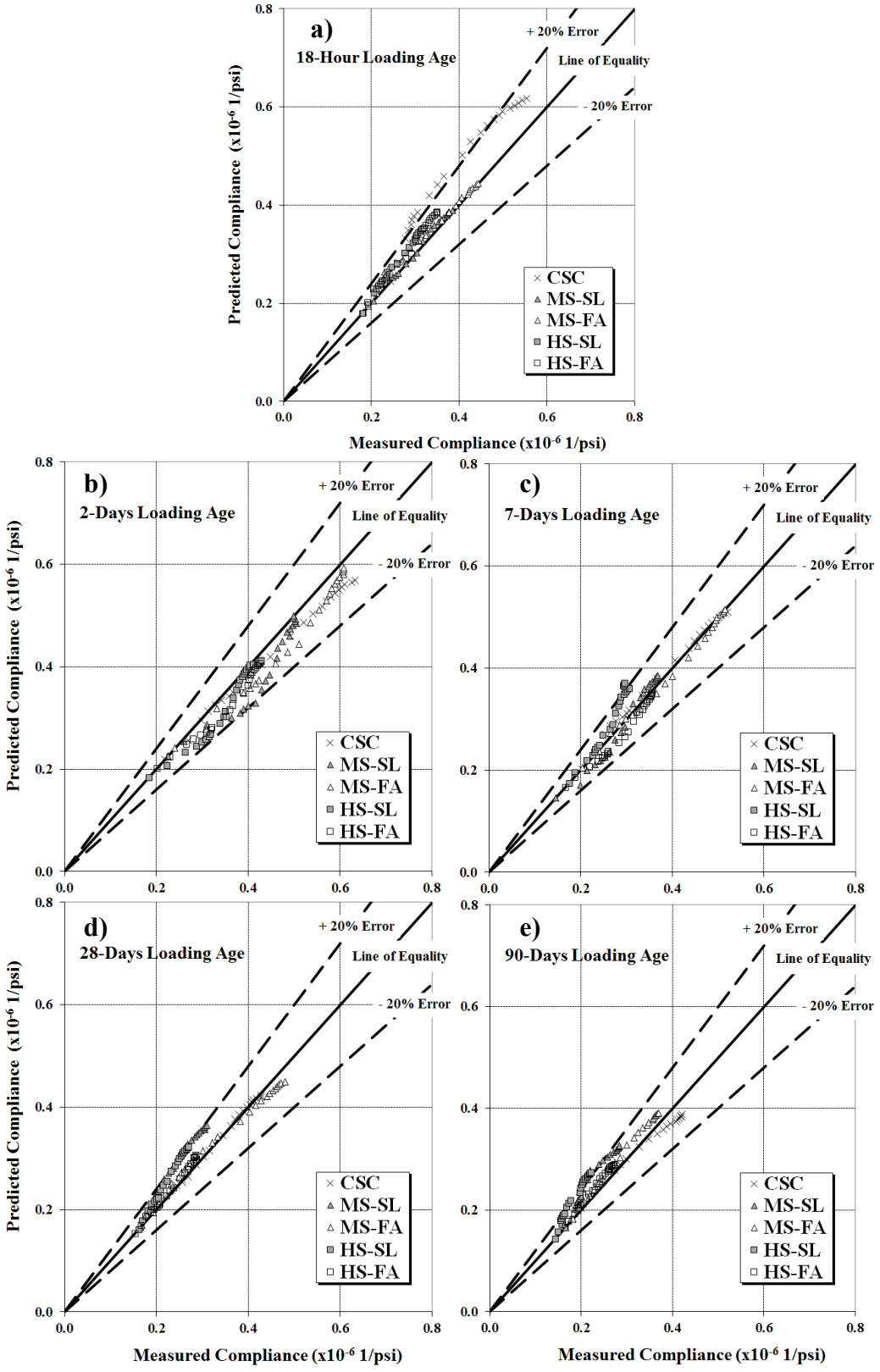

Figure 2-10: CEB 2010 predicted compliance values for all loading ages (Schindler et al. 2017)

2.5.2 Creep Study of Chevire Bridge by Raphael et al. (2018)

The Chevire bridge in France contains segmental spans that has raised many concerns over the years due to the excessive vertical deflections due to creep. This study reports on the work of several different laboratories and research centers that developed a large experimental database, which was used to compare the experimental creep results to the long-term predicted creep results of two design codes that are used in practice today: the BPEL code and CEB MC 2010 (Raphael et al. 2018). Also, a coupling experiment using a reliability software and a finite-element tool were used to analyze the sensitivity measures of creep parameters in the Chevire bridge (Raphael et al. 2018).

2.5.2.1 Overview of Chevire Bridge and Vertical Displacements

The Chevire bridge is a segmental bridge that is composed of 22 spans that measures 1563 meters in length. As shown in Figure 2-11, the central steel span is supported on two prestressed concrete cantilevers and has a length of 242 meters, and is then followed by two spans of 69.3 meters, while the remaining spans measure 65 meters except the two end spans that measure 38.5 meters (Raphael et al. 2018). The central steel span of the Chevire bridge is the only portion that is not constructed using segmental, concrete units. The remaining spans are all constructed with prestressed, segmental concrete units.

Figure 2-11: Chevire Bridge located in France (Raphael et al. 2018)

Since 1994, the vertical displacement of the Chevire bridge free-end cantilever has been measured and monitored. After 1,275 days of bridge setup, the measured displacement was 3.94 in. (10 cm). When the vertical displacement was measured in the year 2000, the deformation had

grown to approximately 7.17 in. (18.2 cm) as compared to the predicted value by the BPEL code and Eurocode 2 of 1.19 in. (3.01 cm) and 2.41 in. (6.13 cm) respectively (Raphael et al. 2018).

2.5.2.2 Analysis of Results and Coupling Experiment

In this study, two different design codes were considered to compare measured versus predicted vertical displacements in the Chevire bridge: the BPEL code and Eurocode 2. The BPEL code, which was the design code used throughout Europe at the time of construction for the Chevire bridge, was used to evaluate creep phenomenon of the Chevire bridge; however, Eurocode 2 is now used throughout Europe to predict the creep of concrete in structures (Raphael et al. 2018).

In the beginning phase of this study, a large database was created using data that had been collected by several research laboratories and institutions. This database included the results from over 432 creep tests on specimens of different shapes and dimensions under various environmental conditions (Raphael et al. 2018). Also, the test specimens varied in composition, and were subjected to various loading intensities and loading ages.

Once all data had been collected, the accuracy of each design code was evaluated by applying the residual method to the creep compliance, $J(t,t_0)$. These residuals were calculated by taking the difference between the measured and predicted compliance values using Equation 2.98.

$$R_{ij} = \left(ObsX_{ij} - CalX_{ij}\right) \qquad \text{Equation 2.98}$$

Where,

$ObsX_{ij}$= Experimental measured creep compliance at time j of experiment i $(10^{-6}\ MPa)$, and

$CalX_{ij}$= Predicted creep compliance at time j of experiment i $(10^{-6}\ MPa)$.

The focus of this research was to only cover the long-term creep deformations so only time after 3,000 days of loading were considered (Raphael et al. 2018). After all data had been processed, residual plots for both the BPEL code and Eurocode 2 were generated and these are shown in Figure 2-12 and Figure 2-13. Any values that are negative indicate that the model overestimates the compliance, whereas any values that are positive mean that the model underestimates the compliance.

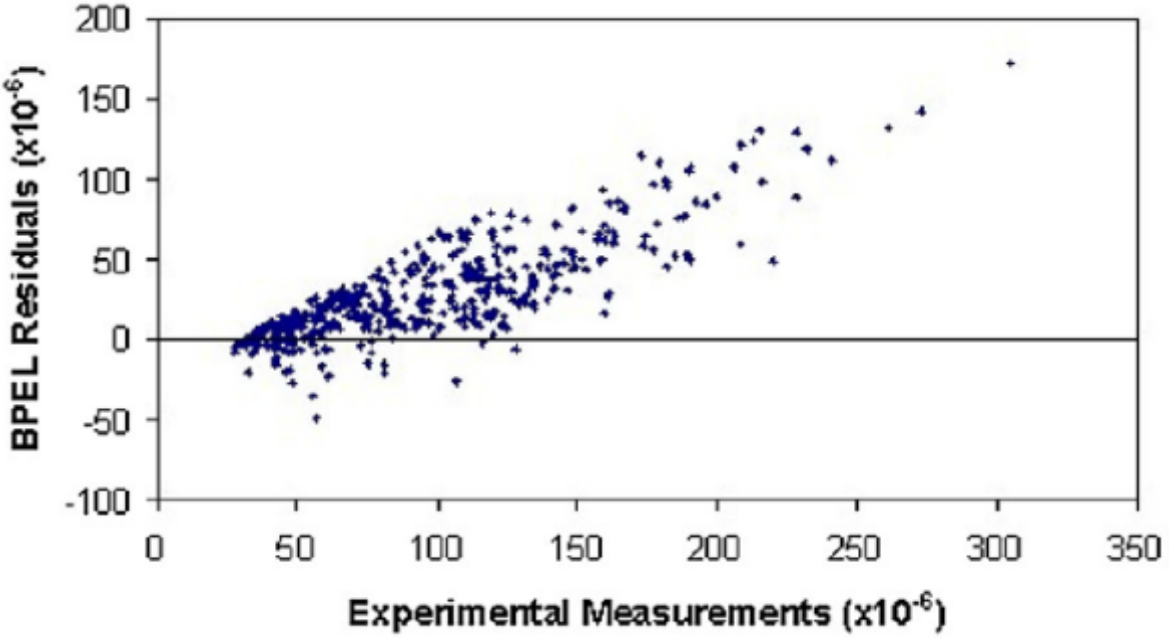

Figure 2-12: Compliance residuals for BPEL (Raphael et al. 2018)

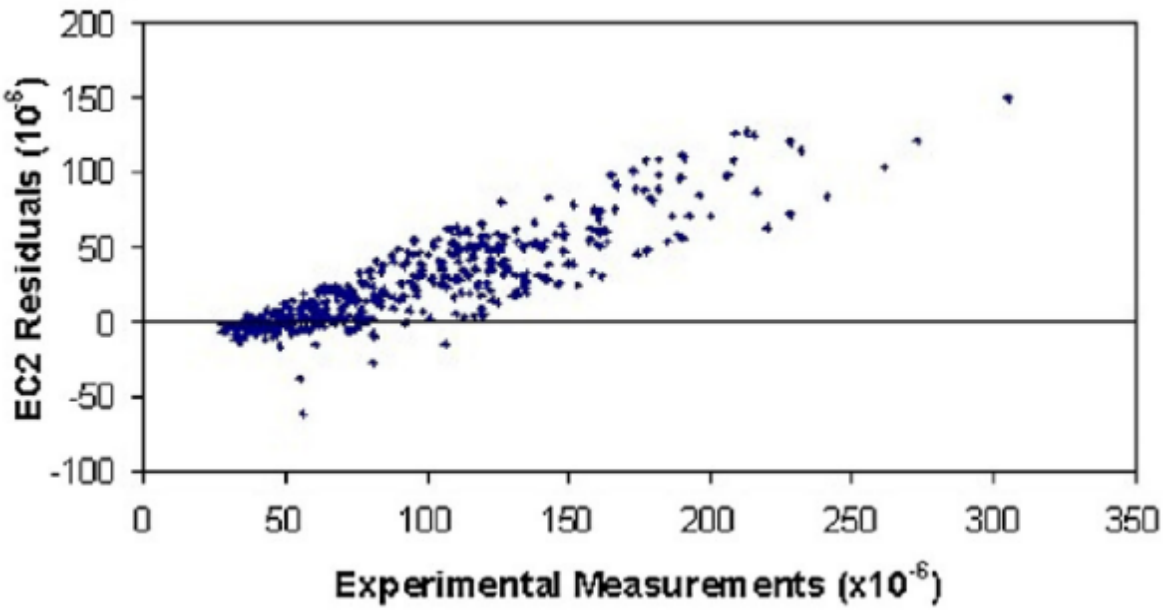

Figure 2-13: Compliance residuals for Eurocode 2 (Raphael et al. 2018)

After reviewing all data points, the overall scatters are mostly grouped in the positive region of the graphs which indicate that both the BPEL code and Eurocode 2 predict lower values of compliance. Further analysis indicates that the long-term compliance is underestimated by more than 300 percent in some cases (Raphael et al. 2018).

Not only was an analysis performed to compare long-term creep deformations in common design codes, but a mechanical-reliability model was also created using the collected data to evaluate the sensitivity measures that affect the creep of concrete (Raphael et al. 2018). This was achieved by using a reliability software known as *PHIMECA* and a finite-element software *ST1.* According to Raphael et al. 2018, an input file of the Chevire bridge was created for *PHIMECA*, and then an iterative scheme is applied where *PHIMECA* performs a number of calls to *ST1I,* which produces the creep deformation for given random variables. After convergence is achieved, *PHIMECA* calculates the sensitivity measures and assesses the probability of failure based on whether the deflection generated by the model is greater than or less than the allowed maximum long-term deflection.

After simulating many different trials and varying the parameters, it is noted that the BPEL predictions could not be well calibrated, thus confirming what was discovered earlier by the residual method: the BPEL code largely underestimates reality (Raphael et al. 2018). This led to an analysis to determine which parameters are more important in each of the design codes considered in this study. The sensitivity measures that were chosen included compressive strength, the cable prestressing force, and the relative humidity. The pie charts presented in Figure 2-14 show the weights that each design code gives to these sensitivity measures.

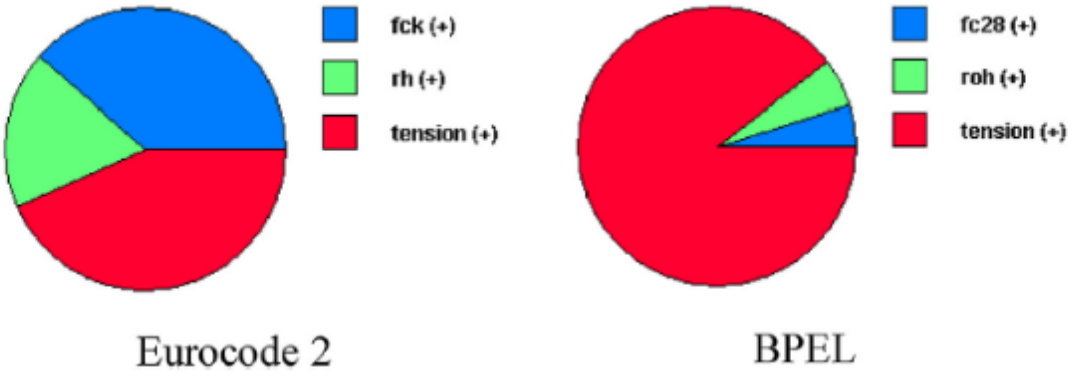

Figure 2-14: Sensitivity parameters of creep in the Chevire bridge (Raphael et al. 2018)

Eurocode 2 is better calibrated to creep deformations as compared to the BPEL code due to each of the three sensitivity measures being closely weighted. The BPEL model relies highly on the prestressing force in the cables while compressive strength and the relative humidity are nearly negligible. Overall, Raphael et al. 2018 conclude that Eurocode 2 is better constructed in a

stable manner to account for creep deformations due to it distributing the weight for each parameter in a more balanced way as compared to the BPEL code.

2.5.3 Creep Study of Grondal Bridge by Malm et al. (2010)

In the study documented by Malm et al. 2010, the time-dependent properties of concrete such as creep and shrinkage were monitored in the construction stage of the Grondal bridge to see which properties are more likely to cause cracking. These properties were entered into a finite-element model of a segmentally constructed, balanced-cantilever bridge, which described the stepwise construction with the nonlinear time-dependent behavior of the material properties (Malm et al. 2010). The analysis of the finite-element model was divided into steps, which would act as a simulation of casting one segment to the next with each segment being assigned material properties that would develop with time to mimic the curing of the concrete.

2.5.3.1 Overview of Grondal Bridge

The Grondal bridge is a prestressed continuous hollow box-girder bridge consisting of 11 spans with a total length of 430 meters (Malm et al. 2010). The balanced-cantilever method was used to erect the main and two adjacent spans, while the remaining spans were erected by the use of supporting scaffolding. Prestressing cables were provided in the top flange during the construction phase, and the cables in the bottom flange were post-tensioned once the bridge superstructure was completed (Malm et al. 2010).

All prestressing cables had to be properly tensioned to account for the weight of the form traveller, the formwork, and the segment that was being cast due to the balanced-cantilever method being the choice of construction. In this type of construction, the previously cast segment serves as the work basis for the next segment, which also increases the moment as the cantilever arm grows with each new segment (Malm et al. 2010).

2.5.3.2 Analysis of Results and Conclusions

In the study conducted by Malm et al. 2010, the time-dependent properties for creep and shrinkage were modeled using the CEB-FIP Model Code 1990 and Eurocode 2 respectively, which were the chosen models by the company who designed the Grondal bridge. In addition to the creep and shrinkage properties, the elastic modulus was also modeled according to the CEB-FIP Model Code 1990, and inputted into the finite-element model. This was done to simulate

how each segment develops strength and stiffness with time and must be taken into account to determine a more realistic time frame of when plastic cracking could occur due to plastic shrinkage.

Two approaches were used to simulate the influence of shrinkage on the overall model. In the first approach, as shown in Figure 2-15, each segment was assigned a single shrinkage curve based on a uniform cross section, i.e. one notional size for the whole cross section of each segment. In the second approach, as shown in Figure 2-16, the top and bottom flanges and the web were each assigned a different shrinkage curve. The notional size is calculated separately for flanges and webs in the cross section to include the effects of thickness dependence on the drying shrinkage (Malm et al. 2010).

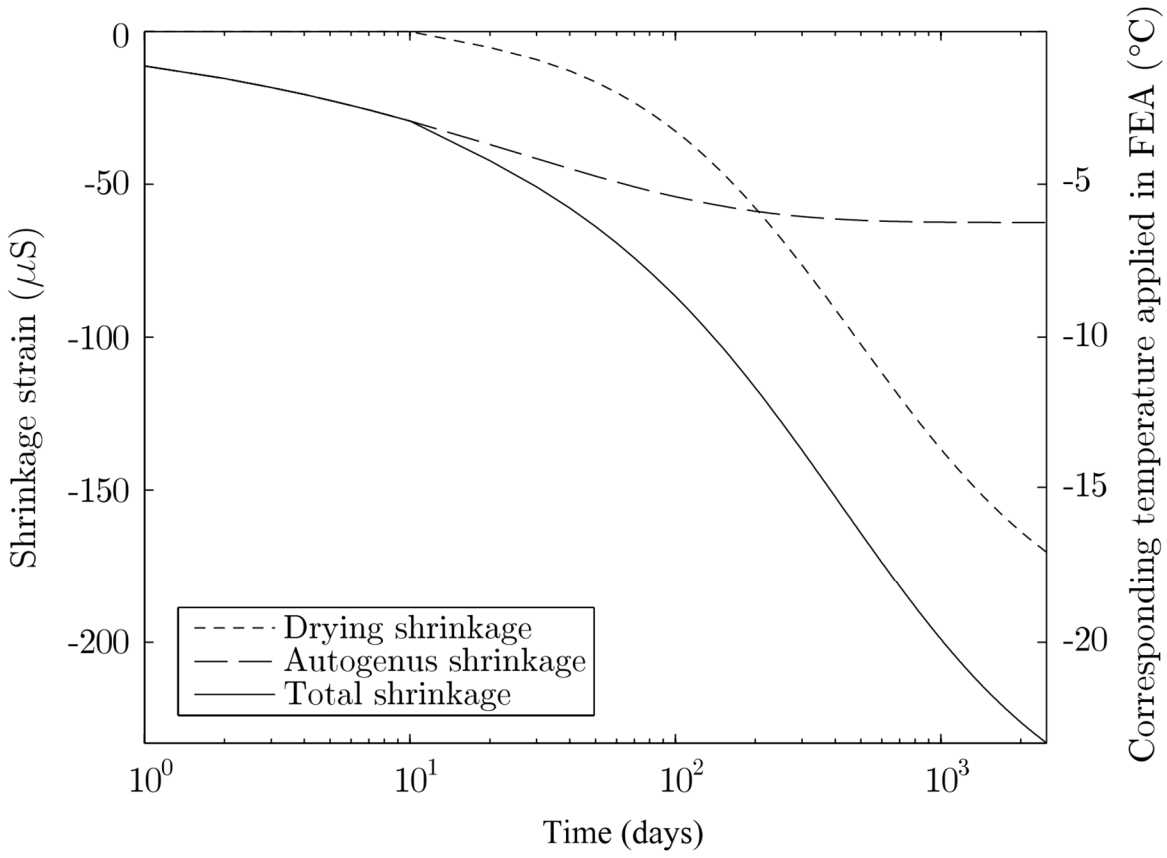

Figure 2-15: Development of Shrinkage Strain (Malm et al. 2010)

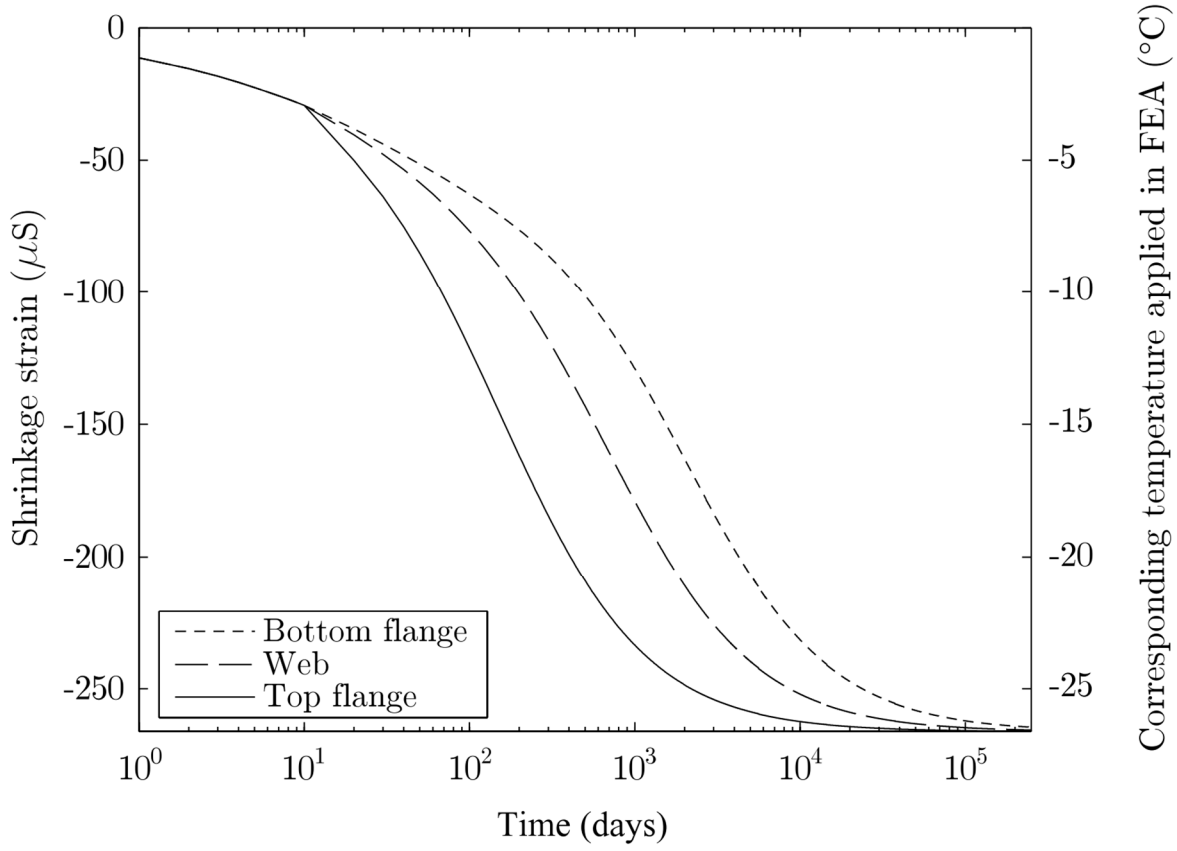

Figure 2-16: Development of non-uniform shrinkage strain (Malm et al. 2010)

The software that was used to create the finite-element model for the Grondal bridge is not suitable when the stresses vary drastically through the cross section; therefore, the creep behavior of each segment was simulated using a visco-elastic material assuming a constant bulk modulus (Malm et al. 2010). The creep coefficient was then calculated based on this visco-elastic material as shown in Figure 2-17 below. The creep behavior is included in the material definition of the finite-element model, which will lead to each element having different creep strains depending on when it is introduced into the model (Malm et al. 2010).

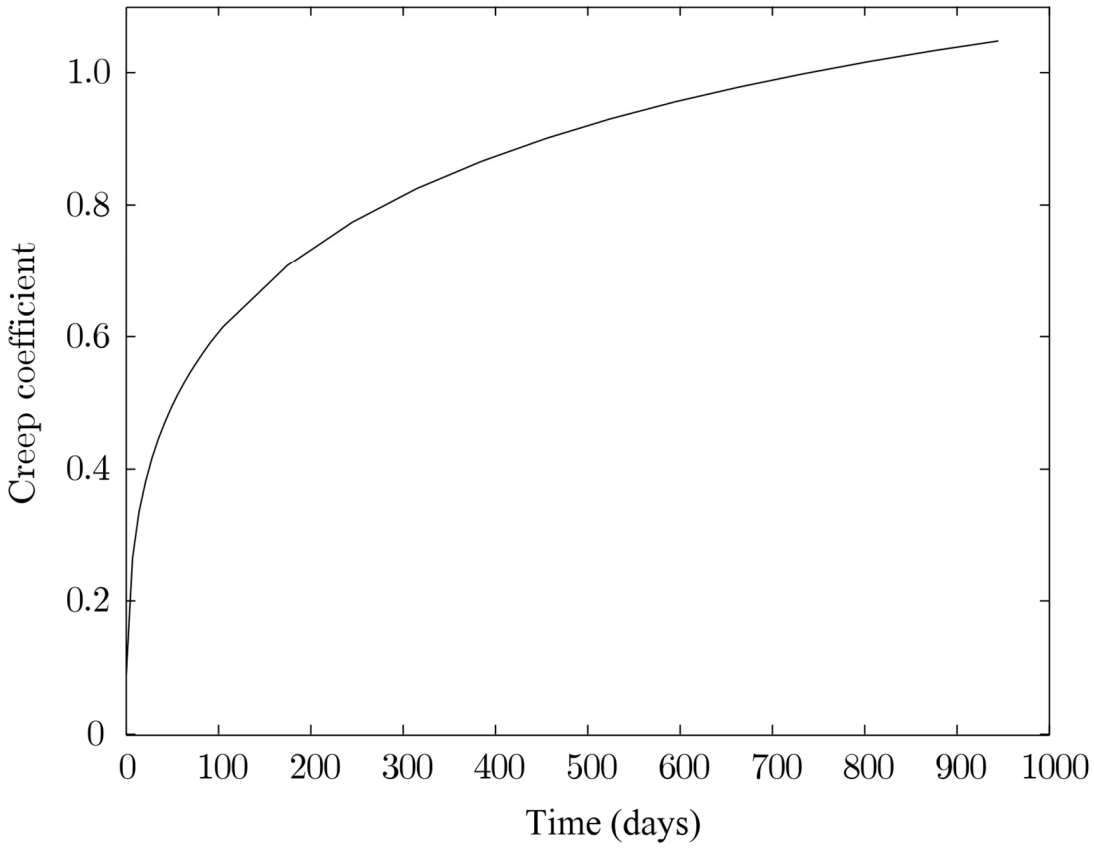

Figure 2-17: Development of creep coefficient (Malm et al. 2010)

Once all time-dependent properties had been properly defined for each segment, the segments were constructed together in the finite-element model to simulate the final plans of the Grondal bridge. The model was executed by activating each segment in steps to simulate the casting procedure that would be used during actual construction. This was done to allow each segment to properly develop the time-dependent material properties that were required before the travelling form could be moved to the location of the next casting.

After the model was properly running, one of the piers was selected to monitor how the camber for each of the cantilever arms would be affected. The generated results are displayed in Figure 2-18 below. The top graph in Figure 2-18 displays the changes in camber for the cantilever arm that extends from the left of the pier towards the main span, and the bottom graph represents the cantilever arm that extends from the right of the pier.

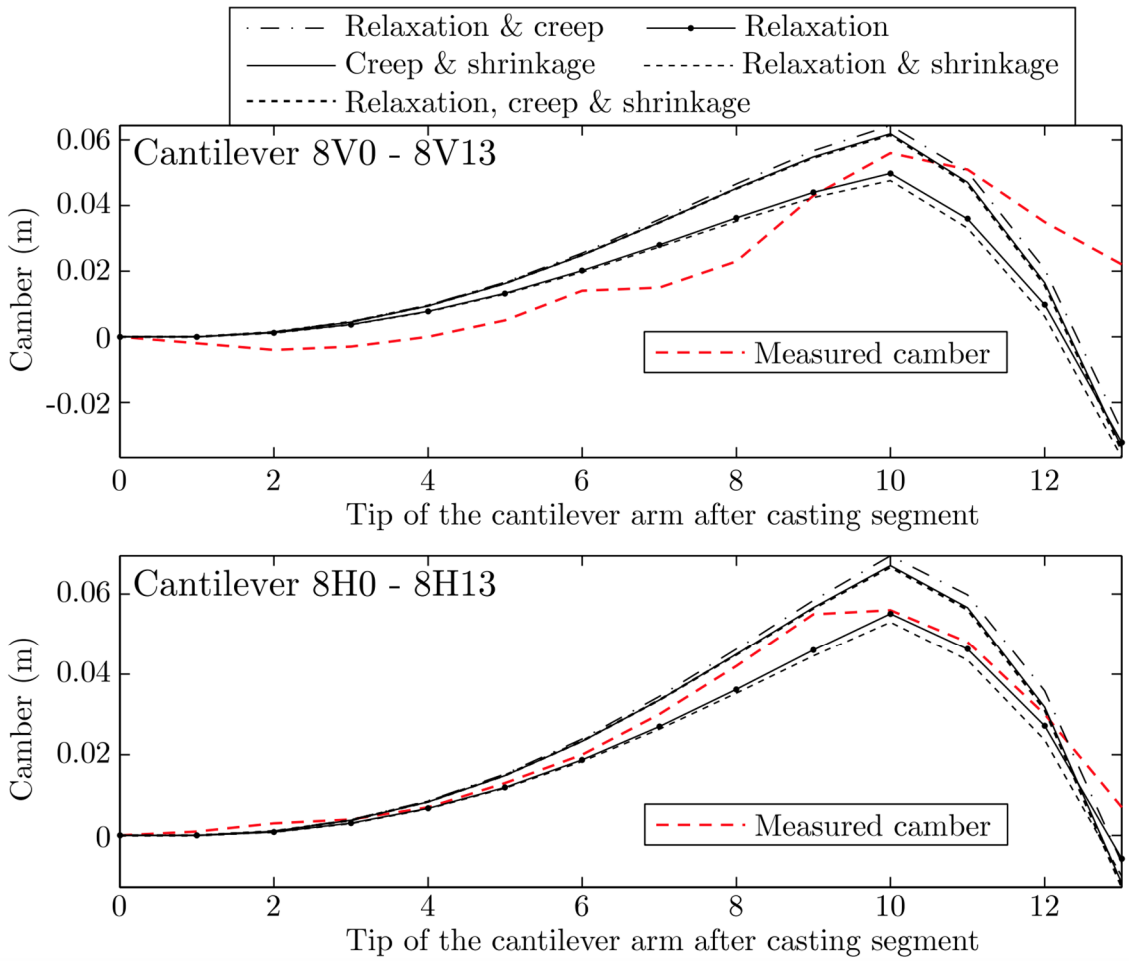

Figure 2-18: Deflections of cantilever arm due to time-dependent properties (Malm et al. 2010)

Each of these models include the evolution of the elastic modulus, creep, shrinkage, and relaxation of the post-tensioning bars (Malm et al. 2010). From the data Malm et al. 2010 concludes that shrinkage has a small effect on the measured deflection whether it is assumed to be a uniform or non-uniform distribution over the cross section. This was expected though due to shrinkage not having a key role until the center segment of the cantilevers are cast. However, when the effect of creep is considered into the analysis, a drastic change is noticed during cantilevering. By the time the center segments of the cantilevers have been cast, the first cast segments have reached approximately 60 percent of their creep strains due to the dead weight of each segment. For the models that include the effects of creep, a higher camber is required; whereas, when the models neglect the effects of creep the camber is reduced by nearly 30 percent (Malm et al. 2010).

CHAPTER 3: EXPERIMENTAL PLAN

3.1 INTRODUCTION

The primary objectives of this research effort were to gain an increase in knowledge of the creep and shrinkage characteristics of concrete mixtures that were used during the construction of the I-59/I-20 segmental bridge in Birmingham, Alabama. Due to this type of construction being new for the State of Alabama, previous research on this type of construction is limited. This chapter details the procedures used to assess the required properties of the concrete mixtures at various loading ages. In this chapter, the reader will find the experimental plan, materials, and testing procedures used.

3.2 EXPERIMENTAL PLAN

The experimental plan for this project consisted of two main phases: field-mixed concrete and laboratory-mixed concrete. The flow chart illustrated in Figure 3-1 shows the logical sequence of these two phases. The first phase consisted of all specimens that were cast on-site by the contractor using the ALDOT approved mixture design that was used throughout the duration of the project. The second phase of this projected consisted of specimens that were cast in the laboratory at Auburn University using the ALDOT approved mixture design with the only change being a substitution of the quartzite coarse aggregate with a limestone coarse aggregate to compare the effects of creep and shrinkage when different coarse aggregate types are used. For both the field-mixed concrete and laboratory-mixed concrete of this project, creep and shrinkage testing was performed.

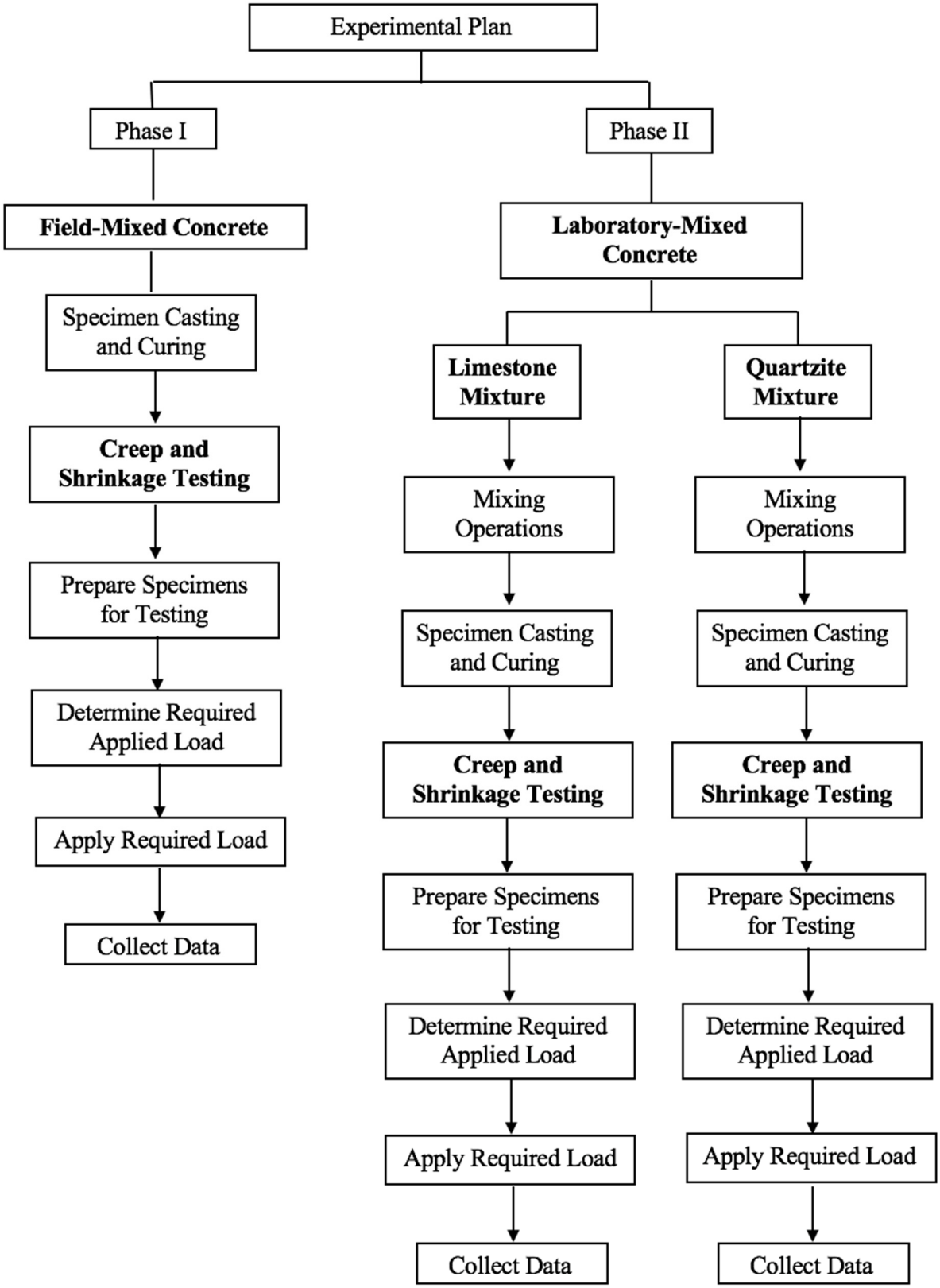

Figure 3-1: Flow of Experimental Work

3.2.1 Requirements for Concrete Mixtures

The following section outlines all performance criteria that were required for the concrete mixture design set forth by ALDOT for this project. These requirements also applied to all laboratory mixtures produced by Auburn University.

3.2.1.1 Fresh Properties

All fresh concrete properties such as slump, air content, unit weight, and temperature were governed by the requirements set forth by ALDOT. The slump of the concrete had to meet the requirement of between 3 to 9 inches and the air content had to be in the range of 3 to 6 percent. The unit weight and temperature of each concrete mixture was also collected for quality control purposes. All requirements for slump, air content, unit weight, and temperature were followed during the mixing of all concrete at Auburn University, which ensured that all concrete mixtures in the laboratory were an accurate representation of the concrete used during construction. If any mixture did not meet the requirement for slump or air content, the mixture was discarded and remixed. The temperature and unit weight of each mixture was collected but did not affect whether the mixture was accepted or rejected.

3.2.1.2 Hardened Properties

For this research study, no specific hardened properties were determined prior to the testing of creep and shrinkage. However, the concrete segments that were cast on-site had to reach a compressive strength of 6,500 psi at 28 days.

3.2.2 Specimen Types and Ages at Loading

Creep behavior is different at each loading age. For this study loading ages of 7 days, 28 days, 91 days, and 182 days were used for all field-mixed concrete, and loading ages of 7 days, 28 days, and 91 days were used for all laboratory-mixed concrete. All specimens were exposed to accelerated curing conditions to represent the way the bridge segments are cured.

As previously explained in Section 2.3, many factors are responsible for volumetric changes in concrete specimens. However, for the purpose of this research effort, three main components were considered to be crucial factors: dying shrinkage, autogenous shrinkage, and creep (Neville 2011).

In order to accurately measure the creep at each of the loading ages previously stated, all three of these mechanisms had to be monitored and recorded. For creep testing, all requirements stated by ASTM C 512 (2018) were followed precisely. Specimens for monitoring both drying and autogenous shrinkage and creep deformations had to be made, which were cast in the form of 6 in. by 12 in. cylinders. The creep specimens were loaded into creep frames, which are detailed at a later time. Creep specimens were placed under a constant stress with a sustained load of 40% of the ultimate compressive strength determined at the time of loading. The changes in deformation for these specimens were due to the initial elastic response immediately upon loading, the effects of creep strains, the effects of drying shrinkage strains, and the effects of autogenous shrinkage within the concrete. The cylindrical shrinkage specimens were not exposed to external loadings, therefore they only exhibited sustained deformation due to drying and autogenous shrinkage.

In addition to creep testing, drying shrinkage testing was also conducted on both the field-mixed concrete and laboratory-mixed concrete in accordance with AASHTO T 160 (2015). All specimens were made in accordance with AASHTO T 160 (2015) which uses 3 in. × 3 in. × 11.25 in. rectangular prims. All concrete prisms were placed on storage shelves after their curing cycle was complete with no type of loading or induced stress.

Illustrated in Table 3-1 are the number and types of cylinders and prisms that were cast for each loading age during the duration of this research effort. Note that the column labeled "Strength Specimen" represents cylinders used to determine the ultimate compressive strength and modulus of elasticity of each loading age immediately before the load is applied in the creep frames. Also, the column labeled “Temperature Cylinder” refers to the cylinder that was equipped with a temperature sensor in the field to measure the temperatures at which all field specimens were exposed too during curing.

All mixtures that were mixed in the laboratory followed the same outline but were adjusted due to the limited amount of resources for steam curing. Therefore, the loading age of 182 days was removed for all laboratory procedures and only 3 drying shrinkage prisms were made. Also, rather than having a separate cylinder to monitor the maturity of the concrete, a temperature sensor was placed in one of the drying shrinkage specimens.

Table 3-1: Specimen Type and Quantity for each Loading Age

		6 in. × 12 in. Cylinders				Drying Shrinkage Prisms
Curing Method	**Loading Age**	**Creep Specimen**	**Shrinkage Specimen**	**Strength/ Elastic Modulus Specimens**	**Temperature Cylinder**	
Accelerated Curing	7 Days	2	3	3	1	6
	28 Days	2		3		
	91 Days	2		3		
	182 Days	2		3		
Column Totals		8	3	12	1	6
Specimen Total		24				6

ASTM C 512 (2018) requires plugs to be used above and below the creep specimens during the testing time period to ensure an even stress distribution throughout the entire system. For this project, plugs previously used were carefully monitored and checked to ensure their structural integrity before being used in each loading sequence. All plugs were cast using a high-strength slag mixture which was made during a previous study performed by Kavanaugh (2008). These plugs were used due to their ultimate strength exceeding that all of test specimens that were cast during the duration of this project. Rather than using sulfur capping to ensure an even contact point between both the plugs and the creep specimens, all plugs and test specimens were ground with an end grinder to remove all imperfections and provide a level loading surface.

3.3 MIXTURE PROPORTIONS

For all test specimens that were prepared on-site, casting was completed by taking samples of concrete from a ready-mixed concrete truck that was used to transport all concrete used during the placement of the precast segmental bridge structure. Wheelbarrows were used to transport the concrete from the location of the ready-mixed concrete truck to a less trafficked area where all cylinders and rectangular prisms were cast in their molds. After casting was complete, all test specimens were transported to their final location before curing began. Table 3-2 below provides the materials and mixture proportions that were approved by ALDOT for the concrete mixture design.

Table 3-2: ALDOT Approved Mixture Proportions

ALDOT Mixture Design	Quantity per yd^3
Type I/II Portland Cement (lbs)	682
Class F Fly Ash (lbs)	170
Fine Aggregate (#100 Concrete Sand, lbs)	878
Coarse Aggregate (#67 Quartzite, lbs)	1800
Water (lbs)	264
MasterAir AE 200 (oz)	25
MasterPozzolith 322 (oz)	30.1
MasterPolyheed 1025 (oz)	68
MasterSet DELVO (oz)	34.1
MasterSet AC 534 (oz)	102.2
Water-to-Cementitious Materials Ratio (w/cm)	0.31

As stated earlier, the second phase of this project consisted of two laboratory-mixed concrete mixtures, where one was mixed using a quartzite coarse aggregate and the other used a limestone coarse aggregate. This was done to monitor how creep and shrinkage behavior is effected when various coarse aggregate types are used. These samples were cast using ALDOT's mixture design as shown in Table 3-2. Based on the volume of concrete needed, the mixture proportions were scaled down to accommodate a volume of concrete of approximately 5.5 cubic feet. The saturated-surface dry (SSD) weights for each of the laboratory mixtures are presented in Table 3-3. As mentioned earlier, the only difference between the two mixtures produced in the laboratory was the coarse aggregate used during mixing.

Table 3-3: Laboratory Mixture Proportions

Mixture Proportions, SSD Weights		
Materials	**Quartzite Mixture**	**Limestone Mixture**
Type I/II Portland Cement (lbs/yd^3)	682	682
Class F Fly Ash (lbs/yd^3)	170	170
Fine Aggregate (lbs/yd^3)	878	878
Coarse Aggregate (lbs/yd^3)	1800	1800
Water (lbs/yd^3)	264	264
MasterAir AE 200 (oz/yd^3)	25	25
MasterPolyheed 1025 (oz/yd^3)	51	51
Water-to-Cementitious Materials Ratio (w/cm)	0.31	0.31

3.4 TEST SPECIMEN IDENTIFICATION SYSTEM

Due to the large number of test specimens that were cast and collected over the duration of this research project, a labeling system had to be implemented to be able to distinctly separate all samples from one another. This was put into action to limit the risk of any confusion that could arise between the samples that were cast in the field or in the laboratory, and to also distinguish between the laboratory samples that were cast with either the quartzite or the limestone coarse aggregate. Figure 3-2 and Figure 3-3 below provide examples of how the creep testing cylinders and the shrinkage rectangular prisms were labeled, respectively.

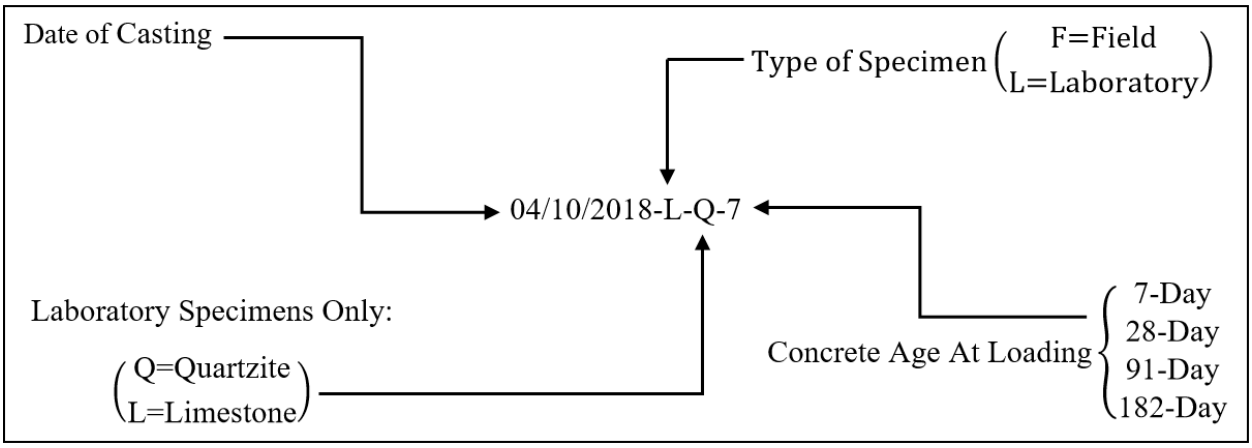

Figure 3-2: Sample Identification System for Creep and Shrinkage Cylinders

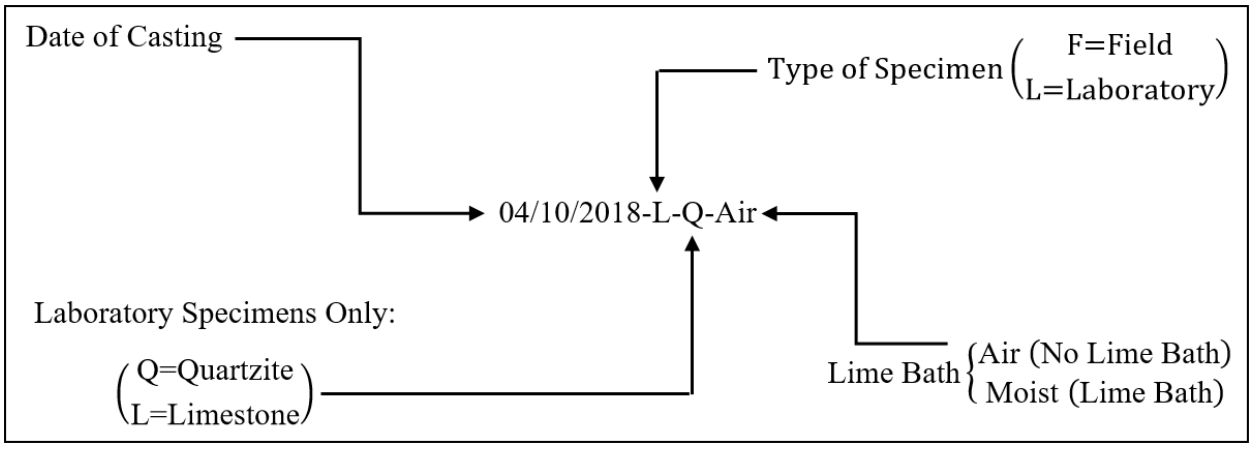

Figure 3-3: Sample Identification System for Shrinkage Prisms

In addition to the system that was implemented to distinguish the difference between field and laboratory test specimens, all shrinkage cylinders and creep cylinders were labeled to avoid any confusion during the data collection process. For each casting-date, three shrinkage

cylinders were required to aid in the prediction of the creep deformations for each loading age. These three shrinkage cylinders were labeled X, Y, and Z. Also, all cylinders used in the testing of shrinkage and creep were fitted with epoxied DEMEC points around the perimeter of the cylinder at three different locations, which were labeled A, B, and C.

3.5 TEST METHODS

This section outlines all procedures and other details that were followed during the duration of this project. All details related to batching, mixing, curing, and testing procedures performed are explained.

3.5.1 Batching and Mixing Procedure

This section covers all procedures and tasks that were performed during the batching and mixing process of the laboratory-testing phase. Topics to be covered include: the collection of raw materials, any moisture corrections that were performed, and the mixing procedure used for making all test samples.

3.5.1.1 Collection of Materials

All materials required to batch for the laboratory samples were collected from the concrete plant used to make the concrete for the I-59/I-20 segmental bridge. All materials were collected in 55-gallon drums and stored in the structures laboratory until they were needed. All coarse and fine aggregates, Class F fly ash, and all chemical admixtures were donated by Kirkpatrick Concrete in Birmingham, Alabama. All cement was donated by National Cement in Ragland, Alabama. Prior to batching, all material proportions were based on the ADLOT approved mixture design and were scaled to accommodate the volume of concrete that was needed for each laboratory mixture. After determining the mixture proportions of each material, the materials were distributed into five-gallon buckets, and were properly sealed to prevent any moisture loss.

3.5.1.2 Moisture Corrections

Immediately prior to batching, all moisture corrections were made in accordance with ASTM D 2216 to account for water that was present in both the coarse and fine aggregates. During the batching process, all coarse and fine aggregates were weighed out into 5-gallon buckets and were evenly mixed to create a more homogenous moisture distribution throughout the materials.

After both the fine and coarse aggregates had been homogenized, the mass of two pans was recorded. This value will later be subtracted from the mass sample that had been dried to determine the oven-dry mass of each sample. Once the mass of each pan had been recorded, then at least 500 grams of the coarse and the fine aggregate was weighed into the pans. Then the total weight of the pan plus the sample was recorded, which is referred to as the moist sample mass. After each sample was weighed, both of the aggregates were placed on a hot plate and allowed to dry. The mass of each pan was periodically taken until no significant change in mass was noticeable. With these values for both the oven-dry and moist sample mass, the moisture content could then be calculated. With this value, all moisture corrections for the concrete mixture could then be made to account for water in the aggregates.

3.5.2 Mixing Process

The following section outlines all techniques and procedures that were followed in the laboratory during the production of the quartzite and limestone mixtures.

3.5.2.1 Buttering the Mixer

Before mixing the raw materials, the mixer was buttered with a mixture to coat the inside of the drum. The buttering mixture that was used contained thirteen pounds of Type I/II portland cement and thirteen pounds of fine aggregate. These materials were added to the mixer along with water until the mixture had a fluid-like consistency. This mixture was allowed to mix for approximately five minutes or until all parts inside the drum were adequately coated. After the inside of the drum was properly coated, this mixture was fully discharged before the mixing process continued. A picture of the 12 cubic feet mixer used during the duration of the laboratory casting process is shown in Figure 3-4.

Figure 3-4: 12-ft^3 mixer used for all mixing operations

A procedure had to be developed for mixing of the concrete to create a uniform and consistent end product for all laboratory mixtures. The procedure that was developed is described below:

1. Add 33% of mixing water
2. Add one-third of the coarse and fine aggregates to mixer.
3. Mix for one minute.
4. Stop mixing. Then add one-third of all powdered materials such as cement and any supplementary cementitious materials.
5. Mix for two minutes.
6. While mixing, add one-third of any chemical admixtures that are being used in the mixture.
7. Cover the opening of the mixer.
8. Stop mixing.
9. Repeat steps 1-8 until all materials have been added to the mixer.
10. Mix concrete for five minutes.

11. Stop mixing and allow to rest for three minutes.
12. Run mixer for three minutes.
13. Stop mixer. Test the slump. If the slump is too low, add more HRWR admixture. Run the mixer for one minute and test again. Continue the process until target slump is reached.
14. Once the desired slump has been achieved. Perform the remaining fresh concrete quality control tests: air content, unit weight, and temperature.
15. Return all unused concrete to mixer, except for the concrete used in the air content test, and mix for one minute.
16. Make all specimens for testing hardened properties.

3.5.3 Methods for Testing Fresh Concrete Properties

All concrete mixtures that were mixed in Auburn University's structural laboratory were subjected to the same quality control tests that were applied to all fresh concrete at the construction site. These tests were used to ensure that all concretes were of the same consistency and met all specifications required by ALDOT. This section outlines all tests that were used and the process of how they were performed.

3.5.3.1 Slump

The slump of all concrete mixtures provides an indication of how workable the concrete will be during placement. For all laboratory mixtures, the slump was tested in accordance with AASHTO T 119 (2015). To conduct this test, the slump cone and base plate shown in Figure 3-5 need to be dampened to ensure that no concrete sticks to the surfaces during testing. For this study, all concrete mixtures in the laboratory had to be in the desired slump range of 3 in. to 9 in. which was required by both ALDOT and the contractor.

Once the cone and base plate have been dampened, lock the cone onto the base plate by either placing your feet on the flanges at the base of the cone or using the lock-down wings provided on the base plate. Once the cone is in position, place concrete into the cone in three separate lifts with 25 rods after each lift. After the cone has been filled, strike off any excess concrete from the top. Then remove the lock-down wings from the cone while applying pressure downward to keep the cone in the desired position. Then lift the cone in a smooth manner, and

allow the concrete to subside into its desired shape. Measure the difference in height from the top of the cone to the center of the concrete, and record the slump.

Figure 3-5: Equipment used to determine slump of all laboratory mixtures

3.5.3.2 Air Content and Unit Weight

The air content of all laboratory mixtures was determined in accordance with AASHTO T 121 (2015). The device used to measure the air content and also determine the unit weight of the concrete is illustrated in Figure 3-6 below. For this study, all concrete mixtures in the laboratory had to be in the desired air content range of 3% to 6% which was required by both ALDOT and the contractor. If the mixture did not meet the required air content, it was discarded and remixed. The unit weight of each mixture was also recorded but did not determine whether the mixture was accepted or rejected.

Figure 3-6: Equipment used to determine air content and unit weight of laboratory mixtures

3.5.3.3 Fresh Concrete Temperature

The fresh concrete temperature was taken in accordance with AASHTO T 309 (2015) in an effort to accurately record the environmental conditions that the concrete was susceptible too during mixing. The fresh concrete temperature did not affect whether the mixture was accepted or rejected.

3.5.4 Specimen Preparation and Curing

As noted earlier, this research study consisted of specimens prepared both on-site and in the laboratory. For all trips to the construction site, 24- 6 in. × 12 in. cylinders were prepared for use during creep testing and 6- 3 in. × 3 in. × 11.25 in. prisms were prepared for use during shrinkage testing. All on-site creep and shrinkage cylinders were prepared in accordance with AASHTO T 23 (2015), and all on-site shrinkage rectangular prisms were prepared in accordance with AASHTO T 160 (2015). All specimens being prepared on-site were first cast in their molds in an area where vibrations were limited and were then placed in the formwork where each concrete segment was cast to receive the same heat curing that the contractor exposed each segment too. After a 24-hour period had elapsed, the specimens were transported back to Auburn

University and immediately demolded. All creep cylinders were immediately placed in the creep room and were stored until the desired loading age. For the shrinkage specimens, one set of rectangular prisms were immediately exposed to drying after demolding, while the other set of specimens were submerged in a lime bath for a duration of 7 days before being exposed to drying.

In the laboratory-mixing phase of this project, 18- 6 in. × 12 in. cylinders were prepared for creep testing and 3- 3 in. × 3 in. × 11.25 in. rectangular prisms were prepared for shrinkage testing. The reasoning for the decrease in sample size was due to the limited amount of resources for the match-curing process of the samples. Therefore, the loading age of 182 days was eliminated. All laboratory creep and shrinkage cylinders were prepared in accordance with AASHTO T 126 (2015), and all laboratory shrinkage prisms were prepared in accordance with AASHTO T 160 (2015). To provide a more accurate representation of the curing process that the field specimens were exposed too, the laboratory specimens were match-cured at elevated temperatures through a system known as the SureCure system, which followed a temperature cycle similar to what the field specimens followed during curing. Like the field specimens, after a 24-hour period, the creep cylinders were immediately demolded and placed in the creep room and were stored until the desired loading age. The one set of shrinkage rectangular prisms were demolded and submerged in a lime bath for 7 days and were then exposed to drying.

3.5.4.1 Specimen Preparation

For all specimens that were prepared on-site, the requirements of AASHTO T 23 (2015) and AASHTO T 160 (2015) were followed in the preparation of all creep cylinders and dying shrinkage prisms, respectively. For all specimens that were prepared in the laboratory, the requirements of AASHTO T 126 (2015) and AASHTO T 160 (2015) were followed. Important steps followed include:

- All 6 in. × 12 in. cylinders were cast in three lifts with 25 rods after each lift. (Rodding should be completed with a 5/8 in. diameter steel rod with rounded end). After rodding of each lift was complete, tap the cylinder 10-12 times around the perimeter to remove any entrapped air pockets.
- All 3 in. × 3 in. × 11.25 in. prisms were cast in two lifts with 34 rods after each lift. (Rodding should be completed with a 3/8 in. diameter steel rod with rounded end).

After rodding of each lift was complete, tap the prism mold 10-12 times around the perimeter to remove any entrapped air pockets.

- Ensure that all cylinders and prisms are in a vibration-free environment during casting and during curing.

3.5.4.2 Curing Regimes

Two distinct curing regimes were used during this research effort. Both types of curing regimes required the use of heat to accelerate the curing process, but different techniques were implemented for the on-site specimens versus the specimens that were cast in the laboratory.

Specimens that were cast on-site were subjected to the same curing process the contractor used for all segments of the bridge superstructure. After all creep cylinders and drying shrinkage prisms were cast, each cylinder was sealed to prevent any moisture loss. All drying shrinkage prisms were covered with dampened burlap, and then wrapped in plastic to prevent any moisture loss. Once the specimens had been properly sealed and the contractor finished the placement of the segment for which the concrete was sampled from, the specimens were placed in the formwork of the segment as shown in Figure 3-7.

Figure 3-7: Specimens being placed in formwork for on-site initial curing

After the specimens were placed in the formwork, plastic tarps were used to enclose the entire form in which the segment was cast. Once all plastic tarps were in their desired position and sealed to prevent as much heat/moisture loss as possible, the curing process started. The concrete was not exposed to hot air until after a minimum of 30 minutes or after the initial set of the concrete. Portable torpedo heaters were utilized to add heat for the accelerated curing cycle of the segments. The concrete temperature was monitored and did not exceed 150°F nor did the rise in temperature exceed 40°F per hour. Illustrated in Figure 3-8 is an example of a temperature profile that was measured using the data collected from the temperature sensor that was placed in one of the concrete cylinders.

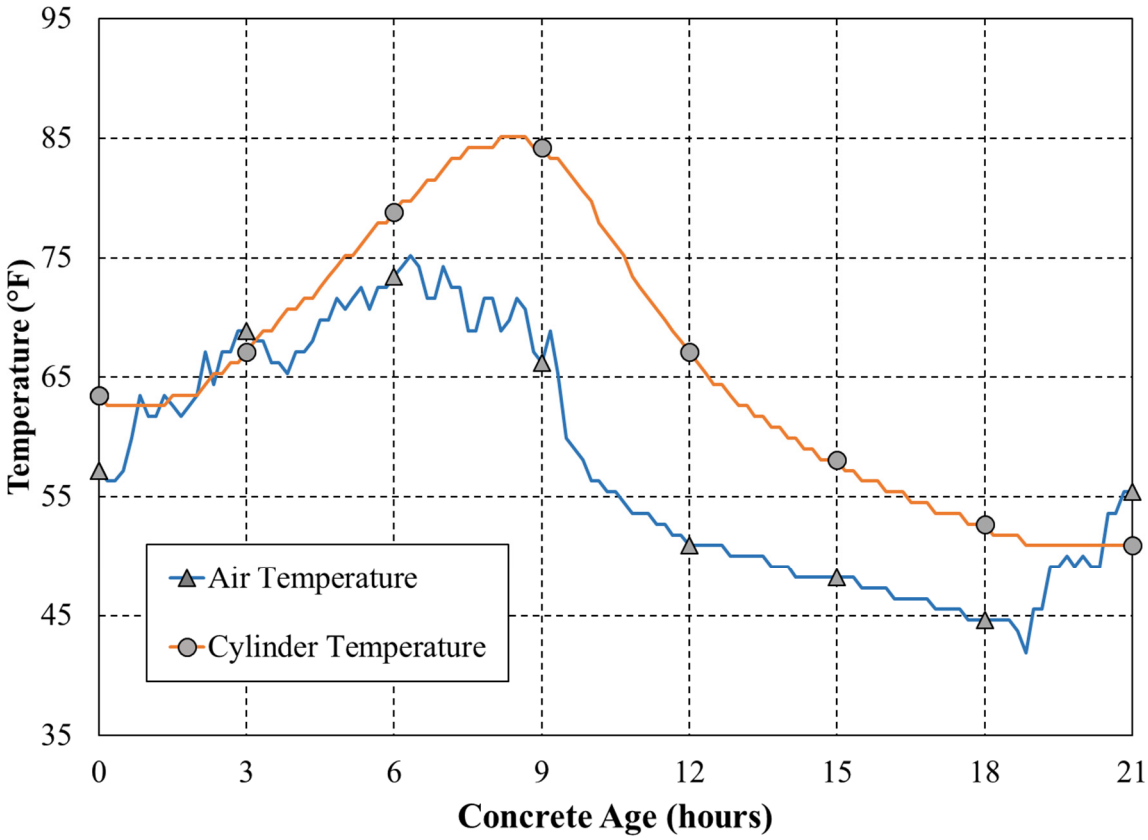

Figure 3-8: Example temperature profile from 03/20/2018 on-site casting

All creep specimens that were cast in the laboratory were subjected to a match-curing regime, which involves forcing all test specimens through an elevated temperature cycle. For the purpose of this study, a target temperature profile was predetermined based on the temperature results that were recorded in one of the on-site cylinders from the 03/20/2018 and 04/10/2018 casting dates.

Match-curing of the laboratory testing specimens was accomplished through the use of the SureCure System. This system, which is shown in Figure 3-9 with a complete channel setup, consists of a main controller box, a slave controller box, 4 in. × 8 in. and 6 in. × 12 in. match-curing sleeves, thermocouples, and power cables. The main controller box consists of eight channels where each channel is capable of curing 2 cylinders at one time by the use of a Y-power chord. However, if more than 16 cylinders are required for testing, the 4 in. × 8 in. match-curing sleeve and a slave controller box must be used to aid in the curing process.

As noted earlier, in the laboratory casting phase of this study, 18 cylinders were required for creep and shrinkage testing. The following procedure was used to setup the SureCure System:

- Connect the main controller box to a computer which has the SureCure software downloaded. (Note: The software is only capable of running on Windows XP or earlier)
- Connect all power cables to the main controller box and to the desired number of match-curing sleeves. (Note: If a slave controller box is needed, the 4 in. × 8 in. match-curing sleeve should be on a channel by itself)
- Once all match-curing sleeves have been connected, plug one thermocouple per channel into one of the match-curing sleeves per channel into the main-controller box as shown in Figure 3-9. (Note: Thermocouples are blue plugs)

Figure 3-9: SureCure System complete channel setup

- If using a slave-controller box, a reference thermocouple will need to be embedded into the 4 in. × 8 in. mold to act as a guide for the match-curing sleeves that are connected to the slave-controller box. The total setup of the slave-controller box can be seen in Figure 3-10.
- After all channels have been connected, open the Plant Manager icon on the computer to start the SureCure software and check to see all thermocouples are properly reading on the home screen.
- Once all thermocouples are reading, program the desired temperature curing profile and start the program.
- After starting the cycle, return to the Plant Manager tab and make sure that all channels are set to start. Once the program starts, if a channel is lower than the set temperature, the channel will activate until the temperature is higher than the set temperature.

Figure 3-10: SureCure System complete setup with slave-controller box

The above procedure was used for both the quartzite and limestone laboratory mixtures. Both mixtures were placed in their desired match-curing sleeve after casting where they were subjected to a five-hour period of room temperature curing before heating began. After five hours, all cylinders were heated at a rate of 12°F per hour until reaching a temperature of 120°F. This temperature was maintained for a duration of 8 hours, and then a gradual cooling process was allowed to take place over the next several hours before al specimens were demolded. A graph illustrating the target temperature profile as well as the recorded temperatures for the quartzite and limestone mixtures that were mixed in the laboratory are presented in Figure 3-11. It can be seen in this figure that very similar curing temperatures were achieved for the limestone and quartzite concretes.

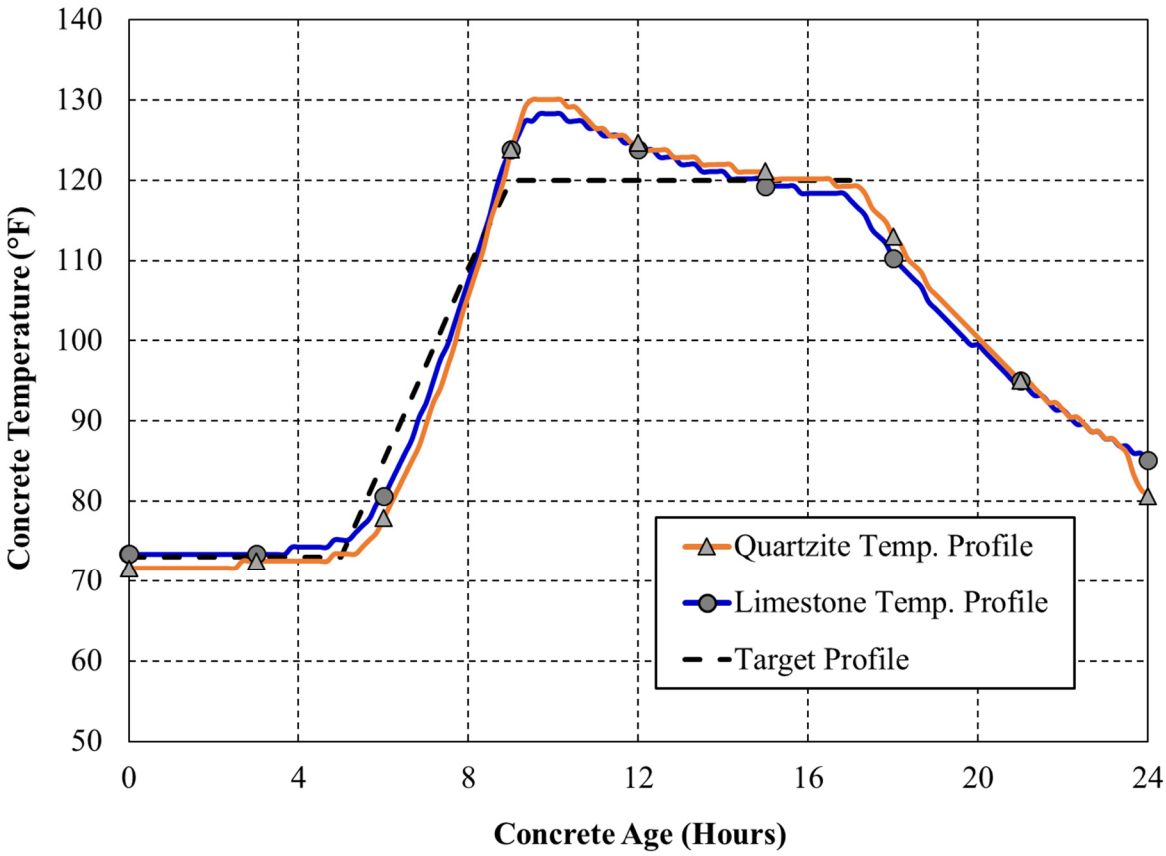

Figure 3-11: Temperature profiles for all laboratory concrete mixtures versus the target profile

Due to the limited amount of resources, the drying shrinkage prisms that were cast in the laboratory were cured in accordance with AASHTO T 160 (2015). All prisms were covered with dampened burlap before being wrapped in plastic to ensure no moisture was lost. After a 24-hour time period had elapsed, the prisms were demolded and placed in a lime-saturated water tank for a duration of seven days before being exposed to dying.

After the field and laboratory test specimens were demolded, they were placed in the creep testing room where they remained for the remainder of this project. ASTM C 512 (2018) requires that the test specimens be stored in an environment where the temperature is maintained at 73°F $\pm$ 1.5°F. Figure 3-12 shows a plot of the temperature profile that was generated using collected temperature data from the creep testing room.

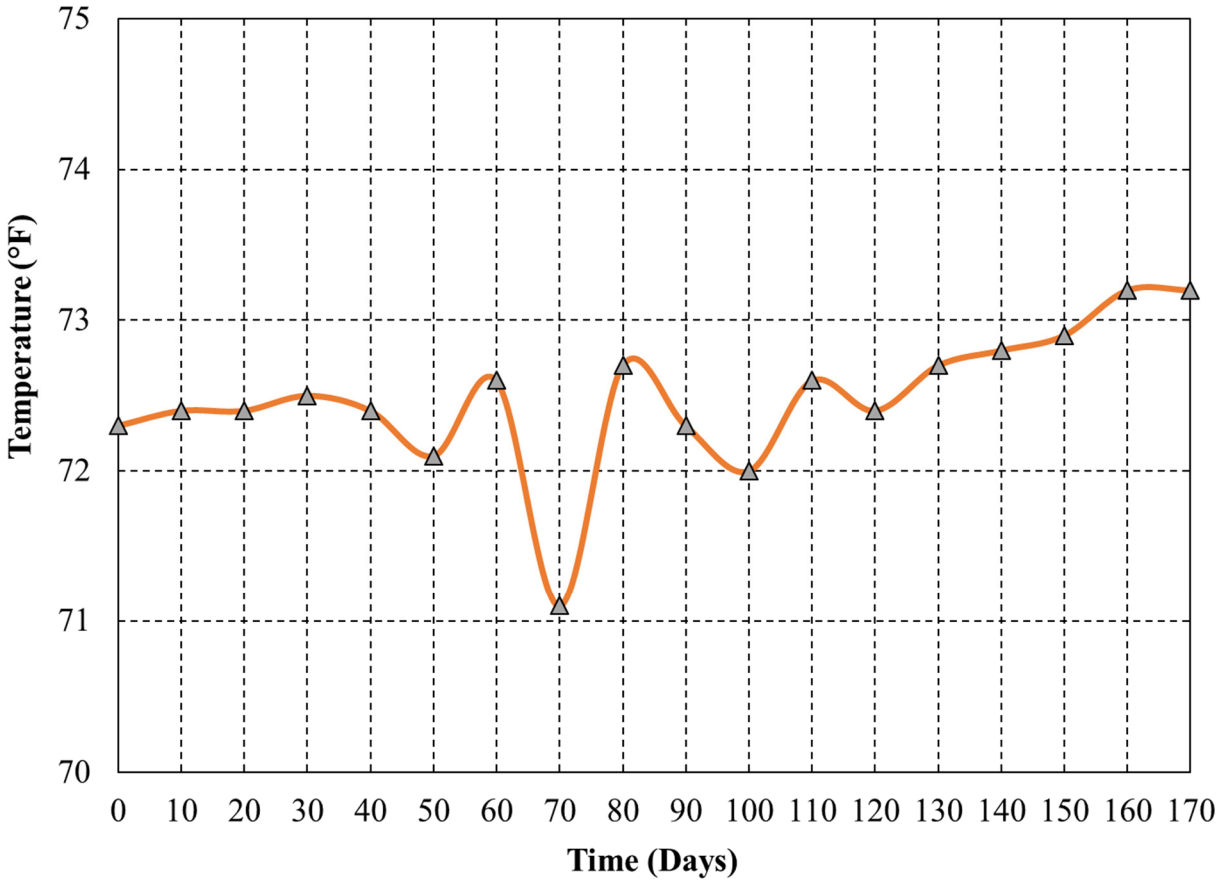

Figure 3-12: Temperature profile of creep testing room during testing

3.5.5 Methods for Testing Hardened Concrete

Many different characteristics of hardened concrete can be tested, but during this research effort only compressive strength, modulus of elasticity, drying shrinkage, and creep was tested. This section outlines the test procedures and equipment used to collect all data related to compressive strength, modulus of elasticity, drying shrinkage, and creep.

3.5.5.1 Compressive Strength

Before creep testing could begin, the compressive strength of each loading age had to be determined in order for the creep specimens to be loaded to 40 percent of its strength. All compressive strength testing was conducted in accordance with ASSHTO T 22 (2015). Each specimen was prepped by grinding each end to ensure a level loading surface, and then the cylinders were placed into a Forney QC400 compressive testing machine and were loaded at a

target rate of 60,000 lbs/min. until failure. The 400-kip capacity compressive machine is shown in Figure 3-13.

Figure 3-13: Forney QC400 compression machine

3.5.5.2 Modulus of Elasticity

After determining the compressive strength of one cylinder for each loading age, the modulus of elasticity was determined on the remaining cylinders in accordance with ASTM C 469 (2018). Before testing commenced, the compressometer displayed in Figure 3-14, was calibrated using the specifications outlined in ASTM C 469 (2018).

Figure 3-14: Compressometer used for modulus of elasticity testing

The cylinders were placed into the same Forney QC400 compressive testing machine that was previously used to determine the compressive strength for each loading age. After the modulus of elasticity test was performed on each cylinder, the compressive strength outlined in 3.5.5.1 was performed to obtain an accurate compressive strength that would be used at a later date in creep testing.

3.5.5.3 Drying Shrinkage

The drying shrinkage of each concrete mixture was tested in accordance with AASHTO T 160 (2015). This was done by using 3 in. × 3 in. × 11.25 in. prisms fitted with gage studs at each end. All readings for the drying shrinkage specimens were taken at the same time intervals as to that of the creep specimens. All length changes related to drying shrinkage were monitored using the standard length comparator shown in Figure 3-15. Readings were taken immediately after exposure to drying, 2 to 6 hours after exposure, once a day for the first week, once a week for the first month, and once a month for the first year. During the on-site portion of this

research study, two sets of drying shrinkage prisms were cast with each set containing three prisms. Once both of these sets were transported back to Auburn University, one set was immediately demolded and exposed to drying while the other was submerged in a lime-saturated bath for 7 days and then exposed to drying.

For the laboratory phase of this project, only one set of drying shrinkage prisms were cast, and were placed in the lime-saturated bath for a duration of 7 days once they were removed from their molds. After a duration of 7 days, the laboratory specimens were exposed to drying.

Figure 3-15: Instrumentation used to monitor length changes in drying shrinkage prisms

In order to isolate the creep of each concrete mixture, 6 in. × 12 in. cylinders were cast and their shrinkage strains were measured. All drying shrinkage cylinders were fitted with Demountable Mechanical (DEMEC) strain points and then measured using a DEMEC strain gauge. Also, the cylinders that were loaded in each of the creep frames were fitted with DEMEC points. This was done to ensure that all data collected during the creep testing process were

measured in the same manner. A completed cylinder fitted with DEMEC points is shown in Figure 3-16. The DEMEC strain gauge used for this project is shown in Figure 3-17.

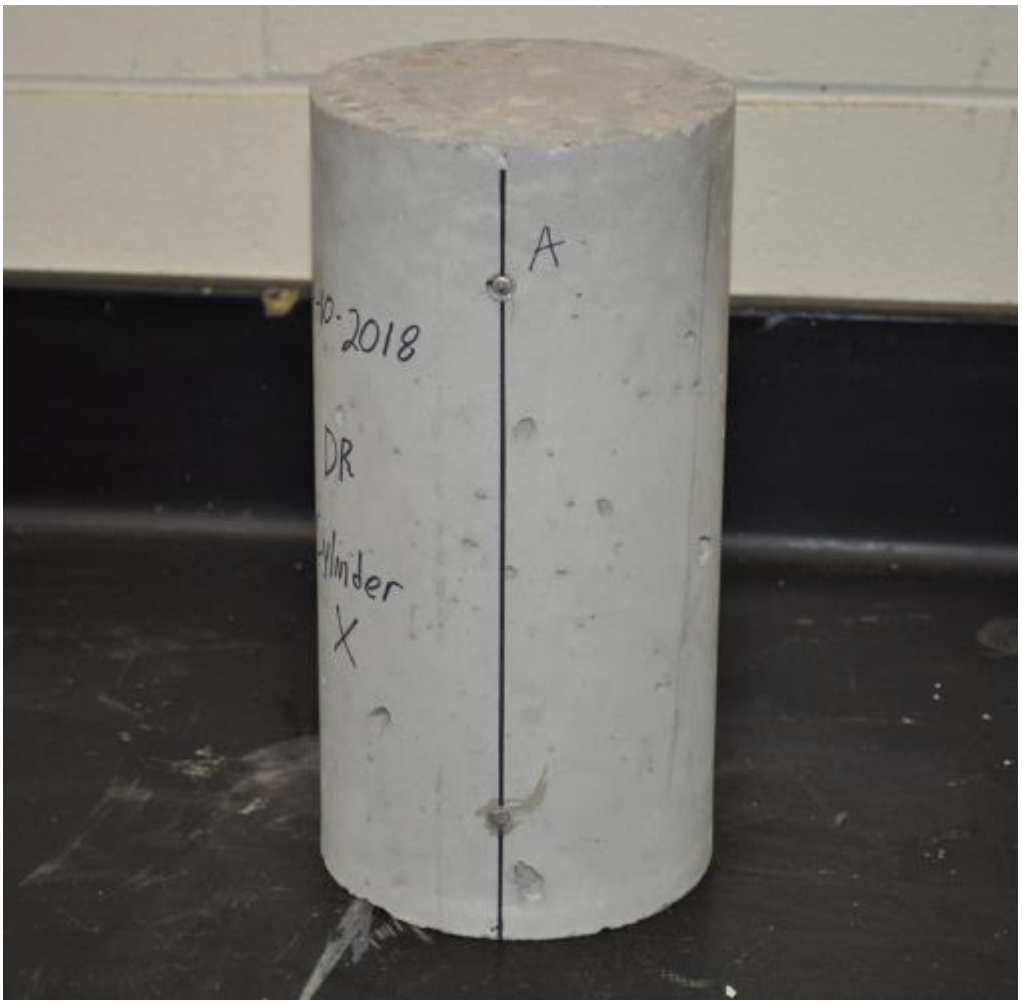

Figure 3-16: Test cylinder fitted with DEMEC points

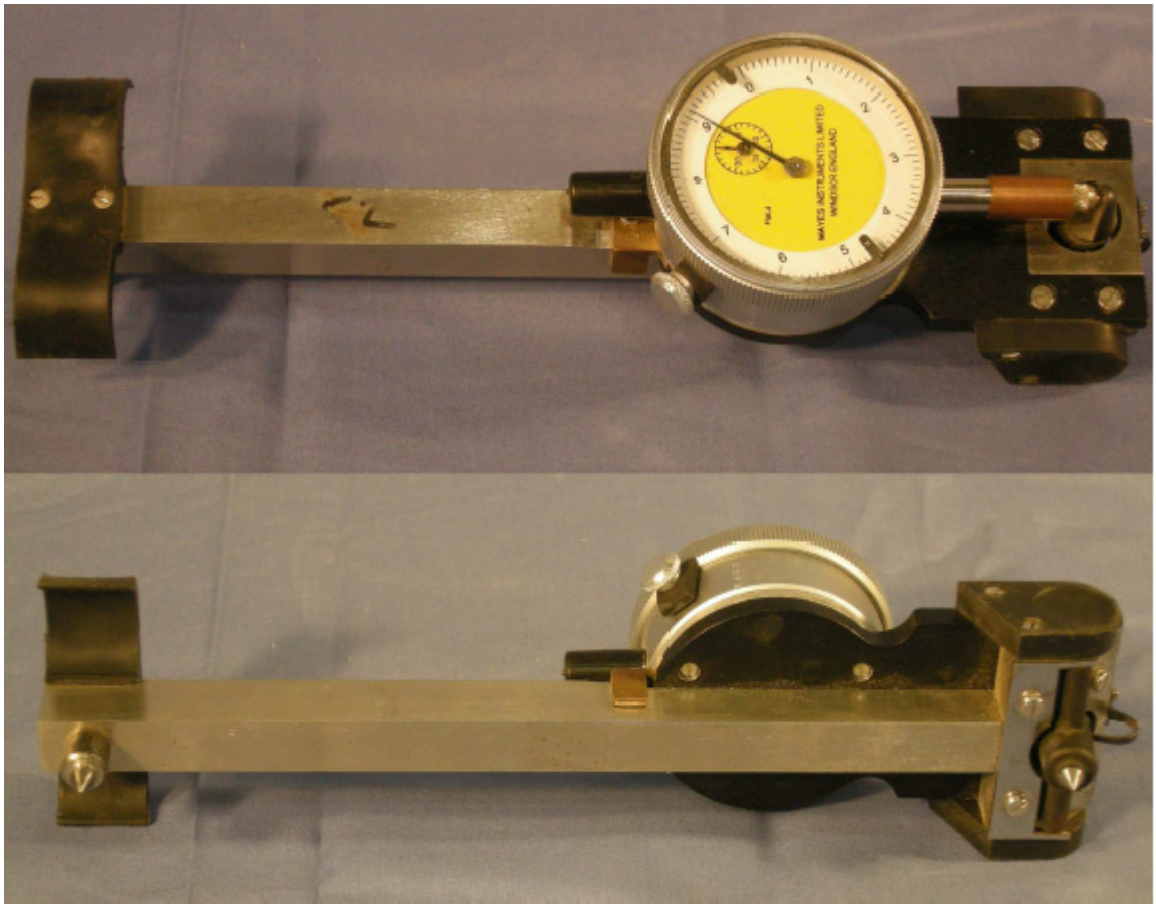

Figure 3-17: DEMEC strain gauge used during this project (Kavanaugh 2008)

All DEMEC readings for drying shrinkage cylinders were taken at the same time intervals as that of the creep cylinders in accordance with ASTM C 512 (2018). These intervals included readings taken prior to loading, immediately after loading, 2 to 6 hours after loading, once a day for the first week, once a week for the first month, and once a month for the first year.

3.5.6 Creep Testing

During the duration of this research effort, all creep testing was completed in accordance with ASTM C 512 (2018). In this section, the entire testing procedure is outlined along with all details of testing equipment and methods used.

3.5.6.1 Creep Frames

For the purposes of this research project, 11 creep testing frames were used in order to monitor the creep behavior for four different loading ages of different concretes. In accordance with

ASTM C 512 (2018), each frame should be able to maintain +/- 2% of the target load to the concrete specimen. The load was applied to each frame using a hydraulic ram and load cell to accurately read the load being applied. Figure 3-18 illustrates the hydraulic ram and load cell, while Figure 3-19 shows an actual frame that was used during testing. Figure 3-20 and Figure 3-21 show schematics of the creep frames used during this research project (Kavanaugh 2008).

Figure 3-18: Hydraulic Ram and Load Cell used during the loading of creep frames

Figure 3-19: Actual creep frame that was used during testing (Kavanaugh 2008)

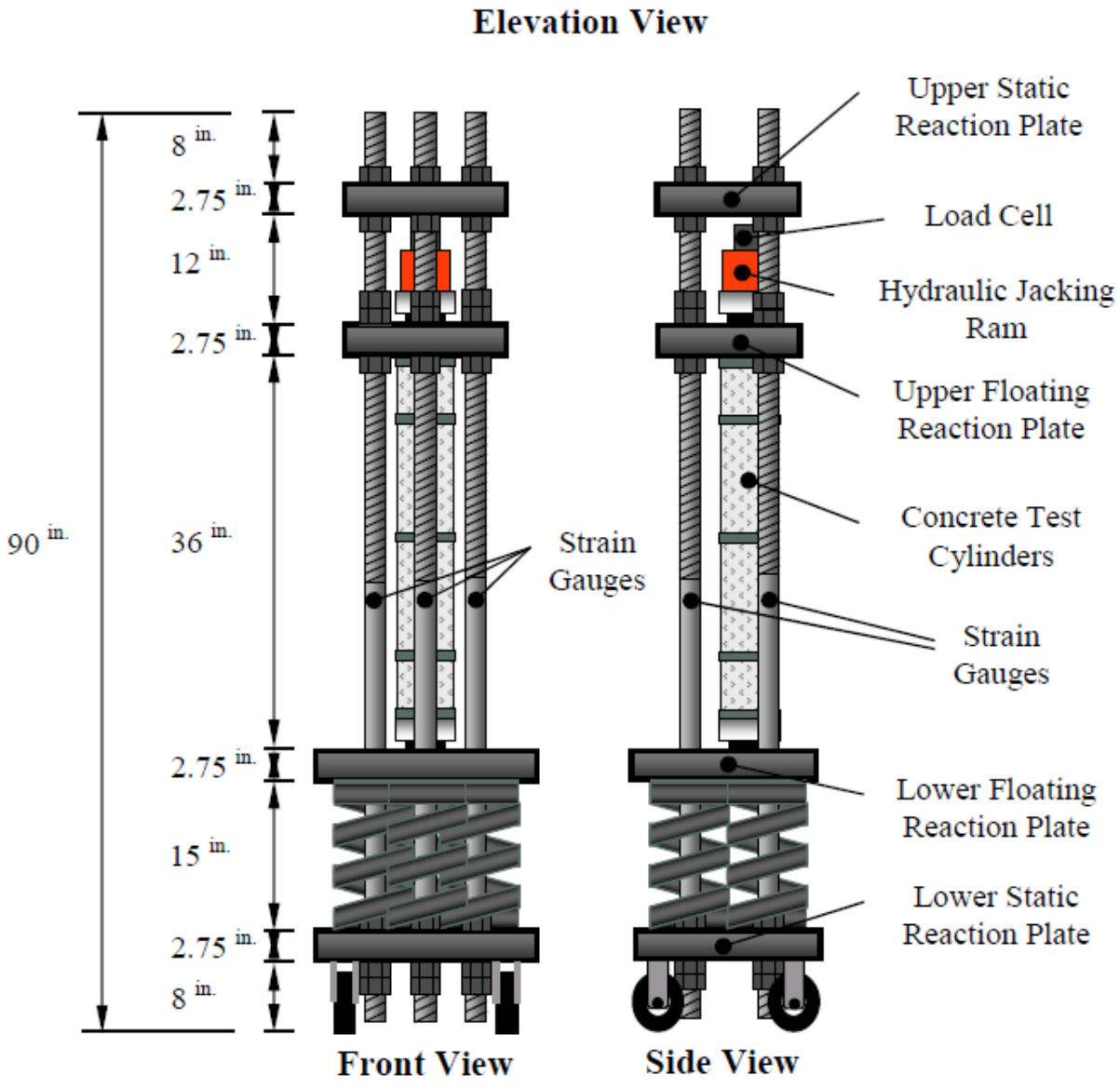

Figure 3-20: Schematic of a creep frame used during testing (Kavanaugh 2008)

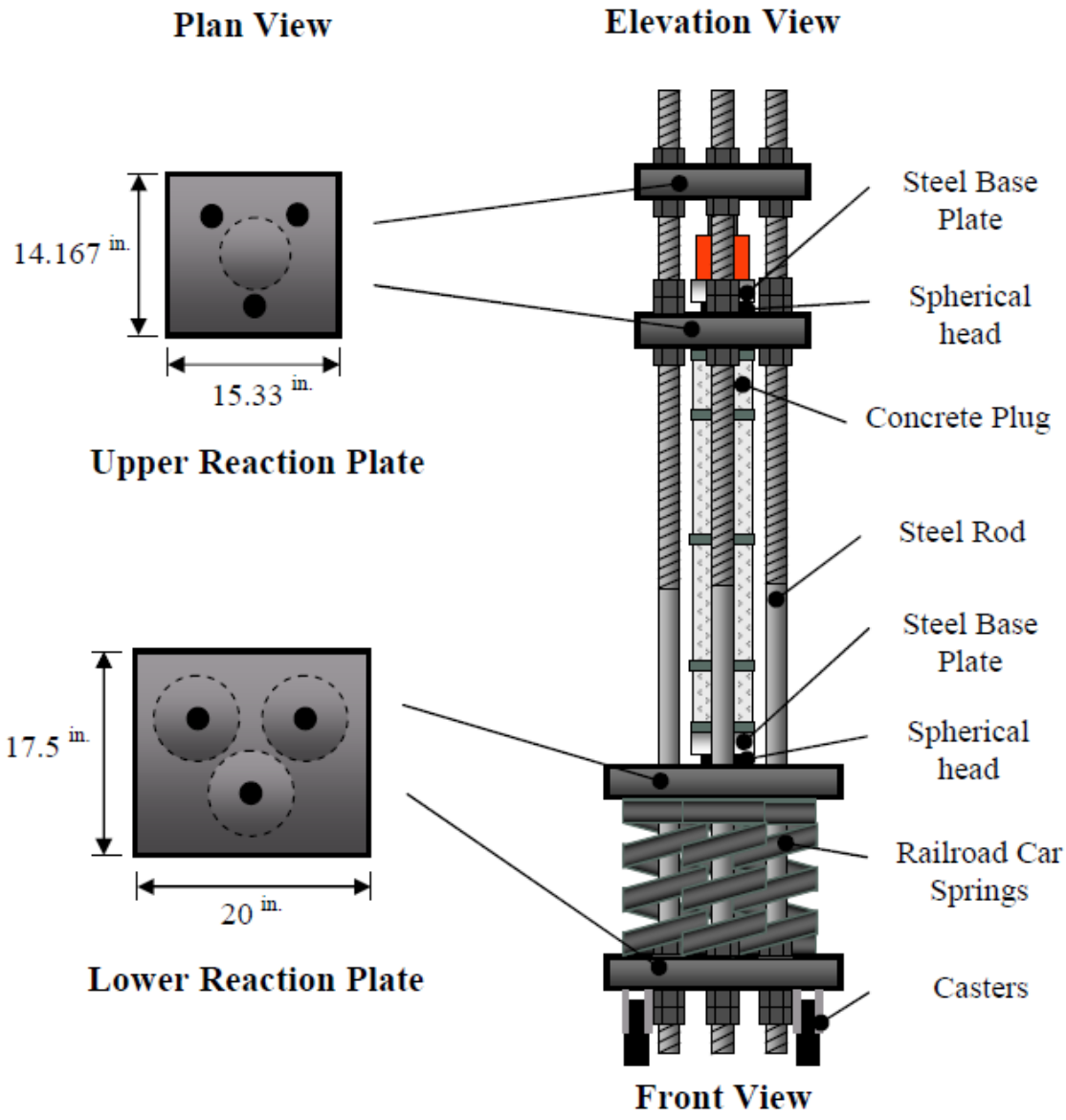

Figure 3-21: Schematic of a creep frame used during testing (Kavanaugh 2008)

The following description of the materials used for each creep frame are based on previous testing performed by Bryan Kavanaugh (2008). During the preliminary design phase, it was concluded that each frame must be able to withstand 40% of the ultimate strength of each concrete loading age. It was determined that 2¾ in.- thick Grade 50 steel plates were required to be able to withstand the load demand for each frame. To assist with alignment during loading, 6 in. diameter marks were scribed into the underside of the upper floating reaction plate. This was

used to ensure that all specimens were properly aligned in the frame and to minimize any eccentricities forming during loading.

From Figure 3-21 it can be seen that three threaded rods with nuts were used to hold the applied load in the frame once the hydraulic ram was released. Each rod needed to be able to safely hold roughly 50 kips of force while also having negligible relaxation. In order to obtain this requirement, 1¾ in. diameter steel rods with a yield stress of 65 ksi and an ultimate stress of 80 ksi were used during testing. Each rod is 90 in. in length and was threaded for the first 10 in. of the lower end of the bar and along the first 50 in. of top portion. With the size of bars that was used for each frame, 1¾ in. Grade 8, heavy-duty hex nuts were threaded onto the rods to hold the floating reaction plates in the desired locations. Each frame required six of these nuts, which were made from C 1045 steel having a minimum Rockwell hardness of C24 and a minimum ultimate tensile stress of 150 ksi. The nuts performed reasonably well, however, due to tolerance issues, approximately 2% of the applied load was lost when load from the hydraulic ram is removed from the frame. This required the target load to be over applied by 4% in order to reach the desired 42% of the ultimate stress since the target load could be +/- 2%.

The plates and rods act together to hold the applied loads once the hydraulic ram was removed, but the railroad car springs are what was used to maintain the applied load as the concrete specimens deformed over time. Each frame required three of these springs, each of which had a spring constant of 25,000 lbs./in. These springs were designed and constructed specifically for these creep frames. They were manufactured by Duer/Carolina Coil, Inc. of Reidville, SC. Each spring was made of ASTM-A-304, Grade 220 steel and was 15 in. in height and had an 8½ in. outer diameter. As compared to other springs used in this area of research, the springs designed for Auburn University were highly flexible allowing for greater length change to occur before a 4% reduction in the applied load occurred.

3.5.6.2 The Creep Room

ASTM C 512 (2018) requires that both temperature and the relative humidity be controlled at 73°F $\pm$ 1.5°F and 50% $\pm$ 4%, respectively. Previous testing performed by past researchers at Auburn University has required similar environmental conditions with minimal changes to temperature while testing. To accurately create these conditions, a climate-controlled room was

built that allowed both temperature and relative humidity to be controlled. Figure 3-22 shows the general layout of the room with the positions of the creep frames during the duration of testing.

Figure 3-22: Environmentally controlled creep room

Also, storage racks are present along the walls of the room to hold specimens, such as drying shrinkage prisms or creep specimens that are awaiting their respected loading age that must be subjected to the same exposure conditions after their curing process has been complete. Once these specimens are ready to be loaded into a creep frame, they are removed from the storage area and then placed in the appropriate frame to commence creep testing. During testing, the temperature and relative humidity of the creep room were recorded using a Dickson Data Collection system to accurately determine the average environmental conditions throughout the duration of testing. These average values were later used in creep prediction models mentioned in Section 2.4.

3.5.6.3 Creep Testing Procedure

All creep testing procedures used followed the requirements outlined in ASTM C 512 (2018). After all specimens were removed from their respected curing regime, they were either prepped to be loaded into the creep frames, or they were stored in the creep room until their loading age date and then they were placed into the creep frames for loading. An outline of the creep testing procedure used during testing is presented below. Some steps were adopted from Bryan Kavanaugh's (2008) testing procedure with a few modifications throughout the process.

1. Remove creep, shrinkage, and strength specimens from curing conditions.
2. Place all specimens in an end grinder to achieve a level surface for loading.
3. After end grinding, prep all shrinkage and creep specimens with DEMEC points at 120-degree intervals around the perimeter. Allow epoxy to fully harden before taking initial reading.
4. Determine the ultimate compressive strength in accordance with AASHTO T 22 (2015) of first specimen, and then perform the Modulus of Elasticity test in accordance with ASTM C 469 (2018) on the next two strength specimens before breaking these.
5. Place two creep specimens into the frame, and determine proper alignment to limit eccentricities during testing. Cylinders should align with scribe mark on the bottom of the upper reaction plate.
6. Lower the upper floating reaction plate, and ensure that cylinders are properly aligned and level within the frame.
7. Record initial strain measurements for test cylinders, dying shrinkage cylinders, and both DEMEC points and drilled DEMEC points on each steel bar.
8. After recording the initial measurements, position the hydraulic jacking mechanism on top of the upper reaction plate and then place the load cell in the center on top. Plumb the entire setup to ensure that no loading errors occur.
9. Attach the load cell to the strain indicator.
10. Slowly begin to apply load until 102% of the target applied load is reached. (Note: During loading, it is imperative to take intermediate readings to ensure no load eccentricities are present)

11. After reaching the desired load, lock each nut in place with use of a pipe wrench. Additional lock nuts may be tightened as well with the wrench to check that no load is lost.
12. Gently retract jacking mechanism, and then take readings of DEMEC points and drilled DEMEC points along each steel bar to ensure the applied load is within 2% of the desired value. Reapply load as necessary.
13. Record concrete strain measurements resulting from load applications and corresponding drying shrinkage strains immediately following the loading process.

In the tightening process of the lock nuts from Step 11, after each frame was loaded to its desired load that was determined prior, the nuts were tightened fully with the pipe wrench to ensure that no load was lost after the hydraulic ram was released. This step was determined by running trial tests on dummy cylinders that were available for use in the creep room.

After the above procedure was completed, strain measurement readings were taken on both the creep and drying shrinkage specimens in the time intervals outlined by ASTM C 512 (2018). These readings were taken using the DEMEC strain gauge discussed earlier in section 3.5.2.3. The time intervals required by ASTM C 512 (2018) include immediately after the load is applied, 2 to 6 hours after loading, once a day for the first week, one a week for the first month, and once a month for the duration of the testing period.

During the testing procedure, the applied load in the frames had to be monitored to ensure that none had been lost due to eccentricities in the alignment of the specimens, due to relaxation in the steel bars, or the nuts being loosened due to the high amount of force being applied to each to hold the upper reaction plate in place. Each bar was equipped with DEMEC points at two locations 180 degrees apart from each other as seen in Figure 3-23.

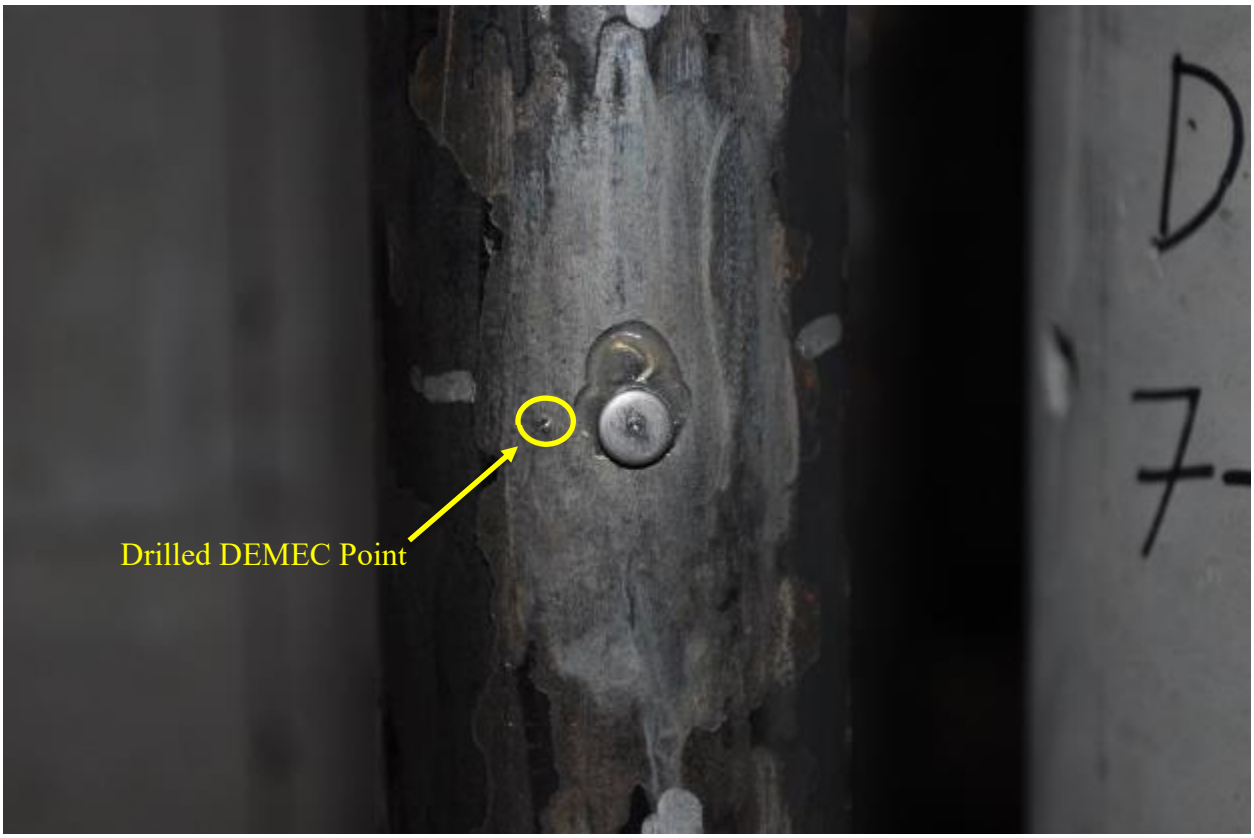

Figure 3-23: Epoxied and drilled DEMEC point locations on steel rods of each creep frame

The readings taken at each DEMEC location were inputted into an Excel spreadsheet that would calculate the strain that each bar was under due to the applied load. With this strain, the stress for each bar was then computed and multiplied by the area to calculate the force that was in each bar. The sum of the three bars determined the total force that was in the frame, and then lead to whether the hydraulic ram had to be used to reapply some force to meet the loading requirements for creep testing. Also, each bar was fitted with drilled DEMEC points by using a 1-mm diameter drill bit at two locations 180 degrees apart from each other. These drilled locations acted as a secondary reading to monitor the load in the frame, and to ensure that the epoxied DEMEC points were providing accurate results.

3.6 MATERIALS

During the duration of this research project, raw materials were collected from the concrete batch plant used to produce the bridge segments. These materials were collected and used to accurately

represent the raw materials that were being used by the contractor during the mixing process for all concrete. This section provides more in-depth details of each of these raw materials.

3.6.1 Cementitious Materials

Two types of cementitious materials were used for both the quartzite and limestone laboratory mixtures for this research study. These cementitious materials consisted of Type I/II portland cement and Class F fly ash. These are the cementitious materials that were approved by ALDOT for use in the segments of the I-59/I-20 segmental bridge.

3.6.1.1 Type I/II Portland Cement

The Type I/II portland cement that was used in all laboratory mixtures during this research study was manufactured in Ragland, Alabama by National Cement. National Cement provides a large amount of cementitious materials to Kirkpatrick Concrete Inc. located in Birmingham, Alabama who developed a concrete mixture design that was used during construction.

3.6.1.2 Class F Fly Ash

Kirkpatrick Concrete Inc. in Birmingham, Alabama provided the Class F fly ash that was used in all laboratory mixtures. They provided two types of Class F fly ash: one type was manufactured by The SEFA Group located in Cumberland City, Tennessee and the other was manufactured by Headwaters Construction Materials. Only the fly ash manufactured by the SEFA Group was used in the laboratory mixtures to ensure that the concrete mixture would share similar fresh and hardened properties to the concrete produced by Kirkpatrick Concrete Inc.

3.6.2 Chemical Admixtures

Two of the chemical admixtures that were used in the field were also used in both laboratory mixture designs to achieve the slump and air content that was required by ALDOT during this project. The two admixtures that were used consisted of a mid-range water-reducing admixture (mid-range WRA) and an air-entraining admixture (AEA). Samples of both the mid-range WRA and the AEA were collected from Kirkpatrick Concrete, Inc. in Birmingham, Alabama.

3.6.2.1 Mid-Range Water-Reducing Admixture

MasterPolyheed 1025 was the mid-range water-reducing admixture that was utilized during the mixing process of both laboratory mixtures. It is a product of BASF Construction Chemicals located in Cleveland, Ohio. This water-reducing admixture was used to help achieve the required slump.

3.6.2.2 Air-Entraining Admixture

MasterAir AE 200 was the air-entraining admixture that was used in each of the laboratory mixtures. It provided each concrete mixture with the appropriate air content that was previously mentioned in Section 3.2.1.1. This admixture is also a product of BASF Construction Chemicals.

3.6.3 Coarse Aggregate

Two different coarse aggregate types were used in the laboratory mixing phase of this project. The two aggregate types that were chosen included No. 67 crushed limestone and No. 67 crushed quartzite. Both aggregate types were collected from Kirkpatrick Concrete, Inc. in Birmingham, Alabama. This section will provide details pertaining to the absorption capacity and specific gravities for each of these coarse aggregates.

3.6.3.1 Crushed Limestone

The No. 67 crushed limestone that was used in one of the laboratory mixtures was supplied by East Thomas Quarry located in Birmingham, Alabama that is operated by Wade Sand and Gravel. The crushed limestone had a bulk specific gravity of 2.71 and a saturated surface dry (SSD) specific gravity of 2.73, which corresponds to an absorption capacity of 1.0%. These values were obtained from the approved list of coarse and fine aggregates by ALDOT.

3.6.3.2 Crushed Quartzite

The No. 67 crushed quartzite that was used in the second laboratory mixtures supplied by Coldwater Mountain Quarry located in Oxford, Alabama that is operated by McCartney Construction Company. The crushed quartzite had a bulk specific gravity of 2.58 and a saturated surface dry (SSD) specific gravity of 2.61, which corresponds to an absorption capacity of 1.0%. These values were obtained from the approved list of coarse and fine aggregates by ALDOT.

3.6.4 Fine Aggregate

The fine aggregate source remained constant for all laboratory mixtures. The fine aggregate used was a No. 100 concrete sand that was supplied by Scott Pitt located in Elmore, Alabama that is operated by Elmore Sand and Gravel. The sand had a bulk specific gravity of 2.77 and a saturated surface dry (SSD) specific gravity of 2.76, which corresponds to an absorption capacity of 0.3%. These values were obtained from the approved list of coarse and fine aggregates previously mentioned in Section 3.6.3.1 and 3.6.3.2.

CHAPTER 4: JOB-SITE OVERVIEW AND CASTING PROCEDURES OF THE I-59/I-20 BIRMINGHAM SEGMENTAL BRIDGE

4.1 INTRODUCTION

As previously mentioned, all samples that were collected at the job-site were cast using concrete that was used in the placement of segments that would later be erected in the segmental bridge replacement at the junction of the I-59/I-20 interchange in Birmingham, Alabama. This section will provide a brief overview of the job-site and cover the procedures that used by the contractor to cast each segment.

4.2 JOB-SITE LOCATION AND CONDITIONS

The erection of segmental bridges requires large amounts of materials, laborers, and a large area of workspace for storage of materials, construction equipment, and the completed concrete segments themselves. For the duration of this project, an abandoned steel mill located at 1503 50th Street North Birmingham, Alabama 35212, which is next to the Birmingham-Shuttlesworth International Airport, was leased and used as the construction site for all casting and storage of the concrete segments. This area of land surrounding the steel mill provided a large amount of space that ensured that all materials and concrete segments could be safely and efficiently stored until they were needed at later stages of the project. Also, parts of the steel mill itself were utilized as a storage building for all aggregates, post-tensioning cables, construction vehicles, and also housed an on-site quality control testing laboratory.

4.3 SEGMENTAL FORMWORK

This project required extensive preliminary setup before any concrete segments could be cast. Before segments could be cast, specially fabricated forms had to be manufactured. The forms were fabricated by a third-party contractor and were then shipped to the jobsite where they were erected in their final configuration for the duration of the project. A completed form is shown in Figure 4-1 and Figure 4-2.

Figure 4-1: Segmental formwork used during casting

Figure 4-2: Segmental formwork used during casting

After each of these forms were properly erected, they were carefully reviewed to ensure that all dimensions, tightness, and cleanliness were adequate. Once all these checks were approved, the releasing agent that was approved by ALDOT could then be applied to the surface of the formwork. After the releasing agent was applied to the form, the steel reinforcement cage was carefully placed in the formwork. The steel reinforcement cage was erected prior to placement in the formwork in a specially fabricated box as shown in Figure 4-3. This cage was transported by a crane to the formwork and set into their final configuration. Once the steel reinforcement cage was properly installed, a pre-pour inspection was completed to ensure that all requirements had been fulfilled.

Figure 4-3: Pre-fabrication of steel reinforcement cage prior to being placed in formwork

After the pre-pour inspection and all necessary adjustments had been made, the placement of concrete could begin. During this construction project, the match-casting method was implemented to aid in ensuring proper fit between adjacent segments. As mentioned earlier in Section 2.2.1, match-casting is the process of casting one segment and then casting the next segment against the preceding one so that they fit exactly as cast. After the placement of one segment had been completed and adequate strength had been achieved, the segment was stripped

away from the forms, and slid out of the formwork using the specially made hydraulic conveyor system that each form was equipped with as shown in Figure 4-4. This conveyor system allowed for an increase in the production rate as one segment could be removed and allowed to cure further while the next segment could be cast.

Figure 4-4: Hydraulic conveyor system used to slide each segment from the formwork

4.4 CASTING OF SEGMENTS

Before any concrete segments could be cast, the concrete had to be mixed using the concrete mixture design approved by ALDOT. Due to this project being of significant size, the contractor deemed it beneficial to erect their own batch plant on-site as shown in Figure 4-5. This allowed the contractor to have all necessary materials available on-site and eliminated the wait time that would have to be accounted for if an outside concrete supplier provided all concrete needed for the segments. However, in the early stages of the project, the batch plant was still in the construction phase and was not in operation. Until the batch plant was running and meeting all specifications and requirements, all of the concrete was provided by a ready-mixed concrete producer.

Figure 4-5: On-site batch plant for all mixing of concrete

Before the placement of each batch of concrete, each ready-mixed concrete truck would have a sample taken by the quality control technicians to ensure that all concrete mixtures met the fresh properties that were required by ALDOT as shown in Figure 4-6. The fresh properties that were monitored included total air content, slump, concrete temperature, and unit weight.

Figure 4-6: Quality control testing prior to placement of the concrete

After each ready-mixed concrete truck had been tested and all fresh concrete properties had met the given requirements, the placement of each concrete segment could begin. In order for each segment to be properly placed, the concrete had to be raised to an elevated height to efficiently fill the formwork. This task was performed with two different methods. In the beginning stages of the project, the concrete was raised to the desired elevated height by using a concrete truck specially equipped with a belt conveyor. Due to the significant amount of time that was needed for this type of placement, the contractor then changed to use the method of discharging concrete from a ready-mixed concrete truck into a concrete bucket, which could then be raised and lowered by a crane to the top of the formwork.

As mentioned earlier, the first method involved using a ready-mixed concrete truck that was equipped with a belt conveyor to feed the concrete to the top of the formwork as shown in Figure 4-7. The end of each belt conveyor was equipped with tremie pipes to avoid a concrete free-fall of more than four feet to eliminate the possibility segregation once the concrete comes into contact with the steel reinforcement.

Figure 4-7: Ready-mixed concrete truck equipped with belt conveyor

Once the ready-mixed concrete truck equipped with the belt conveyor was in place and the boom was in its desired location, the truck was backed into the correct position. Once the truck was in place, the concrete was discharged from the drum onto the belt conveyor and transported to the top of the formwork as shown in Figure 4-8. After a sufficient amount of concrete had been placed in its desired position in the formwork, laborers would move the boom of the belt conveyor until the entire segment was fully placed. Figure 4-8 shows how the concrete was discharged from the ready-mixed concrete truck onto the belt conveyor and then transported to the top of the formwork for casting. Once the concrete made it to the top of the conveyor, workers controlled the placement of the concrete by placing the boom in the desired location until movement was necessary.

Figure 4-8: Concrete being discharged onto to belt conveyor for transport to the segment

When placing each segment, the belt conveyor system proved to be highly time consuming due to its slow rate of concrete transport. Each segment could take as long as four hours to place, so the contractor explored another method that could decrease the amount of time needed to place each segment. The method that the contractor selected was the use of a concrete bucket as shown in Figure 4-9. This method involved each ready-mixed concrete truck discharging concrete into the concrete bucket, which was attached to a crane. Once the bucket was full, the crane would then lift the bucket into the desired position and laborers would open the gate on the bottom to release the concrete into the formwork as shown in Figure 4-10. This allowed concrete to be placed at much higher rates, and proved to cut placement time of each segment to approximately two hours.

Figure 4-9: Concrete being discharged into a concrete bucket for transport to the segment

Figure 4-10: Placement of concrete by use of the concrete bucket

Unlike self-consolidating concrete, conventional slump concrete must be consolidated during its placement. This was achieved through the use of portable vibrators as shown in Figure 4-11. Each of these electric internal vibrators had to have a minimum frequency of 8,000 vibrations per minute, and is inserted into the concrete until all consolidation requirements have been met.

Figure 4-11: Portable vibrator used to achieve the desired consolidation

4.5 FINISHING TECHNIQUES

After placement and consolidation of the concrete segment was completed, the procedure for finishing each segment could then commence. The finishing techniques for all segments remained constant through the duration of the process. For the top surface of the segments, finishing was completed using an aluminum or magnesium screed as shown in Figure 4-12.

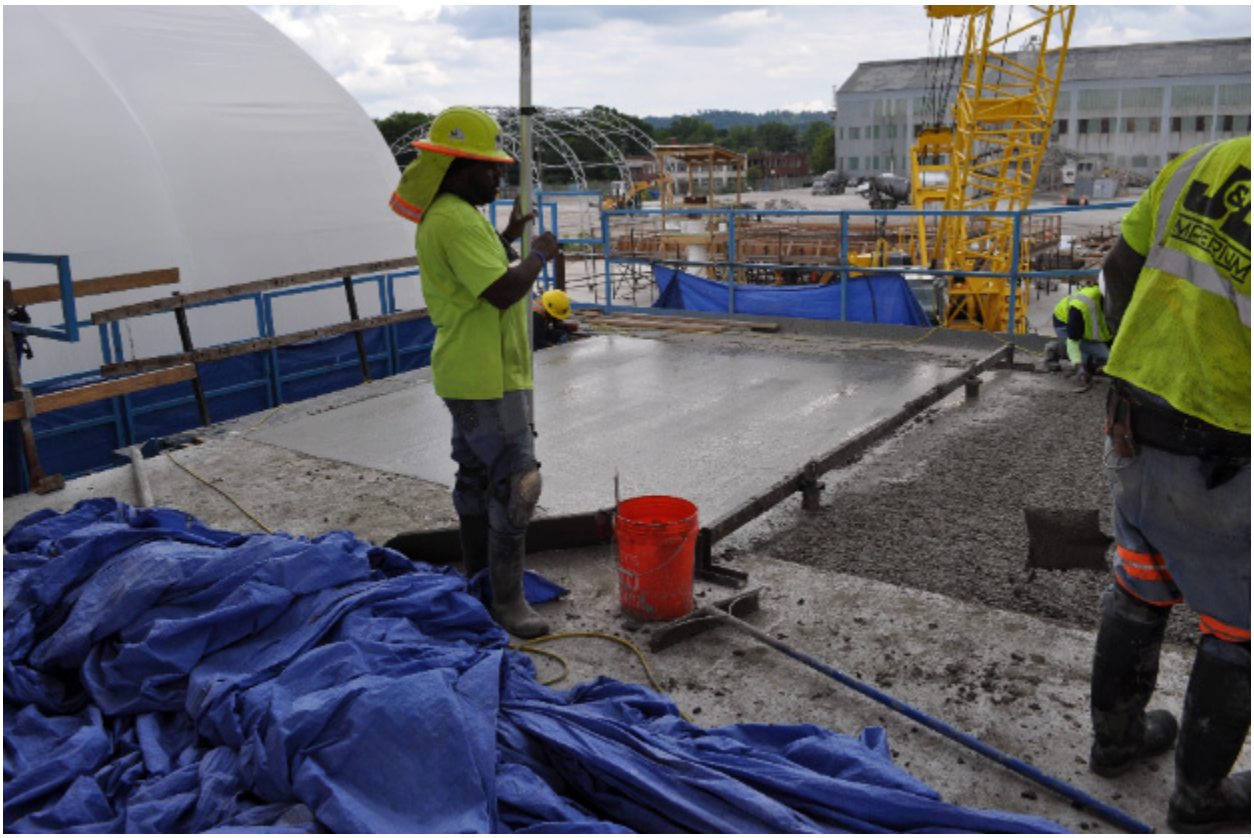

Figure 4-12: Float finishing of a concrete segment

After finishing of each segment was completed, each segment was then properly cured as stated by the quality control plan laid out by the contractor. All segments were appropriately sealed from moisture loss and were then subject to radiant heat for approximately 16 hours before the tarps were removed and then exposed to drying. A more in-depth discussion of this procedure was covered in Section 3.5.4.2. After the curing process was completed, quality control cylinders were then subjected to compression testing to determine the compressive strength. If the compressive strength of the cylinders met the minimum requirement of 2,500 psi, the forms of the segment could be stripped, and the segment moved and setup to be the match-cast segment to the next segment. If the compressive strength of the cylinders was less than 2,500 psi, the segment remained in the form until adequate strength was achieved. Also, before 100% stressing could be applied to the transverse post-tensioning, a minimum strength requirement of 4,000 psi was required. After a period of 28 days, quality assurance cylinders for each segment were subjected to compression testing again. If the compressive strength was 6,500 psi or more, the segments can be shipped and prepped for erection.

Once the preceding segment had been match-cast to its counterpart, one of two ship cranes as shown in Figure 4-13 were used to transport the segment to the storage yard. After being transported to its desired location in the storage yard, the segments remained stationary until it was time for each to be shipped to the location where each would be used in the erection of the segmental bridge.

Figure 4-13: Crane used to transport segments to the storage yard

CHAPTER 5: PRESENTATION AND ANALYSIS OF RESULTS

5.1 INTRODUCTION

This chapter covers all fresh and hardened properties of three concrete mixtures that were sampled from where concrete segments were fabricated. Also, the fresh and hardened properties of two CSC mixtures that were mixed at Auburn University and underwent the same testing as the field specimens will also be presented in this chapter. The fresh properties of both the field and laboratory specimens can be found in Section 5.2, while the mechanical and hardened properties can be found in Sections 5.3 and 5.5, respectively. It is important to note that ASTM C 512 (2018) calls for creep testing to be monitored for a load duration of one year; however, this research study covers all creep and shrinkage values up to October 8, 2018.

Also, a calculation comparing the results from epoxied DEMEC points on the steel bars to the drilled DEMEC points is located in Section 5.4. This section covers the results from testing and be used to determine which method is more efficient in accurately tracking the applied load over the duration of the project. Additionally, the environmental conditions for which testing was completed are covered in Section 5.6. General recommendations that were discovered during the duration of testing to improve the methods of ASTM C 512 (2018), such as how to efficiently load specimens or specimen preparation before testing commenced, are covered in Section 5.7.

5.2 FRESH PROPERTIES

In this section, all fresh properties of each concrete mixture used during the duration of testing are presented. All fresh properties for specimens that were sampled in the field can be found in Section 5.2.1, and all fresh properties for specimens that were cast using concrete that was mixed in the laboratory at Auburn University can be found in Section 5.2.2.

5.2.1 Field Specimens

Each set of the field test specimens were sampled from a ready-mixed concrete truck that was transporting the concrete to the segment that was being cast at that particular time. Due to each

set of field specimens being sampled from a different batch of concrete and the proportions of each batch changed, it was necessary to tabulate the mixture proportions of each concrete mixture for which samples were taken. Table 5-1 provides the tabulated saturated-surface dry (SSD) weights for each concrete mixture.

Table 5-1: Mixture proportions for each concrete mixture sampled from in the field

Items	ALDOT Approved Mixture Proportions	03/20/2018-F Mixture Proportions	04/10/2018-F Mixture Proportions	07/09/2018-F Mixture Proportions
Type I/II Cement, lb/yd^3	682	670	595	674
Class F Fly Ash, lb/yd^3	170	167	157	170
Fine Aggregate, lb/yd^3 (#100 Concrete Sand, SSD)	878	965	1021	976
Coarse Aggregate, lb/yd^3 (#67 Quartzite, SSD)	1800	1762	1835	1796
Water, lb/yd^3	264	267	265	270
MasterAir AE 200, oz/yd^3	2	3.4	5.25	8.4
MasterPolyheed 1025, oz/yd^3	68	51	50	50.6
MasterSet DELVO, oz/yd^3	34.1	---	15	10.2
MasterSet AC 534, oz/yd^3	102	153	136	118
Water-to-Cementitous Materials Ratio (w/cm)	0.31	0.32	0.35	0.32

Also, the results from the fresh property testing of all concrete mixtures that were sampled from in the field are presented in Table 5-2. These results were collected from the technicians representing ALDOT that were performing all mandatory fresh property tests for each concrete mixture that was used in the casting of the segments.

Table 5-2: Fresh concrete properties for all concrete mixtures from the field

	Mixture ID		
Fresh Concrete Properties	**03/20/2018-F**	**04/10/2018-F**	**07/09/2018-F**
Slump (in.)	7.5	5.5	6.25
Total Air Content (%)	5.6	4.4	4.2
Unit Weight (lb/ft^3)	144	144	141
Concrete Temperature (°F)	72	76	87

5.2.1.1 Slump

All concrete mixtures used in the casting of the segments had to meet the fresh property requirements that were set by ALDOT for the duration of this project. For this project, all concrete mixtures had to have a slump that fell within the range of 3 to 9 inches. All concrete mixtures that were sampled during the duration of testing fell within the requirements set by ALDOT.

5.2.1.2 Total Air Content

The total air content for all concrete mixtures for this project had to fall within the specified range of 3 to 6 percent as stated by ALDOT. All concrete mixtures that were sampled from that were used in creep and shrinkage testing for the duration of this project fell within the requirements ranging from 4.2 to 5.6 percent. If a mixture failed to meet this specification, it was rejected and discarded.

5.2.1.3 Unit Weight

ALDOT did not have a specification set for the unit weight for each concrete mixture. However, the unit weight of all concrete mixtures that were used in the casting of all segments were recorded to ensure that all mixtures were consisted with one another. The average value for the concrete mixtures that were sampled from for all testing purposes was 143 lb/ft^3. This value is close to a unit weight of 145 lb/ft^3, which is commonly assumed in most concrete design standards.

5.2.2 Laboratory Specimens

The results from the fresh property testing of all laboratory mixtures that were mixed in the Structures Laboratory at Auburn University are presented in Table 5-3. These results were collected through the testing of each concrete mixture using the applicable AASHTO specifications.

Table 5-3: Fresh concrete properties for each laboratory mixture

Fresh Concrete Properties	Mixture ID	
	05/03/2018-L-Q	05/09/2018-L-L
Slump (in.)	3.75	7.25
Total Air Content (%)	3.3	3.4
Unit Weight (lb/ft^3)	148	149
Concrete Temperature (°F)	74	74

5.2.2.1 Slump

Both concrete mixtures that were mixed at Auburn University were required to meet the same specifications as the concrete mixtures that were sampled from in the field. As stated earlier, the slump range specified by ALDOT was 3 to 9 inches. Both concrete mixtures met this requirement with a slump of 3.75 inches and 7.25 inches for the quartzite and limestone mixtures, respectively.

5.2.2.2 Total Air Content

The total air content for all laboratory mixtures for this project had to fall within the specified range of 3 to 6 percent as stated by ALDOT. All concrete mixtures that were mixed and tested at Auburn University for the duration of this project fell within the requirements with an air content of 3.3 and 3.4 percent for the quartzite and limestone mixtures, respectively.

5.2.2.3 Unit Weight

ALDOT did not have a specification set for the unit weight for each concrete mixture. The average value for the two concrete mixtures that were mixed in the laboratory was 148.5 lb/ft^3. Much like the unit weight value of the field specimens, this value is consistent with the unit weight of 145 lb/ft^3, which is commonly assumed in most concrete design standards.

5.3 MECHANICAL PROPERTIES

The results for compressive strength testing, modulus of elasticity testing, measured concrete temperatures, and all maturity calculations are covered in this section. All mechanical properties for specimens that were sampled in the field can be found in Section 5.3.1, and all mechanical

properties for specimens that were cast using concrete that was mixed in the laboratory can be found in Section 5.3.2.

5.3.1 Field Specimens

All results that were collected through the testing of compressive strength and modulus of elasticity for all field specimens can be found in Table 5-4 below. Each of these tests were performed in the materials laboratory at Auburn University immediately prior to loading of the creep specimens. In addition, Table 5-5 provides a comparison of the 28-day compressive strengths that were measured at Auburn University for creep testing to the 28-day compressive strengths that were measured by the testing laboratory representing ALDOT for quality assurance purposes.

In addition to the mechanical properties for the 04/10/2018-F and 07/09/2018-F specimens, the 7-day compressive strength and elastic modulus for the 03/20/2018-F specimens were also recorded, which can be seen in Table 5-6. Even though no creep testing was conducted on the 03/20/2018-F specimens, some of the shrinkage prediction models considered in this research study require the 28-day compressive strength and elastic modulus. However, the 28-day compressive strength nor the elastic modulus were recorded for the 03/20/2018-F specimens. The 28-day compressive strength for both the 04/10/2018-F and 07/09/2018-F specimens increased by 20 percent in relation to the 7-day compressive strength and the 28-day elastic modulus increased by approximately 3 percent. This assumption was used to predict the 28-day compressive strength and elastic modulus for the 03/20/2018-F specimens as listed in Table 5-6. These values were then used in the shrinkage prediction models that require this input.

Table 5-4: Mechanical properties for each set of field specimens that were used in creep testing

Mechanical Concrete Properties				
	Compressive Strength (psi)			
	Loading Age			
Mixture ID	**7 Days**	**28 Days**	**91 Days**	**182 Days**
04/10/2018-F	5,100	6,100	6,000	6,400
07/09/2018-F*	5,600	6,700	7,100	---
	Modulus of Elasticity (ksi)			
	Loading Age			
	7 Days	**28 Days**	**91 Days**	**182 Days**
04/10/2018-F	3,800	4,050	3,850	4,150
07/09/2018-F*	4,250	4,250	4,200	---

182-Day loading age has not commenced

Table 5-5: 28-day compressive strength comparison of laboratory testing versus testing in the field

	Testing performed by Auburn University	**Testing performed by Contractor for Quality Assurance**
Mixture ID	**Compressive Strength at 28 Days (psi)**	
04/10/2018-F	6,100	6,000
07/09/2018-F	6,700	6,300

Table 5-6: Mechanical Properties for 03/20/2018-F specimens

	Compressive Strength (psi)	
Mixture ID	**7-day Measured Strength**	**28-day Predicted Strength**
03/20/2018-F	4,200	5,000
	Modulus of Elasticity (ksi)	
	7-day Measured Elastic Modulus	**28-day Predicted Elastic Modulus**
03/20/2018-F	3,300	3,400

5.3.1.1 Compressive Strength and Modulus of Elasticity

As shown in Table 5-4, the compressive strength for the tested loading ages for the field specimens that were sampled on April 10, 2018 range in value from 5,100 psi to 6,400 psi. The

compressive strengths for the tested loading ages for the field specimens that were sampled on July 9, 2018 range in value from 5,600 psi to 7,100 psi. The modulus of elasticity was also determined in accordance with ASTM C 469 (2018) for each loading age for all field collected samples. For the field specimens that were collected on April 10, 2018, the modulus of elasticity ranged in value from 3,800 ksi to 4,150 ksi. The field specimens that were collected on July 9, 2018 had a modulus of elasticity that ranged from 4,200 ksi to 4,250 ksi.

It is seen in Table 5-4 that both the compressive strength and the elastic modulus for the 07/09/2018-F specimens tested higher for each loading age as compared to the 04/10/2018-F specimens. The compressive strength of the 07/09/2018-F specimens for the 7-day and 28-day loading ages tested approximately 10% higher as compared to the 7-day and 28-day loading ages for the 04/10/2018-F specimens, and the compressive strength tested 18% higher at the 91-day loading age for the 07/09/2018-F specimens. The elastic modulus for the 7-day loading age for the 07/09/2018-F specimens tested 10% higher than the elastic modulus for the 7-day loading age for the 04/10/2018-F specimens, but the elastic modulus at the 28-day loading age for the 07/09/2018-F specimens only tested 5 percent higher than the elastic modulus for the 28-day loading age of the 04/10/2018-F specimens.

5.3.1.2 ACI 209 Predicted Modulus of Elasticity for Field Specimens

By using the both the fresh and hardened properties that were determined prior to creep testing, the predicted modulus of elasticity values could be determined for each model. By using the predicted modulus of elasticity for each model, a more accurate representation of the predicted compliance as previously discussed in Section 2.5.1.2 is provided for each model. Each of the predicted modulus of elasticity values were compared to the measured modulus of elasticity values that were determined through testing as outlined in ASTM C 469 (2018). Equation 5.1 is a representation of the predicted modulus of elasticity that is used in ACI 209 (2008).

$$E_{cmto} = 33\gamma_c^{1.5}\sqrt{f_{cmto}} \qquad \text{Equation 5.1}$$

Where,

E_{cmto} = Modulus of elasticity at time of loading (psi),

γ_c = unit weight of concrete (lb/ft^3), and

f_{cmto} = mean concrete compressive strength at time of loading (psi).

By using Equation 5.1 along with the compressive strength that was determined for the indicated loading age as shown in Table 5-4, the predicted modulus of elasticity values shown in Table 5-7 were calculated. A positive percent error indicates that the predicted value is higher than the value that was measured through testing in the laboratory, and a negative value indicates that the predicted value is lower than the measured.

Table 5-7: Comparison of measured elastic moduli to the predicted elastic moduli using the ACI 209 model for all field specimens

Mixture ID	**04/10/2018-F**		
Loading Age (Days)	**Measured Modulus of Elasticity (ksi)**	**ACI 209 Predicted Modulus of Elasticity (ksi)**	**Error (%)**
7	3,800	4,070	7%
28	4,050	4,450	10%
91	3,850	4,420	15%
182	4,150	4,560	10%
Mixture ID	**07/09/2018-F**		
Loading Age (Days)	**Measured Modulus of Elasticity (ksi)**	**ACI 209 Predicted Modulus of Elasticity (ksi)**	**Error (%)**
7	4,250	4,130	-3%
28	4,250	4,520	6%
91	4,200	4,660	11%
182*	---	---	---

Data not available for indicated loading age

According to Table 5-7, the predicted modulus of elasticity values for each set of field specimens are overestimated for all loading ages with the exception of the 7-day loading age for the 07/09/2018-F test specimens. However, since all predictions are within $\pm$ 20% of the measured results, it can concluded that Equation 5.1 accurately predicts the measured modulus of elasticity.

5.3.1.3 AASHTO 2017 Predicted Modulus of Elasticity for Field Specimens

As previously stated, it was determined that using the predicted modulus of elasticity values of each model would provide a more accurate representation of the predicted compliance

values associated with the model being considered. Equation 5.2 was obtained from AASHTO LRFD Section 5.4.2.4 (2017).

$$E_c = 120{,}000 K_1 {w_c}^{1.5} {f'_c}^{0.33} \quad \text{Equation 5.2}$$

Where,

E_c = the modulus of elasticity (ksi),

K_1 = the aggregate factor (Taken as 1.0 unless proven by other testing),

w_c = the unit weight of the concrete (kips/ft^3), and

f'_c = the compressive strength at age of loading (ksi).

By using Equation 5.2 along with the compressive strength that was determined for the indicated loading age as shown in Table 5-4, the predicted modulus of elasticity values shown in Table 5-8 below were calculated. The percent error associated with the predicted and measured modulus of elasticity values are also presented. A positive percent error indicates that the predicted value is higher than the value that was measured through testing in the laboratory, and a negative value indicates that the predicted value is lower than the measured.

Table 5-8: Comparison of measured elastic moduli to the predicted elastic moduli using AASHTO LRFD 2017 standards for all field specimens

Mixture ID	**04/10/2018-F**		
Loading Age (Days)	**Measured Modulus of Elasticity (ksi)**	**AASHTO 5.4.2.4 Modulus of Elasticity (ksi)**	**Error (%)**
7	3,800	4,260	12%
28	4,050	4,520	12%
91	3,850	4,490	17%
182	4,150	4,590	11%
Mixture ID	**07/09/2018-F**		
Loading Age (Days)	**Measured Modulus of Elasticity (ksi)**	**AASHTO 5.4.2.4 Modulus of Elasticity (ksi)**	**Error (%)**
7	4,250	4,210	-1%
28	4,250	4,470	5%
91	4,200	4,560	9%
182*	---	---	---

Data not available for indicated loading age

For all specimens that were sampled on April 10, 2018, it can be concluded that AASHTO 5.4.2.4 generally tends to overestimate the modulus of elasticity values of those determined through testing. However, for the specimens that were sampled on July 9, 2018, it can be concluded that the predicted modulus of elasticity values are similar as to those that were determined through testing. However, since all predictions are within $\pm$ 20% of the measured results, it can concluded that Equation 5.1 accurately predicts the measured modulus of elasticity.

5.3.1.4 CEB 2010 Predicted Modulus of Elasticity for Field Specimens

When using the CEB 2010 method to predict the modulus of elasticity many factors must be considered when using this method such as curing method, the type of aggregate and cement being used, and the compressive strengths at time of loading. Also, remember that CEB MC 2010 is a European based code so careful conversions must be calculated when switching between U.S. Customary and SI units.

Before the modulus of elasticity can be predicted for any time *t,* the 28-day predicted modulus must be calculated using Equation 5.3.

$$E_{ci} = E_{c0}\alpha_E\left(\frac{f_{cm}}{10}\right)^{1/3} \qquad \text{Equation 5.3}$$

Where,

E_{ci} = Modulus of elasticity at 28-days (MPa),

E_{c0} = 21.5 x 10^3 MPa if aggregate type not found in Table 5-9,

f_{cm} = mean concrete compressive strength at 28-days (MPa), and

α_E = Aggregate correction factor found in Table 5-9.

Table 5-9: Effect of type of aggregates on modulus of elasticity (fib 2012)

Types of Aggregates	$\boldsymbol{\alpha_E}$	$\boldsymbol{E_{c0}\alpha_E}$ **(MPa)**
Basalt, dense limestone aggregates	1.2	25,800
Quartzite aggregates	1.0	21,500
Limestone aggregates	0.9	19,400
Sandstone aggregates	0.7	15,100

After the predicted modulus of elasticity at 28-days has been calculated, Equation 5.4 can be used to determine the elastic modulus at any time, *t*.

$$E(t)_{ci} = \beta_{cc}(t)^{0.5} E_{ci}$$ Equation 5.4

Where,

$E(t)_{ci}$ = Modulus of elasticity at an age t (MPa)

E_{ci} = Modulus of elasticity at 28-days (MPa)

$\beta_{cc}(t)$ = Time-development function

With,

$$\beta_{cc}(t) = \exp\{s\{1 - (28/t)^{0.5}]\}$$ Equation 5.5

Where,

t = the adjusted concrete age in Table 2-14 using the CEB MC 2010 values

s= coefficient depending on the strength class of cement from Table 5-10

Table 5-10: *s* values to be used based on different strength classes of cement and hardening characteristics

Strength Class of Cement	32.5 N (≤ 60 MPa)	32.5 R, 42.5 N (≤ 60 MPa)	42.5 R, 52.5 N, 52.5 R (> 60 MPa)
s	0.38	0.25	0.20

For the field specimens, the aggregate correction factor (α_E) was assumed to be 1.0 to account for the quartzite coarse aggregate that was used in the concrete mixtures. Also, the *s* value that was used to account for the strength class of cement was taken as 0.38.

By using the Equations 5.3 through 5.5, the predicted modulus of elasticity values were generated and are in Table 5-11. All of the elastic modulus values are presented in U.S Customary units for comparison purposes. The CEB MC 2010 overestimated the predicted modulus of elasticity values for all loading ages for both the 04/10/2018-F and 07/09/2018-F specimens. In comparison purposes, the CEB MC 2010 predicted elastic modulus values of the 07/09/2018-F specimens were slightly more accurate as compared to the predicted elastic modulus values of the 04/10/2018-F specimens. As seen in Table 5-11, the predicted modulus of elasticity values for each loading age of the 04/10/2018-F specimens had a larger percent error as

compared to the respected loading age for the 07/09/2018-F specimens. Also, the CEB MC 2010 method was one of the less accurate methods in predicting the modulus of elasticity. From Table 5-11, only the loading age of 7 days had a percent error lower than 20% for both each set of field specimens.

Table 5-11: Comparison of measured elastic moduli to the predicted elastic moduli using the CEB MC 2010 standards for all field specimens

Mixture ID	**04/10/2018-F**		
Loading Age (Days)	**Measured Modulus of Elasticity (ksi)**	**CEB MC 2010 Predicted Modulus of Elasticity (ksi)**	**Error (%)**
7	3,800	4,400	16%
28	4,050	5,000	24%
91	3,850	5,500	43%
182	4,150	5,700	37%
Mixture ID	**07/09/2018-F**		
Loading Age (Days)	**Measured Modulus of Elasticity (ksi)**	**CEB MC 2010 Predicted Modulus of Elasticity (ksi)**	**Error (%)**
7	4,250	4,500	6%
28	4,250	5,200	22%
91	4,200	5,700	36%
182*	---	---	---

Data not available for indicated loading age

5.3.1.5 GL 2000 Predicted Modulus of Elasticity for Field Specimens

In this section, the predicted modulus associated with the GL 2000 Model is presented. Much like the ACI 209 and AASHTO 2017 prediction models, one of the key parameters associated with the predicted elastic moduli is the compressive strength at the time of loading, f_{cmt}. Equation 5.6 represents the predicted modulus of elasticity when using the GL 2000 Model.

$$E_{cmt} = 500{,}000 + 52{,}000\sqrt{f_{cmt}} \qquad \text{Equation 5.6}$$

Where,

E_{cmt} = Modulus of elasticity at time of loading (psi), and

f_{cmt} = mean concrete compressive strength at time of loading (psi).

By using Equation 5.6 and the compressive strengths from Table 5-4 that were determined prior to creep testing, the predicted modulus of elasticity values as shown in Table 5-12 were generated. As done with the previous models, the predicted modulus values were then compared to the measured modulus values to monitor the accuracy.

Table 5-12: Comparison of measured elastic moduli to the predicted elastic moduli using the GL 2000 Model for all field specimens

Mixture ID	**04/10/2018-F**		
Loading Age (Days)	**Measured Modulus of Elasticity (ksi)**	**GL 2000 Predicted Modulus of Elasticity (ksi)**	**Error (%)**
7	3,800	4,210	11%
28	4,050	4,560	13%
91	3,850	4,530	18%
182	4,150	4,660	12%
Mixture ID	**07/09/2018-F**		
Loading Age (Days)	**Measured Modulus of Elasticity (ksi)**	**GL 2000 Predicted Modulus of Elasticity (ksi)**	**Error (%)**
7	4,250	4,390	3%
28	4,250	4,760	12%
91	4,200	4,880	16%
182*	---	---	---

Data not available for indicated loading age

The GL 2000 Model overestimated the predicted modulus of elasticity values for all loading ages for both sets of field specimens with the most accurate value being the 7-day loading age of the 07/09/2018-F test specimens, which had a percent error of 3.29%. However, all other loading ages had a percent error under 20 percent for both sets of field specimens concluding that the GL 2000 Model was accurate in the prediction of the modulus of elasticity.

5.3.1.6 B3 Model Predicted Modulus of Elasticity for Field Specimens

In a similar manner as the CEB MC 2010 method, in order for the elastic modulus to be predicted for any time *t,* the predicted modulus at 28 days first had to be calculated using Equation 5.7.

$$E_{cm28} = 57{,}000\sqrt{f_{cm28}} \qquad \text{Equation 5.7}$$

Where,

E_{cm28} = Predicted modulus of elasticity at 28 days (psi), and

f_{cmt} = Mean concrete compressive strength at 28 days (psi).

After predicting the modulus of elasticity at 28 days, Equation 5.8 can now be used to predict the modulus of elasticity at any time *t*.

$$E_{cmt} = E_{cm28}\left(\frac{t}{4 + 0.85t}\right)^{0.5} \qquad \text{Equation 5.8}$$

Where,

E_{cmt} = Predicted modulus of elasticity at time considered (psi)

t = Age of concrete (days)

By using Equation 5.8, the predicted modulus of elasticity values were generated as seen in Table 5-13 below. For both the 04/10/2018-F and 07/09/2018-F field specimens, the B3 Model slightly underestimated the predicted elastic modulus at the loading age of 7-days, and overestimated the modulus of elasticity for all other loading ages. However, the percent error between the measured and predicted values is either below or approximately equal to 20% for all loading ages for each set of field specimens indicating that the B3 Model accurately predicted the modulus of elasticity.

Table 5-13: Comparison of measured elastic moduli to the predicted elastic moduli using the B3 Model for all field specimens

Mixture ID	**04/10/2018-F**		
Loading Age (Days)	**Measured Modulus of Elasticity (ksi)**	**B3 Model Predicted Modulus of Elasticity (ksi)**	**Error (%)**
7	3,800	3,730	-2%
28	4,050	4,450	10%
91	3,850	4,710	22%
182	4,150	4,770	15%
Mixture ID	**07/09/2018-F**		
Loading Age (Days)	**Measured Modulus of Elasticity (ksi)**	**B3 Model Predicted Modulus of Elasticity (ksi)**	**Error (%)**
7	4,250	3,920	-8%
28	4,250	4,670	10%
91	4,200	4,940	18%
182*	---	---	---

Data not available for indicated loading age

5.3.1.7 Maturity Calculations

The creep behavior of concrete is greatly impacted by the maturity that it has reached at the time of loading. The maturity of the concrete itself is affected by the temperature at which the concrete is exposed to during the curing cycle, and thus greatly impacts the compressive strength. As mentioned in Section 3.5.4.2, the temperature cycle that each set of field specimens was subjected to during the curing procedure was recorded using a temperature sensor that was inserted into one of the concrete cylinders that was cast. These temperature cycles are illustrated in Figures 5-1 through 5-3. After plotting the temperature cycles for each set of field specimens, the equivalent age at loading could then be determined for use with creep models that use equivalent age.

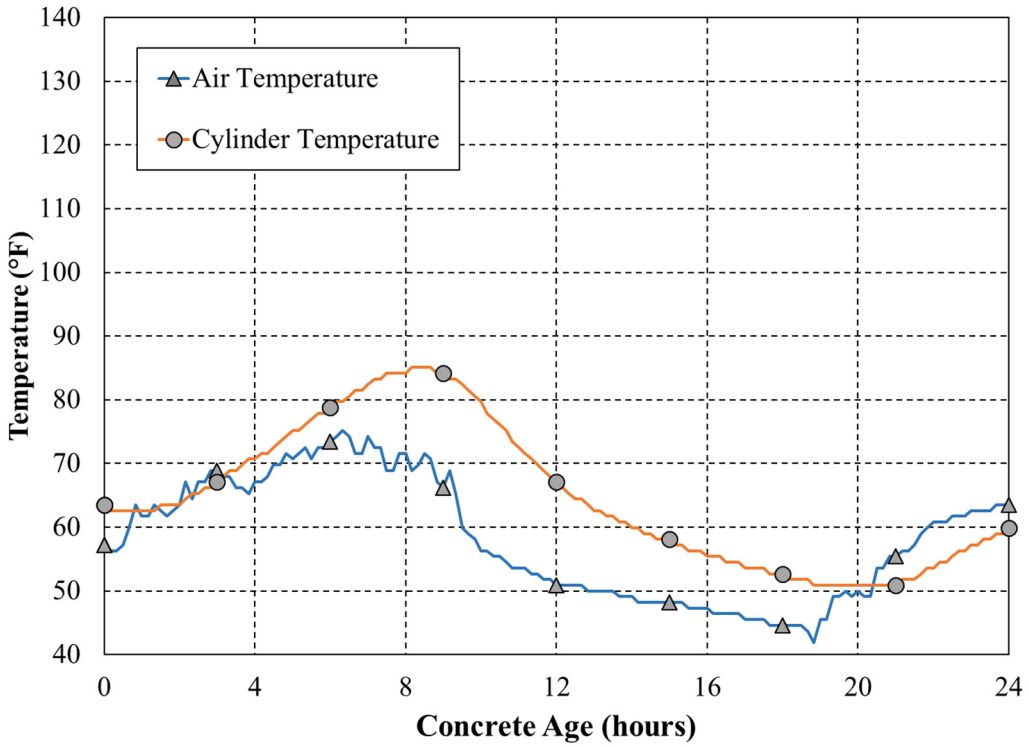

Figure 5-1: Temperature profile for field specimens collected on March 20, 2018

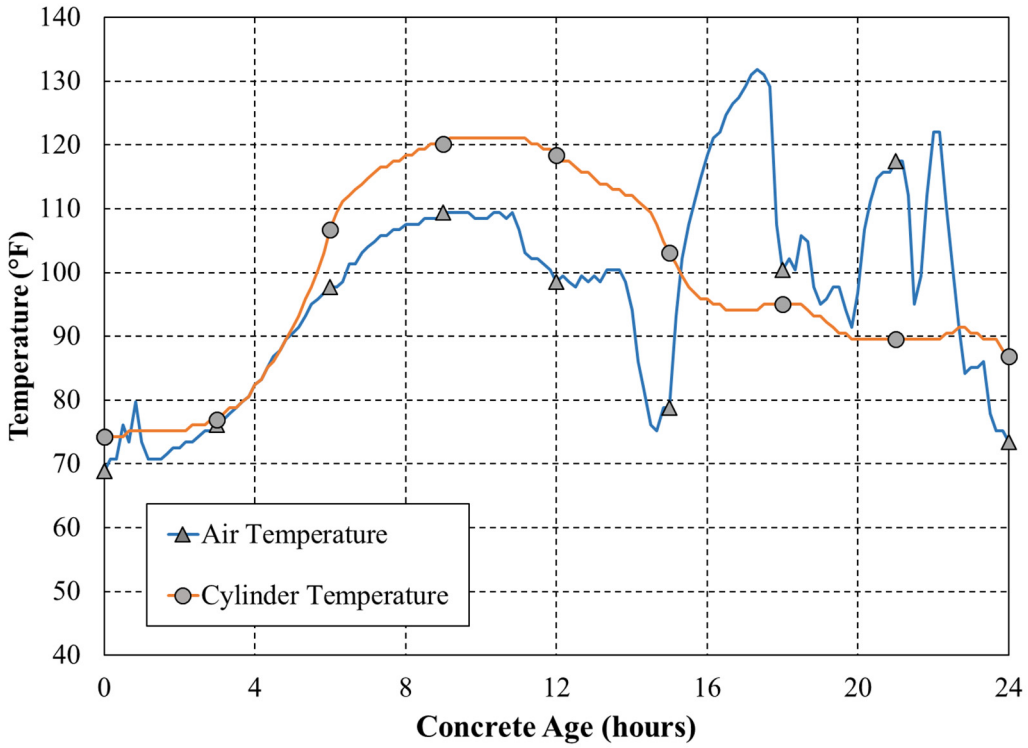

Figure 5-2: Temperature profile for field specimens collected on April 10, 2018

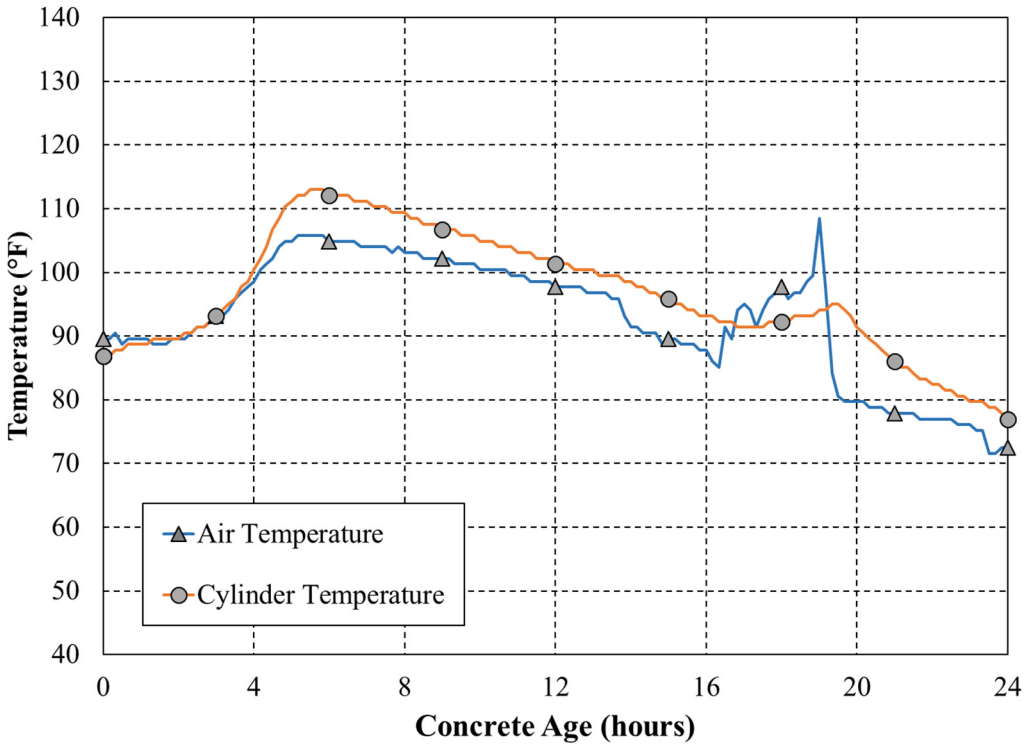

Figure 5-3: Temperature profile for field specimens collected on July 9, 2018

Recall that the GL 2000 Model, CEB MC 2010, and the B3 Model all require the equivalent-age maturity of the concrete to be taken into account in the prediction of creep strains. As mentioned in Section 2.4.3, CEB MC 2010 has a set maturity equation based on an activation energy of 33 kJ/mol that is to be used when determining the equivalent age at loading. Also, the B3 Model was developed with its own maturity method based on an activation energy of 42 kJ/mol as described in Section 2.4.5. However, the GL 2000 method does not have a set maturity equation for this calculation, but according to Gardner and Lockman (2001) the equivalent age maturity can be calculated with the Arrhenius method. The Arrhenius maturity function is shown in Equation 5.9 and was assumed to have an activation energy of 45 kJ/mol (ASTM C 1074 2018). This assumption was made based on the type and amount of both portland cement and supplementary cementitious materials that were used.

$$t_e = \sum_{0}^{t} \exp\left(-\frac{E}{8.3144} * \left[\frac{1}{273 + T_c} - \frac{1}{273 + T_r}\right]\right) \Delta t \qquad \text{Equation 5.9}$$

Where,

t_e = the equivalent age (hours),

E = the activation energy (J/mol),

T_c = the average concrete temperature during the time interval, Δt, (°C), and

T_r = the reference curing temperature (°C).

After determining the appropriate maturity functions to be used for each model, the equivalent age for each set of field specimens could then be calculated using the temperature profiles shown earlier in Figures 5-1 through 5-3. After the specimens were demolded and placed in the creep room, the average temperature of the creep room, which was 72.4°F, was used in determining the equivalent age at loading for all creep specimens. Also, the Arrhenius method requires a reference temperature when calculating the equivalent age of the concrete, which was taken as 73°F. Table 5-14 shows the equivalent age that was calculated for each loading age for all sets of field specimens. Note that the Arrhenius method used for the GL 2000 Model calculates the equivalent age in hours and must be converted into days when being used in the creep prediction models.

Table 5-14: Maturity calculations for each set of field specimens

Total Equivalent Age at Loading, t_0									
	Casting Date								
	3/20/2018			4/10/2018			7/9/2018		
	Maturity Method			Maturity Method			Maturity Method		
	CEB MC 2010	GL 2000 Model	B3 Model	CEB MC 2010	GL 2000 Model	B3 Model	CEB MC 2010	GL 2000 Model	B3 Model
Loading Age	t_0 (Days)	t_0 (Days)	t_0 (Days)	t_0 (Days)	t_0 (Days)	t_0 (Days)	t_0 (Days)	t_0 (Days)	t_0 (Days)
7 Days	7.7	6.7	8.0	9.0	8.5	9.9	8.9	8.2	9.6
28 Days	31.2	27.3	32.4	32.5	29.1	34.3	32.3	28.8	34.0
91 Days	101.6	88.9	105.7	102.9	90.7	107.6	102.7	90.4	107.2
182 Days	203.3	177.9	211.5	204.6	179.7	213.4	204.4	179.4	213.1

5.3.2 Laboratory Specimens

All results that were collected through the testing of compressive strength and modulus of elasticity for all laboratory specimens can be found in Table 5-15. Like the field specimens, each of these tests were performed in the concrete materials laboratory at Auburn University immediately prior to loading of the creep specimens.

Table 5-15: Mechanical properties for each laboratory mixture that was used in creep testing

Mechanical Concrete Properties			
	Compressive Strength (psi)		
	Loading Age		
Mixture ID	**7 Days**	**28 Days**	**91 Days**
05/03/2018-L-Q	7,200	8,500	8,800
05/09/2018-L-L	6,000	6,800	7,200
	Modulus of Elasticity (ksi)		
	Loading Age		
	7 Days	**28 Days**	**91 Days**
05/03/2018-L-Q	4,700	4,700	4,700
05/09/2018-L-L	5,300	5,350	5,200

5.3.2.1 Compressive Strength and Modulus of Elasticity

As shown in Table 5-3, the compressive strength for the concrete mixture containing the quartzite aggregate ranged from 7,200 psi to 8,800 psi while the compressive strength for the mixture containing the limestone aggregate ranged from 6,000 psi to 7,200 psi. The modulus of elasticity was also calculated for the laboratory specimens in the same manner that was used for the field specimens. The modulus of elasticity for the mixture containing the quartzite aggregate had a consistent reading of 4,700 ksi while the modulus of elasticity for the mixture containing the limestone aggregate ranged from 5,200 ksi to 5,350 ksi.

By analyzing the data, it is concluded that the laboratory mixture containing the limestone coarse aggregate showed a higher stiffness in comparison to the mixture that contained the quartzite coarse aggregate. In fact, the elastic modulus of the 05/09/2018-L-L specimens tested approximately 12 percent higher for each loading age as compared to the 05/03/2018-L-Q specimens. However, the compressive strength of the 05/03/2018-L-Q specimens tested approximately 20 percent higher for each loading age as compared to the compressive strength of the 05/09/2018-L-L specimens.

5.3.2.2 ACI 209 Predicted Modulus of Elasticity for Laboratory Specimens

As previously covered in Section 5.3.1.2, the ACI 209 model of predicting the elastic modulus was used to gain a more accurate representation of the predicted compliance values that are presented later in this thesis. These predicted modulus of elasticity values were compared to the

measured values from testing at Auburn University to monitor the accuracy of predicted values. The comparison of the two can be seen in Table 5-16.

Table 5-16: Comparison of measured elastic moduli to the predicted elastic moduli using the ACI 209 model for all laboratory specimens

Mixture ID	**05/03/2018-L-Q**		
Loading Age (Days)	**Measured Modulus of Elasticity (ksi)**	**ACI 209 Predicted Modulus of Elasticity (ksi)**	**Error (%)**
7	4,700	5,040	7%
28	4,700	5,480	17%
91	4,700	5,570	19%
Mixture ID	**05/09/2018-L-L**		
Loading Age (Days)	**Measured Modulus of Elasticity (ksi)**	**ACI 209 Predicted Modulus of Elasticity (ksi)**	**Error (%)**
7	5,300	4,650	-12%
28	5,350	4,950	-7%
91	5,200	5,090	-2%

As Table 5-16 shows, the ACI 209 predicted modulus of elasticity values for the mixture containing the quartzite coarse aggregate were overestimated, and also increased in percent error as the loading age increased as well. For the mixture containing the limestone coarse aggregate however, the ACI 209 predicted modulus of elasticity values were underestimated for all loading ages, but the percent error decreased as the loading age approached 91-days. However, the predicted values for all of the loading ages for both the quartzite and limestone mixtures are within $\pm$ 20% of the measured values indicating the ACI 209 model is accurate in the prediction of the modulus of elasticity.

5.3.2.3 AASHTO 2017 Predicted Modulus of Elasticity for Laboratory Specimens

The same process that was used in Section 5.3.1.3 to determine the predicted modulus of elasticity values for each loading age for all field specimens was also implemented for all loading ages for the laboratory specimens that were cast at Auburn University. Using Equation 5.2 as previously mentioned from AASHTO 5.4.2.4, the following values in Table 5-17 were generated.

Table 5-17: Comparison of measured elastic moduli to the predicted elastic moduli using AASHTO LRFD 2017 standards for all laboratory specimens

Mixture ID	**05/03/2018-L-Q**		
Loading Age (Days)	**Measured Modulus of Elasticity (ksi)**	**AASHTO 5.4.2.4 Modulus of Elasticity (ksi)**	**Error (%)**
7	4,700	5,040	7%
28	4,700	5,330	13%
91	4,700	5,390	15%
Mixture ID	**05/09/2018-L-L**		
Loading Age (Days)	**Measured Modulus of Elasticity (ksi)**	**AASHTO 5.4.2.4 Modulus of Elasticity (ksi)**	**Error (%)**
7	5,300	4,810	-9%
28	5,350	5,020	-6%
91	5,200	5,110	-2%

For the concrete mixture containing the quartzite coarse aggregate, the AASHTO LRFD (2017) predicted modulus of elasticity values were overestimated; however, were within 20 percent of the measured values. For the concrete mixture containing the limestone coarse aggregate, the AASHTO LRFD (2017) predicted modulus of elasticity values were underestimated, but were still within 20 percent of the measured values concluding that Equation 5.2 from Section 5.3.1.3 is accurate when predicting the modulus of elasticity.

5.3.2.4 CEB 2010 Predicted Modulus of Elasticity for Laboratory Specimens

This section covers the predicted modulus of elasticity values that were calculated using the CEB 2010 method as shown in Equations 5.3 through 5.5. As done with the predicted values from previous methods, the modulus of elasticity values predicted using CEB 2010 were compared to the ones that were measured using ASTM C 469 (2018) as shown in Table 5-18.

Recall that Equation 5.3 uses an aggregate correction factor (α_E), which was assumed to be 1.0 for the concrete mixture containing the quartzite aggregate and 0.9 for the mixture containing the limestone aggregate. Also, Equation 5.5 uses a *s* value to account for the strength class of cement was taken as 0.38 for both laboratory mixtures.

Table 5-18: Comparison of measured elastic moduli to the predicted elastic moduli using the CEB 2010 method for all laboratory specimens

Mixture ID	**05/03/2018-L-Q**		
Loading Age (Days)	**Measured Modulus of Elasticity (ksi)**	**CEB MC 2010 Predicted Modulus of Elasticity (ksi)**	**Error (%)**
7	4,700	4,900	4%
28	4,700	5,600	19%
91	4,700	5,900	26%
Mixture ID	**05/09/2018-L-L**		
Loading Age (Days)	**Measured Modulus of Elasticity (ksi)**	**CEB MC 2010 Predicted Modulus of Elasticity (ksi)**	**Error (%)**
7	5,300	4,100	-23%
28	5,350	4,700	-12%
91	5,200	5,200	0%

As Table 5-18 shows, the CEB 2010 predicted modulus of elasticity values for the mixture containing the quartzite coarse aggregate were overestimated, and also increased in percent error significantly as the loading age increased. In fact, the percent error grew as much as 21.2% from the 7-day to 91-day loading age. For the mixture containing the limestone coarse aggregate however, the CEB 2010 predicted modulus of elasticity values were underestimated for all loading ages, with the exception of the 91-day loading age where the measured and predicted modulus of elasticity were equally calculated.

Overall, the CEB MC 2010 method was accurate in the prediction of the modulus of elasticity values for both the quartzite and limestone mixtures; however, for the 7-day and 91-day loading ages for the 05/09/2018-L-L and 05/03/2018-L-Q specimens, respectively, the percent error was greater than 20 percent indicating that the CEB MC 2010 method was inaccurate in the modulus of elasticity predictions for these loading ages.

5.3.2.5 GL 2000 Predicted Modulus of Elasticity for Laboratory Specimens

The GL 2000 prediction method, as previously discussed in Section 5.3.1.5, was used to predict the modulus of elasticity. The comparison of the measured to the predicted elastic modulus values can be seen in Table 5-19.

Table 5-19: Comparison of measured elastic moduli to the predicted elastic moduli using the GL 2000 method for all laboratory specimens

Mixture ID	**05/03/2018-L-Q**		
Loading Age (Days)	**Measured Modulus of Elasticity (ksi)**	**GL 2000 Predicted Modulus of Elasticity (ksi)**	**Error (%)**
7	4,700	4,910	4%
28	4,700	5,290	13%
91	4,700	5,380	15%
Mixture ID	**05/09/2018-L-L**		
Loading Age (Days)	**Measured Modulus of Elasticity (ksi)**	**GL 2000 Predicted Modulus of Elasticity (ksi)**	**Error (%)**
7	5,300	4,530	-15%
28	5,350	4,790	-11%
91	5,200	4,910	-6%

In a similar nature to the other methods, the GL 2000 predicted modulus of elasticity values were overestimated for the mixture containing the quartzite coarse aggregate with an increase in percent error as the loading age increased from 7 days to 91 days. For the predicted values for the limestone mixture however, the GL 2000 underestimated the predicted values at a greater error in the early-ages of loading as compared to the predicted values at the loading age of 91 days. Overall, all of the predictions are within $\pm$ 20 percent of the measured results, which concludes that Equation 5.6 accurately predicts the measured modulus of elasticity for both the quartzite and limestone mixtures.

5.3.2.6 B3 Model Predicted Modulus of Elasticity for Laboratory Specimens

As mentioned earlier in Section 5.3.1.6, Equations 5.7 and 5.8 for the B3 Model were used to predict the modulus of elasticity values for both the quartzite and limestone mixtures as shown in Table 5-20.

Table 5-20: Comparison of measured elastic moduli to the predicted elastic moduli using the B3 Model for all laboratory specimens

Mixture ID	**05/03/2018-L-Q**		
Loading Age (Days)	**Measured Modulus of Elasticity (ksi)**	**B3 Model Predicted Modulus of Elasticity (ksi)**	**Error (%)**
7	4,700	4,410	-6%
28	4,700	5,260	12%
91	4,700	5,560	18%
Mixture ID	**05/09/2018-L-L**		
Loading Age (Days)	**Measured Modulus of Elasticity (ksi)**	**B3 Model Predicted Modulus of Elasticity (ksi)**	**Error (%)**
7	5,300	3,940	-26%
28	5,350	4,700	-12%
91	5,200	4,970	-4%

Unlike the other methods, the B3 Model underestimated the modulus of elasticity at the 7-day loading age of the mixture containing the quartzite coarse aggregate, but overestimated the values for both the 28- and 91-day loading ages. For the mixture containing the limestone coarse aggregate, the B3 Model significantly underestimated the modulus of elasticity values for the 7-day loading age but increased in accuracy as the loading increased to 91-days. Overall, the predicted modulus of elasticity values for both the quartzite and limestone mixtures were accurate and fell within $\pm$ 20 percent of the measured results with the exception of the 7-day loading age for the 05/09/2018-L-L specimens. This is an indication that Equations 5.7 and 5.8 accurately predict the measured modulus of elasticity for both the quartzite and limestone mixtures.

5.3.2.7 Maturity Calculations

As mentioned previously in Section 5.3.1.7, the maturity of concrete impacts strength, modulus of elasticity, and creep behavior. All specimens that were mixed and cast in the laboratory were also subjected to curing at elevated temperatures to accurately simulate the same conditions as the specimens that were cast in the field as previously stated in Section 3.5.4.2. Both the quartzite and the limestone mixtures were monitored using temperature sensors to accurately

determine the equivalent age at loading. The temperature profile for both the mixtures are shown in Figure 5-4.

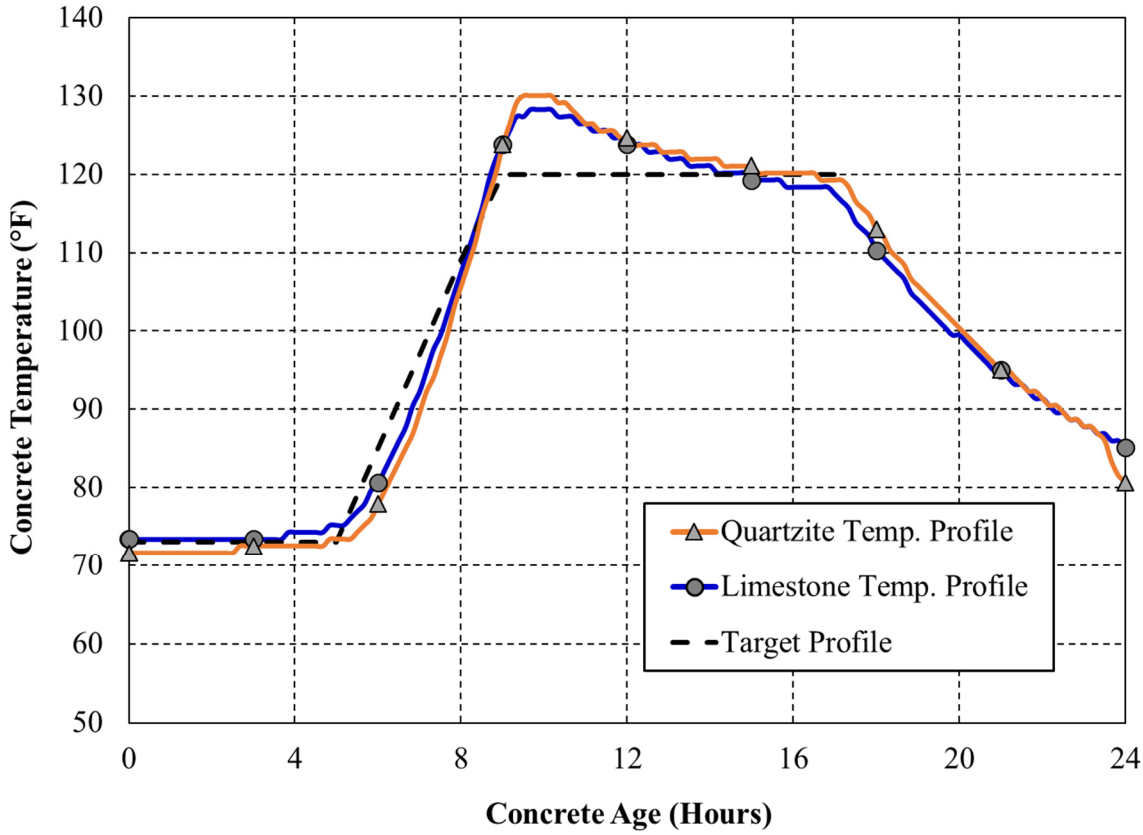

Figure 5-4: Temperature profile used by match-curing system for each laboratory mixture

Using the same maturity functions that were previously discussed in Section 5.3.1.2, the equivalent age at loading was determined for both the quartzite and limestone mixtures and is shown in Table 5-21.

Table 5-21: Maturity calculations for each set of laboratory specimens

Total Equivalent Age at Loading, t_0						
	Casting Date					
	05/09/2018-L-L			05/03/2018-L-Q		
	Maturity Method			Maturity Method		
	CEB MC 2010	GL 2000 Model	B3 Model	CEB MC 2010	GL 2000 Model	B3 Model
Loading Age	t_0 (Days)	t_0 (Days)	t_0 (Days)	t_0 (Days)	t_0 (Days)	t_0 (Days)
7 Days	9.3	9.0	10.3	9.3	9.0	10.3
28 Days	32.8	29.5	34.8	32.8	29.5	34.8
91 Days	103.2	91.1	108.0	103.2	91.1	108.0

5.4 LOADING DATA

In this section, the methods used to accurately track and maintain the applied loads to each frame are covered. An analysis comparing the loading accuracy of the epoxied DEMEC points to the drilled DEMEC points is also presented to aid in further testing as to which method is better.

5.4.1 Tracking and Maintaining Applied Load

ASTM C 512 (2018) requires the applied load on each set of test specimens be maintained within $\pm$ 2 percent of the target load during the duration of creep testing. If there is an increase or decrease in the applied load that does not meet this threshold, the load must be adjusted until all requirements are met.

Unlike many creep frames, the frames that were specifically designed for Auburn University used a series of flexible springs to apply the load to each set of test specimens. The use of these flexible springs allows a greater displacement to occur before any type load adjustment is required. In fact, many of the frames did not need any adjustment in load and if so, the readjustment occurred at the early stage of loading when the effect of creep is the greatest. A graph to effectively track the load was created for each frame, and an example is shown in Figure 5-5. This figure illustrates the tracked load for the test specimens that were mixed on April 10, 2018 and were loaded at 7 days.

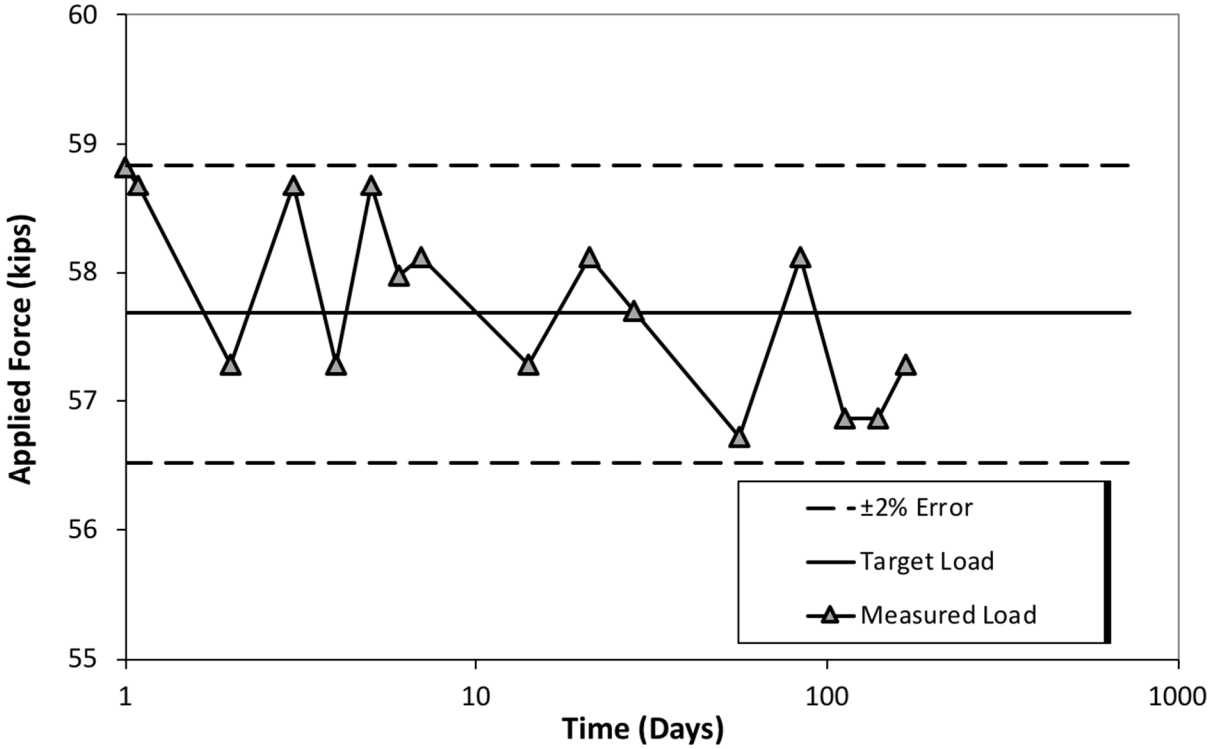

Figure 5-5: The applied load for the 04/10/2018-F specimen loaded at 7 days

Tables 5-22 and 5-23 below provide the maximum positive and negative percent errors in the applied load for each of the frames that were used during the duration of this project for both the field and laboratory test specimens, respectively. From these tables, it can be seen that each of the frames used during the duration of testing for both the field and laboratory test specimens stayed within the $\pm$ 2% target load range.

Even though the mechanical properties for the 182-day loading age of the 04/10/2018-F specimens was presented earlier in Table 5-4, the data collected for this loading age will not be considered in creep testing due to the collected amount of data being so limited. The same guidelines will also apply for the 91-day loading age of the 07/09/2018-F specimens.

Table 5-22: Maximum positive and negative percent errors in applied load for field specimens for each loading age

Mixture ID	Maximum Negative Error in Applied Load, (%)	Maximum Positive Error in Applied Load, (%)
04/10/2018-F (7 Day)	-1.66	1.98
04/10/2018-F (28 Day)	-1.98	1.87
04/10/2018-F (91 Day)	-1.85	1.24
07/09/2018-F (7 Day)	-1.19	1.68
07/09/2018-F (28 Day)	---	1.11

Table 5-23: Maximum positive and negative percent errors in applied load for laboratory specimens for each loading age

Mixture ID	Maximum Negative Error in Applied Load, (%)	Maximum Positive Error in Applied Load, (%)
05/03/2018-L-Q (7 Day)	-1.34	1.93
05/03/2018-L-Q (28 Day)	-1.57	1.78
05/03/2018-L-Q (91 Day)	-1.91	0.05
05/09/2018-L-L (7 Day)	-1.91	1.80
05/09/2018-L-L (28 Day)	-1.13	1.60
05/09/2018-L-L (91 Day)	-1.14	1.95

5.4.2 Epoxied DEMEC versus Drilled DEMEC points

In past creep testing, the strain in each of the three steel bars of each frame was measured using epoxied DEMEC points and then translated into a corresponding force. However, in addition to the epoxied DEMEC points, drilled DEMEC points were located on each steel bar as previously described in Section 3.5.6.3. The drilled DEMEC points were used in the same manner by measuring the strain of each of the three steel bars, and then translating that strain into a corresponding force.

However, the two methods produced different results in the applied load. In order to see which method was more accurate in determining the applied load, a statistical analysis was conducted using the predicted force readings of each method. By using the predicted force readings for each method, the compliance, as previously described in Section 2.5.1.2, was

calculated and compared to the measured readings that were obtained through testing. Tables 5-24 and 5-25 below show the compliance results when using either the epoxied DEMEC or drilled DEMEC points for the loading age of 7 days for the 04/10/2018-F and the 05/03/2018-L-Q test specimens, respectively. Both tables include the results for the duration of five months.

Table 5-24: Statistical comparison of epoxied DEMEC points vs. drilled DEMEC points for the 7-day 04/10/2018-F specimens

04/10/2018-F (7-Day Loading Age)					
Time Interval	**Measured Compliance (1×10^{-6}/psi)**	**Compliance for Epoxied DEMEC Points (1×10^{-6}/psi)**	**Compliance for Drilled DEMEC Points (1×10^{-6}/psi)**	**Epoxied DEMEC Points Error, (%)**	**Drilled DEMEC Points Error, (%)**
Post-Load	0.315	0.315	0.311	-0.02%	-1.52%
2-6 Hour	0.354	0.354	0.348	0.16%	-1.69%
Day 1	0.433	0.445	0.434	2.60%	0.16%
Day 2	0.471	0.472	0.448	0.16%	-4.87%
Day 3	0.491	0.504	0.485	2.60%	-1.19%
Day 4	0.512	0.512	0.489	0.16%	-4.40%
Day 5	0.528	0.535	0.498	1.36%	-5.63%
Day 6	0.544	0.551	0.510	1.19%	-6.23%
Day 7	0.557	0.571	0.530	2.60%	-4.87%
Week 2	0.636	0.644	0.605	1.19%	-4.87%
Week 3	0.684	0.697	0.661	1.89%	-3.30%
Week 4	0.724	0.750	0.707	3.69%	-2.34%
Month 2	0.811	0.821	0.792	1.19%	-2.34%
Month 3	0.856	0.885	0.852	3.32%	-0.52%
Month 4	0.868	0.897	0.869	3.32%	0.15%
Month 5	0.893	0.917	0.884	2.65%	-0.98%

Table 5-25: Statistical comparison of epoxied DEMEC points vs. drilled DEMEC points for the 7-day 05/03/2018-L-Q specimens

05/03/2018-L-Q (7-Day Loading Age)					
Time Interval	Measured Compliance (1×10^{-6}/psi)	Compliance for Epoxied DEMEC Points (1×10^{-6}/psi)	Compliance for Drilled DEMEC Points (1×10^{-6}/psi)	Epoxied DEMEC Points Error, (%)	Drilled DEMEC Points Error, (%)
Post-Load	0.248	0.248	0.251	-0.02%	0.97%
2-6 Hour	0.271	0.268	0.278	-1.10%	2.75%
Day 1	0.316	0.314	0.326	-0.74%	3.14%
Day 2	0.333	0.329	0.339	-1.22%	1.98%
Day 3	0.349	0.352	0.364	0.85%	4.19%
Day 4	0.357	0.358	0.372	0.11%	4.06%
Day 5	0.363	0.357	0.376	-1.58%	3.53%
Day 6	0.372	0.373	0.391	0.11%	5.13%
Day 7	0.381	0.387	0.396	1.48%	3.80%
Week 2	0.421	0.424	0.448	0.85%	6.50%
Week 3	0.445	0.452	0.473	1.73%	6.36%
Week 4	0.450	0.443	0.466	-1.46%	3.66%
Month 2	0.491	0.495	0.525	0.85%	6.92%
Month 3	0.508	0.509	0.541	0.23%	6.64%
Month 4	0.511	0.516	0.559	1.00%	9.39%
Month 5	0.526	0.526	0.573	0.05%	9.00%

ASTM C 512 (2018) requires that the results of two properly conducted tests by the same operator on the same material not differ by more than 6 percent. As Tables 5-24 and 5-25 show, the drilled DEMEC points for both the 04/10/2018-F and the 05/03/2018-L-Q test specimens have data that exceed this limit with a maximum value of -6.23 percent and 9.39 percent, respectively. From the results, it is concluded that the epoxied DEMEC points provided more accurate results in determining the applied load. Therefore, during the duration of this project, all results were determined using the applied load that was determined using the epoxied DEMEC points.

5.5 RESULTS FROM CREEP AND SHRINKAGE TESTING

The results from creep and shrinkage testing for both the field and laboratory specimens are presented in this section. Section 5.5.1 and 5.5.2 contain all creep results, compliance results, and results for both the drying shrinkage cylinders and rectangular prisms for each set of field and laboratory specimens, respectively. As stated earlier, ASTM C 512 (2018) requires that all creep testing be performed for at least one year, but this portion of this project only presents the 196-

day dying shrinkage strains for the 03/20/2018-F rectangular prism specimens, the 175-day creep and shrinkage strains for the 04/10/2018-F test specimens, and the 91-day creep and shrinkage strains for the 07/09/2018-F test specimens. For creep testing, only the 7-day, 28-day, and 91-day loading ages are presented for the 04/10/2018-F test specimens, and the 7-day and 28-day loading ages are presented for the 07/09/2018-F specimens. This is due to the collected creep data for the 182-day loading age of the 04/10/2018-F specimens and collected creep data for the 91-day loading age of the 07/09/2018-F specimens being so limited due to these loading ages being so recent. For both the quartzite and limestone laboratory mixtures, the 147-day creep and shrinkage strains are presented. The creep data for the 7-day, 28-day, and 91-day loading ages are presented for each laboratory mixture, with a discussion of how coarse aggregate type affects creep and shrinkage behavior.

5.5.1 Creep and Compliance Results for Field Specimens

5.5.1.1 Creep Strain Results

The strain results considering only creep are presented in this section for each set of field specimens that were tested. For each set of raw data, the drying shrinkage and the instantaneous elastic deformation are subtracted to result in only the strain due to creep. Table 5-26 contains the 168-day creep results for all field specimens that were collected on April 10, 2018, and also the 91-day creep results for all field specimens that were collected on July 9, 2018. The measured creep for each set of field specimens can be seen in Figures 5-6 and 5-7 below.

Table 5-26: Creep strains for specified loading ages for each set of field samples

	175-Day Creep Strain (1×10^{-6} in./in.)		
	Loading Age		
Mixture ID	**7 Day**	**28 Day**	**91 Day**
04/10/2018-F	-1256	-1181	-637
	91-Day Creep Strain (1×10^{-6} in./in.)		
	Loading Age		
Mixture ID	**7 Day**	**28 Day**	***91 Day**
07/09/2018-F	-867	-717	---

*Sufficient amount of data not available

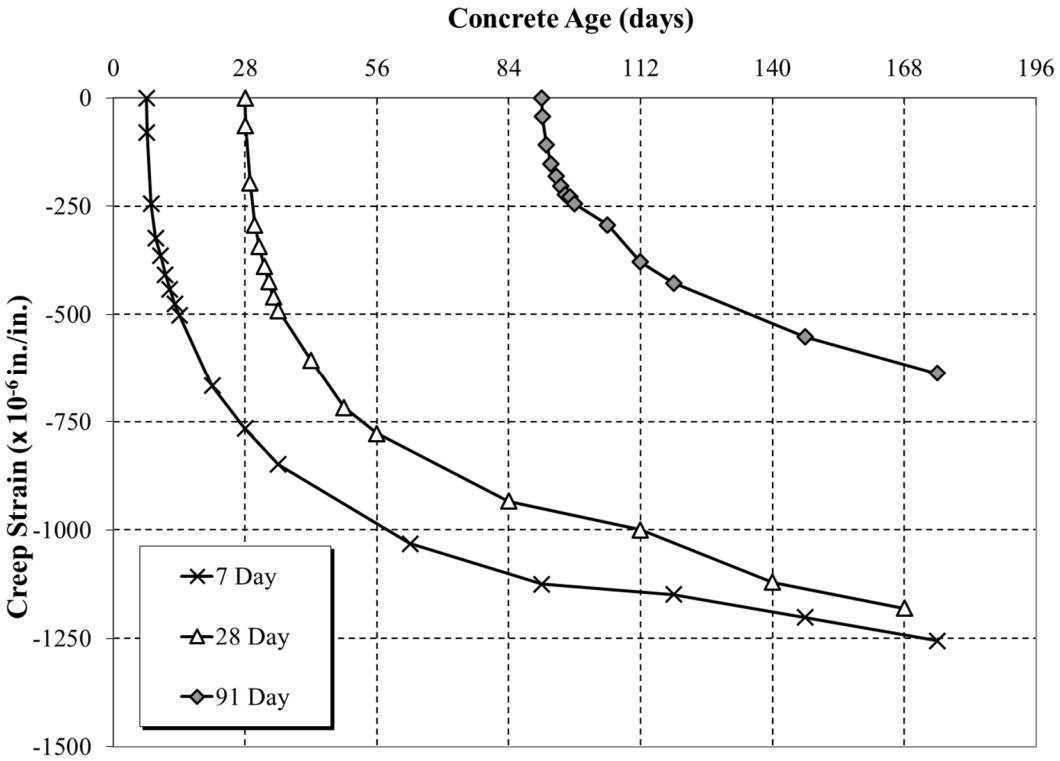

Figure 5-6: Creep strain development for the 04/10/2018-F field specimens

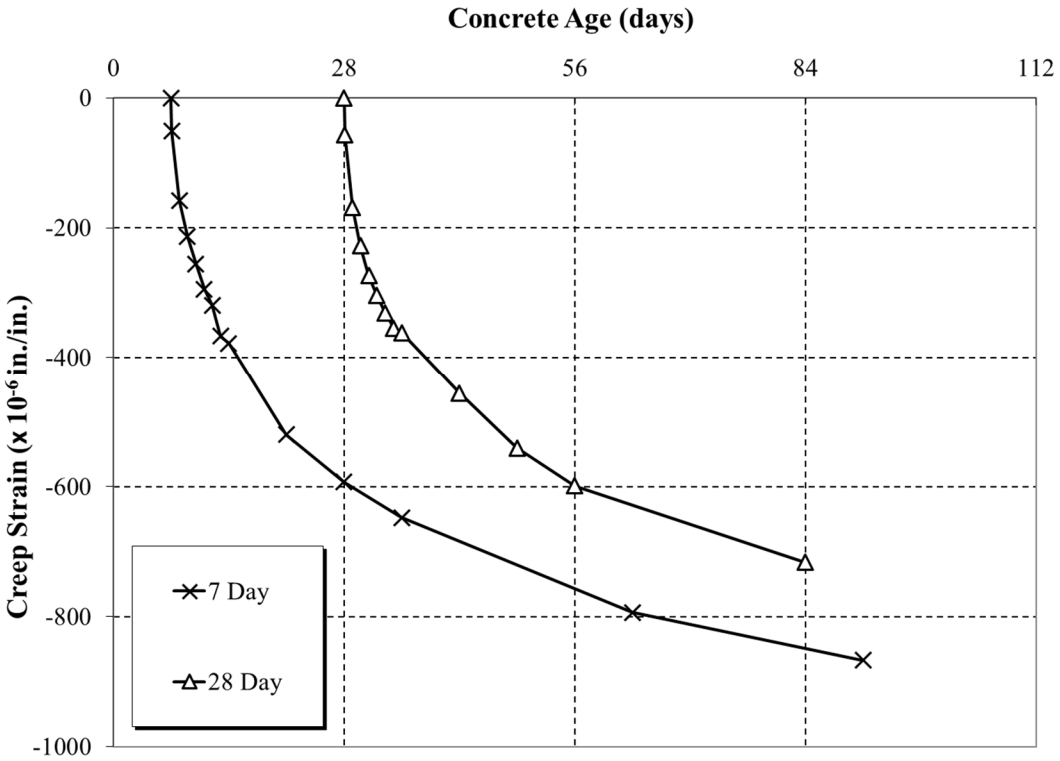

Figure 5-7: Creep strain development for the 07/09/2018-F field specimens

5.5.1.2 Compliance Results

As mentioned previously in Section 2.5.1.2, ACI Committee 209 (2008) defines compliance as follows:

$$J(t,t_0) = \frac{(Elastic\ Strain + basic\ creep + drying\ creep)}{stress} \quad \text{Equation 5.10}$$

Where,

$J(t,t_0)$ = the creep compliance at age t caused by a unit uniaxial sustained load applied at age t_0 (110^{-6}/psi)

t = age of concrete (days), and

t_0 = age of concrete at loading (days).

According to ACI Committee 209 (2008), compliance values allow for a more accurate comparison of creep results because they are normalized for applied load levels. Table 5-27 contains the 168-day compliance results for all field specimens that were collected on April 10, 2018, and also the 91-day compliance results for all field specimens that were collected on July 9, 2018. The measured compliance values for both sets of field specimens can be seen in Figures 5-8 and 5-9.

Table 5-27: Compliance results for field specimens during the duration of testing

	175-Day Compliance Results (1×10^{-6}/psi)		
	Loading Age		
Mixture ID	**7 Day**	**28 Day**	**91 Day**
04/10/2018-F	0.919	0.814	0.556
	91-Day Compliance Results (1×10^{-6}/psi)		
	Loading Age		
Mixture ID	**7 Day**	**28 Day**	***91 Day**
07/09/2018-F	0.664	0.535	---

*Sufficient amount of data not available

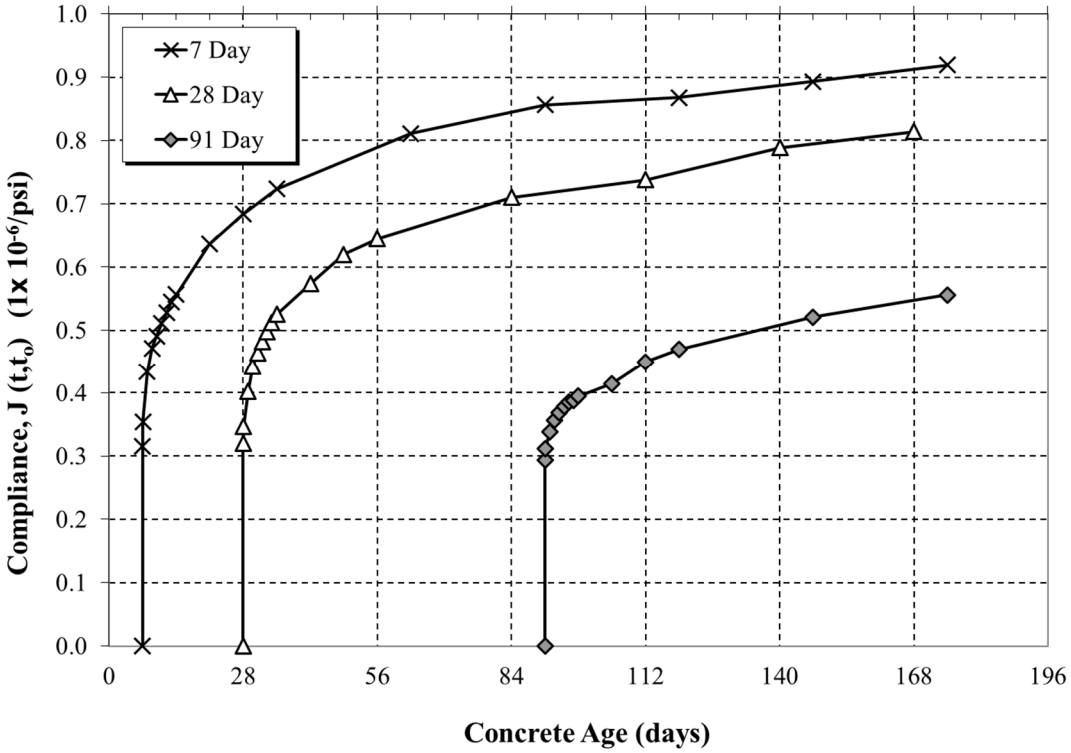

Figure 5-8: Compliance results for the 04/10/2018-F test specimens

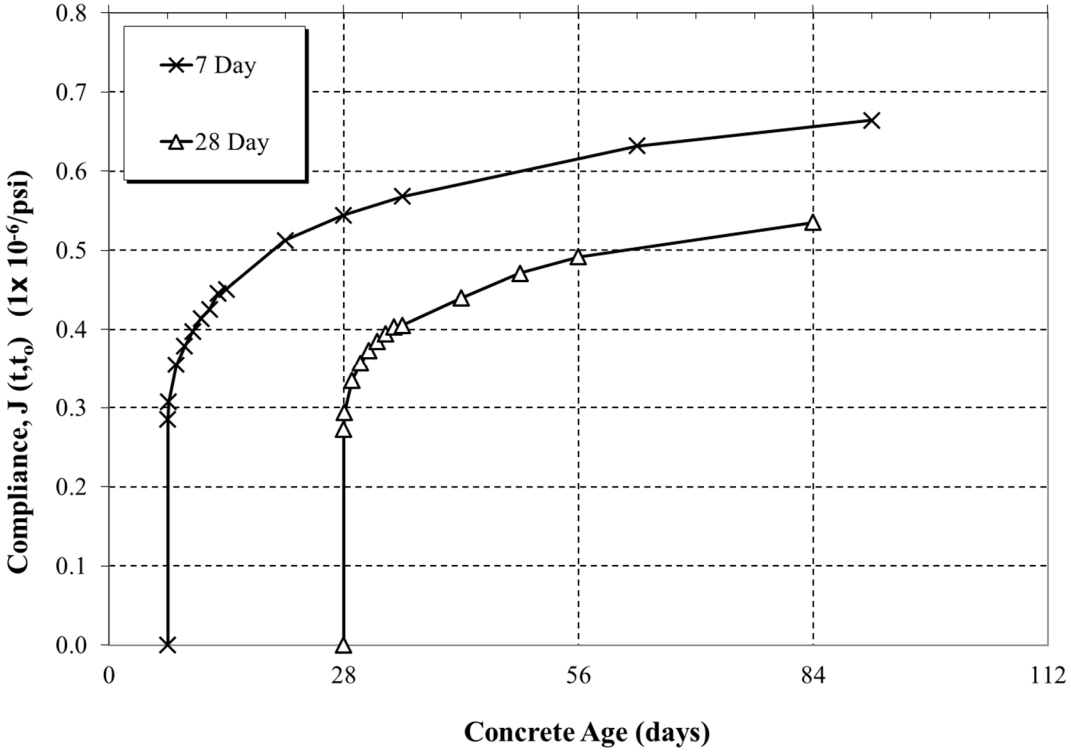

Figure 5-9: Compliance results for the 07/09/2018-F test specimens

5.5.1.3 Drying Shrinkage Results

The drying shrinkage results for both the concrete cylinders used in creep testing and the concrete rectangular prisms are presented in this section. Due to the field specimens being collected at various times throughout the year, the drying shrinkage results for both the cylinders and rectangular prisms will vary. The drying shrinkage results for the concrete cylinders used in creep testing are summarized in Table 5-28. Note, the specimens that were collected on April 10, 2018 were monitored for 175 days while the specimens that were collected on July 9, 2018 were monitored for 91 days. Note the drying shrinkage cylinders used in creep testing for each set of field specimens were the same for all loading ages; therefore, the drying shrinkage results started at the loading age of 7 days. The drying shrinkage values measured on cylindrical specimens for both sets of field specimens can be seen in Figure 5-10.

Table 5-28: Drying shrinkage results for 6 in. × 12 in. concrete cylinders of field specimens

Mixture ID	**175-Day Drying Shrinkage Results for Cylindrical Specimens (1×10^{-6} in./in.)**
04/10/2018-F	-529
Mixture ID	**91-Day Drying Shrinkage Results for Cylindrical Specimens (1×10^{-6} in./in.)**
07/09/2018-F	-425

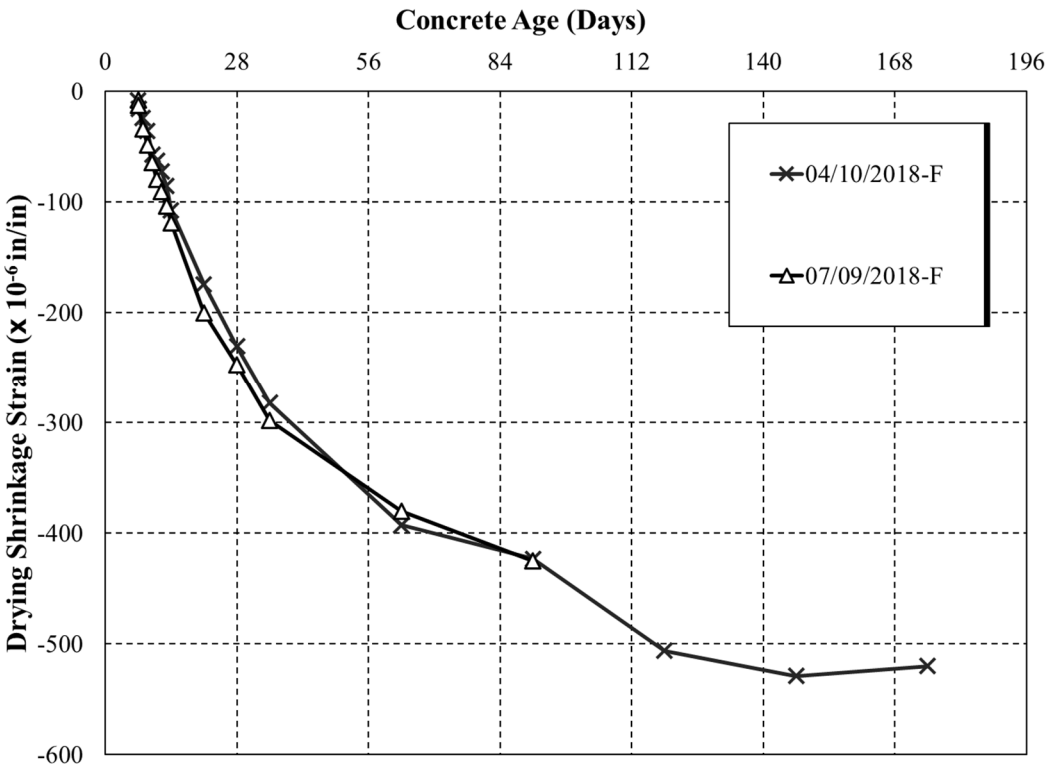

Figure 5-10: Development of drying shrinkage strains for 6" x 12" concrete cylinders of field specimens

As previously mentioned, the drying shrinkage results for the rectangular prisms will also vary due to the field specimens being collected at various times throughout the year. The 196 days, 175 days, and 91 days rectangular prism drying shrinkage results for the 03/20/2018-F, 04/10/2018-F, and 07/09/2018-F test specimens can be found in Table 5-29 below, respectively. Table 5-29 includes the results for both the air-cured and moist-cured specimens. Figures 5-11 and 5-12 show the measured values for the air-cure and moist-cure rectangular prisms that were collected in the field during this project. As previously described in Section 3.5.4, the air-cured rectangular prisms were cured for one day and were demolded and exposed to drying immediately upon arrival at Auburn University. The moist-cured rectangular prisms were cured in the same manner as the air-cured specimens; however, once the moist-cured specimens were demolded, they were placed in a lime bath for 7 days and then exposed to drying.

Table 5-29: Drying shrinkage strains for rectangular prisms of field specimens

Mixture ID	196-Day Drying Shrinkage Results for Rectangular Prisms (1×10^{-6} in./in.)
03/20/2018-F-Air	-992
03/20/2018-F-Moist	-1150
Mixture ID	**175-Day Drying Shrinkage Results for Rectangular Prisms (1×10^{-6} in./in.)**
04/10/2018-F-Air	-745
04/10/2018-F-Moist	-783
Mixture ID	**91-Day Drying Shrinkage Results for Rectangular Prisms (1×10^{-6} in./in.)**
07/09/2018-F-Air	-740
07/09/2018-F-Moist	-657

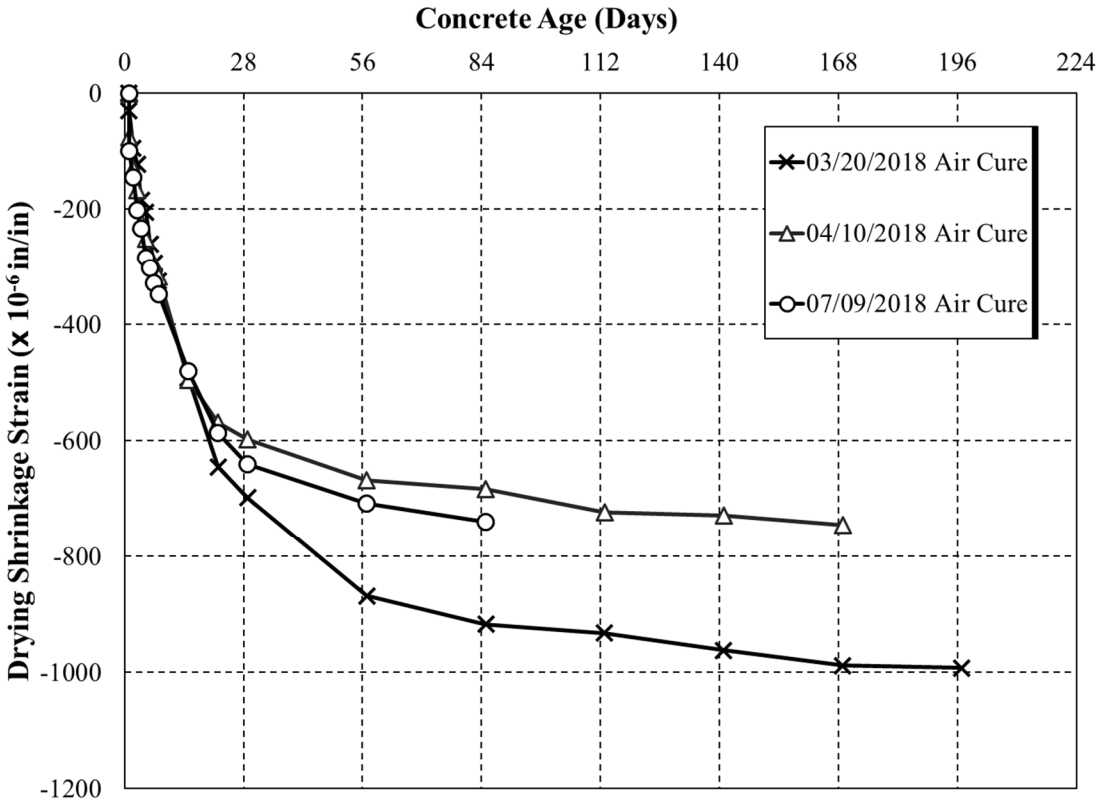

Figure 5-11: Drying shrinkage strains for air-cured rectangular prisms of field specimens

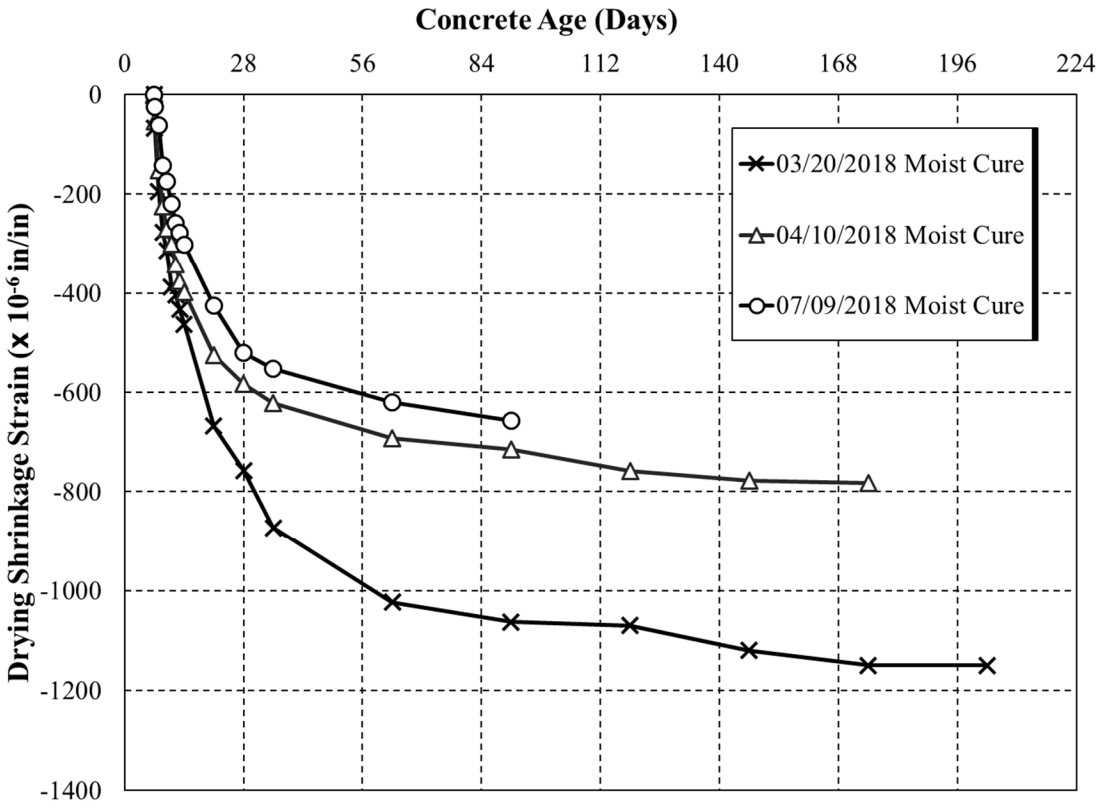

Figure 5-12: Drying shrinkage strains for moist-cured rectangular prisms of field specimens

5.5.2 Creep and Compliance Results for Laboratory Specimens

5.5.2.1 Creep Strain Results

The strain results considering only creep are presented in this section for each set of laboratory specimens that were tested. Similar to the creep strains for the field specimens, the drying shrinkage and the instantaneous elastic deformation are subtracted from each set of raw data to result in only the strain due to creep. Table 5-30 contains the 147-day creep results for both the quartzite and limestone concrete specimens that were cast in the laboratory. The measured creep strains for the 05/03/2018-L-Q and 05/09/2018-L-L test specimens can be seen in Figures 5-13 and 5-14.

Table 5-30: 147-day creep strain results for each set of laboratory specimens

Mixture ID	147-Day Creep Strain (1 x 10^{-6} in./in.)		
	Loading Age		
	7 Day	28 Day	91 Day
05/03/2018-L-Q	-801	-820	-517
05/09/2018-L-L	-853	-787	-479

As seen in Figures 5-13 and 5-14, the creep strains exhibited at each loading age for both the 05/03/2018-L-Q and 05/09/2018-L-L strains were similar. From Table 5-30, the 147-day creep strains for the 05/03/2018-L-Q specimens were slightly larger than the 147-day creep strains for the 05/09/2018-L-L specimens at the loading ages of 28 days and 91 days. However, the 147-day creep strains for the 05/09/2018-L-L specimens were slightly higher than the 147-day creep strains for the 05/03/2018-L-Q specimens for the loading age of 7 days. This is a clear indication that the substitution of the limestone coarse aggregate for the quartzite coarse aggregate did not have a significant impact on the overall measured creep strains.

While the substitution of coarse aggregate type did not have a major impact on the creep strains exhibited at each loading age between the 05/03/2018-L-Q and 05/09/2018-L-L specimens, Figure 5-13 shows that the laboratory mixture containing the quartzite coarse aggregate exhibited higher creep strains after 147 days for the 28-day loading age as compared to the 7-day loading age. The difference between the 147-day creep strains for the 28-day loading age as compared to the 7-day loading age for the 05/03/2018-L-Q specimens was roughly a 2% increase; whereas, the difference between the 147-day creep strains for the 28-day loading age as compared to the 7-day loading age for the 05/09/2018-L-L specimens was approximately a 8% decrease.

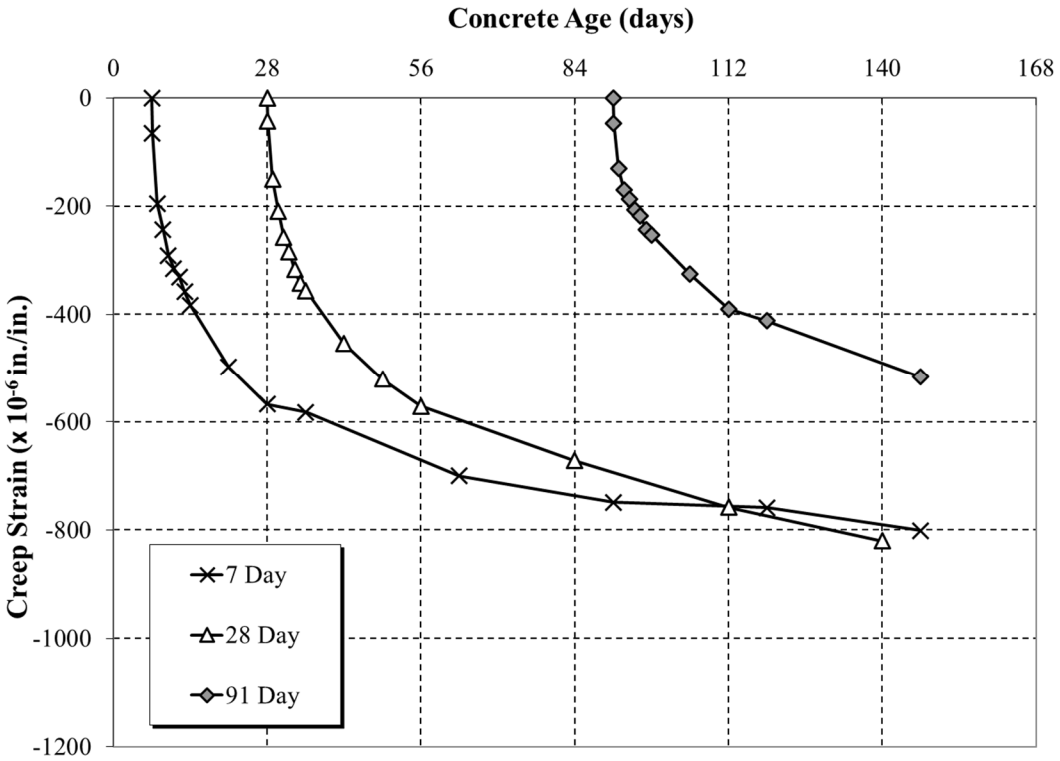

Figure 5-13: Creep strain development for all loading ages of the 05/03/2018-L-Q specimens

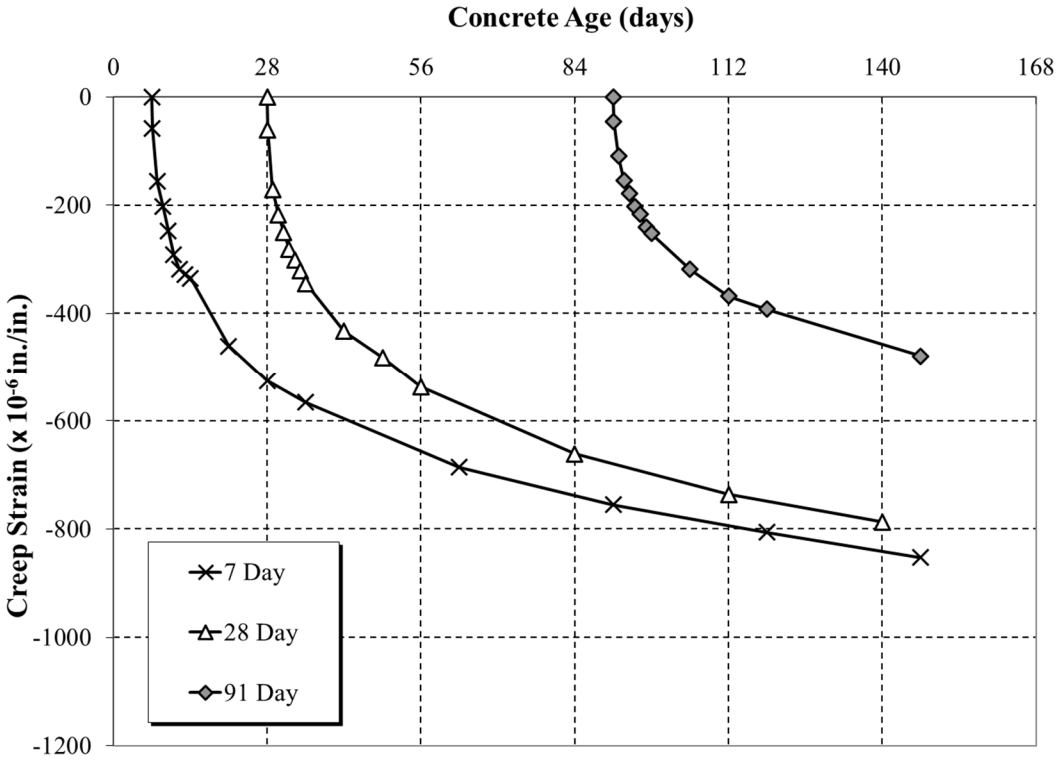

Figure 5-14: Creep strain development for all loading ages of the 05/09/2018-L-L specimens

5.5.2.2 Compliance Results

In the same manner as the field specimens, the compliance results for each set of laboratory specimens were recorded as well. Table 5-31 contains the 147-day compliance results for each loading age for both the quartzite and limestone concrete mixtures that were mixed in the laboratory. The measured compliance for the 05/03/2018-L-Q and 05/09/2018-L-L test specimens can be seen in Figures 5-15 to 5-16, respectively.

Table 5-31: 147-day compliance results for each set of laboratory specimens

	147-Day Compliance Results (1 x 10^{-6}/psi)		
	Loading Age		
Mixture ID	**7 Day**	**28 Day**	**91 Day**
05/03/2018-L-Q	0.526	0.503	0.401
05/09/2018-L-L	0.585	0.530	0.374

As seen in Figures 5-15 and 5-16, the measured compliance values for the 05/03/2018-L-Q and 05/09/2018-L-L test specimens were similar to one another for each loading age. From Table 5-31, the 05/09/2018-L-L specimens exhibited a slightly larger compliance at 147-days for the 7 day and 28 day loading ages as compared to the 147-day compliance values for the 7 day and 28 day loading ages for the 05/03/2018-L-Q specimens. However, the 147-day compliance values for the 91 day loading age for the 05/03/2018-L-Q specimens were slightly larger than the 147-day compliance values for the 91 day loading age for the 05/09/2018-L-L specimens. Similar to the creep strain results, the compliance results for the 05/03/2018-L-Q and 05/09/2018-L-L specimens indicated that the substitution of the coarse aggregate content did not have a significant impact.

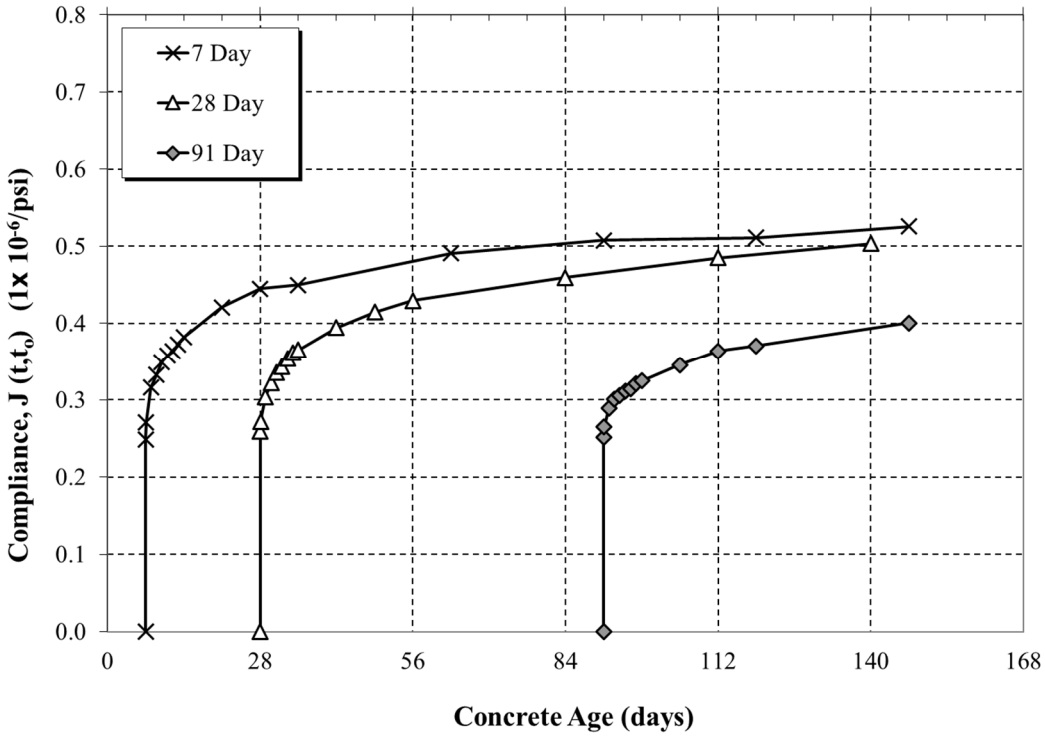

Figure 5-15: Compliance results for all loading ages of the 05/03/2018-L-Q test specimens

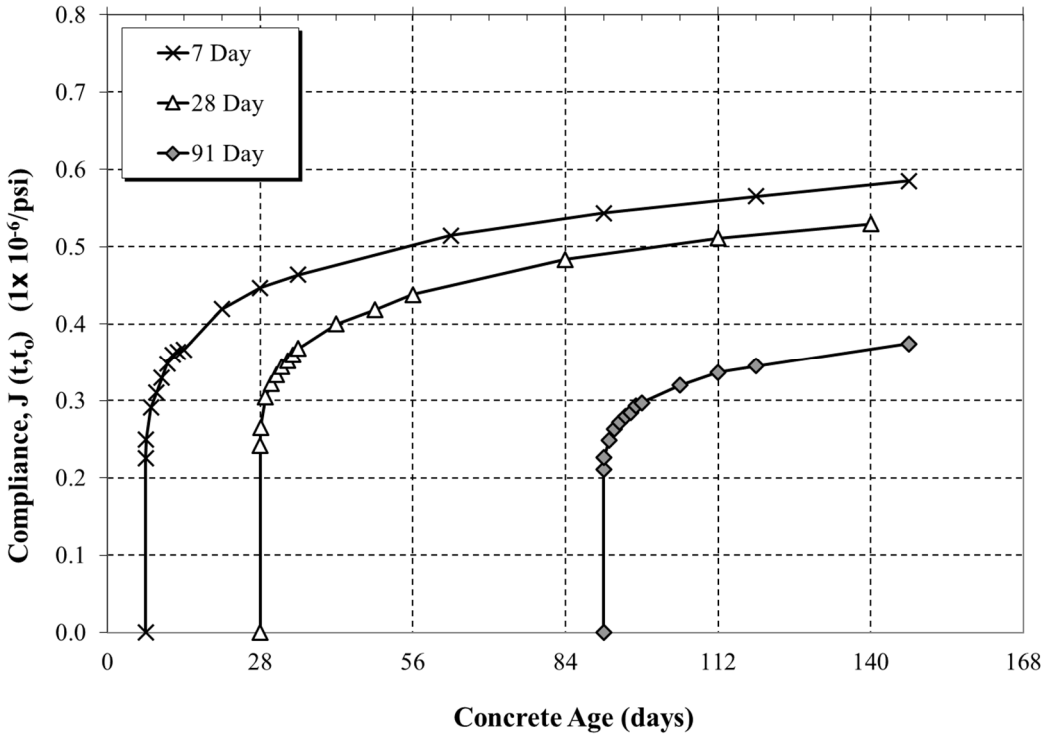

Figure 5-16: Compliance results for all loading ages of the 05/09/2018-L-L test specimens

5.5.2.3 Drying Shrinkage Results

The drying shrinkage results for both the concrete cylinders used in creep testing and the concrete rectangular prisms for each set of laboratory specimens are presented in this section. The 147-day drying shrinkage results for the concrete cylinders used in creep testing are summarized in Table 5-32. Similar to the drying shrinkage cylinders for the field specimens, the drying shrinkage cylinders for both sets of laboratory specimens were the same for all loading ages, and were monitored starting at the loading age of 7-days. The measured drying shrinkage values for both sets of specimens can be seen in Figure 5-17.

Table 5-32: Drying shrinkage results for 6 in. × 12 in. concrete cylinders of laboratory specimens

Mixture ID	147-Day Drying Shrinkage Results for Cylindrical Specimens (1 x 10^{-6} in./in.)
05/03/2018-L-Q	-478
05/09/2018-L-L	-387

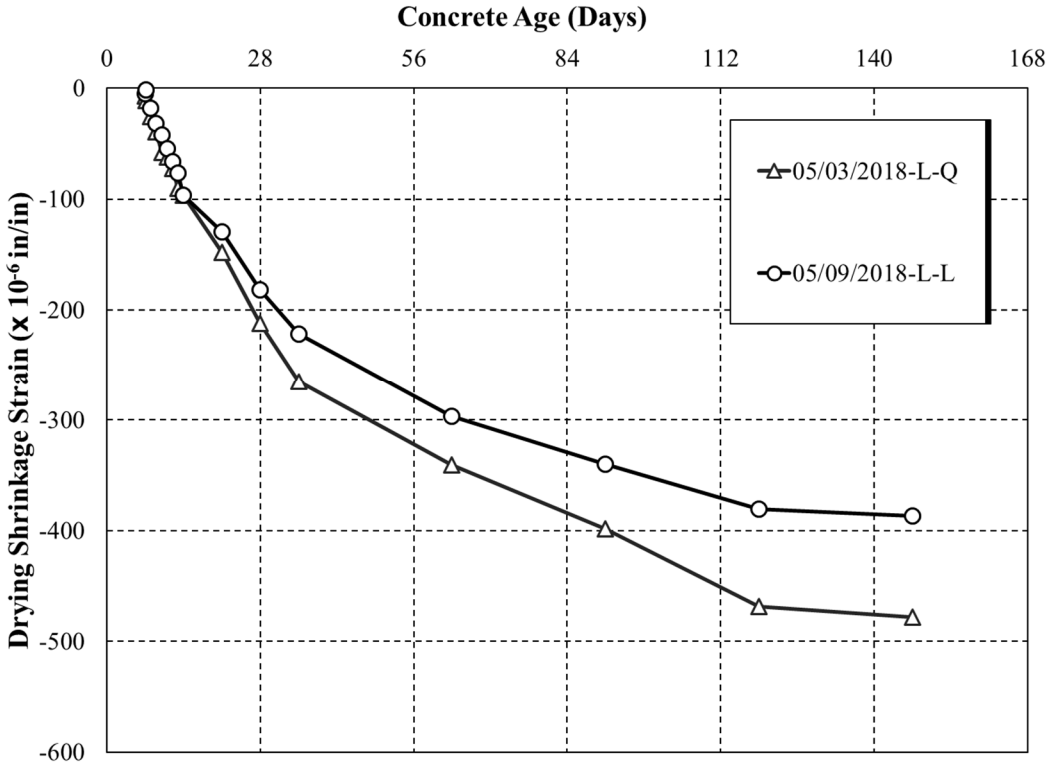

Figure 5-17: Development of drying shrinkage strains for 6 in. 12 in. concrete cylinders of laboratory specimens

As seen in Figure 5-17, the cylindrical shrinkage specimens containing the quartzite coarse aggregate exhibited higher shrinkage strains as compared to the cylindrical shrinkage specimens that contained the limestone coarse aggregate. In the early stages of drying, the cylindrical shrinkage strains for both the 05/03/2018-L-Q and 05/09/2018-L-L specimens were almost identical, but as time progressed, the 05/03/2018-L-Q specimens exhibited an increase in shrinkage of approximately 24 percent when compared to the 05/09/2018-L-L specimens.

In addition to the cylindrical shrinkage strains, the 147-day drying shrinkage results for the rectangular prisms for both the quartzite and limestone mixtures can be seen in Table 5-33. Both of sets of specimens were exposed to a lime bath for a duration of 7-days, and then placed in the creep-testing room for the duration of testing.

Table 5-33: 147-day drying shrinkage strains for rectangular prisms of laboratory specimens

Mixture ID	147-Day Drying Shrinkage Results for Rectangular Prisms (1×10^{-6} in./in.)
05/03/2018-L-Q	-642
05/09/2018-L-L	-612

Figure 5-18 shows the measured values for the moist-cure rectangular prisms that were cast in the laboratory and tested during the duration of this project. As shown in Figure 5-18, the shrinkage strains experienced by both the 05/03/2018-L-Q and 05/09/2018-L-L rectangular prism specimens were similar throughout the duration of testing. Overall, the substitution of limestone coarse aggregate for the quartzite coarse aggregate did not have major effects on shrinkage.

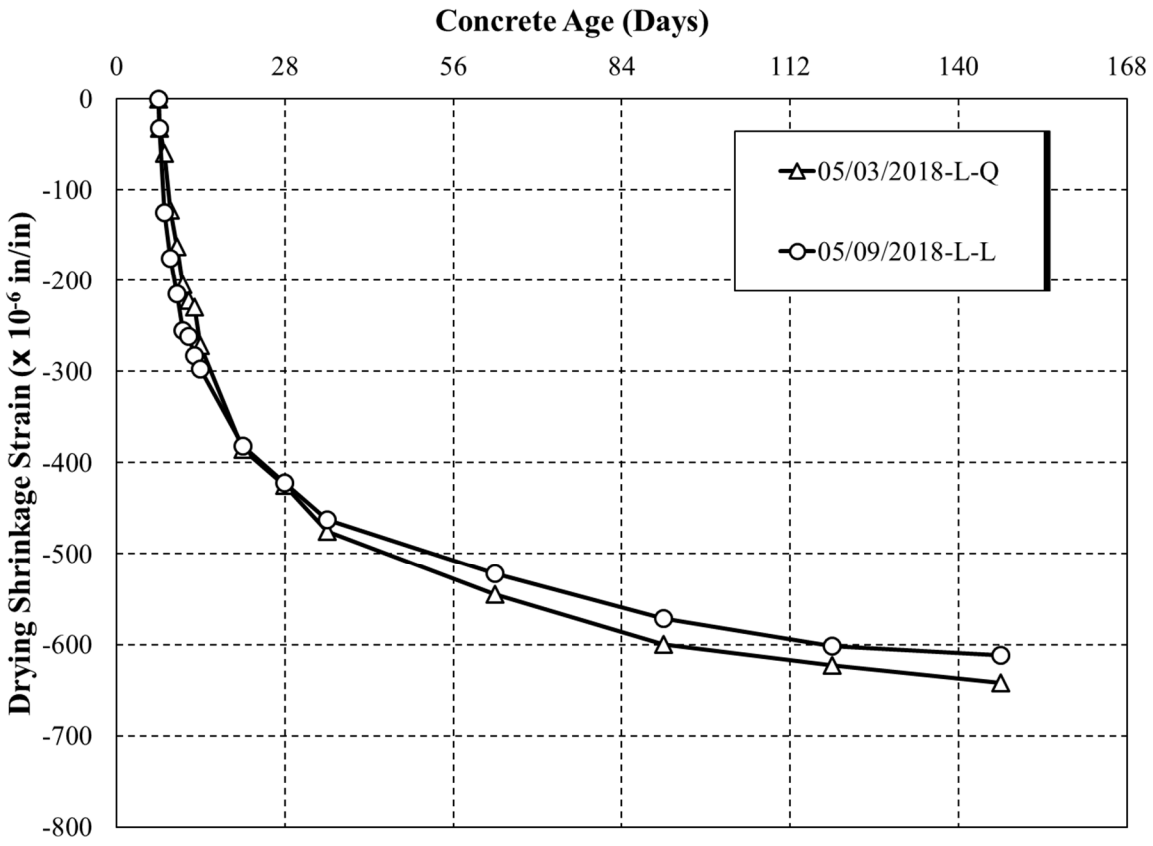

Figure 5-18: Drying shrinkage results for rectangular prisms of laboratory specimens

5.6 ENVIRONMENTAL CONDITIONS

All creep and drying shrinkage testing was completed in a climate-controlled room, which was detailed earlier in Section 3.5.6.2. The temperature and relative humidity conditions in which all specimens were exposed were recorded using a data logger. During the duration of testing, the average temperature was 72.4°F, while the maximum and minimum temperatures that occurred were 76.4°F and 69.9°F, respectively. Also, the average relative humidity of the room during the duration of testing was 49.3%, while the maximum and minimum relative humidity values measured were 59.4% and 41.2%, respectively. Figure 5-19 and Figure 5-20 provide a visual aid to show the distribution of temperature and relative humidity data during this project, respectively.

As seen in Figure 5-19, the temperature of the creep testing room, as required by ASTM C 512 (2018), was maintained extremely well during this project. There were a few data points outside of the required temperature range, but this could be attributed to the data collection

system being located next to the entry door of the creep room or also due to the data collection system and the thermostat of the HVAC system being calibrated differently. As shown in Figure 5-20, the relative humidity data distribution of the creep-testing room was more wide spread but for the most-part was within the requirements stated by ASTM C 512 (2008). The reason for some of the data being outside of the required range can be attributed to the either the dehumidifier or the humidifier of the creep-testing room being temporarily out-of-service and having to be repaired. The relative humidity was also highly sensitive when the creep-testing room was occupied during the loading of a frame or when data collection was taking place. Another reason for the relative humidity to appear to be outside the required range can be due to the humidistat and the data collection system being calibrated differently. It was not uncommon for the humidistat to show the relative humidity to be 47 percent, but the data collection system would show the relative humidity to be approximately 44 percent.

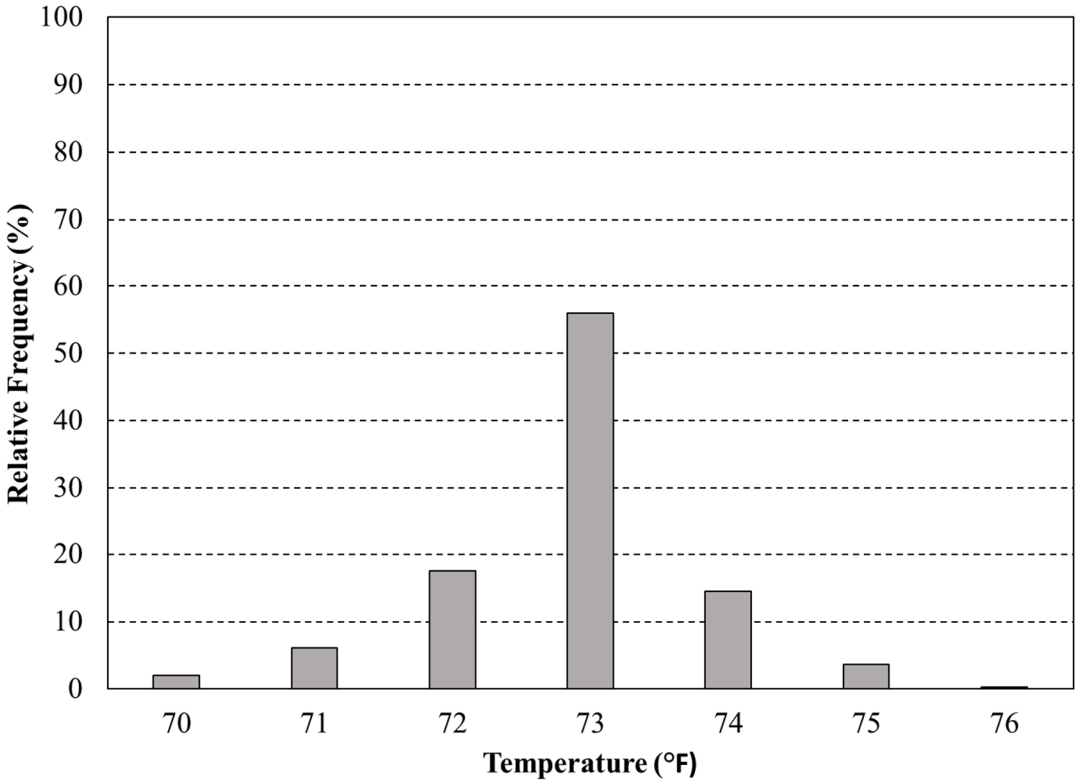

Figure 5-19: Creep-testing room temperature distribution

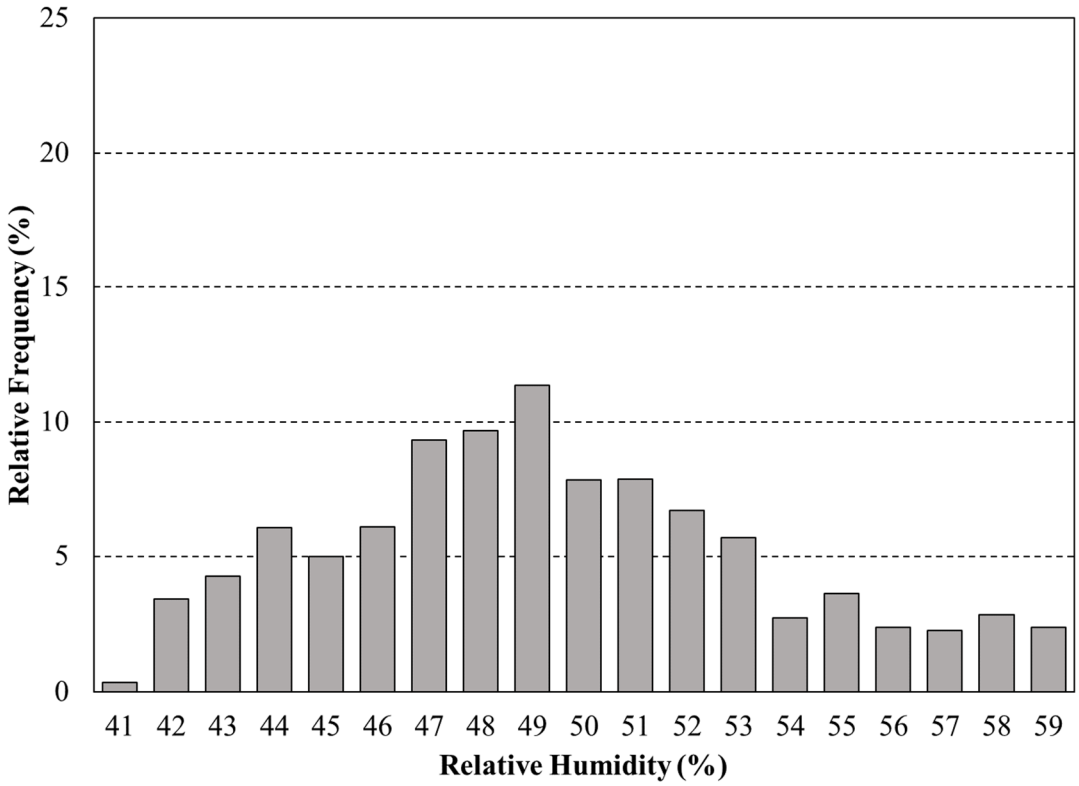

Figure 5-20: Creep-testing room relative humidity distribution

5.7 LESSONS LEARNED THROUGH TESTING

This section details information regarding all experience that was gained throughout the duration of this project in the area of specimen preparation, creep testing, and drying shrinkage testing.

5.7.1 Specimen Preparation

During the specimen preparation phase of this project, many lessons were learned during the mixing, casting, and final preparation for both the field and laboratory specimens. This section covers in detail the experience gained and all information to help eliminate any mistakes that could be made during future research.

5.7.1.1 Casting of Field Specimens

During the casting phase of each set of field specimens, initial setup was crucial. In the beginning of the project, all specimens were prepared on a flat, level surface next to the segment in which the contractor was casting on that date. This did not cause any major concerns except transporting the specimens to the formwork to be cured took an extended amount time. At later

stages of the project, the field specimens were cast on the concrete pad to which the segmental formwork was attached too. This significantly decreased the amount of time to transport the field specimens to the formwork for curing.

5.7.1.2 Mixing and Casting of Laboratory Specimens

During the mixing and casting phase of all laboratory specimens, no significant issues occurred that resulted in any adjustments having to be made. During the mixing process, only a single batch of concrete had to be mixed for both the quartzite and limestone mixtures. This prevented any non-uniformities that could arise if multiple batches had to be mixed.

5.7.1.3 Final Specimen Preparation

After curing was completed, both the field and laboratory specimens to be used in creep testing were prepared for end-grinding. In past studies, a sulfur-based compound was used to cap each of the cylinders to ensure that a level contact surface was used to prevent any stress concentrations, but for this project, it was decided that end-grinding the cylinders until each of their surfaces were level would be most beneficial. Once end-grinding was complete, it was best to immediately attach the Demountable Mechanical (DEMEC) points. This proved to be the most efficient use of time due to all cylinders being stored in the creep room until their respective loading age.

5.7.2 Conducting Creep and Shrinkage Testing

This section covers in detail all lessons learned through creep and shrinkage testing, and provides information to help produce repeatable results when conducting test as outlined in ASTM C 512 (2018) or AASHTO T 160 (2015).

5.7.2.1 Creep Testing

ASTM C 512 (2018) is a test that is not commonly performed. For this reason, there is a certain level of uncertainty involved, but after performing the process several times, many lessons were learned that allowed for more accurate testing.

In the beginning phases of testing for each frame, many data points are collected and must be properly processed to ensure accurate results. It is recommended that the individual performing the research make a schedule of all data points that need to be collected and on which

date. Also, a data collection template proved to be very beneficial in collecting all data, and properly keeping all records during testing.

The second lesson learned pertains to properly aligning all test specimens in the creep frame before applying any load. This is crucial because if any load eccentricities arise in the test specimens, errors can occur in the strain readings. To ensure that all specimens were properly aligned before being placed into the frame, a level was placed on each end of the cylinders and plugs to ensure that all surfaces did not have any non-uniformities. Once all specimens and plugs were level, they were then placed into the creep frame and rotated until the epoxied DEMEC points were in the desired position so that readings could be taken without interference from the steel bars of each frame.

After the specimens were placed into the frame, the vertical alignment was also monitored to ensure that no load eccentricities could result due to the test specimens being out of plumb. This was accomplished by using the alignment marks on the bottom of the upper reaction plate as previously described in Section 3.5.6.1. Once all specimens were properly aligned, 10 percent of the required load was applied to the specimens, and then strain readings were taken to ensure that no load eccentricities were present. If any load eccentricities were noticed, the 10 percent load was removed and the test specimens were realigned to remove these eccentricities.

5.7.2.2 Drying Shrinkage Testing

During the duration of this project, no significant lessons were learned to help increase the accuracy of the shrinkage results. All procedures and requirements outlined in AASHTO T 160 (2015) were followed.

5.8 SUMMARY OF RESULTS

5.8.1 Fresh Properties

From this research, the following conclusion can be drawn related to fresh properties of both the field and laboratory concrete mixtures that underwent testing:

- Both the slump and air content for the field and laboratory mixtures fell within the specified range that was required by ALDOT during the duration of this project.

- The unit weight and temperature of both the field and laboratory mixtures were highly similar, and were all within reasonable limits of typical conventional slump concrete mixtures.

5.8.2 Hardened Properties

5.8.2.1 Field Specimens

From this research, the following conclusions can be drawn related to the hardened properties for each set of field specimens:

- The samples collected on July 9, 2018 exhibited a higher compressive strength at each loading age as compared to the samples collected on April 10, 2018.
- The samples collected on July 9, 2018 exhibited a higher modulus of elasticity at each loading age as compared to the samples collected on April 10, 2018.
- In general, each model was accurate in the prediction of the modulus of elasticity values for all loading ages for both the 04/10/2018-F and 07/09/2018-F specimens, with the exception of the CEB MC 2010.
- The ACI 209 predicted modulus of elasticity values were the most accurate for all loading ages, while the CEB MC 2010 predicted modulus of elasticity values were the most inaccurate.
- Each set of field specimens exhibited approximately equal values for the equivalent age for each loading age based on the CEB MC 2010 and B3 Model maturity index.
- The GL 2000 maturity index exhibited a lower equivalent age for each loading age when compared to the CEB MC 2010 and B3 Model for all sets of field specimens.
- The measured creep strains for the samples collected on July 9, 2018 are much smaller than the measured creep strains for the samples collected on April 10, 2018 for each respected loading age.
- The measured compliance values for the samples collected on July 9, 2018 are much smaller than the measured compliance values for the samples collected on April 10, 2018 for each respected loading age.
- The rectangular prism drying shrinkage strains of the moist-cured specimens are greater than the rectangular prism drying shrinkage strains of the air-cured specimens with the exception of the samples collected on July 9, 2018. For the 07/09/2018-F

rectangular prisms, the air-cured drying shrinkage strains are larger than the drying shrinkage strains of the moist-cured samples.

- Also, both the air-cured and moist-cured rectangular prisms collected on April 10, 2018 and July 9, 2018 experienced highly similar shrinkage strains unlike the air-cured and moist-cured rectangular prisms that were collected on March 20, 2018 which exhibited much higher shrinkage strains.
- The shrinkage strains exhibited by the 04/10/2018-F and 07/09/2018-F cylindrical specimens were similar throughout the duration of testing.

5.8.2.2 Laboratory Specimens

From this research, the following conclusions can be drawn related to the hardened properties for each set of laboratory specimens:

- The laboratory mixture containing the quartzite coarse aggregate exhibited a higher compressive strength at each loading age than the laboratory mixture containing the limestone coarse aggregate.
- However, the laboratory mixture containing the limestone coarse aggregate exhibited a higher modulus of elasticity at each loading as compared to the laboratory mixture containing the quartzite coarse aggregate.
- In general, each model was accurate in the prediction of the modulus of elasticity values for all loading ages for both the quartzite and limestone mixtures.
- AASHTO LRFD 2017 performed the best in the prediction of the modulus of elasticity for the laboratory specimens, while the CEB MC 2010 was the most inaccurate.
- Both the quartzite and limestone coarse aggregate mixtures exhibited approximately equal values for the equivalent age for each loading age based on the CEB MC 2010 and B3 Model maturity index.
- The GL 2000 maturity index produced a lower equivalent age for each loading age when compared to the CEB MC 2010 and B3 Model for both the 05/03/2018-L-Q and 05/09/2018-L-L specimens.

- The measured creep strains for each loading age for both the quartzite and limestone mixtures were highly similar indicating that the substitution of one coarse aggregate type for the other lead to no significant changes in creep behavior.
- For the 05/03/2018-L-Q specimens, the creep strains for the 28-day loading age grew larger than the creep strains for the 7-day loading age as the concrete age increased.
- The measured compliance values for each loading age for both the quartzite and limestone mixtures were highly similar indicating that the substitution of one coarse aggregate type for the other lead to very little changes in measured compliance values.
- The rectangular prim drying shrinkage strains for both the quartzite and limestone mixtures were also highly similar to one another showing that once again, the substitution between the quartzite and limestone coarse aggregate had very little effect on shrinkage during the duration of testing.
- The shrinkage strains exhibited by the 05/03/2018-L-Q cylindrical specimens were larger than the shrinkage strains exhibited by the 05/09/2018-L-L cylindrical specimens.

CHAPTER 6: PREDICTION OF THE CREEP AND SHRINKAGE OF THE CONCRETE IN THE I-59/I-20 BIRMINGHAM SEGMENTAL BRIDGE

6.1 INTRODUCTION

One of the primary objectives of this research project was to compare creep and shrinkage strains of the concrete mixtures sampled at the segmental bridge jobsite to the prediction models that were discussed in Section 2.4. This was accomplished by comparing the measured creep and shrinkage strains to the estimated values predicted by the following methods:

- ACI 209 (ACI Committee 209 2008),
- AASHTO LRFD (2017),
- CEB MC 2010 (fib 2012),
- GL 2000 (Gardner and Lockman 2001), and
- B3 Model (Bazant and Baweja 2000).

The results for both the field and laboratory test specimens from this analysis are presented in this chapter. In Sections 6.2 through 6.6, a graphical comparison of how each model performed when predicting the measured creep and shrinkage strains as well as discussion on the accuracy of each model. In Section 6.7, a statistical comparison of how each model performed is covered, as well as a discussion as to which models performed the best during this research project. In Section 6.8, the method that produced the most accurate results is calibrated to further improve the overall creep and shrinkage estimations for the concrete mixtures that were collected in the field. Section 6.9 will contain a summary and conclusions that were made in relation to the prediction models considered in this study.

6.2 CREEP AND SHRINKAGE PREDICTION WITH THE ACI 209 MODEL

The ACI 209 creep and shrinkage prediction method does not clearly state whether the cement content is strictly the amount of cement used in the concrete mixture or if it is the total cement content (cement plus SCMs); therefore, in this study is was decided that cement content would be the latter. Also, ACI 209 was developed before the use of water-reducing admixtures;

therefore, the wet slump before the addition of water-reducing admixtures was used in the slump correction factor. If the slump value resulting from the addition of water-reducing admixtures was used, unrealistic creep and shrinkage correction factors would result leading to unrealistic strain predictions. A summary of the inputs and the justification behind the reasoning why each input was selected for both the creep and shrinkage prediction models are presented in Tables 6-1 and 6-2. With this being decided, all creep and shrinkage predictions were evaluated using the method outlined in Section 2.4.1.

As stated earlier in Section 5.3.1.2, the predicted modulus of elasticity values that were calculated using the prediction methods outlined by each method were used in the calculation of the predicted compliance values. This step was considered the most beneficial to accurately predict the initial elastic response that is experienced by the test specimens as soon as the load is applied in addition to the time-dependent response that is experienced during creep testing.

Table 6-1: ACI 209 creep prediction model summary of inputs for field and laboratory mixtures

Field Mixtures		**Laboratory Mixtures**	
Input	***Justification***	***Input***	***Justification***
Relative humidity = 50 percent	ASTM C512 (2018)	Relative humidity = 50 percent	ASTM C512 (2018)
Volume-to-surface ratio = 1.5	Computed excluding cylinder ends not exposed to atmosphere	Volume-to-surface ratio = 1.5	Computed excluding cylinder ends not exposed to atmosphere
Slump= 0.0 in.	Assumed pre-admixture slump (ACI 209 2008)	Slump= 0.0 in.	Assumed pre-admixture slump (ACI 209 2008)
Cement Factor	Assumed total cementitious material content	Cement Factor	Assumed total cementitious material content
Air Content	Table 5-2	Air Content	Table 5-3
Predicted modulus of elasticity for each loading age	Table 5-7	Predicted modulus of elasticity for each loading age	Table 5-16

Table 6-2: ACI 209 shrinakge prediction model summary of inputs for field and laboratory mixtures

Field Mixtures		**Laboratory Mixtures**	
Input	***Justification***	***Input***	***Justification***
Relative humidity = 50 percent	AASHTO T 160 (2015)	Relative humidity = 50 percent	AASHTO T 160 (2015)
Volume-to-surface ratio = 1.5	Computed excluding cylinder ends not exposed to atmosphere	Volume-to-surface ratio = 1.5	Computed excluding cylinder ends not exposed to atmosphere
Volume-to-surface ratio for rectangular prisms = 0.66	Calculated based on all six sides being exposed to drying	Volume-to-surface ratio for rectangular prisms = 0.66	Calculated based on all six sides being exposed to drying
Slump= 0.0 in.	Assumed pre-admixture slump (ACI 209 2008)	Slump= 0.0 in.	Assumed pre-admixture slump (ACI 209 2008)
Cement Factor	Assumed total cementitious material content	Cement Factor	Assumed total cementitious material content
Air Content	Table 5-2	Air Content	Table 5-3

6.2.1 Predicted Creep and Compliance Values for Field Specimens

Figures 6-1 and 6-2 show comparisons of the measured creep strain values to the estimated creep strain values for the field test specimens that were collected on April 10, 2018 and July 9, 2018, respectively. These figures were created using the data predicted using the ACI 209 model. Figure 6-1 contains the loading ages of 7 days, 28 days, and 91 days for the 04/10/2018-F specimens and Figure 6-2 contains the loading ages of 7 days and 28 days for the 07/09/2018-F specimens.

It can be seen in both Figure 6-1 and 6-2 that ACI 209 underestimates predicted creep strains for the loading ages of 7 days and 28 days for each set of field specimens, especially for the 04/10/2018-F specimens. However, ACI 209 was more accurate in the predicted creep strains for the loading age of 91 days for the 04/10/2018-F test specimens.

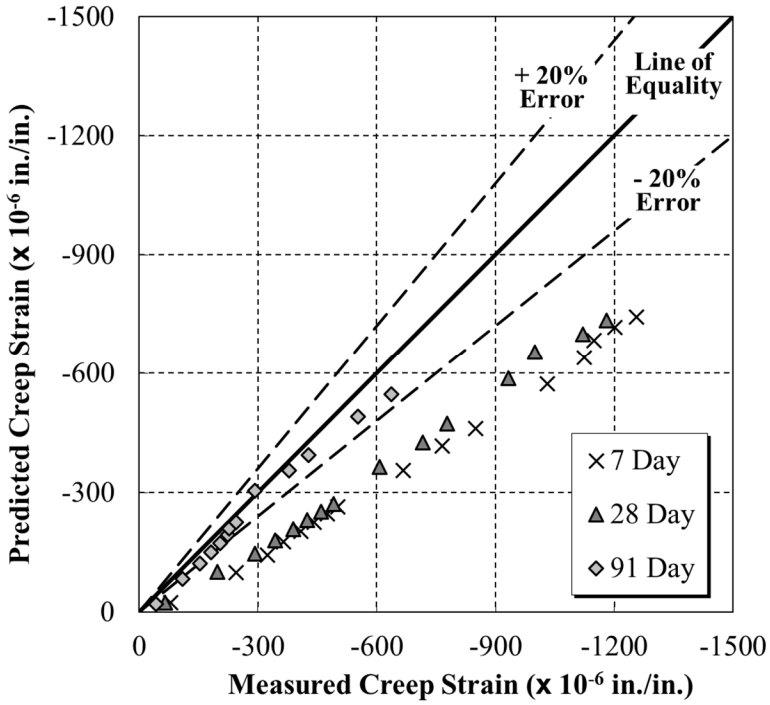

Figure 6-1: Measured versus predicted creep strains for the 04/10/2018-F field specimens using the ACI 209 model

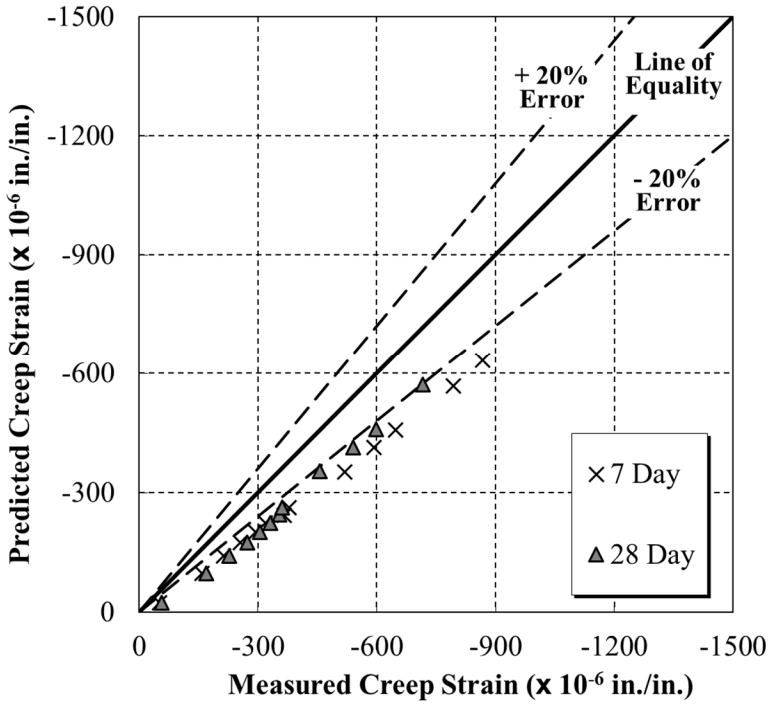

Figure 6-2: Measured versus predicted creep strains for the 07/09/2018-F field specimens using the ACI 209 model

Figures 6-3 and 6-4 show the predicted compliance values to the measured compliance values for the 04/10/2018-F and 07/09/2018-F test specimens, respectively. As compared to the predicted creep strains, the predicted compliance values for each loading age for each set of test specimens were more accurate. However, similar to the predicted creep strains, the predicted compliance values for all the loading ages for each set of test specimens were underestimated.

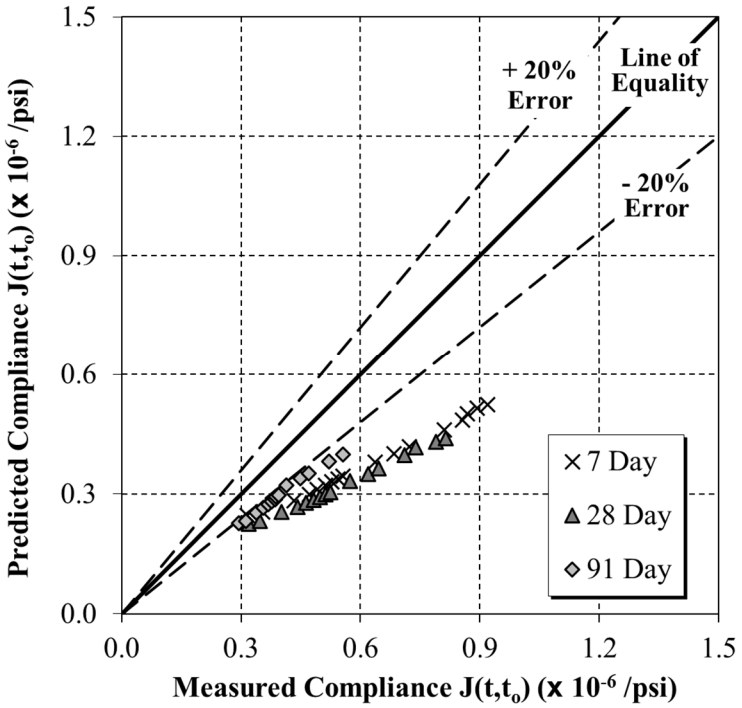

Figure 6-3: Measured versus predicted compliance values for the 04/10/2018-F field specimens using the ACI 209 model

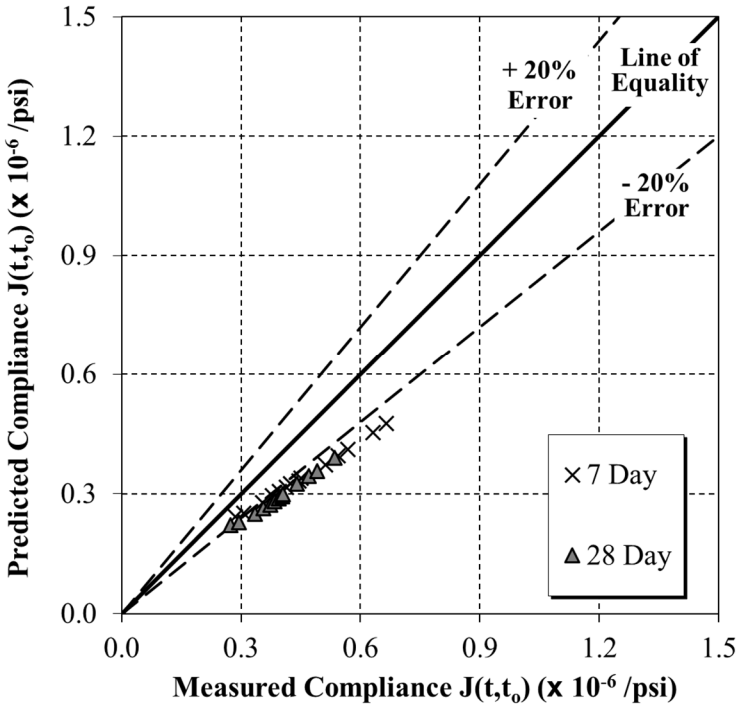

Figure 6-4: Measured versus predicted compliance values for the 07/09/2018-F field specimens using the ACI 209 model

6.2.2 Predicted Creep and Compliance Values for Laboratory Specimens

Figures 6-5 and 6-6 show the comparisons of the predicted creep strains to the measured creep strains by the ACI 209 model for 05/03/2018-L-Q and 05/09/2018-L-L test specimens. Each graph shows all loading ages for each concrete mixture. As shown Figures 6-5 and 6-6, the ACI 209 predicted creep strains for the 05/03/2018-L-Q test specimens were much more accurate as compared to the predicted creep strains of the 05/09/2018-L-L samples, which were underestimated for each loading age.

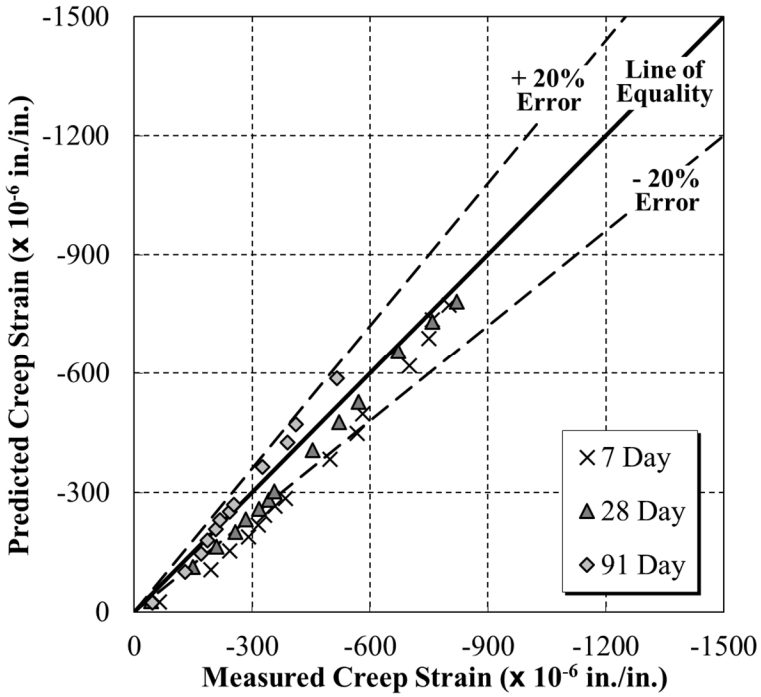

Figure 6-5: Measured versus predicted creep strains for the 05/03/2018-L-Q laboratory specimens using the ACI 209 model

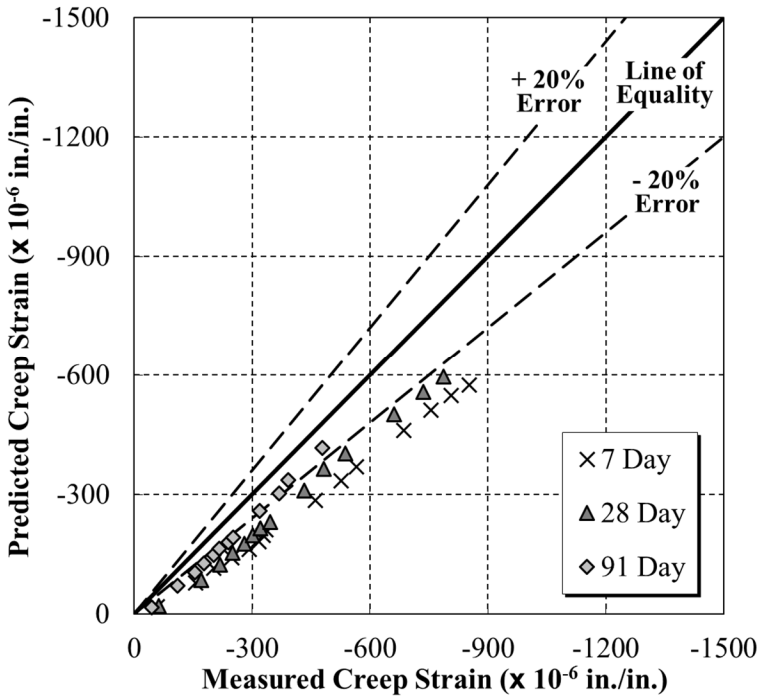

Figure 6-6: Measured versus predicted creep strains for the 05/09/2018-L-L laboratory specimens using the ACI 209 model

Figures 6-7 and 6-8 show the predicted compliance values to the measured compliance values for the 05/03/2018-L-Q and 05/09/2018-L-L test specimens, respectively. Unlike the predicted creep strains for 05/03/2018-L-Q test specimens, ACI 209 underestimated the predicted compliance values for all loading ages as seen in Figure 6-7. This statement also holds true for the predicted compliance values for the 05/09/2018-L-L test specimens as seen in Figure 6-8.

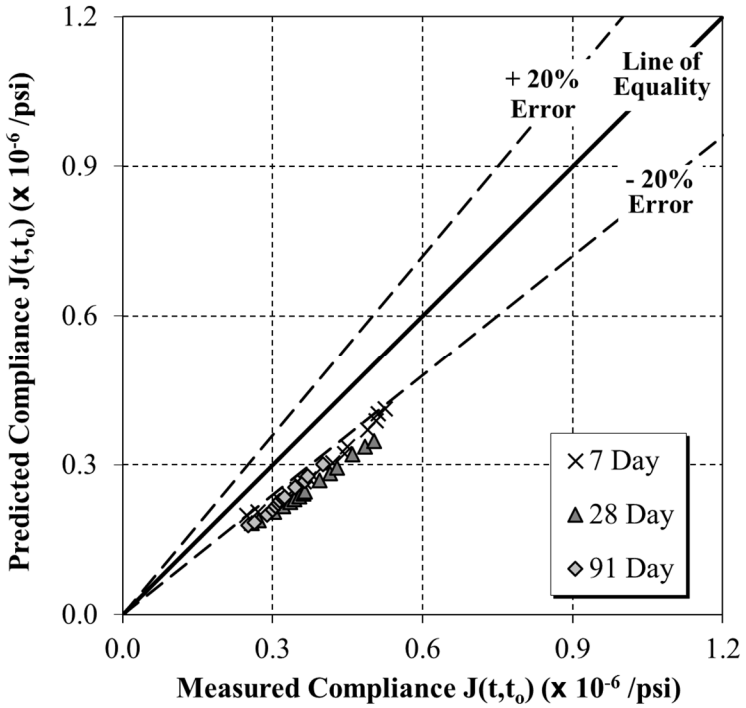

Figure 6-7: Measured versus predicted compliance values for the 05/03/2018-L-Q laboratory specimens using the ACI 209 model

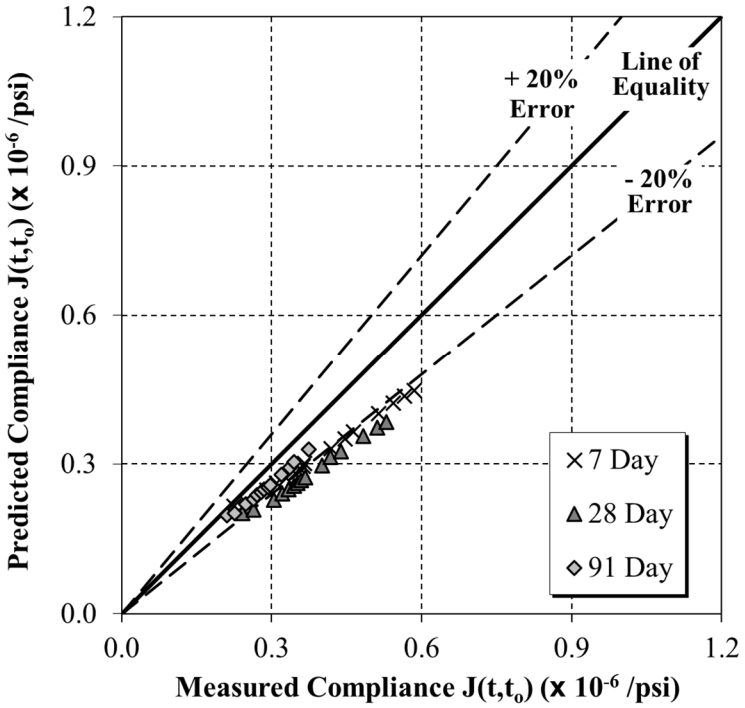

Figure 6-8: Measured versus predicted compliance values for the 05/09/2018-L-L laboratory specimens using the ACI 209 model

6.2.3 Predicted Shrinkage Values for Field Specimens

Figures 6-9 and 6-10 show the comparisons of the predicted drying shrinkage strains to the measured drying shrinkage strains as predicted by ACI 209. Figure 6-9 contains the drying shrinkage results for 03/20/2018-F-Air, 04/10/2018-F-Air, and 07/09/2018-F-Air rectangular prisms that were only subjected to air curing while Figure 6-10 contains the drying shrinkage results 03/20/2018-F-Moist, 04/10/2018-F-Moist, and 07/09/2018-F-Moist rectangular prisms that were exposed to a lime bath for a duration of 7 days. As can be seen in Figures 6-9 and 6-10, ACI 209 does not accurately predict the drying shrinkage strains for any of the field specimens that were collected.

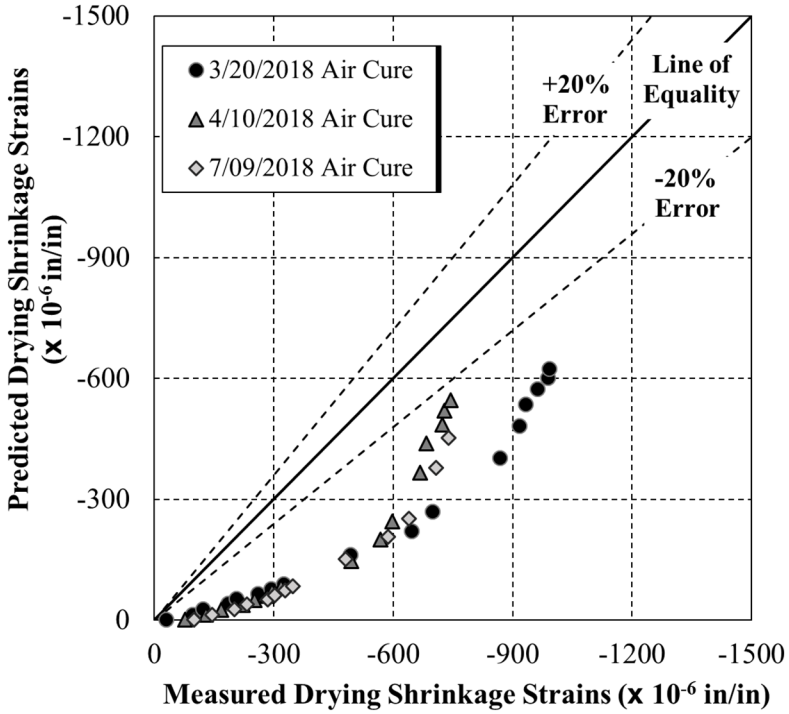

Figure 6-9: Measured versus predicted drying shrinkage strains for the air-cured field rectangular prisms using the ACI 209 model

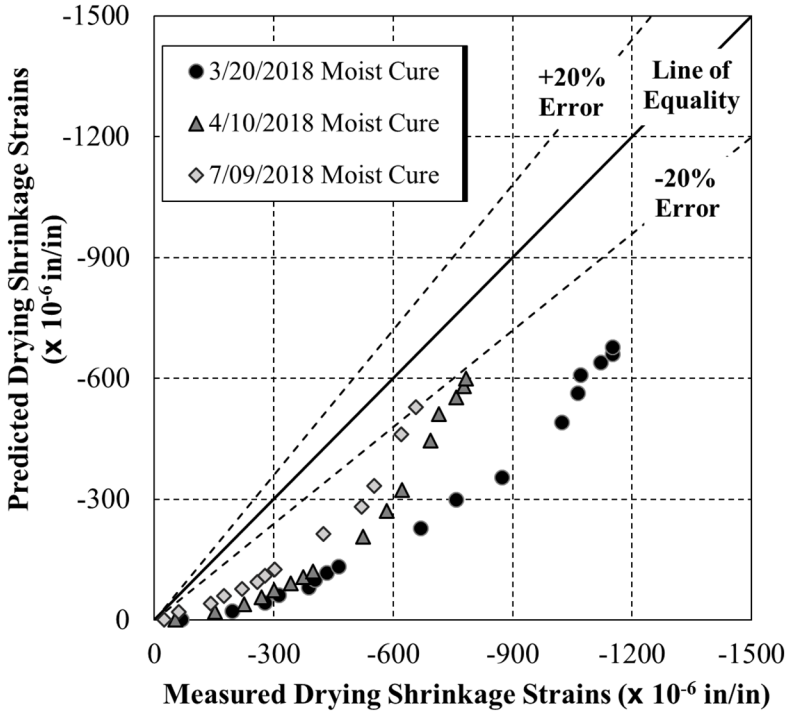

Figure 6-10: Measured versus predicted drying shrinkage strains for the moist-cured field rectangular prisms using the ACI 209 model

In addition to the ACI 209 predicted shrinkage values for the rectangular prism specimens, Figure 6-11 shows the ACI 209 predicted versus measured shrinkage values for the cylindrical field specimens that were used during creep testing. As seen in Figure 6-11, ACI 209 underestimated the shrinkage values for both the 04/10/2018-F and 07/09/2018-F cylindrical test samples.

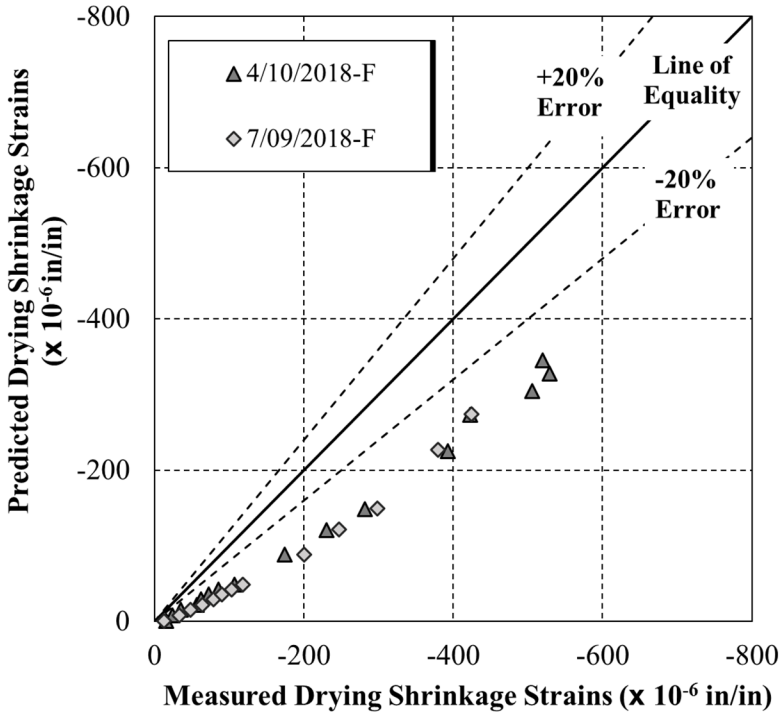

Figure 6-11: Measured versus predicted drying shrinkage strains for cylindrical field specimens using the ACI 209 model

6.2.4 Predicted Shrinkage Values for Laboratory Specimens

Figure 6-12 shows the comparison of the predicted drying shrinkage strains to the measured drying shrinkage strains for the 05/03/2018-L-Q and 05/09/2018-L-L laboratory mixtures. As seen in Figure 6-12, ACI 209 does not accurately predict the drying shrinkage strains in the early ages of drying, but as time progresses the predicted results tend to converge to the measured values for both the 05/03/2018-L-Q and 05/09/2018-L-L laboratory mixtures.

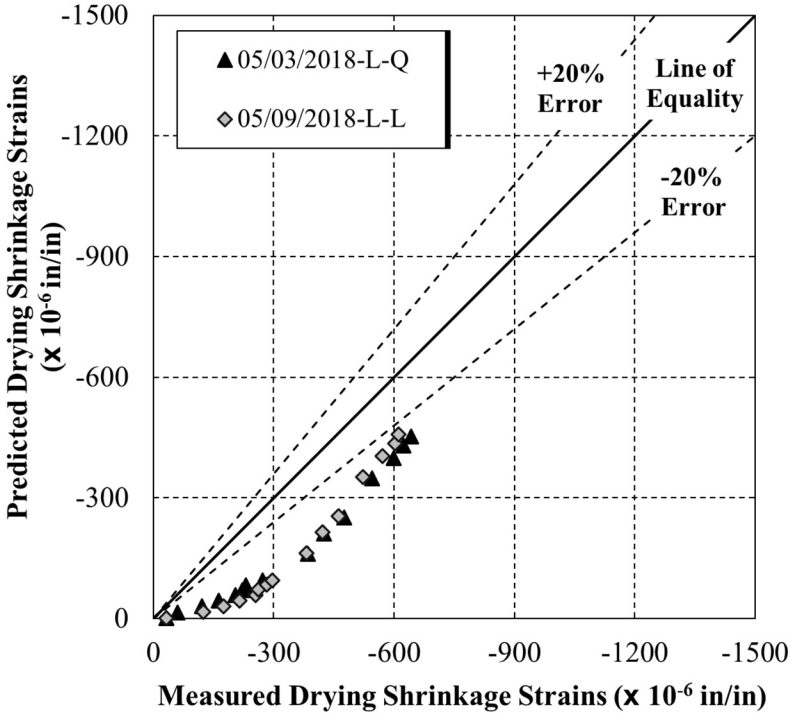

Figure 6-12: Measured versus predicted drying shrinkage strains for rectangular laboratory prisms using the ACI 209 model

As previously performed with the cylindrical field specimens, the ACI 209 predicted versus measured shrinkage strains for the cylindrical laboratory specimens can be found in Figure 6-13. As can be seen in Figure 6-13, the predicted shrinkage values for the cylindrical specimens containing the limestone aggregate are more accurate as compared to the predicted shrinkage strains for the cylindrical specimens that were cast using the quartzite aggregate.

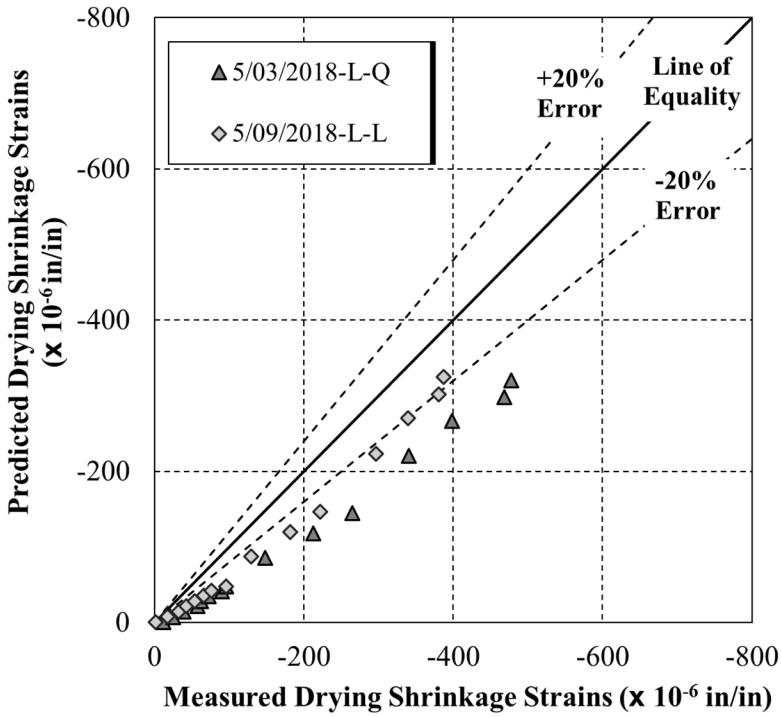

Figure 6-13: Measured versus predicted drying shrinkage strains for cylindrical laboratory specimens using the ACI 209 model

6.3 CREEP AND SHRINKAGE PREDICTION WITH THE AASHTO 2017 MODEL

Unlike the ACI 209 creep and shrinkage prediction methods, no assumptions had to be made in regard to any of the input parameters of the AASHTO 2017 method. A summary of the inputs used in both the creep and shrinkage prediction methods can be found in Table 6-3 and Table 6-4, respectively. All creep and shrinkage prediction calculations were evaluated using the AASHTO 2017 model outlined in Section 2.4.2.

Table 6-3: AASHTO 2017 creep prediction model summary of inputs for field and laboratory mixtures

Field Mixtures		**Laboratory Mixtures**	
Input	***Justification***	***Input***	***Justification***
Relative humidity = 50 percent	ASTM C512 (2018)	Relative humidity = 50 percent	ASTM C512 (2018)
Volume-to-surface ratio = 1.5	Computed excluding cylinder ends not exposed to atmosphere	Volume-to-surface ratio = 1.5	Computed excluding cylinder ends not exposed to atmosphere
Chronological age at the application of loading	Based on AASHTO LRFD 2017 provisions	Chronological age at the application of loading	Based on AASHTO LRFD 2017 provisions
Duration of loading ($t-t_o$)	Based on AASHTO LRFD 2017 provisions	Duration of loading ($t-t_o$)	Based on AASHTO LRFD 2017 provisions
Compressive strength at loading	Table 5-4	Compressive strength at loading	Table 5-15
Predicted modulus of elasticity for each loading age	Table 5-8	Predicted modulus of elasticity for each loading age	Table 5-17

Table 6-4: AASHTO 2017 shrinakge prediction model summary of inputs for field and laboratory mixtures

Field Mixtures		**Laboratory Mixtures**	
Input	***Justification***	***Input***	***Justification***
Relative humidity = 50 percent	AASHTO T 160 (2015)	Relative humidity = 50 percent	AASHTO T 160 (2015)
Volume-to-surface ratio = 1.5	Computed excluding cylinder ends not exposed to atmosphere	Volume-to-surface ratio = 1.5	Computed excluding cylinder ends not exposed to atmosphere
Volume-to-surface ratio for rectangular prisms = 0.66	Calculated based on all six sides being exposed to drying	Volume-to-surface ratio for rectangular prisms = 0.66	Calculated based on all six sides being exposed to drying
Duration of drying, $(t-t_c)$	Based on AASHTO LRFD 2017 provisions	Duration of drying, $(t-t_c)$	Based on AASHTO LRFD 2017 provisions
For specimens exposed to drying before 5 days of curing, increase shrinkage predictions by 20%	Based on AASHTO LRFD 2017 provisions	For specimens exposed to drying before 5 days of curing, increase shrinkage predictions by 20%	Based on AASHTO LRFD 2017 provisions
Compressive strength at 7 days	04/10/2018-F and 07/09/2018-F: Table 5-4 03/20/2018-F: Table 5-6	Compressive strength at 7 days	Table 5-15

6.3.1 Predicted Creep and Compliance Values for Field Specimens

Figures 6-14 and 6-15 show comparisons of the measured creep strain values to the estimated creep strain values for the field test specimens that were collected on April 10, 2018 and July 9, 2018, respectively. These figures were created using the data predicted using the AASHTO 2017 method. Each figure contains all loading ages for each set of test specimens that were collected in the field. As can be seen in Figures 6-14 and 6-15, AASHTO 2017 does not predict the creep strains of 7- and 28-day loading ages with reasonably accuracy during the early ages of loading,

but the predicted strains do tend to converge towards the measured values as concrete age progresses. However, AASHTO 2017 does tend to predict the 91-day creep strains with a higher accuracy at a much lower concrete age.

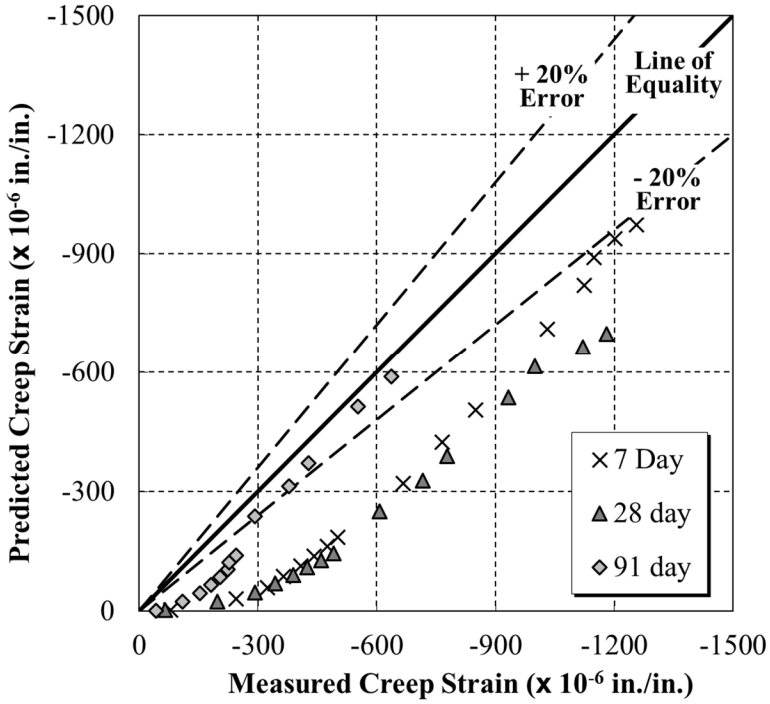

Figure 6-14: Measured versus predicted creep strains for the 04/10/2018-F field specimens using the AASHTO 2017 model

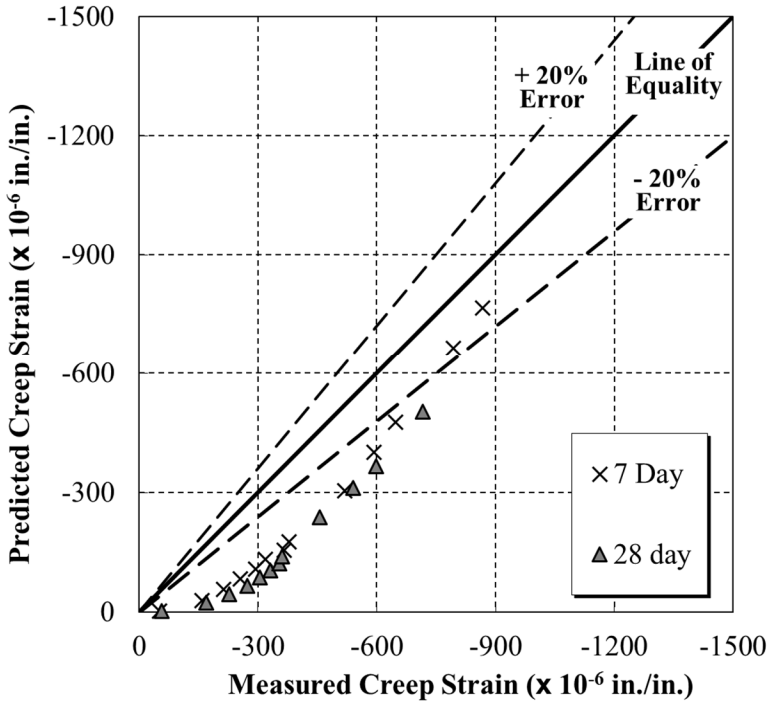

Figure 6-15: Measured versus predicted creep strains for the 07/09/2018-F field specimens using the AASHTO 2017 model

Figures 6-16 and 6-17 show the AASHTO 2017 predicted compliance values to the measured compliance values for the 04/10/2018-F and 07/09/2018-F test specimens, respectively. As compared to the predicted creep strains for each set of test specimens, the predicted compliance values are much more accurate. This is due to a portion of the compliance being composed of the elastic response, which has less error leading to decrease in the overall percent error for the full compliance. As can be seen in Figures 6-16 and 6-17, AASHTO 2017 tends to underestimate the compliance values, especially during the early ages after loading. Much like the predicted creep strains though, the predicted compliance values tend to converge towards the measured values as the concrete age increases.

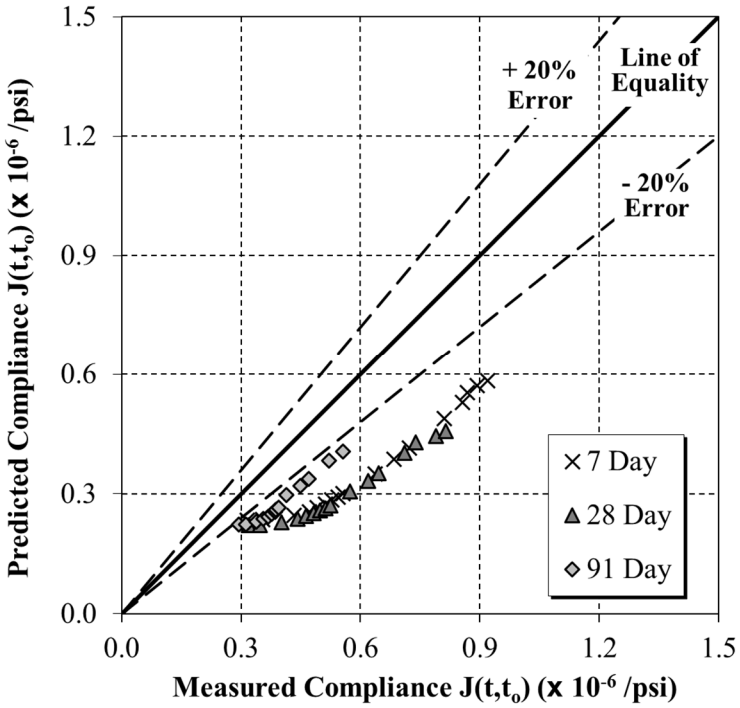

Figure 6-16: Measured versus predicted compliance values for the 04/10/2018-F field specimens using the AASHTO 2017 model

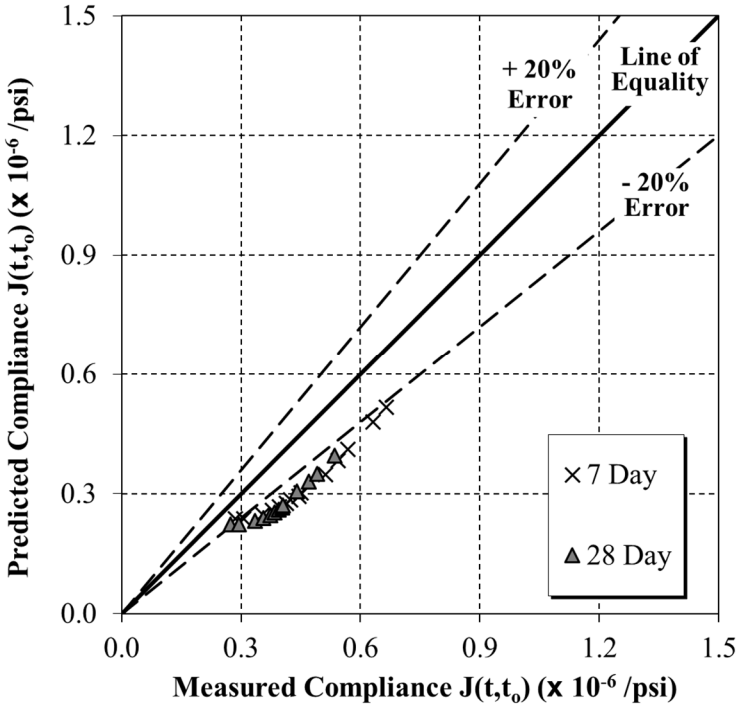

Figure 6-17: Measured versus predicted compliance values for the 07/09/2018-F field specimens using the AASHTO 2017 model

6.3.2 Predicted Creep and Compliance Values for Laboratory Specimens

Figures 6-18 and 6-19 show the comparisons of the predicted creep strains to the measured creep strains by the AASHTO 2017 method for the 05/03/2018-L-Q and 05/09/2018-L-L laboratory test specimens. Similar to both sets of field test specimens, AASHTO 2017 greatly underestimates the predicted creep strains for both the 05/03/2018-L-Q and 05/09/2018-L-L mixtures in the early ages after loading is applied. However, as the concrete ages the predicted values tend to become much more accurate as they tend to converge towards the measured creep strains. As seen in Figures 6-18 and 6-19, the predicted creep values do not fall within the $\pm$ 20% range until much later ages of testing.

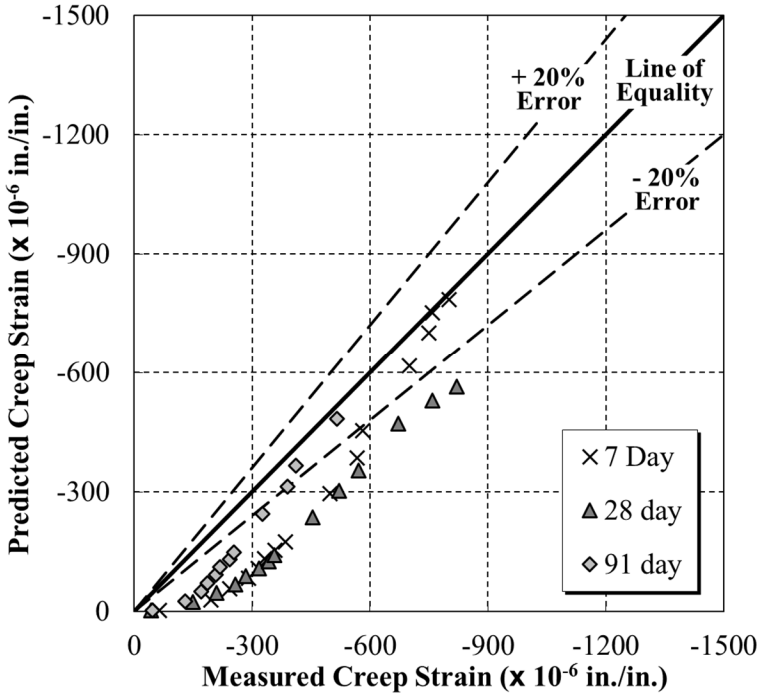

Figure 6-18: Measured versus predicted creep strains for the 05/03/2018-L-Q laboratory specimens using the AASHTO 2017 model

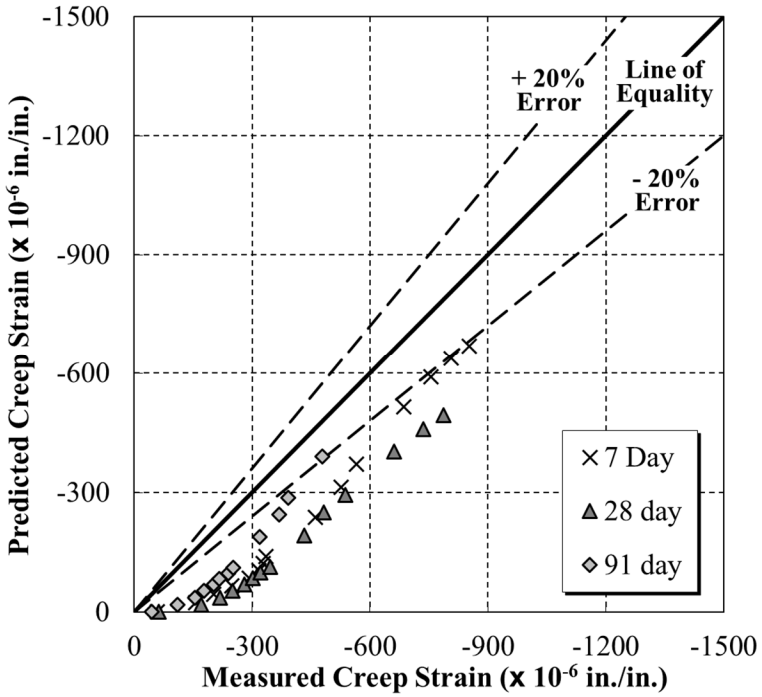

Figure 6-19: Measured versus predicted creep strains for the 05/09/2018-L-L laboratory specimens using the AASHTO 2017 model

Figures 6-20 and 6-21 show the AASHTO 2017 predicted compliance values versus the measured compliance values for the 05/03/2018-L-Q and 05/09/2018-L-L laboratory test specimens, respectively. As compared to the predicted creep strains for each set of test specimens, the predicted compliance values are much more accurate. As can be seen in Figures 6-20 and 6-21, AASHTO 2017 tends to underestimate the compliance values, especially during the early ages after loading. Unlike the predicted creep strains, the predicted compliance values for both the quartzite and limestone laboratory mixtures were much closer to the $\pm$ 20% target range. In similarity to the predicted creep strains, the predicted compliance values tend to converge towards the measured values as the concrete age increases.

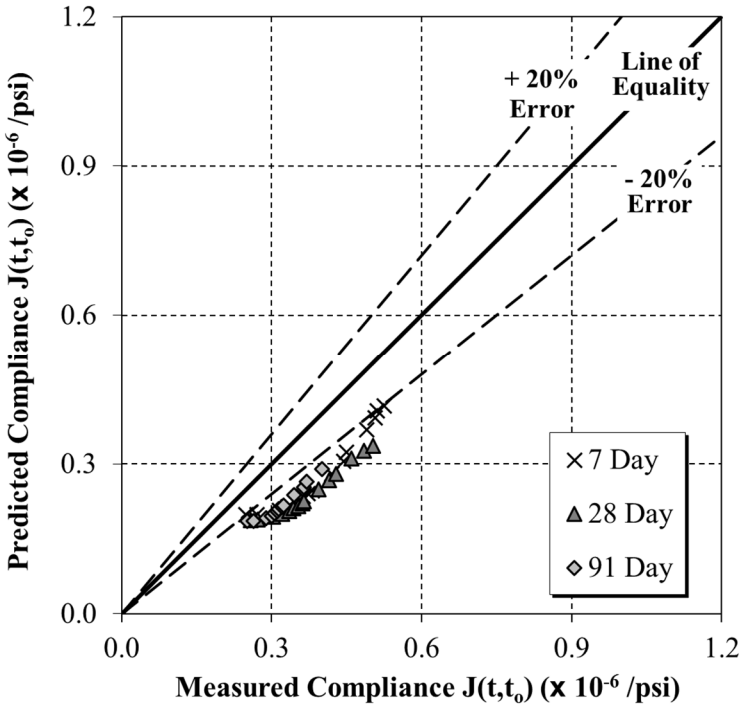

Figure 6-20: Measured versus predicted compliance values for the 05/03/2018-L-Q laboratory specimens using the AASHTO 2017 model

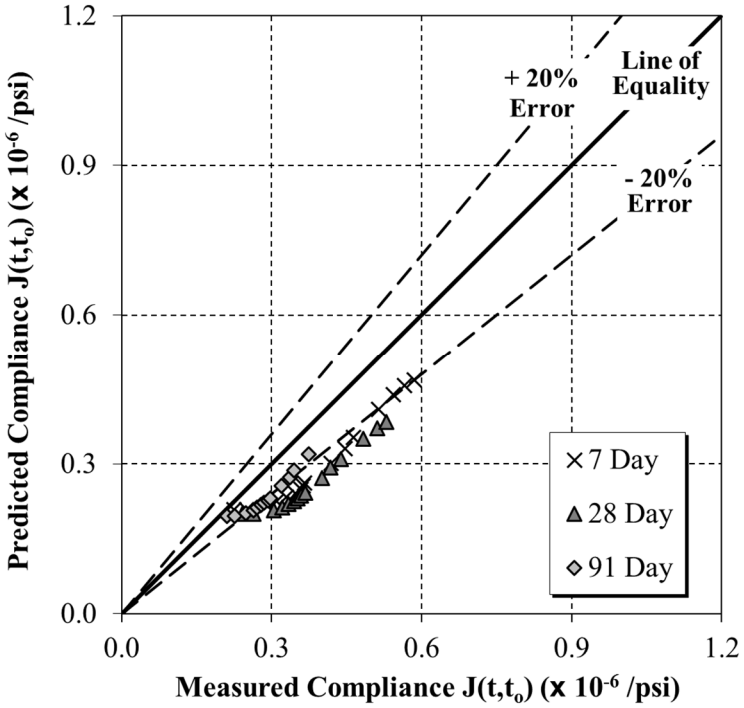

Figure 6-21: Measured versus predicted compliance values for the 05/09/2018-L-L laboratory specimens using the AASHTO 2017 model

6.3.3 Predicted Shrinkage Values for Field Specimens

Figures 6-22 and 6-23 show the comparisons of the predicted drying shrinkage strains versus the measured drying shrinkage strains as predicted by AASHTO 2017. Figure 6-22 contains the drying shrinkage results for 03/20/2018-F-Air, 04/10/2018-F-Air, and 07/09/2018-F-Air rectangular prisms that were only subjected to air curing, while Figure 6-23 contains the drying shrinkage results 03/20/2018-F-Moist, 04/10/2018-F-Moist, and 07/09/2018-F-Moist rectangular prisms that were exposed to a lime bath for a duration of 7-days.

As can be seen in Figures 6-22 and 6-23, AASHTO 2017 performs much better at predicting the drying shrinkage results for the field specimens that were subjected to only air curing as compared to the predicted values of ACI 209. However, AASHTO 2017 does not predict the drying shrinkage results for the moist cured field specimens with any more accuracy than that of ACI 209.

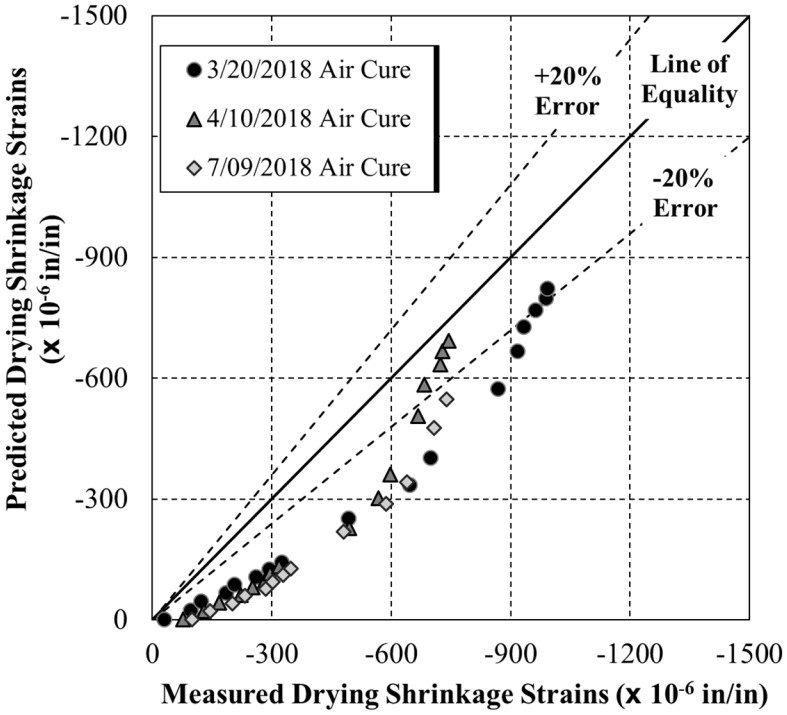

Figure 6-22: Measured versus predicted drying shrinkage strains for the air-cured field rectangular prisms using the AASHTO 2017 model

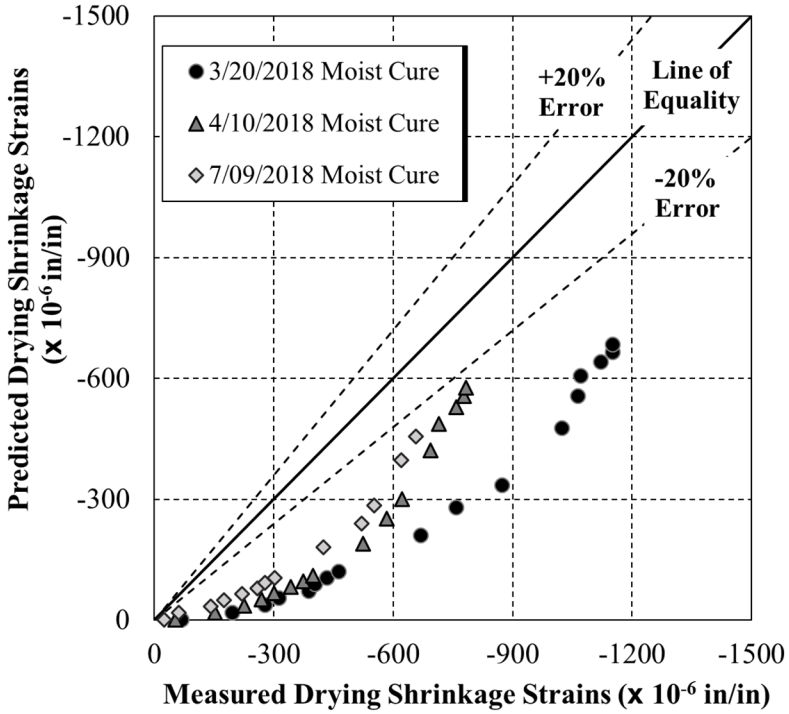

Figure 6-23: Measured versus predicted drying shrinkage strains for the moist-cured field rectangular prisms using the AASHTO 2017 model

Figure 6-24 shows the predicted versus measured drying shrinkage strains for the cylindrical field specimens using the AASHTO 2017 method. As compared to the rectangular field prisms, the accuracy of the AASHTO 2017 predicted shrinkage values for the cylindrical specimens is much better. As can be seen in Figure 6-24, the predicted versus measured values fall on the line of equality indicating that the predicted shrinkage values are very similar to those measured during testing.

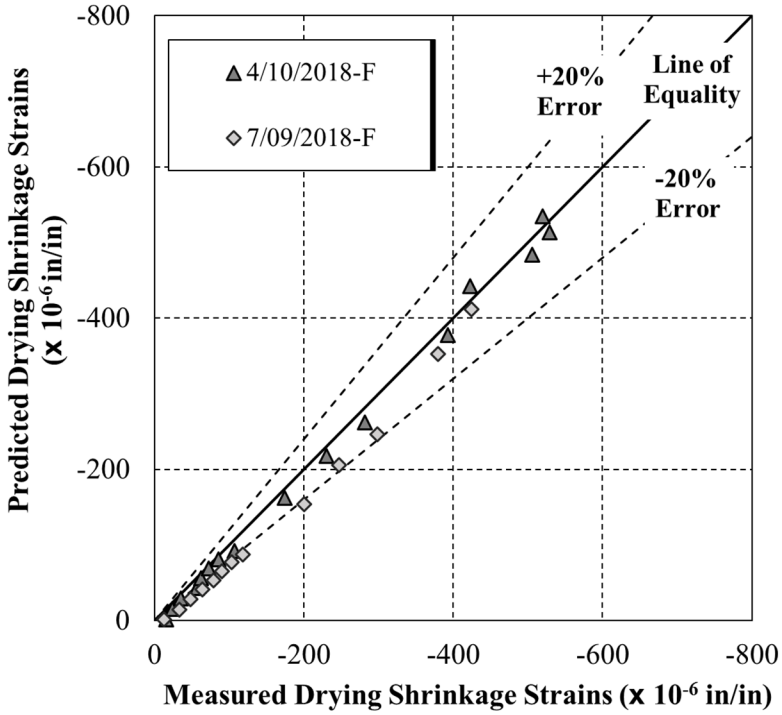

Figure 6-24: Measured versus predicted drying shrinkage strains for cylindrical field specimens using the AASHTO 2017 model

6.3.4 Predicted Shrinkage Values for Laboratory Specimens

Figure 6-25 shows the comparison of the AASHTO 2017 predicted drying shrinkage strains versus the measured drying shrinkage strains for the 05/03/2018-L-Q and 05/09/2018-L-L laboratory mixtures. As compared to the predicted values of ACI 209, AASHTO 2017 predicts the drying shrinkage strains with a lower accuracy. As can be seen in Figure 6-25, AASHTO 2017 tends to underestimate the drying shrinkage results much more in the early ages of drying as compared to later ages.

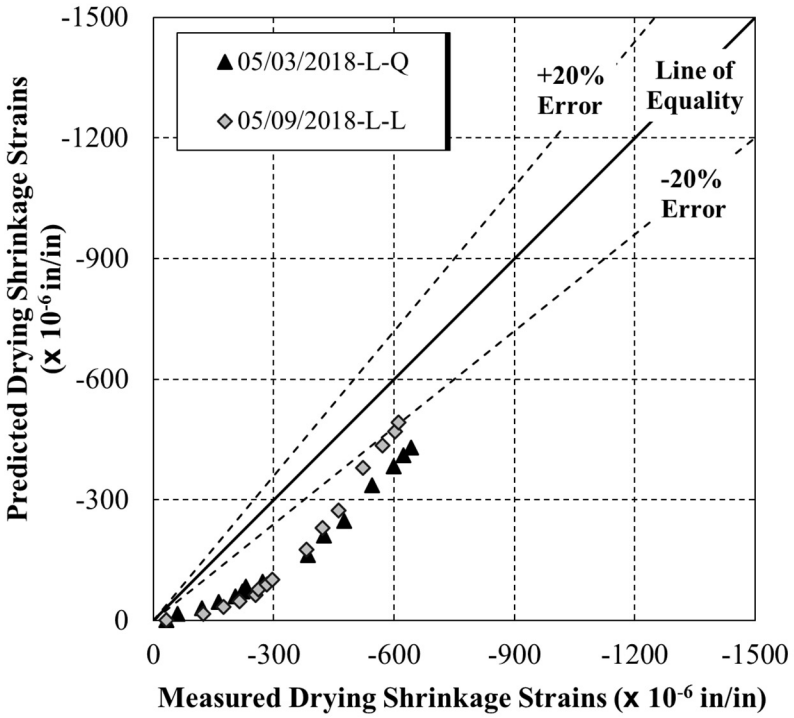

Figure 6-25: Measured versus predicted drying shrinkage strains for rectangular laboratory prisms using the AASHTO 2017 model

Figure 6-26 shows the predicted versus measured shrinkage values for the cylindrical laboratory test specimens using the AASHTO 2017 method. Unlike the rectangular prisms used in laboratory testing, the AASHTO 2017 predicted shrinkage values for the cylindrical test specimens is much greater. As can be seen in Figure 6-26, AASHTO 2017 tends to overestimate the shrinkage values for the laboratory mixture containing the limestone coarse aggregate, and underestimate the shrinkage values for the laboratory mixture containing the quartzite coarse aggregate.

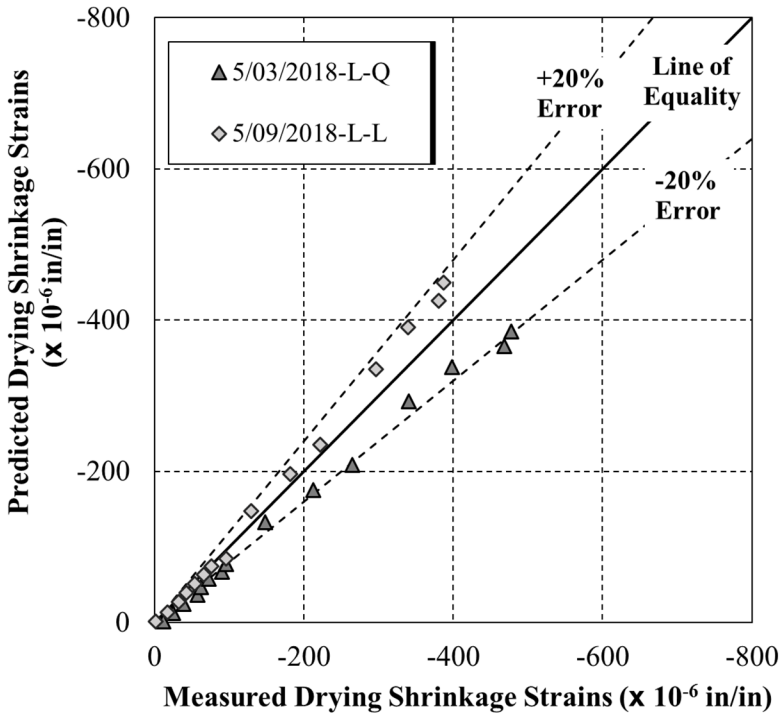

Figure 6-26: Measured versus predicted drying shrinkage strains for cylindrical laboratory specimens using the AASHTO 2017 model

6.4 CREEP AND SHRINKAGE PREDICTION METHOD WITH THE CEB MC 2010 MODEL

Like the AASHTO 2017 method, the CEB MC 2010 creep and shrinkage prediction method did not require any assumptions or corrections be made to the input parameters in order for it to be used to estimate the creep and shrinkage values for either the field or laboratory specimens. Tables 6-5 and 6-6 provide a summary of all inputs that were used for both the creep and shrinkage prediction models, respectively. All calculations were completed using the procedure outlined earlier in Section 2.4.3.

Table 6-5: CEB MC 2010 creep prediction model summary of inputs for field and laboratory mixtures

Field Mixtures		**Laboratory Mixtures**	
Input	***Justification***	***Input***	***Justification***
Relative humidity = 50 percent	ASTM C512 (2018)	Relative humidity = 50 percent	ASTM C512 (2018)
Notional member size: Cylinders = 76.2 mm	Based on CEB MC 2010 provisions	Notional member size: Cylinders = 76.2 mm	Based on CEB MC 2010 provisions
28-day measured compressive strength	Table 5-4	28-day measured compressive strength	Table 5-15
Predicted modulus of elasticity for each loading age	Table 5-11	Predicted modulus of elasticity for each loading age	Table 5-18
Concrete equivalent adjusted age at loading	Table 5-14 (CEB MC 2010)	Concrete equivalent adjusted age at loading	Table 5-21 (CEB MC 2010)
Normal-hardening cement assumed	Based on ALDOT approved mixture design	Normal-hardening cement assumed	Based on ALDOT approved mixture design

Table 6-6: CEB MC 2010 shrinakge prediction model summary of inputs for field and laboratory mixtures

Field Mixtures		**Laboratory Mixtures**	
Input	***Justification***	***Input***	***Justification***
Relative humidity = 50 percent	AASHTO T 160 (2015)	Relative humidity = 50 percent	AASHTO T 160 (2015)
Notional member size: Cylinders = 76.2 mm, Rectangular Prims= 38.1 mm based on AASHTO T 160 rectangular prism sizing	Based on CEB MC 2010 provisions	Notional member size: Cylinders = 76.2 mm, Rectangular Prims= 38.1 mm based on AASHTO T 160 rectangular prism sizing	Based on CEB MC 2010 provisions
28-day measured compressive strength	04/10/2018-F and 07/09/2018-F: Table 5-4 03/20/2018-F: Table 5-6	28-day measured compressive strength	Table 5-15
Concrete age at beginning of drying for rectangular prisms: air-cured = 1 day, moist-cured = 7 days	Air-cured prisms demolded immediately upon arrival at Auburn University. Moist-cured demolded and placed in lime-bath for 7 days.	Concrete age at beginning of drying for rectangular prisms = 7 days	Specimens demolded and placed in lime-bath for 7 days.
Concrete age at beginning of drying for cylinders = 1 day	Demolded immediately upon arrival at Auburn University and placed in creep room.	Concrete age at beginning of drying for cylinders = 1 day	Demolded immediately after curing and placed in creep room.
Normal-hardening cement assumed	Based on ALDOT approved mixture design	Normal-hardening cement assumed	Based on ALDOT approved mixture design

6.4.1 Predicted Creep and Compliance Values for Field Specimens

Figures 6-27 and 6-28 show comparisons of the measured creep strain values versus the estimated creep strain values for the 04/10/2018-F and 07/09/2018-F field specimens. Each of these graphs were created using the CEB MC 2010 predicted creep strain values and include all

loading ages that underwent testing. As can be seen in Figures 6-27 and 6-28, CEB MC 2010 tends to overestimate the creep strains for all loading ages for both the 04/10/2018-F and 07/09/2018-F test specimens. However, CEB MC 2010 does provide accurate results for all loading ages except for the 91-day loading age of the 04/10/2018-F field specimens, which was greatly overestimated as compared to the 7-day and 28-day loading ages.

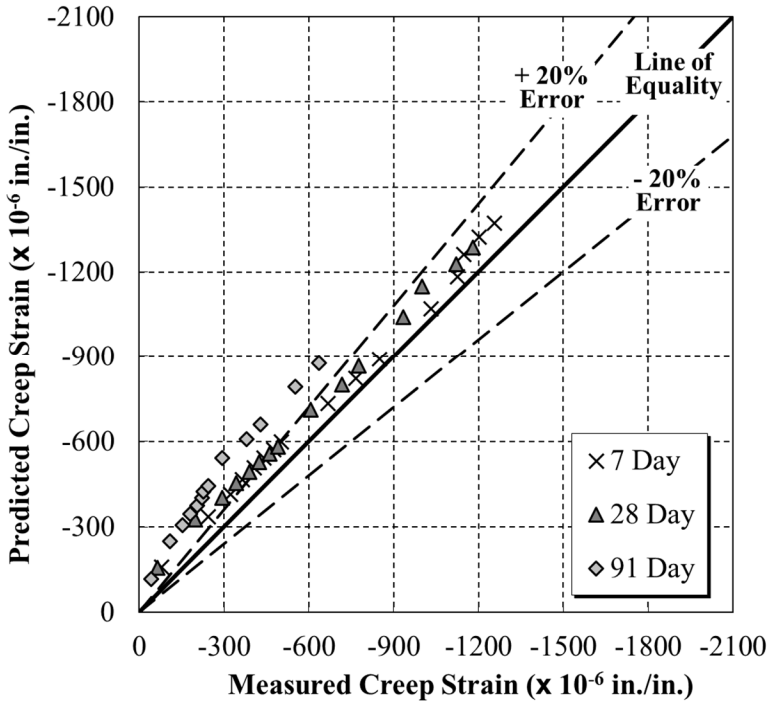

Figure 6-27: Measured versus predicted creep strains for the 04/10/2018-F field specimens using the CEB MC 2010 model

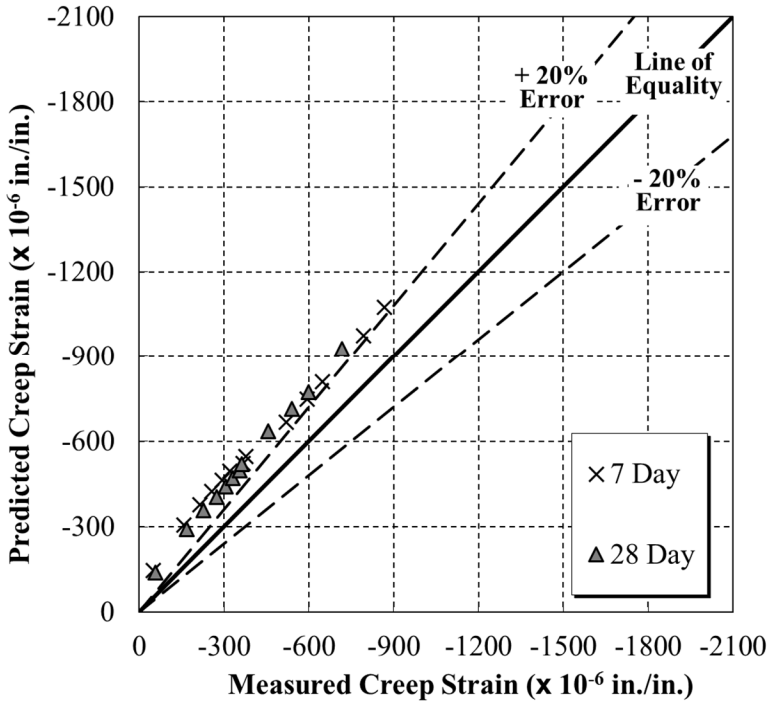

Figure 6-28: Measured versus predicted creep strains for the 07/09/2018-F field specimens using the CEB MC 2010 model

Figures 6-29 and 6-30 show the CEB MC 2010 predicted compliance values versus the measured compliance values for the 04/10/2018-F and 07/09/2018-F test specimens, respectively. As can be seen in Figures 6-29 and 6-30, CEB MC 2010 tended to underestimate the predicted compliance values for both the 04/10/2018-F and 07/09/2018-F specimens. For all loading ages considered for both the 04/10/2018-F and 07/09/2018-F specimens, the predicted compliance values are either below the -20% threshold or falls closely to it during the duration of testing. As Figure 6-29 shows, as the age of the concrete increased for the 7-day and 28-day loading ages for the 04/10/2018-F specimens, the predicted compliance values started to decrease in accuracy. As shown in Figure 6-30, both the 7-day and 28-day loading ages for the 07/09/2018-F specimens maintained a consistent trend of falling extremely closely to the -20% threshold value.

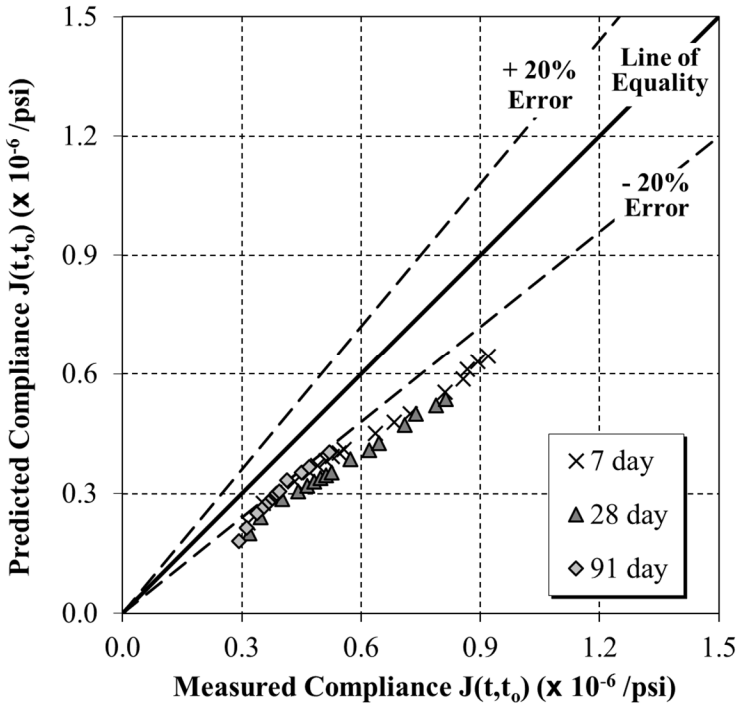

Figure 6-29: Measured versus predicted compliance values for the 04/10/2018-F field specimens using the CEB MC 2010 model

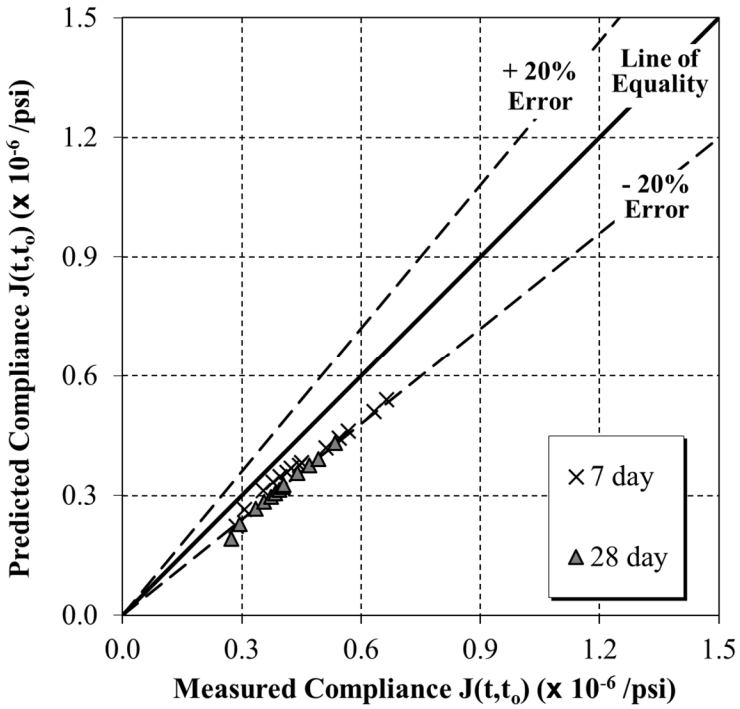

Figure 6-30: Measured versus predicted compliance values for the 07/09/2018-F field specimens using the CEB MC 2010 model

6.4.2 Predicted Creep and Compliance Values for Laboratory Specimens

Figures 6-31 and 6-32 show the comparisons of the predicted creep strains versus the measured creep strains by the CEB MC 2010 method for the 05/03/2018-L-Q and 05/09/2018-L-L laboratory test specimens. According to Figures 6-31 and 6-32, the predicted creep strains for the concrete mixture containing the quartzite coarse aggregate are much more accurate as compared to the mixture containing the limestone coarse aggregate. All loading ages for the 05/03/2018-L-Q test specimens are very close to the $\pm$ 20% target range whereas all loading ages for the 05/09/2018-L-L specimens are well beyond this desired threshold.

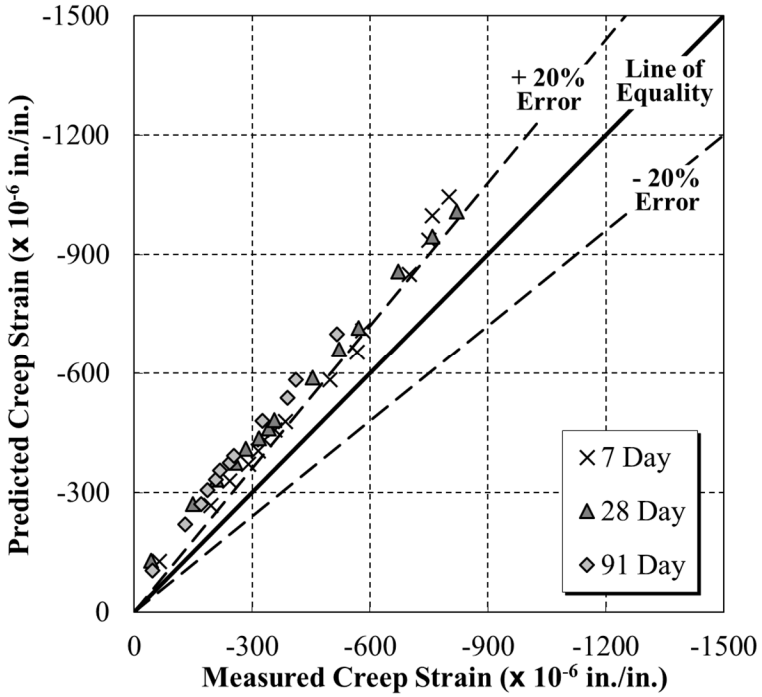

Figure 6-31: Measured versus predicted creep strains for the 05/03/2018-L-Q laboratory specimens using the CEB MC 2010 model

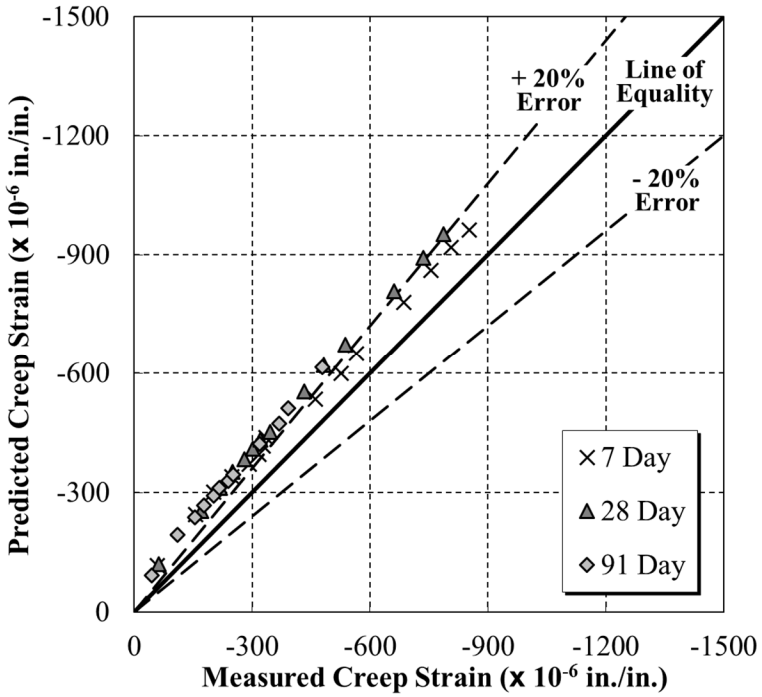

Figure 6-32: Measured versus predicted creep strains for the 05/09/2018-L-L laboratory specimens using the CEB MC 2010 model

Figures 6-33 and 6-34 show the CEB MC 2010 predicted compliance values versus the measured compliance values for the 05/03/2018-L-Q and 05/09/2018-L-L laboratory test specimens, respectively. Unlike the predicted creep strains for the 05/03/2018-L-Q test specimens, CEB MC 2010 tends to slightly underestimate the predicted compliance values for all loading ages for the quartzite coarse aggregate mixture. However, the predicted compliance values by CEB MC 2010 for the 05/09/2018-L-L specimens are extremely accurate and all fall within the $\pm$ 20% target range.

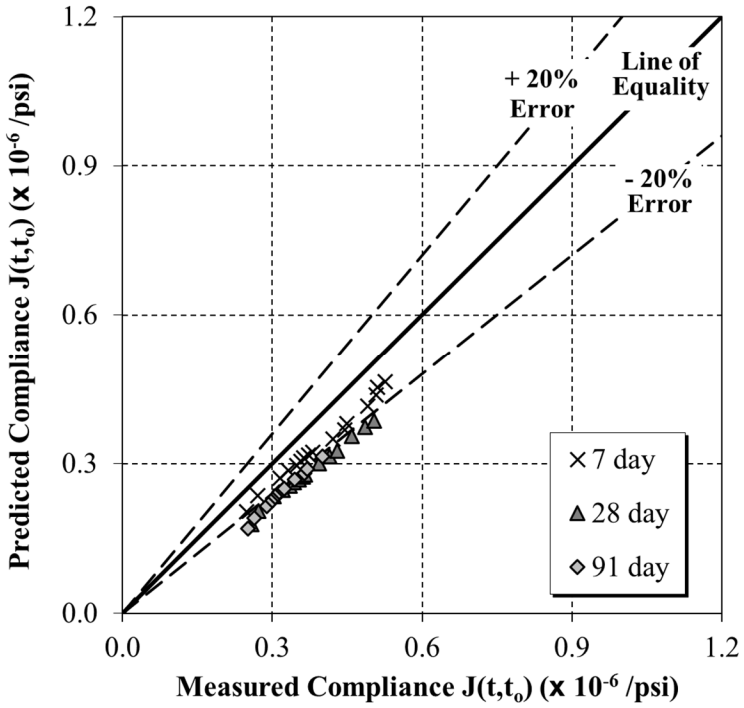

Figure 6-33: Measured versus predicted compliance values for the 05/03/2018-L-Q laboratory specimens using the CEB MC 2010 model

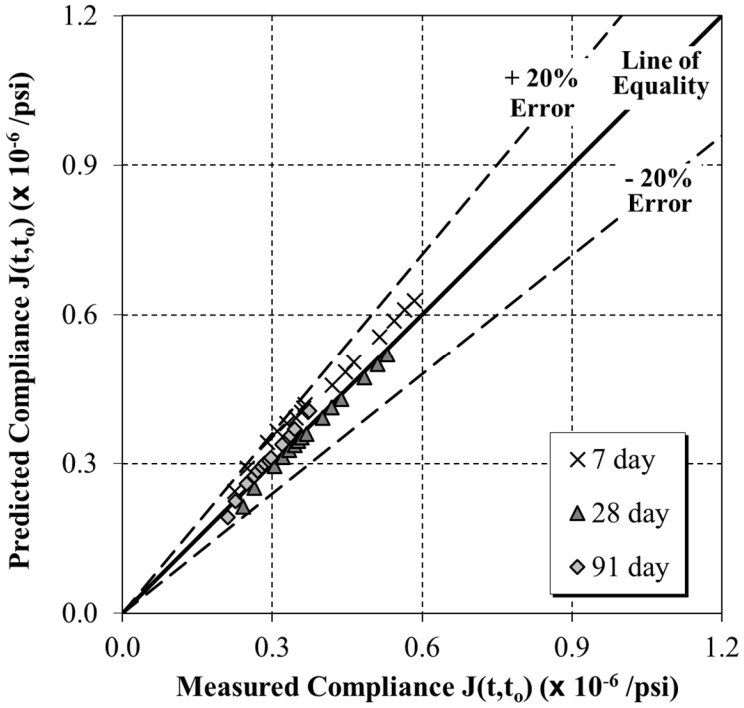

Figure 6-34: Measured versus predicted compliance values for the 05/09/2018-L-L laboratory specimens using the CEB MC 2010 model

6.4.3 Predicted Shrinkage Values for Field Specimens

Figures 6-35 and 6-36 show the comparisons of the predicted drying shrinkage strains versus the measured drying shrinkage strains as predicted by CEB MC 2010. Figure 6-35 contains the drying shrinkage results for 03/20/2018-F-Air, 04/10/2018-F-Air, and 07/09/2018-F-Air rectangular prisms that were only subjected to air curing while Figure 6-36 contains the drying shrinkage results 03/20/2018-F-Moist, 04/10/2018-F-Moist, and 07/09/2018-F-Moist rectangular prisms that were exposed to a lime bath for a duration of 7 days.

As compared to the predicted drying shrinkage strains of both ACI 209 and AASHTO 2017, the CEB MC 2010 predicted shrinkage values for both the air-cured and moist-cured field specimens are much more accurate; however, the majority of the predicted values are still beyond the $\pm$ 20% target range.

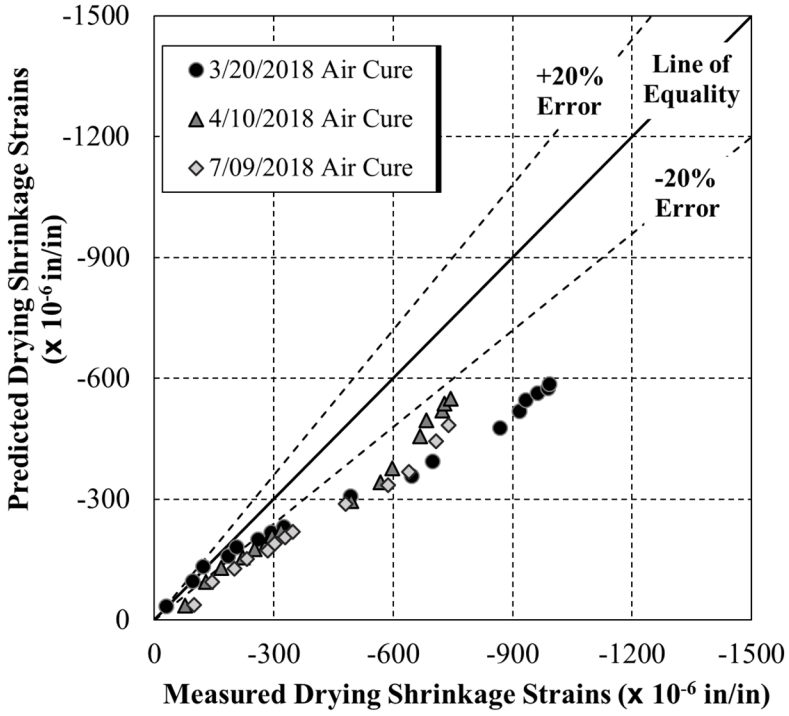

Figure 6-35: Measured versus predicted drying shrinkage strains for the air-cured field rectangular prisms using the CEB MC 2010 model

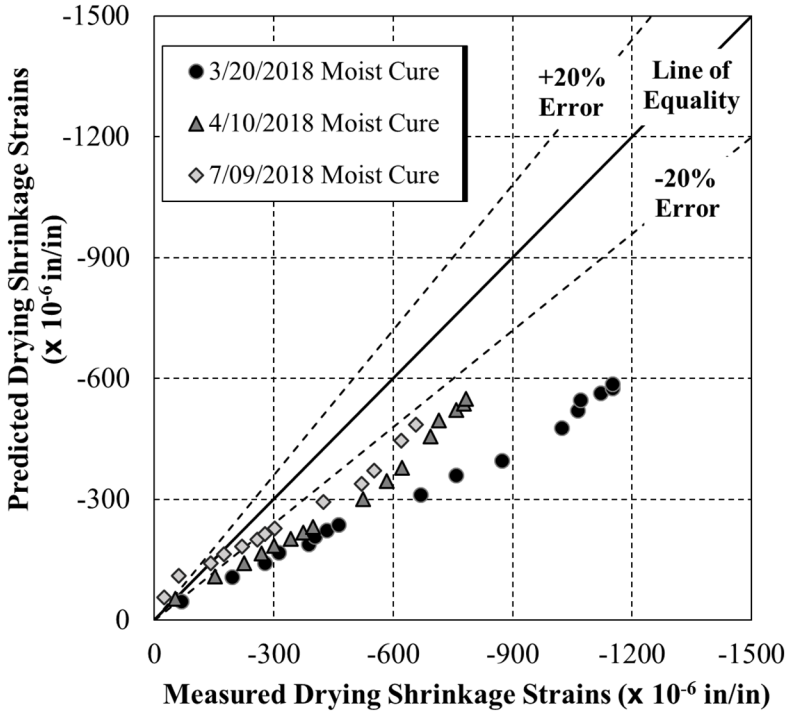

Figure 6-36: Measured versus predicted drying shrinkage strains for the moist-cured field rectangular prisms using the CEB MC 2010 model

Figure 6-37 shows the comparison of the predicted versus measured shrinkage strains of the cylindrical field specimens using the CEB MC 2010 method. As can be seen in Figure 6-37, the CEB MC 2010 predicted shrinkage values of the 04/10/2018-F and 07/09/2018-F cylindrical specimens were highly underestimated as compared to the measured values.

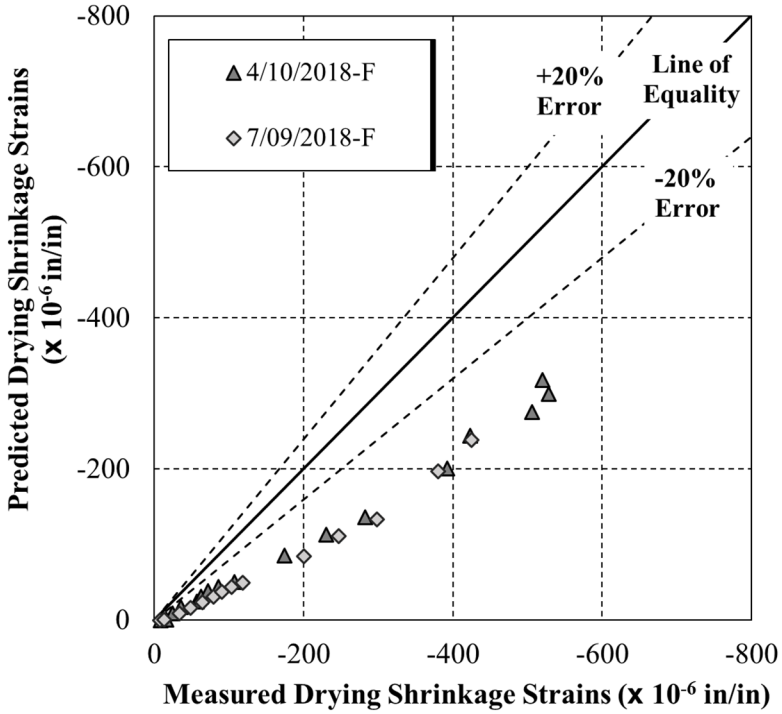

Figure 6-37: Measured versus predicted drying shrinkage strains for the cylindrical field specimens using the CEB MC 2010 model

6.4.4 Predicted Shrinkage Values for Laboratory Specimens

Figure 6-38 shows the comparison of the CEB MC 2010 predicted drying shrinkage strains to the measured drying shrinkage strains for the 05/03/2018-L-Q and 05/09/2018-L-L test specimens. As compared to predicted shrinkage values of ACI 209 and AASHTO 2017, CEB MC 2010 is much more accurate in the predicted shrinkage strains of both the laboratory mixtures. Also the CEB MC 2010 performed much better with the predicted shrinkage strains of the laboratory specimens as compared to the predicted shrinkage values of the field specimens.

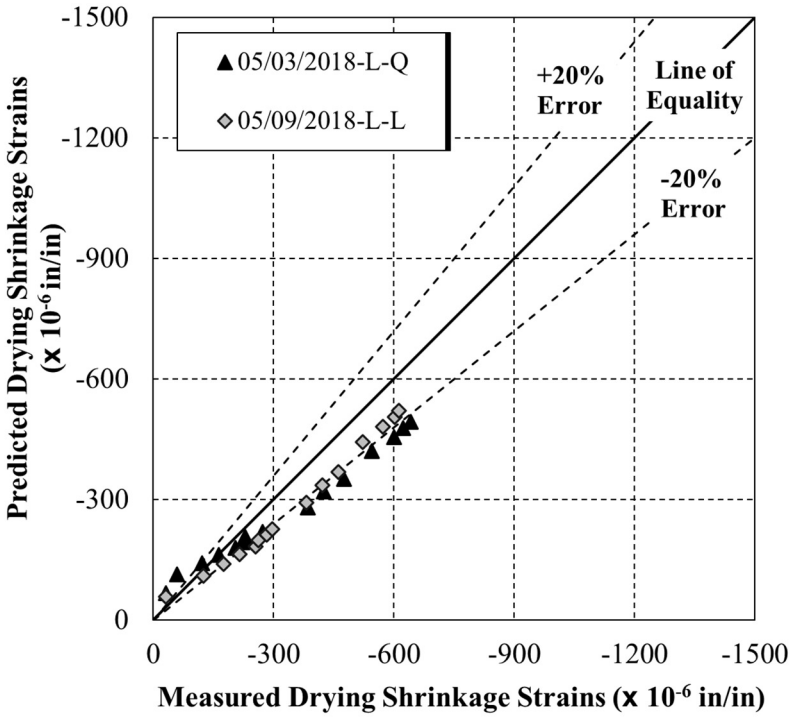

Figure 6-38: Measured versus predicted drying shrinkage strains for rectangular laboratory prisms using the CEB MC 2010 model

Figure 6-39 shows the predicted versus measured shrinkage values for the cylindrical laboratory specimens using the CEB MC 2010 method. Similar to the predicted shrinkage values of the cylindrical field specimens using CEB MC 2010, the predicted values of the cylindrical laboratory specimens were also underestimated when compared to the measured values from testing. As seen in Figure 6-39, the predicted shrinkage values of the laboratory mixture containing the limestone coarse aggregate were more accurate as compared to the laboratory mixture containing the quartzite coarse aggregate.

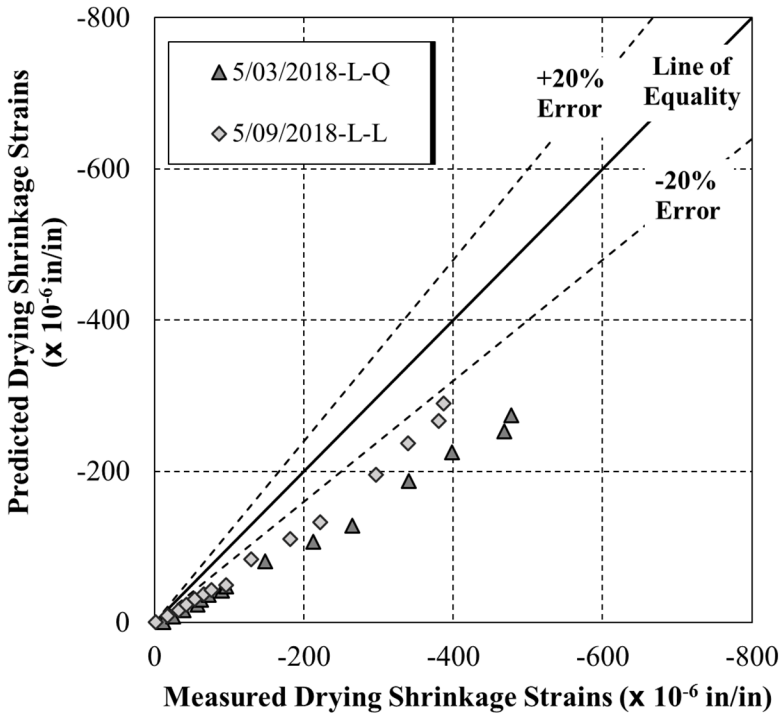

Figure 6-39: Measured versus predicted drying shrinkage strains for cylindrical laboratory specimens using the CEB MC 2010 model

6.5 CREEP AND SHRINKAGE PREDICTION WITH THE GL 2000 MODEL

Like both the AASHTO 2017 and CEB MC 2010 creep and shrinkage prediction models, no assumptions had to be made in order for the GL 2000 Model to be used with both the field and laboratory concrete mixtures. However, the equivalent age maturity for each loading age for both the field and laboratory specimens was calculated as previously described in Sections 5.3.1.2 and 5.3.2.2, respectively for use in all creep and compliance predictions. Besides this change, all procedures as outlined in Section 2.4.4 were followed. Tables 6-7 and 6-8 provide a summary of the inputs for both the creep and shrinkage prediction methods that were used for the GL 2000 Model.

Table 6-7: GL 2000 creep prediction model summary of inputs for field and laboratory mixtures

Field Mixtures		**Laboratory Mixtures**	
Input	***Justification***	***Input***	***Justification***
Relative humidity = 50 percent	ASTM C512 (2018)	Relative humidity = 50 percent	ASTM C512 (2018)
Volume-to-surface ratio = 1.5	Computed excluding cylinder ends not exposed to atmosphere	Volume-to-surface ratio = 1.5	Computed excluding cylinder ends not exposed to atmosphere
28-day measured compressive strength	Table 5-4	28-day measured compressive strength	Table 5-14
Predicted modulus of elasticity for each loading age	Table 5-12	Predicted modulus of elasticity for each loading age	Table 5-19
Concrete equivalent adjusted age at loading	Table 5-14	Concrete equivalent adjusted age at loading	Table 5-21
Concrete age at beginning of drying for cylinders = 1 day	Demolded immediately upon arrival at Auburn University and placed in creep room.	Concrete age at beginning of drying for cylinders = 1 day	Demolded immediately after curing and placed in creep room.

Table 6-8: GL 2000 shrinakge prediction model summary of inputs for field and laboratory mixtures

Field Mixtures		Laboratory Mixtures	
Input	***Justification***	***Input***	***Justification***
Relative humidity = 50 percent	AASHTO T 160 (2015)	Relative humidity = 50 percent	AASHTO T 160 (2015)
Volume-to-surface ratio = 1.5	Computed excluding cylinder ends not exposed to atmosphere	Volume-to-surface ratio = 1.5	Computed excluding cylinder ends not exposed to atmosphere
Volume-to-surface ratio for rectangular prisms = 0.66	Calculated based on all six sides being exposed to drying	Volume-to-surface ratio for rectangular prisms = 0.66	Calculated based on all six sides being exposed to drying
28-day measured compressive strength	04/10/2018-F and 07/09/2018-F: Table 5-4 03/20/2018-F: Table 5-6	28-day measured compressive strength	Table 5-15
Concrete age at beginning of drying for rectangular prisms: air-cured = 1 day, moist-cured = 7 days	Air-cured prisms demolded immediately upon arrival at Auburn University. Moist-cured demolded and placed in lime-bath for 7 days.	Concrete age at beginning of drying for rectangular prisms = 7 days	Specimens demolded and placed in lime-bath for 7 days.
Concrete age at beginning of drying for cylinders = 1 day	Demolded immediately upon arrival at Auburn University and placed in creep room.	Concrete age at beginning of drying for cylinders = 1 day	Demolded immediately after curing and placed in creep room.

6.5.1 Predicted Creep and Compliance Values for Field Specimens

Figures 6-40 and 6-41 show comparisons of the measured creep strain values to the estimated creep strain values for the 04/10/2018-F and 07/09/2018-F field specimens. Each of these graphs were created using the GL 2000 predicted creep strain values and include all the tested loading ages. As can be seen in Figure 6-40, the GL 2000 Model predicted creep strains were highly

accurate in the early ages after loading, but tended to underestimate the creep strains as concrete-age progressed for all loading ages for the 04/10/2018-F specimens.

As can be seen in Figure 6-41, the GL 2000 Model predicted creep strains for the 07/09/2018-F test specimens were overestimated for both the 7-day and 28-day loading ages, but tended to fall within the $\pm$ 20% threshold.

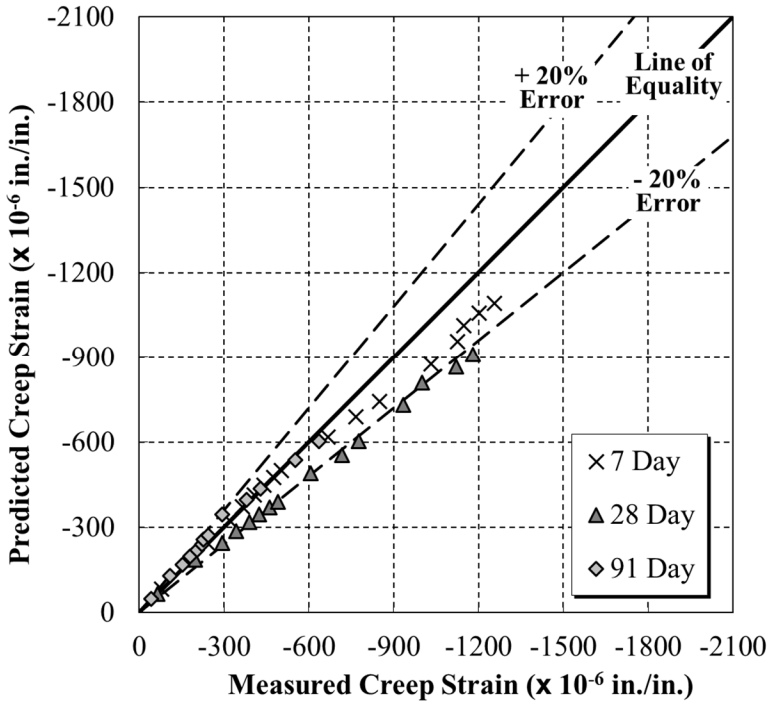

Figure 6-40: Measured versus predicted creep strains for the 04/10/2018-F field specimens using the GL 2000 Model

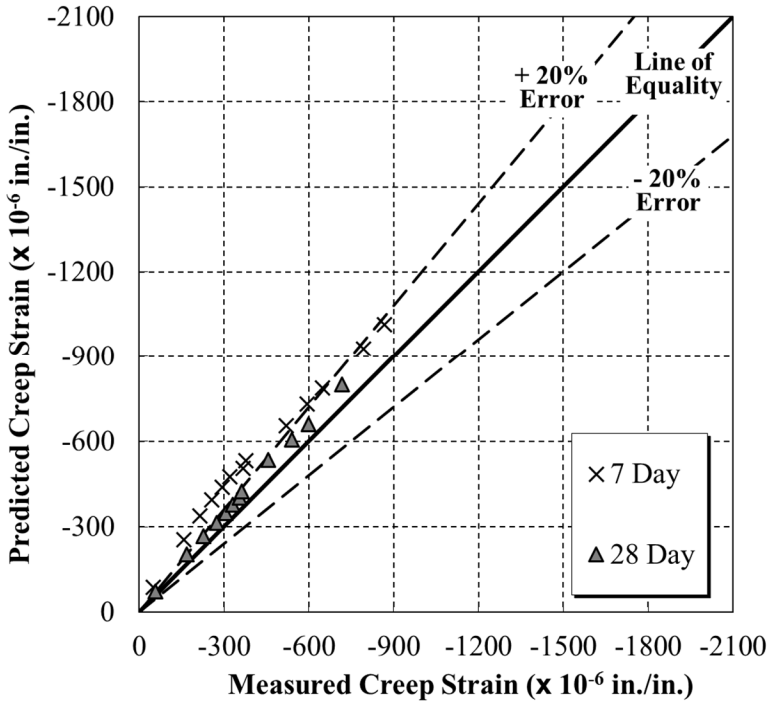

Figure 6-41: Measured versus predicted creep strains for the 07/09/2018-F field specimens using the GL 2000 Model

Figures 6-42 and 6-43 show the GL 2000 Model's predicted compliance values versus the measured compliance values for the 04/10/2018-F and 07/09/2018-F test specimens, respectively. As can be seen in Figures 6-42 and 6-43, the GL 2000 Model predicted the compliance values for the 07/09/2018-F test specimens with much better accuracy as compared to the 04/10/2018-F samples. The predicted values for all loading ages of the 04/10/2018-F test samples were all underestimated, especially the loading age of 28 days, which fell beyond the $\pm$ 20% target range. However, the predicted values of the 07/09/2018-F test samples for each of the loading ages stayed within the $\pm$ 20% target range. As shown in Figure 6-43, the predicted compliance values for the 7-day loading age for the 07/09/2018-F test samples were very similar to the values that were measured during testing.

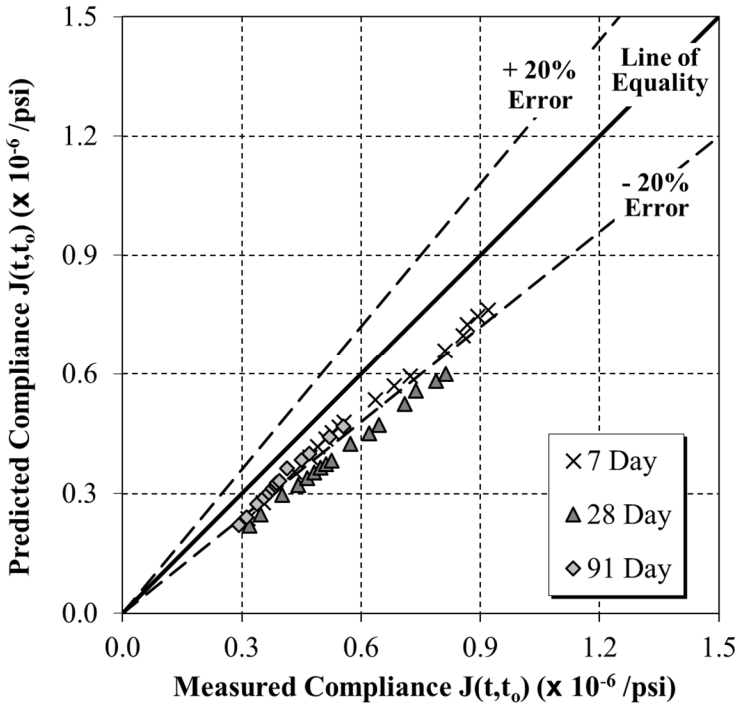

Figure 6-42: Measured versus predicted compliance values for the 04/10/2018-F field specimens using the GL 2000 Model

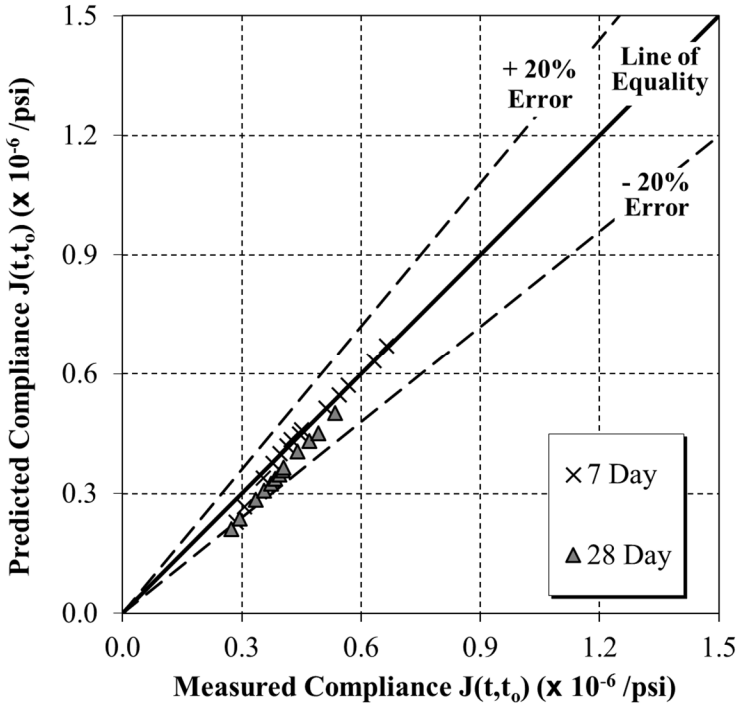

Figure 6-43: Measured versus predicted compliance values for the 07/09/2018-F specimens using the GL 2000 Model

6.5.2 Predicted Creep and Compliance Values for Laboratory Specimens

Figures 6-44 and 6-45 below show the comparisons of the predicted creep strains to the measured creep strains from using the GL 2000 Model for the 05/03/2018-L-Q and 05/09/2018-L-L laboratory test specimens. According to Figures 6-44 and 6-45, the predicted creep strains for the concrete mixture containing the limestone coarse aggregate are slightly more accurate as compared to the mixture containing the quartzite coarse aggregate, but all predicted creep strains are overestimated for both sets of specimens. However, for both sets of laboratory mixtures the 7-day loading age is overestimated much more as compared to the 28- and 91-day loading age.

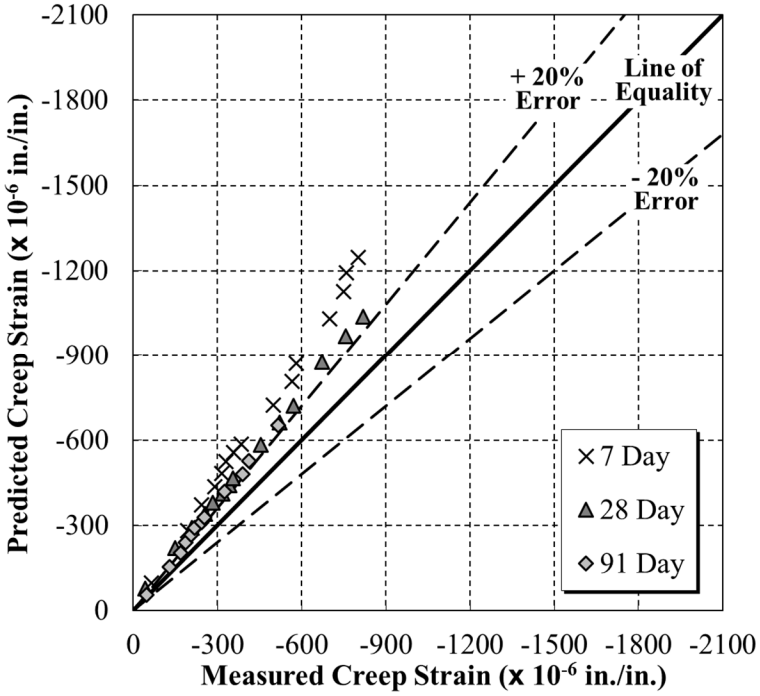

Figure 6-44: Measured versus predicted creep strains for the 05/03/2018-L-Q laboratory specimens using the GL 2000 Model

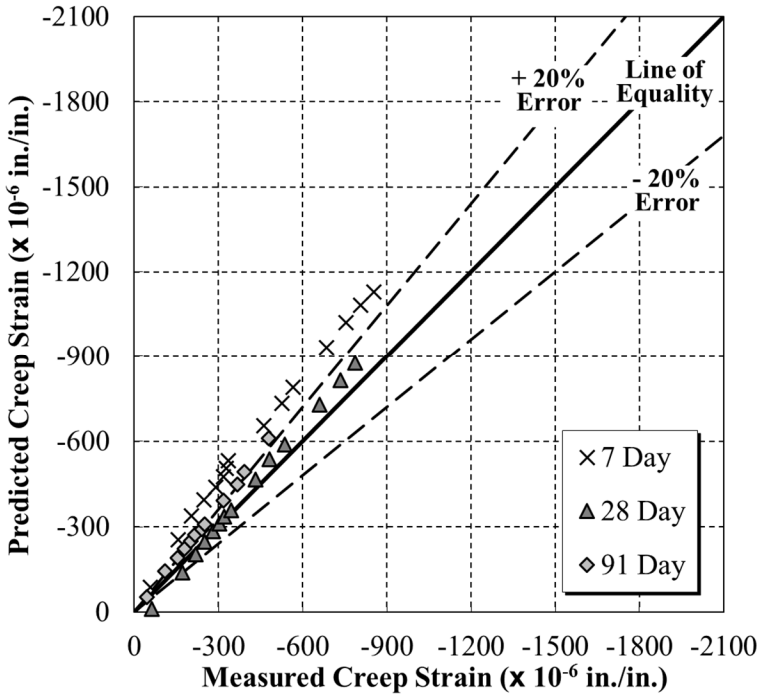

Figure 6-45: Measured versus predicted creep strains for the 05/09/2018-L-L laboratory specimens using the GL 2000 Model

Figures 6-46 and 6-47 show the GL 2000 Model's predicted compliance values versus the measured compliance values for the 05/03/2018-L-Q and 05/09/2018-L-L laboratory test specimens, respectively. The predicted compliance values for all loading ages for both laboratory mixtures were highly accurate throughout the duration of testing, but as time progresses the predicted values of the 7-day loading age for both laboratory mixtures tended to become overestimated as compared to the loading ages of 28 days and 91 days. As seen in Figures 6-46 and 6-47, both the 05/03/2018-L-Q and 05/09/2018-L-L test specimens tend to stay within the $\pm$ 20% target range.

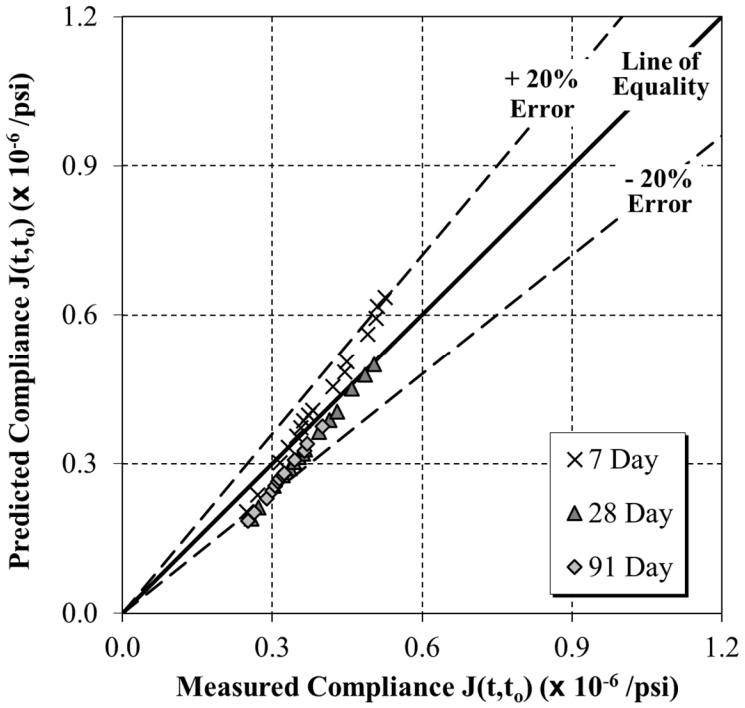

Figure 6-46: Measured versus predicted compliance values for the 05/03/2018-L-Q laboratory specimens using the GL 2000 Model

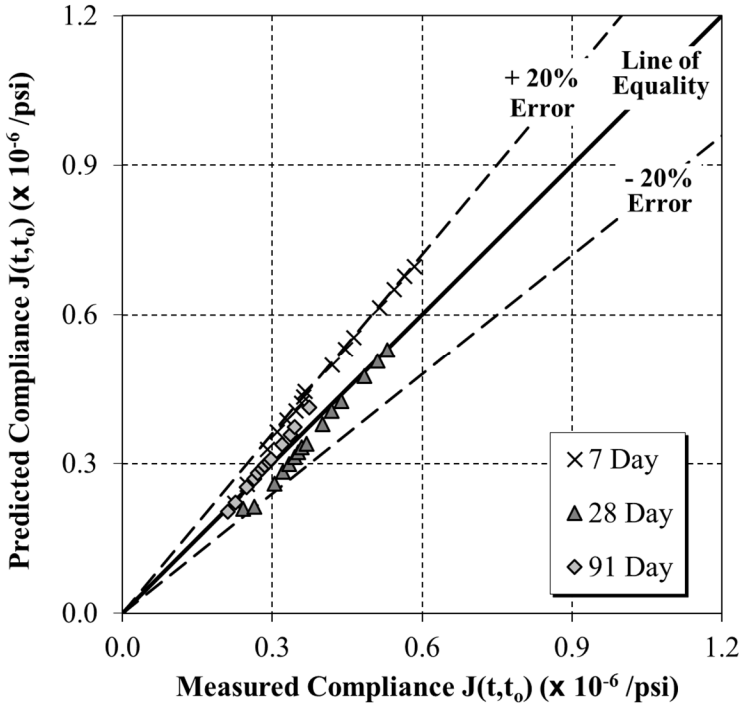

Figure 6-47: Measured versus predicted compliance values for the 05/09/2018-L-L laboratory specimens using the GL 2000 Model

6.5.3 Predicted Shrinkage Values for Field Specimens

Figures 6-48 and 6-49 below show the comparisons of the predicted drying shrinkage strains to the measured drying shrinkage strains as predicted by the GL 2000 Model. Figure 6-48 contains the drying shrinkage results for 03/20/2018-F-Air, 04/10/2018-F-Air, and 07/09/2018-F-Air rectangular prisms that were only subjected to air curing, while Figure 6-49 contains the drying shrinkage results 03/20/2018-F-Moist, 04/10/2018-F-Moist, and 07/09/2018-F-Moist rectangular prisms that were exposed to a lime bath for a duration of 7 days.

In the early stages of drying, the GL 2000 Model provides accurate predictions of drying shrinkage strains, but as drying progresses the model tends to underestimate the measured drying shrinkage values for both the air- and moist-cure specimens. However, both the 04/10/2018-F and 07/09/2018-F air- and moist-cure specimens were extremely close to the lower bound threshold value of −20%.

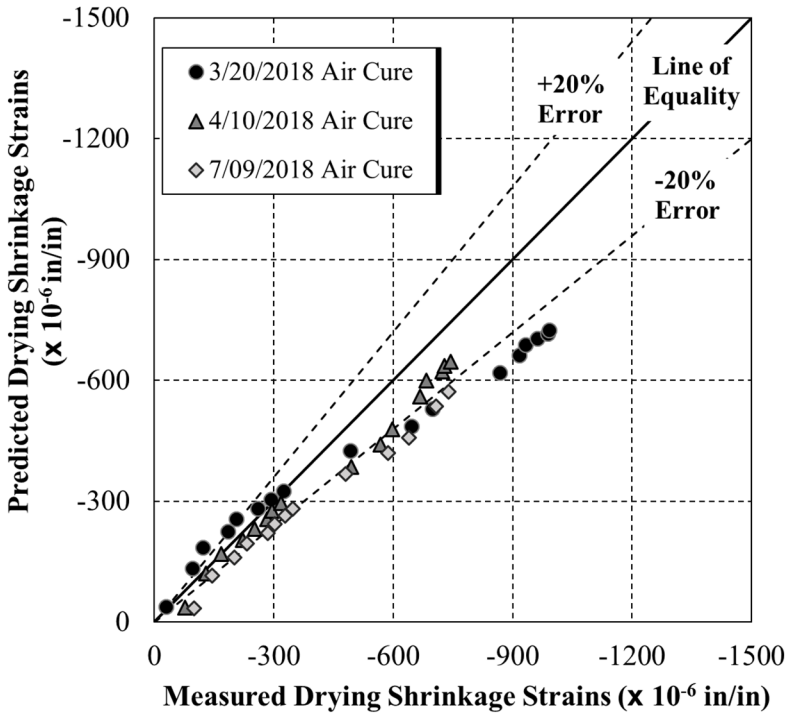

Figure 6-48: Measured versus predicted drying shrinkage strains for the air-cured field rectangular prisms using the GL 2000 Model

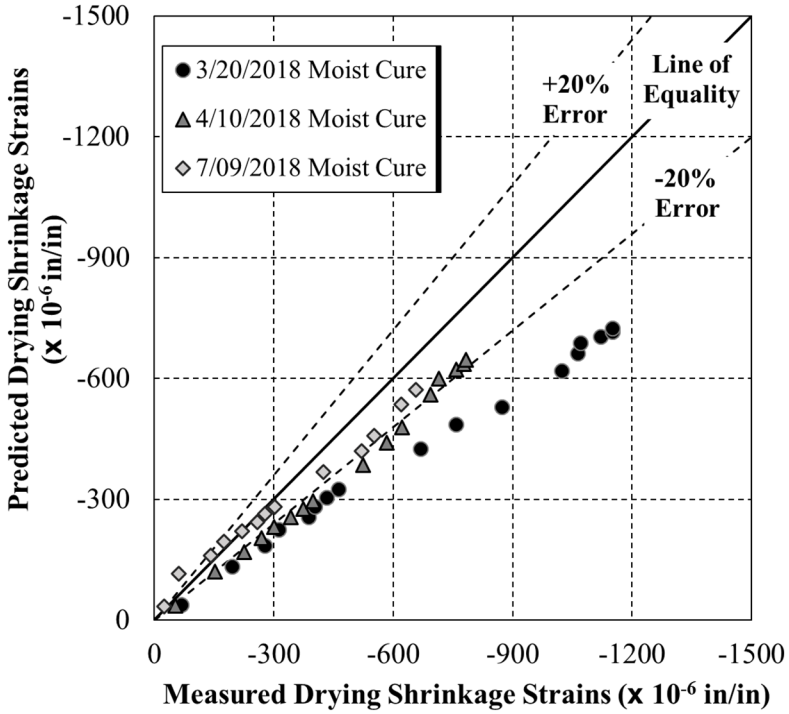

Figure 6-49: Measured versus predicted drying shrinkage strains for the moist-cured field rectangular prisms using the GL 2000 Model

Figure 6-50 shows the predicted versus measured shrinkage values for the cylindrical field specimens using the GL 2000 Model. As compared to the previous methods that have been discussed thus far, the predicted shrinkage using the GL 2000 Model for both the 04/10/2018-F and 07/09/2018-F cylindrical shrinkage specimens are highly accurate with only the AASHTO 2017 predicted shrinkage values being more accurate. The predicted values are more accurate in the early-ages of drying as compared to later-ages for both sets of field specimens.

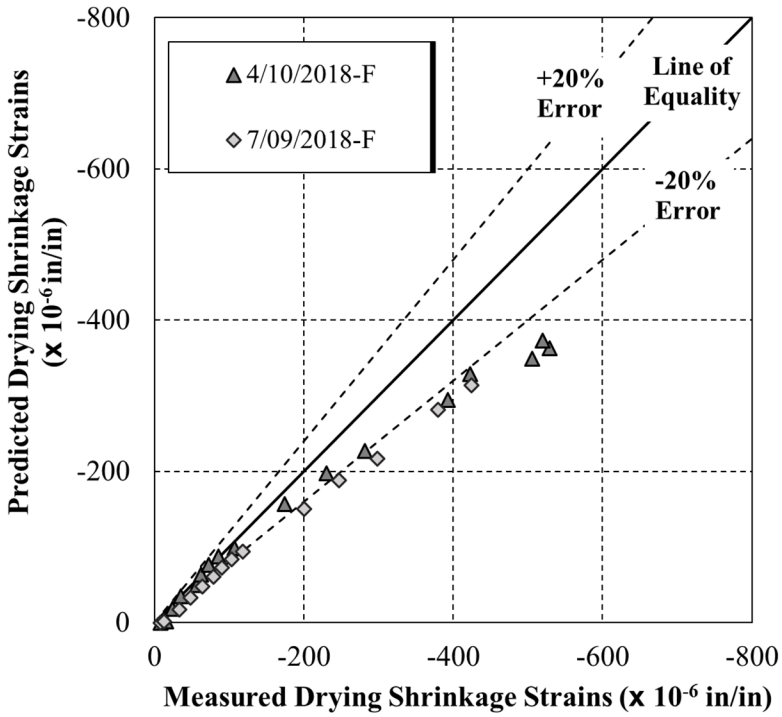

Figure 6-50: Measured versus predicted drying shrinkage strains for cylindrical field specimens using the GL 2000 Model

6.5.4 Predicted Shrinkage Values for Laboratory Specimens

Figure 6-51 shows the comparison of the GL 2000 predicted drying shrinkage strains to the measured drying shrinkage strains for the 05/03/2018-L-Q and 05/09/2018-L-L laboratory mixtures. Much like CEB MC 2010, GL 2000 predicted the drying shrinkage strains for both the quartzite and limestone coarse aggregate mixtures with good accuracy. Figure 6-51indicates that the predicted drying shrinkage strains for the mixture containing quartzite was slightly underestimated as compared to the mixture containing limestone, but both were generally still within the $\pm$ 20% target range.

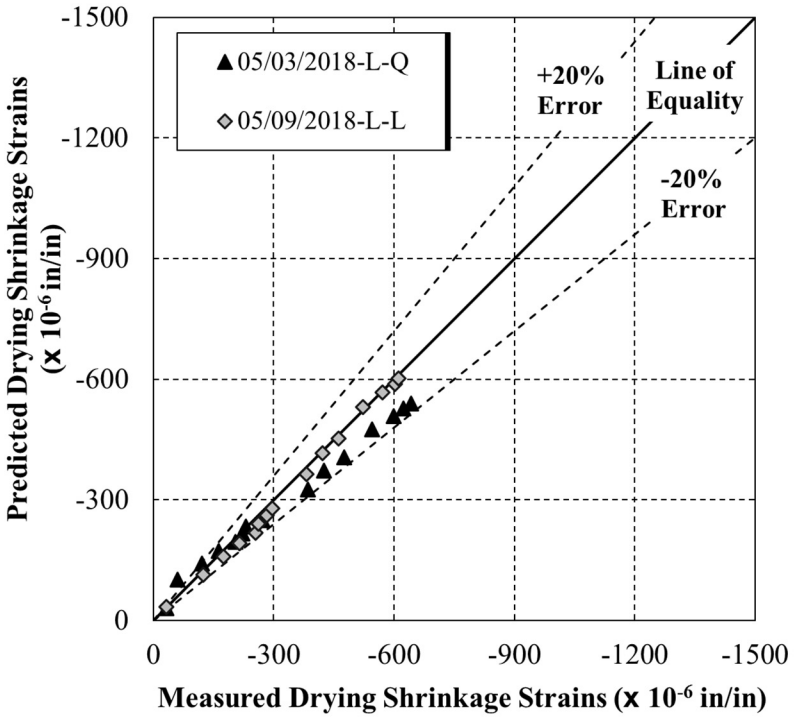

Figure 6-51: Measured versus predicted drying shrinkage strains for rectangular laboratory prisms using the GL 2000 Model

Figure 6-52 shows the predicted versus measured shrinkage values for the cylindrical laboratory specimens using the GL 2000 method. As shown in Figure 6-52, the predicted shrinkage values of the mixture containing the limestone coarse aggregate are much more accurate as compared to the mixture containing the quartzite coarse aggregate. However, the overall predicted shrinkage values of the cylindrical laboratory test specimens using the GL 2000 Model were much more accurate as compared to the predicted values when using other methods.

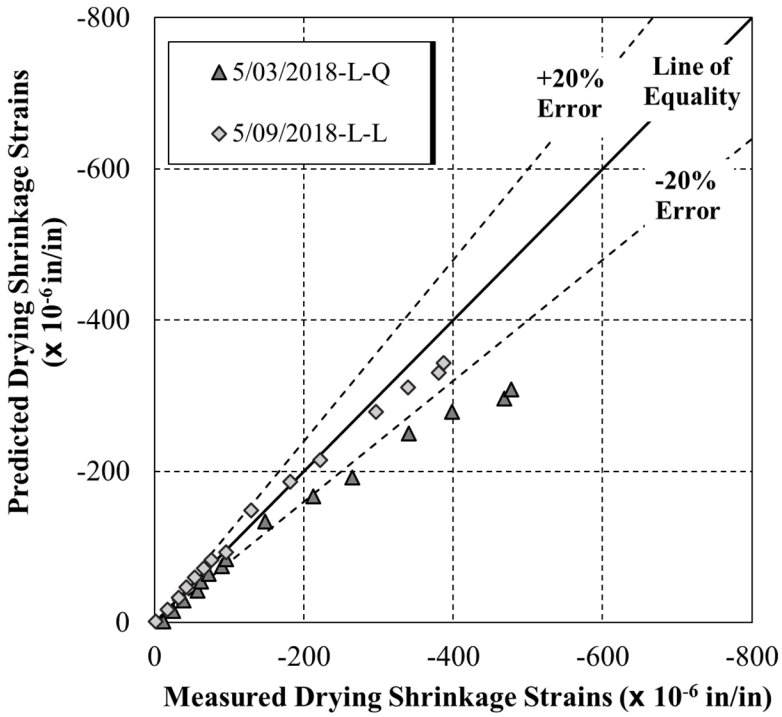

Figure 6-52: Measured versus predicted drying shrinkage strains for cylindrical laboratory specimens using the GL 2000 Model

6.6 CREEP AND SHRINKAGE PREDICTION METHOD WITH THE B3 MODEL

Similar to ACI 209, the B3 Model required one assumption to be made in relation to the cement content. For this research study, the cement content was taken as the total cementitious material content (cement plus SCM's). Besides this one assumption, the outlined procedures from Section 2.4.5 were followed. As provided for the previous methods, a summary of the inputs for the creep and shrinkage parameters are provided in Tables 6-9 and 6-10. The results for all field and laboratory test data are covered in the following sections.

Table 6-9: B3 Model creep prediction model summary of inputs for field and laboratory mixtures

Field Mixtures		**Laboratory Mixtures**	
Input	***Justification***	***Input***	***Justification***
Relative humidity = 50 percent	ASTM C512 (2018)	Relative humidity = 50 percent	ASTM C512 (2018)
Volume-to-surface ratio = 1.5	Computed excluding cylinder ends not exposed to atmosphere	Volume-to-surface ratio = 1.5	Computed excluding cylinder ends not exposed to atmosphere
28-day measured compressive strength	Table 5-4	28-day measured compressive strength	Table 5-15
28-day predicted modulus of elasticity	Table 5-13	28-day predicted modulus of elasticity	Table 5-20
Concrete equivalent adjusted age at loading	Table 5-14	Concrete equivalent adjusted age at loading	Table 5-21
Cement Factor	Assumed total cementitious material content	Cement Factor	Assumed total cementitious material content
Concrete age at beginning of drying for cylinders = 1 day	Demolded immediately upon arrival at Auburn University and placed in creep room.	Concrete age at beginning of drying for cylinders = 1 day	Demolded immediately after curing and placed in creep room.

Table 6-10: B3 Model shrinkage prediction model summary of inputs for field and laboratory mixtures

Field Mixtures		**Laboratory Mixtures**	
Input	***Justification***	***Input***	***Justification***
Relative humidity = 50 percent	AASHTO T 160 (2015)	Relative humidity = 50 percent	AASHTO T 160 (2015)
Volume-to-surface ratio = 1.5	Computed excluding cylinder ends not exposed to atmosphere	Volume-to-surface ratio = 1.5	Computed excluding cylinder ends not exposed to atmosphere
Volume-to-surface ratio for rectangular prisms = 0.66	Calculated based on all six sides being exposed to drying	Volume-to-surface ratio for rectangular prisms = 0.66	Calculated based on all six sides being exposed to drying
28-day measured compressive strength	04/10/2018-F and 07/09/2018-F: Table 5-4 03/20/2018-F: Table 5-6	28-day measured compressive strength	Table 5-15
28-day measured modulus of elasticity	04/10/2018-F and 07/09/2018-F: Table 5-4 03/20/2018-F: Table 5-6	28-day measured modulus of elasticity	Table 5-15
Concrete age at beginning of drying for rectangular prisms: air-cured = 1 day, moist-cured = 7 days	Air-cured prisms demolded immediately upon arrival at Auburn University. Moist-cured demolded and placed in lime-bath for 7 days.	Concrete age at beginning of drying for rectangular prisms = 7 days	Specimens demolded and placed in lime-bath for 7 days.
Concrete age at beginning of drying for cylinders = 1 day	Demolded immediately upon arrival at Auburn University and placed in creep room.	Concrete age at beginning of drying for cylinders = 1 day	Demolded immediately after curing and placed in creep room.

6.6.1 Predicted Creep and Compliance Values for Field Specimens

Figures 6-53 and 6-54 show comparisons of the measured creep strain values versus the estimated creep strain values for the 04/10/2018-F and 07/09/2018-F field specimens. Each of these graphs were created using the B3 Model predicted creep strain values and include all loading ages that underwent testing. As can be seen in Figures 6-53 and 6-54, the B3 Model was more accurate in predicting the creep strains for the 04/10/2018-F specimens as compared to the predicted values of the 07/09/2018-F samples. For the 04/10/2018-F test specimens, the B3 Model overestimated the predicted creep strains in the early stages of loading for all loading ages, but the predicted values did improve in accuracy in the later stages of loading except for the loading age of 91 days, which was overestimated over the entire duration of testing.

Unlike the 04/10/2018-F specimens where some of the predicted values were relatively close to the measured data, the 07/09/2018-F test specimens were overestimated for all loading ages that were considered. However, the predicted creep strains of the 28-day loading age were much closer to the $\pm$ 20% error range as compared to the predicted creep values of the 7-day loading age for the 07/09/2018-F test specimens, but were still over the desired threshold.

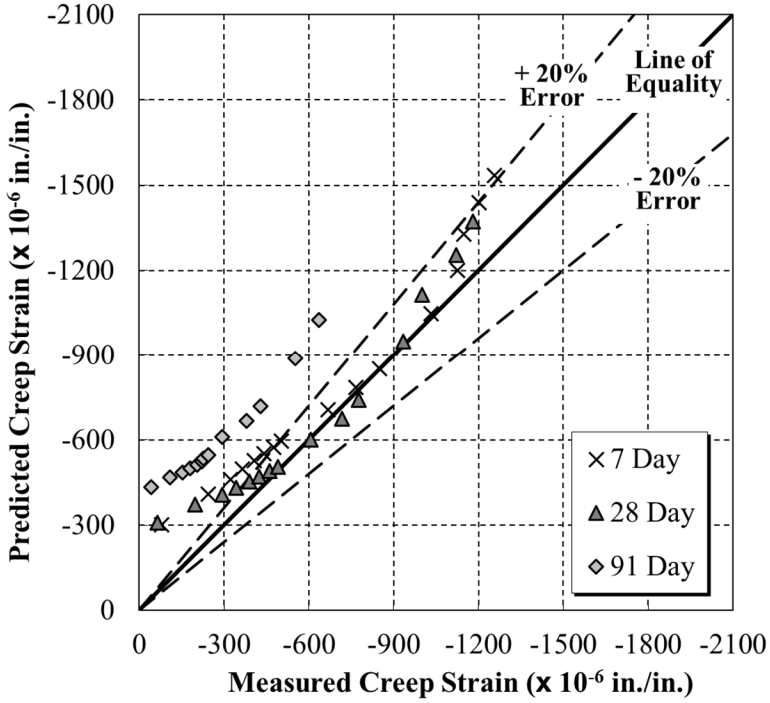

Figure 6-53: Measured versus predicted creep strains for the 04/10/2018-F field specimens using the B3 Model

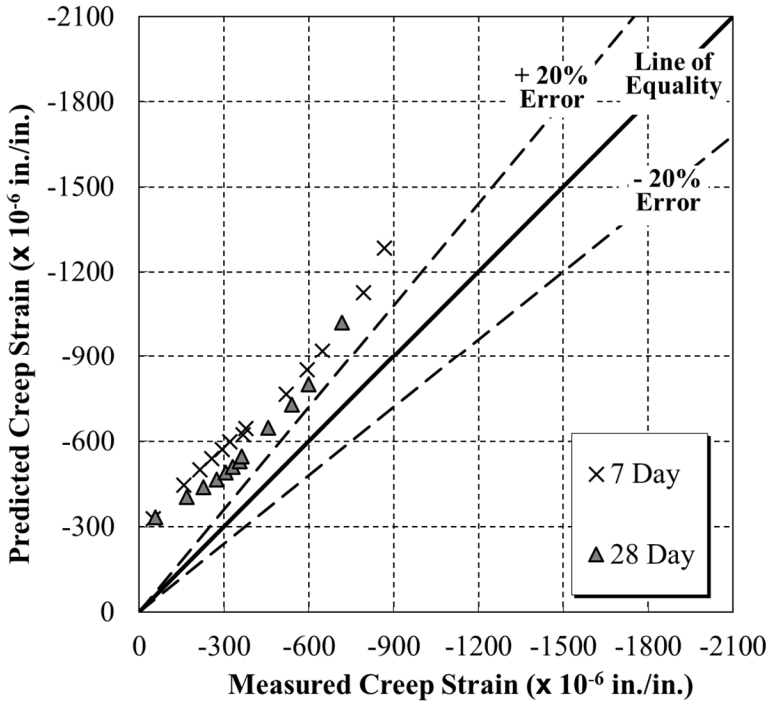

Figure 6-54: Measured versus predicted creep strains for the 07/09/2018-F field specimens using the B3 Model

Figures 6-55 and 6-56 show the B3 Model predicted compliance values versus the measured compliance values for the 04/10/2018-F and 07/09/2018-F test specimens, respectively. Unlike the predicted creep strains for each set of field specimens, the predicted compliance values for both the 04/10/2018-F and 07/09/2018-F samples were much more accurate when compared to the measured data.

As seen in Figure 6-55, the majority of the predicted compliance data for all loading ages for the 04/10/2018-F field samples fall within the $\pm$ 20% error range. In the early stages of testing, B3 tended to slightly overestimate the predicted compliance values for the 7- and 91-day loading ages, but then the data started to trend more to the measured values. However, the loading age of 28 days tended to be underestimated in the early ages of testing, but also started to converge towards the measured value as time progressed.

Figure 6-56 shows that the B3 Model overestimates the compliance values for all loading ages for the 07/09/2018-F field specimens. In fact, the loading age of 7 days is actually slightly above the + 20% threshold for the majority of testing whereas the loading age of 28 days is within the specified error range.

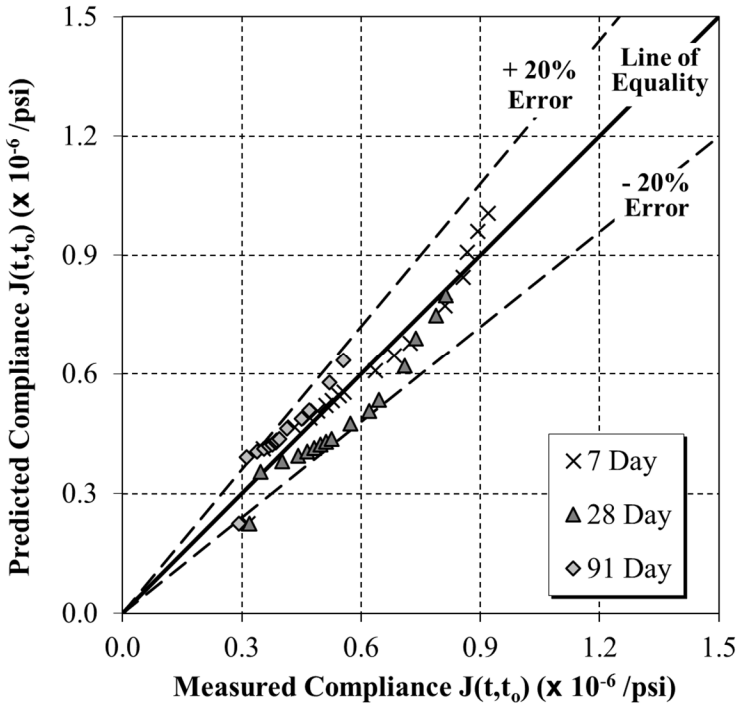

Figure 6-55: Measured versus predicted compliance values for the 04/10/2018-F field specimens using the B3 Model

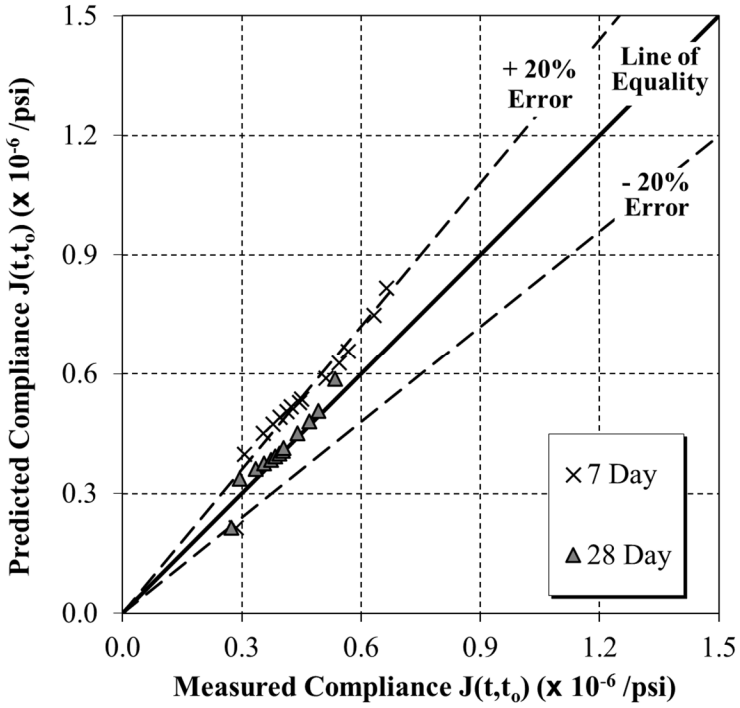

Figure 6-56: Measured versus predicted compliance values for the 07/09/2018-F field specimens using the B3 Model

6.6.2 Predicted Creep and Compliance Values for Laboratory Specimens

Figures 6-57 and 6-58 show the comparisons of the predicted creep strains versus the measured creep strains by using the B3 Model for the 05/03/2018-L-Q and 05/09/2018-L-L laboratory test specimens, respectively. As can be seen in Figures 6-57 and 6-58, the B3 Model does not accurately predict the creep strains for either the 05/03/2018-L-Q or the 05/09/2018-L-L laboratory samples.

For both the 05/03/2018-L-Q and 05/09/2018-L-L specimens, the B3 Model overestimates the predicted creep strains for all loading ages, and as time progressed, the predicted values become less accurate. For all loading ages for both the quartzite and limestone mixtures, the predicted values are above the desired threshold of +20%.

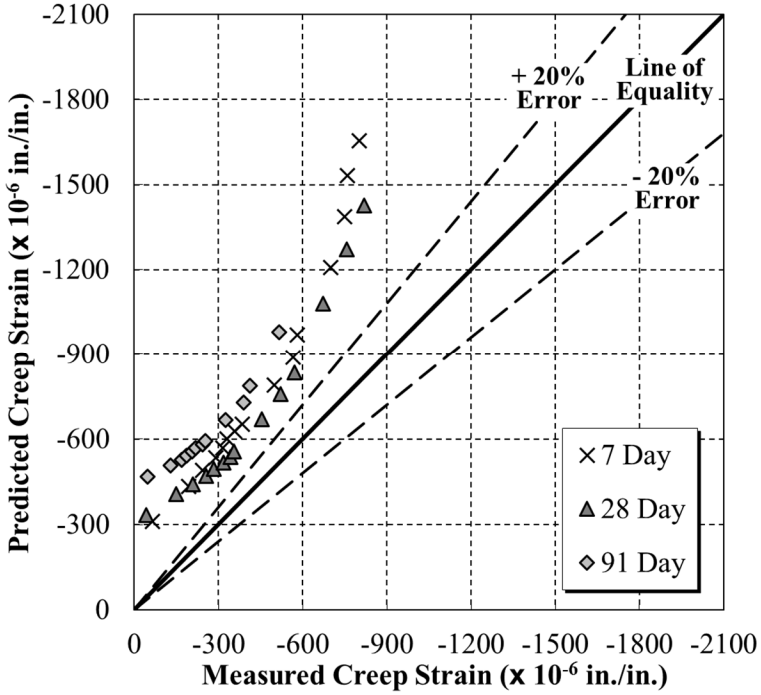

Figure 6-57: Measured versus predicted creep strains for the 05/03/2018-L-Q laboratory specimens using the B3 Model

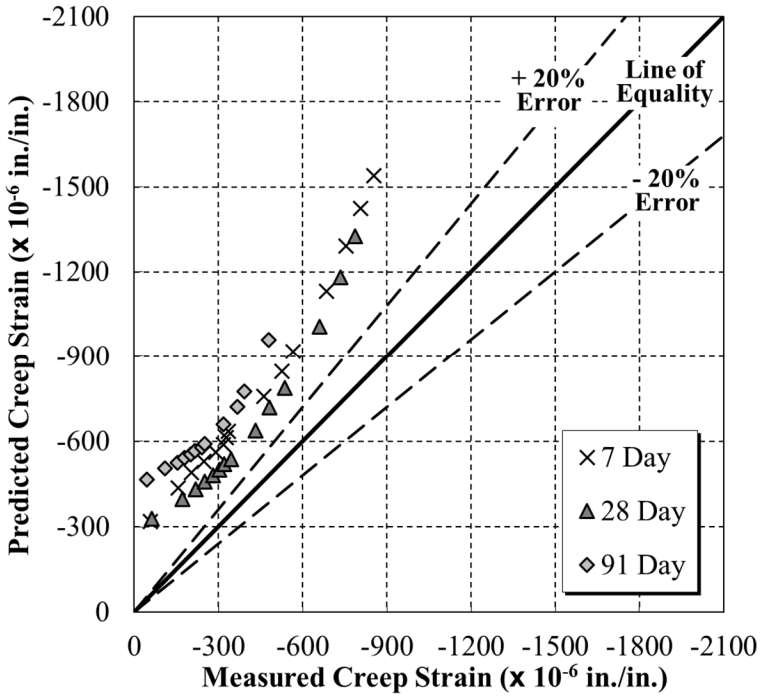

Figure 6-58: Measured versus predicted creep strains for the 05/09/2018-L-L laboratory specimens using the B3 Model

Figures 6-59 and 6-60 show the B3 Model's predicted compliance values versus the measured compliance values for the 05/03/2018-L-Q and 05/09/2018-L-L laboratory test specimens, respectively. As can be seen in Figure 6-59, the B3 Model's predicted compliance values for the 05/03/2018-L-Q specimens were accurate for the 28- and 91-day loading ages in the early ages after loading, but as time progressed, the predicted values tend to become less accurate for each of these loading ages. Also, the predicted compliance values for the 7-day loading age for the 05/03/2018-L-Q specimens were close to the upper bound of the $\pm$ 20% threshold, but fell outside of this threshold as time progressed. Figure 6-60 shows that the B3 Model's predicted compliance values for the 05/09/2018-L-L specimens were less accurate as compared to the 05/03/2018-L-Q specimens for all loading ages. Each of the loading ages for the 05/09/2018-L-L specimens were highly overestimated with the exception of 28-day loading age which falls close to the upper bound of the $\pm$ 20% threshold, but still became less accurate as the time of loading increased.

As previously stated, as compared to the other models that were considered during this study, the B3 Model was one of the more accurate methods in predicting compliance values for

all loading ages for the 05/03/2018-L-Q specimens, but performed the worse in predicting the compliance values for all loading ages for the 05/09/2018-L-L test specimens.

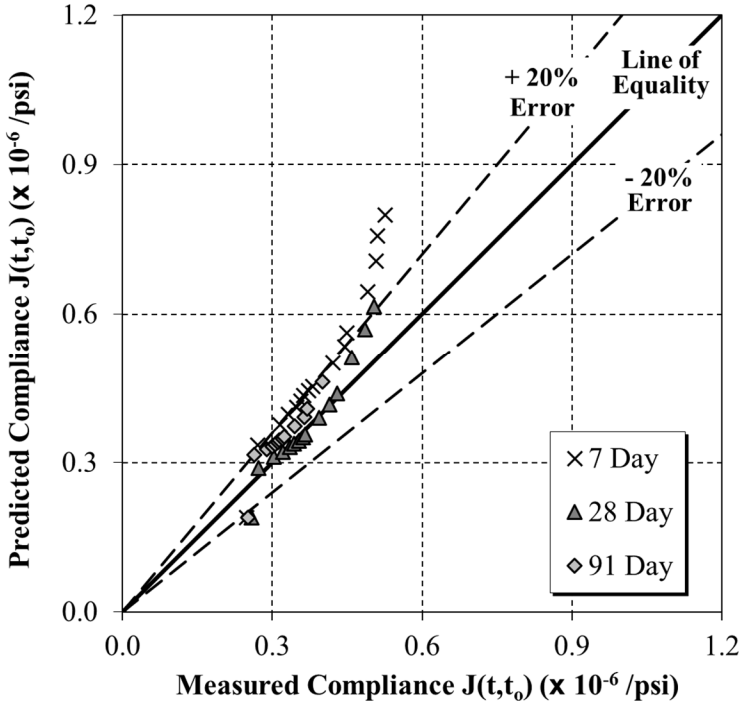

Figure 6-59: Measured versus predicted compliance values for the 05/03/2018-L-Q laboratory specimens using the B3 Model

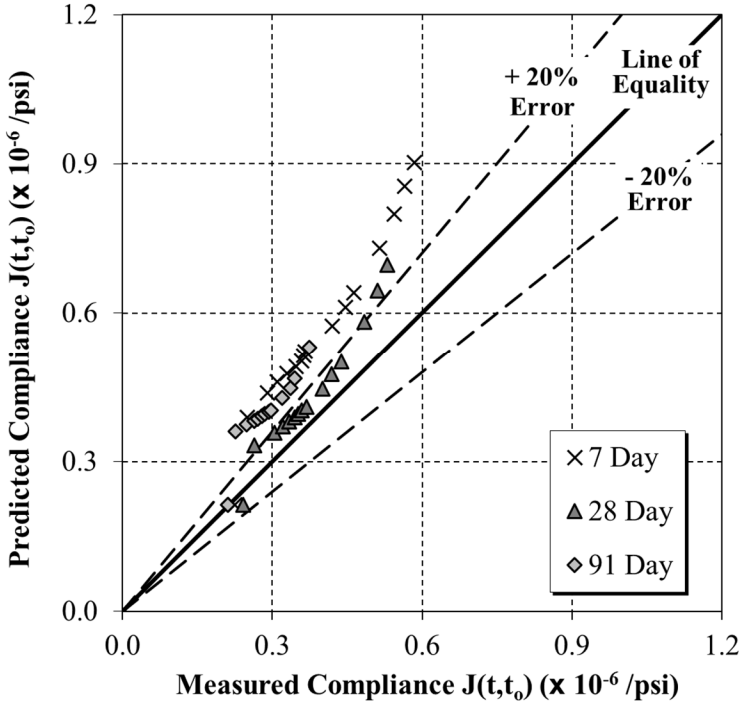

Figure 6-60: Measured versus predicted compliance values for the 05/09/2018-L-L laboratory specimens using the B3 Model

6.6.3 Predicted Shrinkage Values for Field Specimens

Figures 6-61 and 6-62 show the comparisons of the predicted drying shrinkage strains versus the measured drying shrinkage strains as predicted with the B3 Model. Figure 6-61 contains the drying shrinkage results for the 03/20/2018-F-Air, 04/10/2018-F-Air, and 07/09/2018-F-Air rectangular prisms that were only subjected to air curing, while Figure 6-62 contains the drying shrinkage results for the 03/20/2018-F-Moist, 04/10/2018-F-Moist, and 07/09/2018-F-Moist rectangular prisms that were exposed to a lime bath for a duration of 7 days.

As can be seen in Figure 6-61, the B3 Model tends to underestimate the predicted drying shrinkage values for most of the air cure specimens, except for the 04/10/2018-F-Air rectangular prisms that were fairly accurately predicted throughout the duration of testing. As for the 07/09/2018-F-Air rectangular prisms, the B3 Model did not accurately predict the drying shrinkage strains at any time during testing. In fact, the predicted creep strains for the 07/09/2018-F-Air specimens never fell within the desired $\pm$ 20% error range.

Figure 6-62 shows that the B3 Model's predicted shrinkage values for the moist-cured rectangular prisms were more accurate in the early ages of drying as compared to the predicted

shrinkage values at later ages. For the duration of testing, it can be seen that the majority of the predicted drying shrinkage strains for both the 03/20/2018-F-Moist and 04/10/2018-F-Moist rectangular prisms fell within the ± 20% error range. However, the predicted drying shrinkage strains for the 04/10/2018-F-Moist specimens did become overestimated as drying progressed. The B3 Model's predicted shrinkage strains for the 07/09/2018-F-Moist rectangular prisms performed better than the air-cured specimens, but the predicted drying shrinkage strains still fell outside the desired target range.

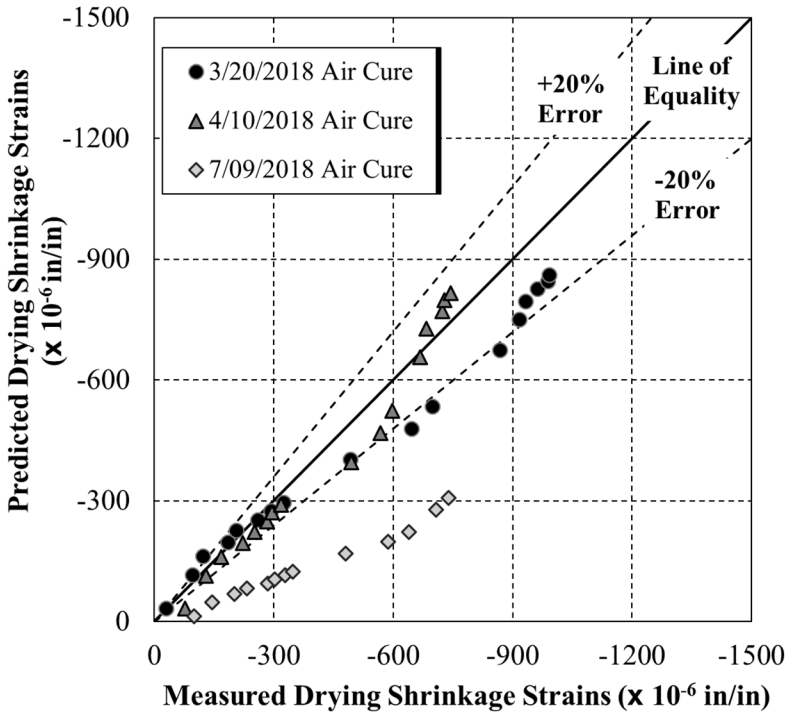

Figure 6-61: Measured versus predicted drying shrinkage strains for the air-cured field rectangular prisms using the B3 Model

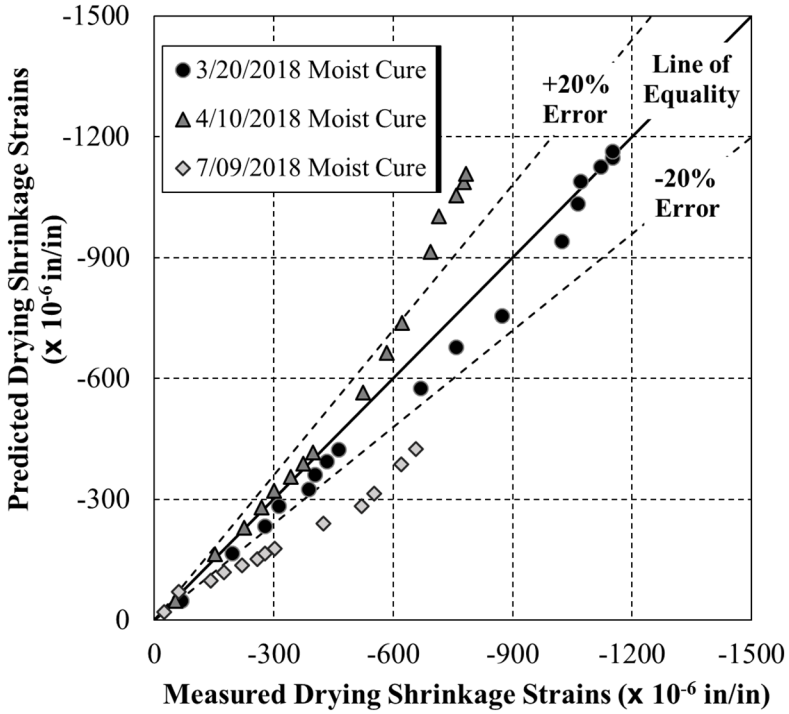

Figure 6-62: Measured versus predicted drying shrinkage strains for the moist-cured field rectangular prisms using the B3 Model

Figure 6-63 represents the predicted versus measured shrinkage values for the cylindrical field specimens using the B3 Model. As shown in Figure 6-63 below, the B3 Model's predicted shrinkage values for both the 04/10/2018-F and 07/09/2018-F cylindrical specimens were more accurate in the early ages of drying as compared to the predicted values of the later ages. It can be seen from Figure 6-63 that in the early ages of drying, the predicted values for both sets of cylindrical field specimens fall within the $\pm$ 20% target range, but as time increases, the predicted shrinkage values tend to fall below this threshold.

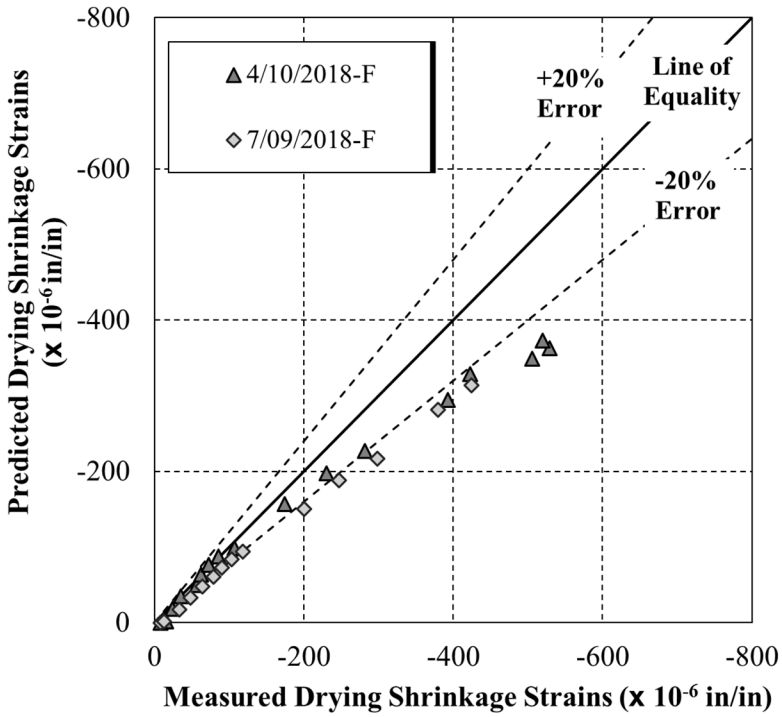

Figure 6-63: Measured versus predicted drying shrinkage strains for cylindrical field specimens using the B3 Model

6.6.4 Predicted Shrinkage Values for Laboratory Specimens

Figure 6-64 below shows the comparison of the B3 Model's predicted drying shrinkage strains versus the measured drying shrinkage strains for the 05/03/2018-L-Q and 05/09/2018-L-L laboratory mixtures. As shown in Figure 6-64, the predicted drying shrinkage strains for both the quartzite and limestone coarse aggregate mixtures were below for the $\pm$ 20% desired threshold duration of testing.

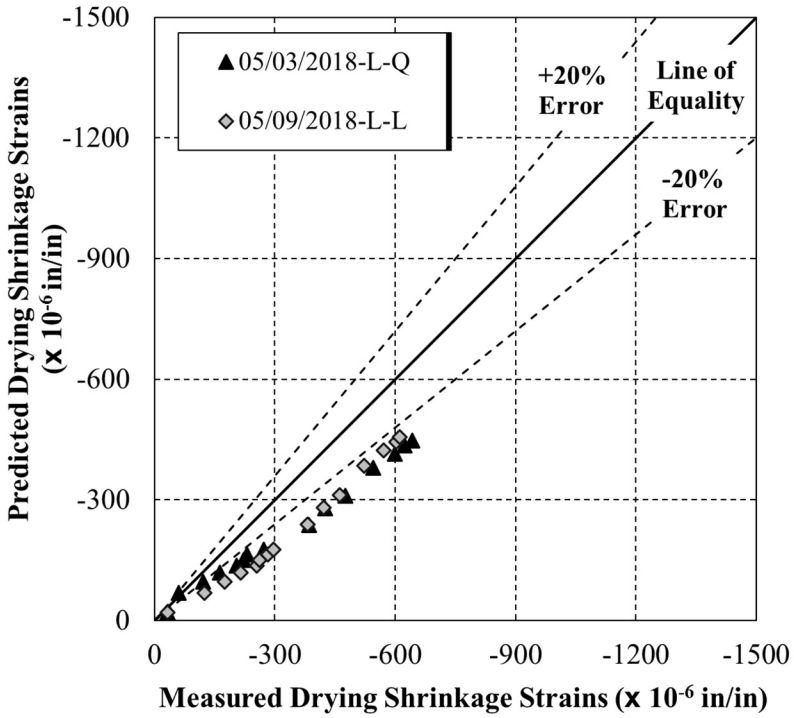

Figure 6-64: Measured versus predicted drying shrinkage strains for rectangular laboratory prisms using the B3 Model

Figure 6-65 shows the predicted versus measured shrinkage values for the laboratory cylindrical specimens using the B3 Model. As seen in Figure 6-65, the B3 Model performed poorly in predicting the shrinkage values for both the 05/03/2018-L-Q and 05/09/2018-L-L cylindrical test specimens, because the predicted shrinkage values for both laboratory mixtures fell well beyond the $\pm$ 20% threshold.

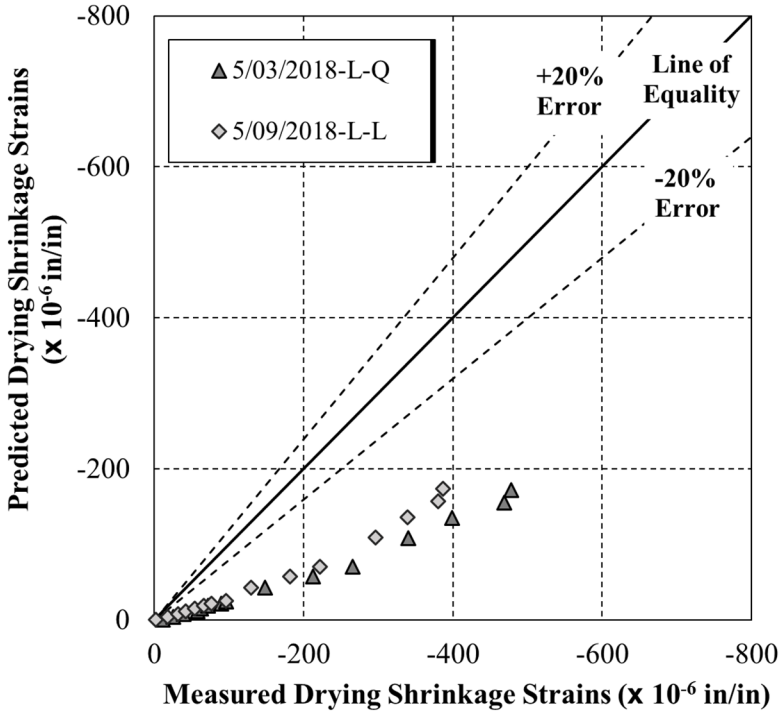

Figure 6-65: Measured versus predicted drying shrinkage strains for cylindrical laboratory specimens using the B3 Model

6.7 STATISTICAL ANALYSIS FOR CREEP AND SHRINKAGE PREDICTION MEHTODS

Once all creep and shrinkage data had been collected and the prediction analysis had been performed for each method, the measured values were then compared to the estimated values to determine which method produced the best overall results. In this study, the accuracy of each method was determined by calculating the percent error and the unbiased estimate of the standard deviation of the error, S_j, as defined by McCuen (1985).

6.7.1 Statistical Comparison Techniques

In this research study, the percent error was determined to be the most beneficial statistical comparison to use in determining the accuracy of both the predicted creep and shrinkage strains to the measured creep and shrinkage strains. This was accomplished by subtracting the measured creep and shrinkage strain from the estimated creep and shrinkage values, respectively. The difference was then divided by the measured creep and shrinkage strain and then multiplied by 100 as shown in Equation 6.1.

$$\%Error = \left(\frac{\hat{y} - \bar{y}}{\bar{y}}\right) \times 100 \qquad \text{Equation 6.1}$$

Where,

$\hat{y}$ = predicted creep or shrinkage strain, and

$\bar{y}$ = measured creep or shrinkage strain.

The range of error that was deemed acceptable was based on a study conducted by Gardner and Lockman (2001) who state that predictions for "shrinkage within 15% would be excellent, and a prediction within 20% would be adequate." Based on this statement, for the duration of this project any predicted creep or shrinkage values that fall within $\pm$ 20% are considered excellent.

Not only was the percent error a means of assessing the accuracy of each model, but the unbiased estimate of the standard deviation of the error was also determined to further identify the most accurate model. As defined by McCuen (1985), the unbiased estimate of the standard deviation of the error, S_j, was determined with Equation 6.2.

$$S_j = \sqrt{\frac{1}{n-1}\sum_{i}^{n} \Delta_i{}^2} \qquad \text{Equation 6.2}$$

Where,

S_j = unbiased estimate of the standard deviation of the error,

Δ_i = the difference between the predicted and measured values, and

n = the number of data points.

6.7.2 Results from Statistical Analysis

The statistical analysis results that were calculated using the methods previously described are presented in this section to evaluate the performance of each prediction method used during this research study. Tables 6-11 through 6-15 show the percent error calculations for the creep prediction methods for both the field and laboratory specimens, the percent error calculations for the drying shrinkage rectangular prisms for the laboratory specimens, the percent error calculations for the laboratory cylindrical drying shrinkage specimens, the percent error calculations for the drying shrinkage rectangular prisms for the field specimens, and the percent

error calculations for the field cylindrical drying shrinkage specimens, respectively. If the percent error is a positive value, this indicates that the predicted strain value was larger than the measured strain value and a negative value indicates that the predicted strain value is smaller than the measured strain value.

Table 6-11: Error calculation results for creep strains for field and laboratory mixtures

Percent Error (%)				
	Field Test Specimens		**Laboratory Test Specimens**	
	04/10/2018-F	**07/09/2018-F**	**05/03/2018-L-Q**	**05/09/2018-L-L**
ACI 209				
Positive Range	3.91	---	15	---
Negative Range	-70.1	-58.4	-60	-66.9
AASHTO 2017				
Positive Range	---	---	---	---
Negative Range	-96.7	-96.0	-96.1	-96.7
CEB MC 2010				
Positive Range	175	187	199	102
Negative Range	---	---	---	---
GL 2000				
Positive Range	18	74	83	66.7
Negative Range	-23	---	---	-82
B3 Model				
Positive Range	909	547	826	847
Negative Range	-6.8	---	---	---

Table 6-12: Error calculation results for rectangular prism drying shrinkage specimens for laboratory mixtures

Percent Error (%)		
	Laboratory Rectangular Prism Test Specimens	
	05/03/2018-L-Q	**05/09/2018-L-L**
ACI 209		
Positive Range	---	---
Negative Range	-95.8	-95.8
AASHTO 2017		
Positive Range	---	---
Negative Range	-95.5	-95.4
CEB MC 2010		
Positive Range	111	80.0
Negative Range	-27.2	-28.6
GL 2000		
Positive Range	70.5	4.16
Negative Range	-15.9	-14.1
B3 Model		
Positive Range	15.6	---
Negative Range	-38.2	-46.7

Table 6-13: Error calculation results for cylindrical drying shrinkage specimens for laboratory mixtures

Percent Error (%)		
	Laboratory Cylindrical Test Specimens	
	05/03/2018-L-Q	05/09/2018-L-L
ACI 209		
Positive Range	---	---
Negative Range	-94.6	-64.5
AASHTO 2017		
Positive Range	---	14.9
Negative Range	-90.7	-34.2
CEB MC 2010		
Positive Range	---	---
Negative Range	-93.7	-58.1
GL 2000		
Positive Range	---	14.6
Negative Range	-88.2	-14.4
B3 Model		
Positive Range	---	---
Negative Range	-96.8	-79.2

Table 6-14: Error calculations for rectangular prism drying shrinkage specimens for field mixtures

Percent Error (%)						
	Field Rectangular Prism Test Specimens					
	03/20/2018-F (Air)	**03/20/2018-F (Moist)**	**04/10/2018-F (Air)**	**04/10/2018-F (Moist)**	**07/09/2018-F (Air)**	**07/09/2018-F (Moist)**
ACI 209						
Positive Range	---	---	---	---	---	---
Negative Range	-96	-97.2	-98.6	-96.8	-98.9	-92.9
AASHTO 2017						
Positive Range	---		---	---	---	---
Negative Range	-93.3	-97.5	-97.6	-97	-98.2	-94
CEB MC 2010						
Positive Range	16	---	---	1.05	---	128
Negative Range	-45.1	-54.8	-52.7	-42.9	-62.6	-35
GL 2000						
Positive Range	51.8	---	---	---	---	85.8
Negative Range	-28.9	-42	-54.3	-33.6	-66.3	-19.2
B3 Model						
Positive Range	18.4	---	9.52	40.3	---	12.2
Negative Range	-34.6	-35.9	-57.4	-10.6	-86.0	-46.0

Table 6-15: Error calculation results for cylindrical drying shrinkage specimens for field mixtures

Percent Error (%)		
	Field Cylindrical Test Specimens	
	04/10/2018-F	**07/09/2018-F**
ACI 209		
Positive Range	---	---
Negative Range	-95.9	-95
AASHTO 2017		
Positive Range	4.6	---
Negative Range	-91.8	-90.6
CEB MC 2010		
Positive Range	---	---
Negative Range	-95.1	-94.2
GL 2000		
Positive Range	5.34	---
Negative Range	-89.7	-88
B3 Model		
Positive Range	---	---
Negative Range	-94.4	-97.1

In addition to the percent error, the S_j values were also calculated and are presented in Tables 6-16 through 6-21 below. Table 6-16 presents the S_j values for the predicted creep strain values for both the field and laboratory test specimens while Table 6-17 illustrates the S_j values for the predicted compliance values for both the field and laboratory specimens. Table 6-18 illustrates the S_j values in the predicted drying shrinkage strains for the laboratory rectangular prism specimens, while Tables 6-19 and 6-20 illustrate the S_j values in the predicted drying shrinkage strains for the air and moist-cured rectangular prism field specimens, respectively. Table 6-21 provides the S_j values for the cylindrical drying shrinkage specimens for both the field and laboratory mixtures. The smaller the S_j value, the closer the predicted and measured values are to each other. Each table also identifies which prediction method produced the best overall result during the duration of testing.

Table 6-16: S_j values for creep strains for all field and laboratory mixtures

Methods	S_j values for creep strains for field and laboratory test specimens (x 10^{-6} in./in.)			
	Field Specimens		Laboratory Specimens	
	04/10/2018-F	07/09/2018-F	05/03/2018-L-Q	05/09/2018-L-L
ACI 209	252	124	59	128
AASHTO 2017	264	183	155	178
CEB MC 2010	132	155	133	101
GL 2000	101	101	177	124
B3 Model	204	252	370	321
Best Method	GL 2000	GL 2000	ACI 209	CEB MC 2010
Second Best	CEB MC 2010	ACI 209	CEB MC 2010	GL 2000

Table 6-17: S_j values for compliance for all field and laboratory mixtures

Methods	S_j values for compliance for field and laboratory test specimens (x 10^{-6} /psi)			
	Field Specimens		Laboratory Specimens	
	04/10/2018-F	07/09/2018-F	05/03/2018-L-Q	05/09/2018-L-L
ACI 209	0.2242	0.1159	0.1065	0.0811
AASHTO 2017	0.2312	0.1318	0.1211	0.0972
CEB MC 2010	0.1691	0.1142	0.1106	0.0403
GL 2000	0.1186	0.0360	0.0481	0.0506
B3 Model	0.0597	0.0729	0.0853	0.1372
Best Method	B3 Model	GL 2000	GL 2000	CEB MC 2010
Second Best	GL 2000	B3 Model	B3 Model	GL 2000

Table 6-18: S_j values for drying shrinkage strains for laboratory test specimens

Methods	S_j values for shrinkage strains for laboratory test specimens (x 10^{-6} in./in.)	
	Rectangular Prism Shrinkage Specimens	
	05/03/2018-L-Q	05/09/2018-L-L
ACI 209	168	175
AASHTO 2017	164	162
CEB MC 2010	92	73
GL 2000	56	17
B3 Model	124	123
Best Method	GL 2000	GL 2000
Second Best	CEB MC 2010	CEB MC 2010

Table 6-19: S_j values for air-cured rectangular prism drying shrinkage specimens for field mixtures

Methods	S_j values for shrinkage strains for field test specimens (x 10^{-6} in./in.)		
	Rectangular Prism Shrinkage Specimens		
	03/20/2018-F (Air)	04/10/2018-F (Air)	07/09/2018-F (Air)
ACI 209	313	245	268
AASHTO 2017	196	170	215
CEB MC 2010	264	150	172
GL 2000	166	75	110
B3 Model	110	52	280
Best Method	B3 Model	B3 Model	GL 2000
Second Best	GL 2000	GL 2000	CEB MC 2010

Table 6-20: S_j values for moist-cured rectangular prism drying shrinkage specimens for field mixtures

Methods	S_j values for shrinkage strains for field test specimens (x 10^{-6} in./in.)		
	Rectangular Prism Shrinkage Specimens		
	03/20/2018-F (Moist)	04/10/2018-F (Moist)	07/09/2018-F (Moist)
ACI 209	395	236	158
AASHTO 2017	402	250	188
CEB MC 2010	388	181	111
GL 2000	282	107	56
B3 Model	54	150	154
Best Method	B3 Model	GL 2000	GL 2000
Second Best	GL 2000	B3 Model	CEB MC 2010

Table 6-21: S_j values for cylindrical drying shrinkage specimens for both field and laboratory mixtures

Methods	S_j values for shrinkage strains for field and laboratory test specimens (x 10^{-6} in./in.)			
	Cylindrical Field Specimens		Cylindrical Laboratory Specimens	
	04/10/2018-F	07/09/2018-F	05/03/2018-L-Q	05/09/2018-L-L
ACI 209	114	94	90	50
AASHTO 2017	14	30	46	27
CEB MC 2010	129	105	111	65
GL 2000	78	53	77	20
B3 Model	79	151	165	124
Best Method	AASHTO 2017	AASHTO 2017	AASHTO 2017	GL 2000
Second Best	GL 2000	GL 2000	GL 2000	AASHTO 2017

6.7.3 Discussion of Statistical Analysis

As stated in Chapter 1, one of the primary objectives was to calibrate the most accurate creep and shrinkage model to improve its prediction of the measured creep and shrinkage strains for the field-mixed concrete test specimens. To effectively determine which model performed the best, the unbiased estimate of the standard deviation of the error (S_j) values as seen in Tables 6-16

through 6-21 were analyzed. The lower the S_j value, the more accurate the model was in the prediction of either the measured creep or shrinkage values.

Tables 6-16 and 6-17 contain the S_j values for the creep and compliance values for each of the prediction models that were studied during this project for both the field and laboratory specimens. As can be seen in Table 6-16, the GL 2000 Model produced the best S_j values for the predicted creep strains for both sets of field specimens with a value of 101 microstrain, while the CEB MC 2010 and ACI 209 model were the second best method for the predicted creep strains of 04/10/2018-F and 07/09/2018-F specimens, respectively. As seen in Table 6-17, the B3 Model and the GL 2000 Model produced the best results for the predicted compliance with calculated S_j values of 0.0597 10^{-6} psi and 0.0729 10^{-6} psi for the 04/10/2018-F and 07/09/2018-F specimens, respectively. As for the laboratory specimens, the GL 2000 Model, the CEB MC 2010, or ACI 209 was either the best or second best method when predicting the creep or compliance. According to Table 6-16, the ACI 209 and the CEB MC 2010 performed the best in the creep prediction for the 05/03/2018-L-Q and 05/09/2018-L-L specimens with S_j values that were calculated to be 59 microstrain and 101 microstrain, respectively.

Tables 6-18 through 6-20 contain the S_j values for the rectangular prisms for the field and laboratory test specimens, while Table 6-21 contains the S_j values for the cylindrical shrinkage specimens that were used in creep testing. As can be seen in Tables 6-18 through 6-20, the GL 2000 Model, the B3 Model, and the CEB MC 2010 were either the best or second best method when predicting the shrinkage strains of the rectangular prisms. As can be seen in Table 6-19, the B3 Model performed the best for the 03/20/2018-F-Air and 04/10/2018-Air specimens with calculated S_j values of 110 microstrain and 52 microstrain, respectively, but as can be seen in Table 6-20, the GL 2000 Model performed the best for the 04/10/2018-F-Moist and 07/09/2018-F-Moist specimens with calculated S_j values of 107 microstrain and 56 microstrain. However, Table 6-21 shows that the AASHTO 2017 model performed the best when predicting the shrinkage strains of the cylindrical specimens for both field sets and the 05/03/2018-L-Q specimens, but the GL 2000 Model was the second best prediction model for each of these sets of specimens.

6.8 CALIBRATION OF GL 2000 MODEL

6.8.1 Why the GL 2000 Model was Chosen

After carefully analyzing all data that was generated by each of the previous models, it was determined that the model that performed the best to predict both the measured creep and shrinkage for the field-mixed concrete was the GL 2000 Model. As discussed in Section 6.7.3, when the predicted creep and shrinkage results of the GL 2000 Model were compared to the predicted creep and shrinkage results of the other models in this study, the GL 2000 Model performed the best or either second best in accuracy for both the field- and laboratory-mixed concretes.

This section will cover the techniques that were used to calibrate the GL 2000 Model to improve both the predicted creep and shrinkage values for the field test specimens, and also note any changes that were made to the creep and shrinkage prediction procedure that was previously described in Section 2.4.4. One of the primary objectives of this project was to accurately predict the creep and shrinkage values of test specimens that were sampled from actual concrete that was used in the casting of segments made for the segmental bridge replacement of the I-59/I-20 exchange in Birmingham, Alabama. Therefore, the only test results that are used for the calibration of the GL 2000 Model the creep testing specimens, the rectangular shrinkage prisms that were subjected only to air during curing, and the cylindrical shrinkage specimens that were used during creep testing for each set of field collected samples.

6.8.2 Techniques Used During Calibration

This section covers the details that were followed to calibrate the GL 2000 Model to obtain the most accurate results possible for both the predicted creep and shrinkage values of all field-mixed concrete.

6.8.2.1 Calibration of GL 2000 Predicted Modulus of Elasticity Equation

Recalling from Section 2.4.4, the modulus of elasticity at the time of loading plays a crucial role in the early prediction values of the compliance; therefore, it was determined that the predicted modulus of elasticity equation, as shown in Equation 6.3, needed to be calibrated so that the predicted values were in much closer agreement with the elastic moduli determined through

testing. After careful evaluation, one empirical parameter labeled as τ in Equation 6.4, was determined to need calibration to improve the predicted modulus of elasticity.

$$E_{cmt} = 500{,}000 + 52{,}000\sqrt{f_{cmt}} \quad \text{Equation 6.3}$$

$$E_{cmt} = 500{,}000 + \tau\sqrt{f_{cmt}} \quad \text{Equation 6.4}$$

Where,

τ = Empirical parameter being calibrated

Figure 6-66 illustrates how varying τ will affect the predicted modulus of elasticity. As shown in Figure 6-66, when the value of τ is increased, the predicted modulus of elasticity also increases and vice versa for when τ is decreased.

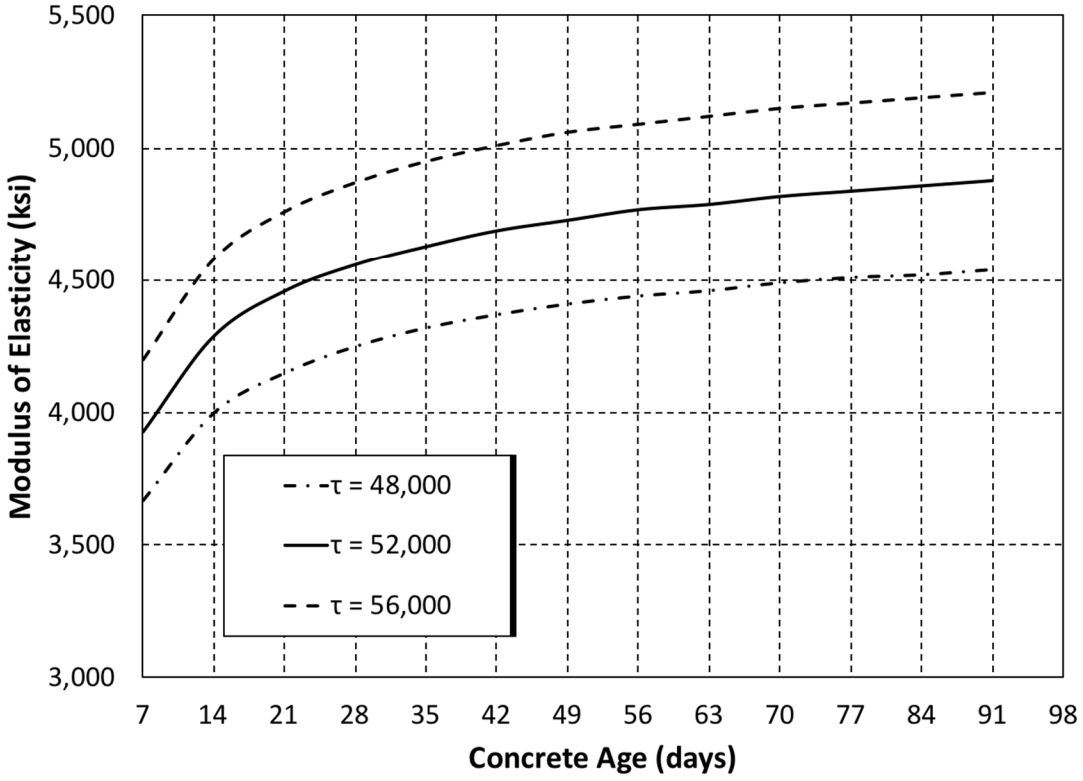

Figure 6-66: Effects of the GL 2000 predicted modulus of elasticity when varying tau (τ)

The modified modulus of elasticity equation for the GL 2000 Model is shown in Equation 6.5 for which the best results were generated for both the 04/10/2018-F and 07/09/2018-F specimens. Table 6-22 contains the calibrated predicted modulus of elasticity values for each set

of field specimens. As can be seen in Table 6-22, the accuracy of the predicted modulus of elasticity values for all loading ages for both sets of field specimens improved significantly. Table 6-23 provides the overall improvement in percent error for all loading ages for both sets of field specimens between the Original GL 2000 Model and the Modified GL 2000 Model. Also, Figure 6-67 provides a visual aid to show the improvement between the predicted modulus of elasticity values when using the Original GL 2000 Model versus the Modified GL 2000 Model.

$$E_{cmt} = 500{,}000 + 48{,}000\sqrt{f_{cmt}} \qquad \text{Equation 6.5}$$

Table 6-22: Modified GL 2000 Predicted Modulus of Elasticity Values

Mixture ID	**04/10/2018-F**		
Loading Age (Days)	**Measured Modulus of Elasticity (ksi)**	**Modified GL 2000 Predicted Modulus of Elasticity (ksi)**	**Error (%)**
7	3800	3930	3
28	4050	4250	5%
91	3850	4220	10%
182	4150	4340	5%
Mixture ID	**07/09/2018-F**		
Loading Age (Days)	**Measured Modulus of Elasticity (ksi)**	**Modified GL 2000 Predicted Modulus of Elasticity (ksi)**	**Error (%)**
7	4250	4090	-4%
28	4250	4430	4%
91	4200	4540	8%
182*	---	---	---

Data not available for indicated loading age

Table 6-23: Percent Error comparison between Original GL 2000 Model and Modified GL 2000 Model

	Overall Improvement of Percent Error in Predicted Modulus of Elasticity Values, (%)
Original GL 2000 Model	12.1%
Modified GL 2000 Model	5.51%

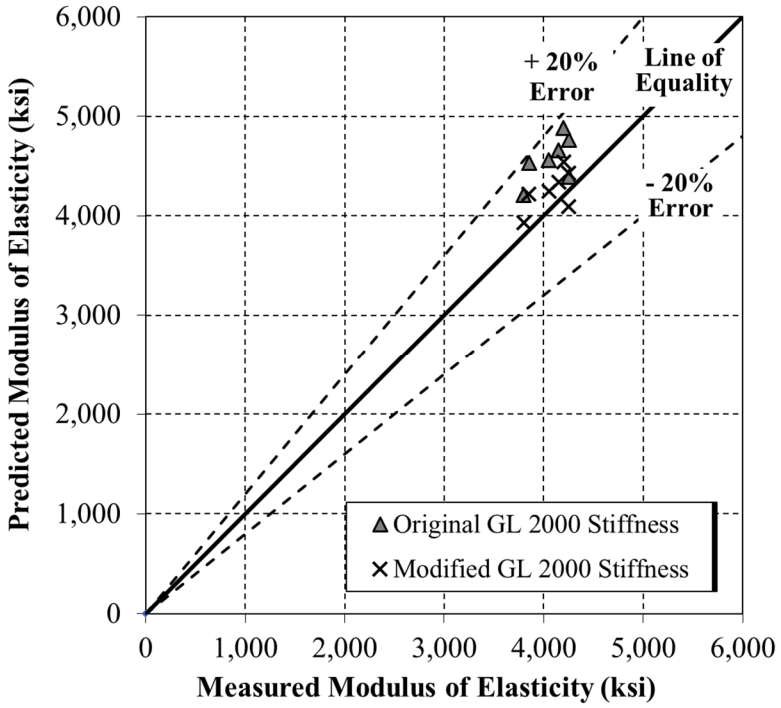

Figure 6-67: Measured versus predicted modulus of elasticity values when using the Original GL 2000 Model and the Modified GL 2000 Model

6.8.2.2 Calibration of GL 2000 Creep and Shrinkage Prediction Methods

In addition to the calibration of the predicted modulus of elasticity, it was determined that the next approach that would generate the best results would be to plot the predicted compliance values for a given loading age using the original GL 2000 Model of the 28-day creep coefficient equation as shown in Equation 6.6. After plotting the predicted compliance using the original 28-day creep coefficient, the next step was to make changes to certain parameters and see how the changes affected the predicted compliance. After carefully studying the equation, two parameters were identified for calibration, which are labeled as λ and ω in the modified formation of the 28-day creep coefficient as shown in Equation 6.7. Note that the same parameters affect the predicted creep values in the same manner so only the effects of the predicted compliance are shown.

$$\Phi(t,t_o) = \Phi(t_c)[2\left(\frac{(t-t_o)^{0.3}}{(t-t_o)^{0.3}+14}\right)+\left(\frac{7}{t_o}\right)^{0.5}(\frac{t-t_o}{t-t_o+7})^{0.5} +2.5(1-1.086h^2)(\frac{t-t_o}{t-t_o+77\left(\frac{v}{s}\right)^2})^{0.5}$$ Equation 6.6

$$\Phi(t,t_o) = \Phi(t_c)[2\left(\frac{(t-t_o)^{0.3}}{(t-t_o)^{0.3}+14}\right)+\left(\frac{7}{t_o}\right)^{0.5}(\frac{t-t_o}{t-t_o+7})^{\lambda} +\omega(1-1.086h^2)(\frac{t-t_o}{t-t_o+77\left(\frac{v}{s}\right)^2})^{0.5}$$ Equation 6.7

Where,

λ and ω = Empirical parameters being calibrated

After determining that λ and ω were the parameters that need calibration, each individual parameter was examined to determine how they affect the predicted values when all other parameters are based on the original formulation of the 28-day creep coefficient. Figures 6-67 and 6-68 show how either decreasing or increasing λ and ω affect the predicted values.

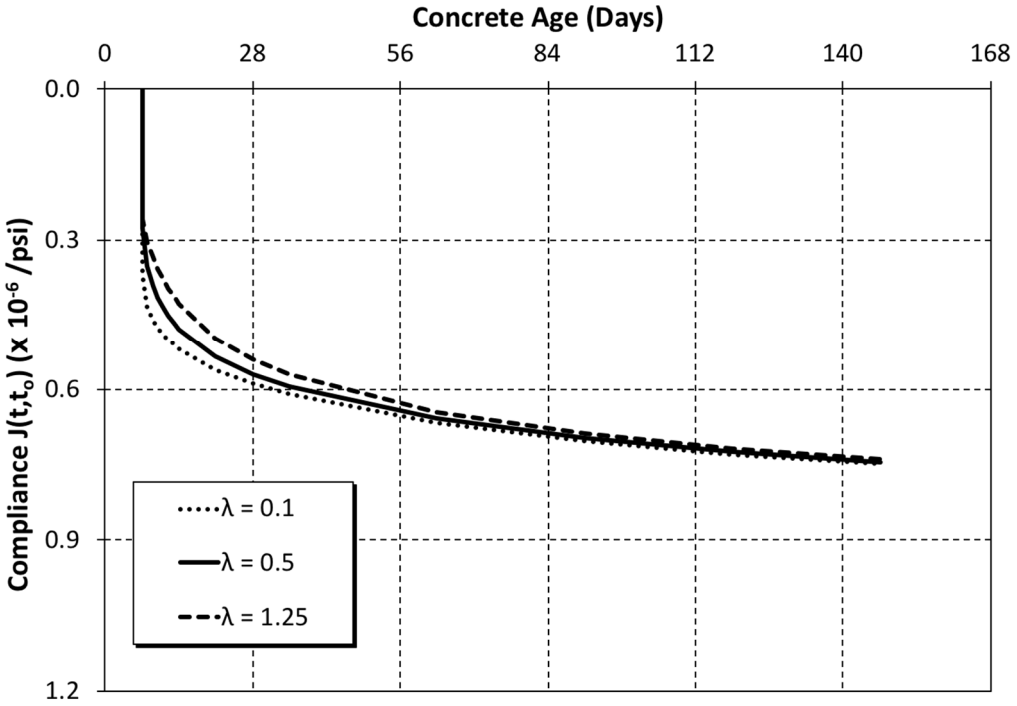

Figure 6-68: Effects of predicted compliance values with the GL 2000 Model when varying lamda (λ)

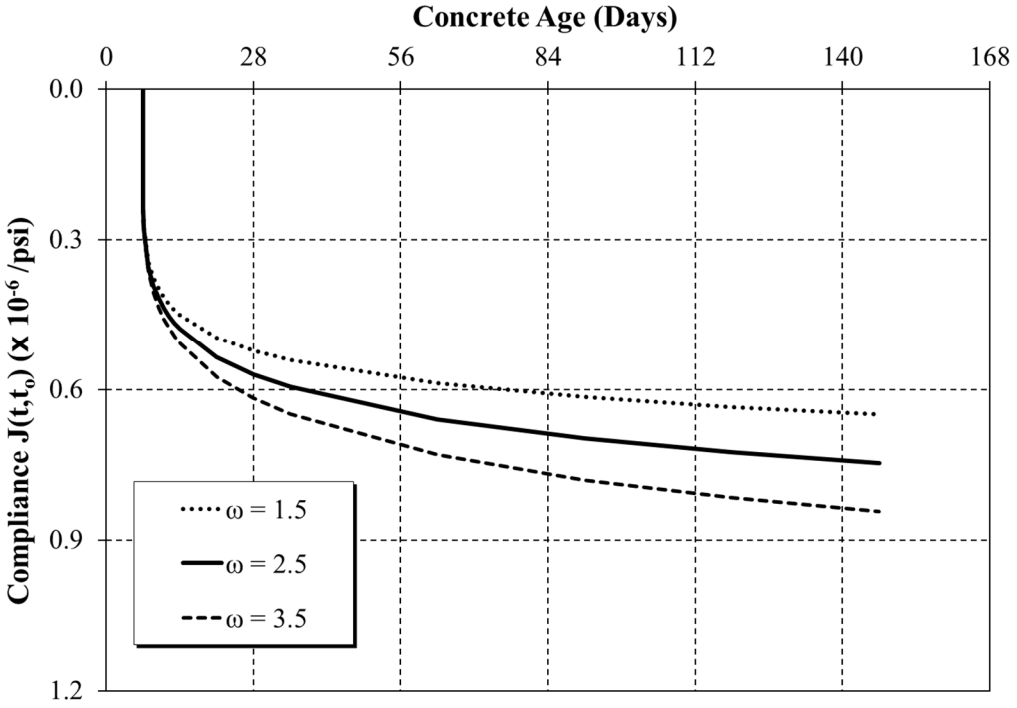

Figure 6-69: Effects of predicted compliance values with the GL 2000 Model when varying omega (ω)

After calibration, the best fit λ of 1.0 and ω of 3.0 were determined, as shown in Equation 6.8. When computing the predicted compliance and creep values, the modified predicted modulus of elasticity equation and the 28-day creep coefficient shown in Equations 6.5 and 6.8 should be used, and all other procedures outlined in Section 2.4.4 may be followed. Section 6.8.3 provides graphs to show the improvement of the creep behavior when using the Modified GL 2000 Model.

$$\Phi(t,t_o) = \Phi(t_c)[2\left(\frac{(t-t_o)^{0.3}}{(t-t_o)^{0.3}+14}\right)+\left(\frac{7}{t_o}\right)^{0.5}(\frac{t-t_o}{t-t_o+7})^{1.0} +3.0(1-1.086h^2)(\frac{t-t_o}{t-t_o+77\left(\frac{v}{s}\right)^2})^{0.5} \quad \text{Equation 6.8}$$

In addition to the calibration of the predicted creep and compliance values, the predicted shrinkage values from using the GL 2000 Model was also calibrated. Similar to the modified 28-day creep coefficient, certain parameters were evaluated to determine which would have the overall largest effect in providing more accurate results for the predicted shrinkage strains. It was determined that the ultimate shrinkage strain (ε_{shu}), had the largest effect on the predicted shrinkage values. The original formulation of the ultimate shrinkage strain equation of the GL 2000 Model is shown in Equation 6.9. Also, the empirical ultimate shrinkage strain formula is presented in Equation 6.10 with the one parameter that plays the overall largest effect, which is labeled θ, that was calibrated to improve the predicted shrinkage strains.

$$\varepsilon_{shu} = 900k(\frac{4350}{f_{cm28}})^{0.5} \times 10^{-6} \quad \text{Equation 6.9}$$

$$\varepsilon_{shu} = \theta k(\frac{4350}{f_{cm28}})^{0.5} \times 10^{-6} \quad \text{Equation 6.10}$$

Where,

θ = Empirical parameter being calibrated

Figure 6-69 shows the results of the predicted shrinkage values when the value of θ is either decreased or increased. The plot that is labeled original θ is a representation of the predicted shrinkage values if the original formulation of the ultimate shrinkage strain was used.

It can be seen from Figure 6-69, if the value of θ is increased that the predicted drying shrinkage increases, and vice versa when θ is decreased.

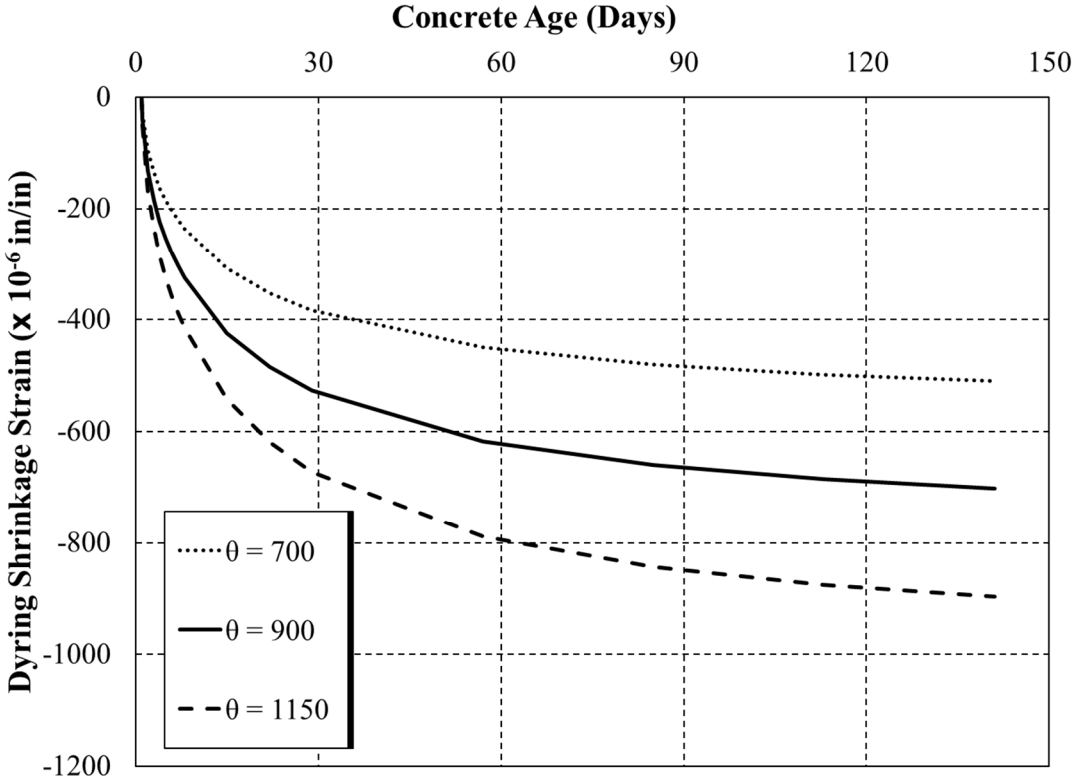

Figure 6-70: Effects of predicted shrinkage values with the GL 2000 Model when varying theta (θ)

After calibration, the modified ultimate shrinkage strain equation that provides the most accurate results is shown in Equation 6.11. This equation was then used in the original shrinkage prediction procedure that is presented in Section 2.4.4.

$$\varepsilon_{shu} = 1150k\left(\frac{4350}{f_{cm28}}\right)^{0.5}10^{-6} \qquad \text{Equation 6.11}$$

Once the calibration process was complete, the inputs presented earlier in Tables 6-7 and 6-8 below were used in predicting the creep and shrinkage values for each of the field specimens using the Modified GL 2000 Model. Notice that most of the inputs did not change for the Modified GL 2000 Model with the exception that the predicted modulus of elasticity from Table 6-22 will now be used in predicting the creep behavior.

6.8.3 Predicted Creep and Compliance Values for Field Specimens

Figures 6-70 and 6-71 show the predicted versus measured creep strains for the 04/10/2018-F and 07/09/2018-F test specimens using the Modified GL 2000 Model. Each graph contains all loading ages that were considered during this study which include the loading ages of 7-days, 28-days, and 91-days for the 04/10/2018-F test specimens and the 7-day and 28-day loading ages for the 07/09/2018-F specimens.

As seen in Figure 6-70, the Modified GL 2000 Model accurately predicts the creep strains for the 04/10/2018-F specimens for the loading ages of 7 days and 28 days as the age of the concrete increases. However, the Modified GL 2000 predicted creep strains for the loading age of 91 days were slightly overestimated as compared to the original GL 2000 predicted creep strains as shown in Figure 6-40.

As seen in Figure 6-7, the Modified GL 2000 Model predicted creep strains of the 07/09/2018-F test specimens exhibit a different response as compared to the 04/10/2018-F samples. The predicted creep strains for both the 7-day and 28-day loading ages of the 07/09/2018-F specimens were more accurate at earlier ages unlike the predicted creep strains of the 04/10/2018-F specimens which were more accurate as the age of the concrete increased.

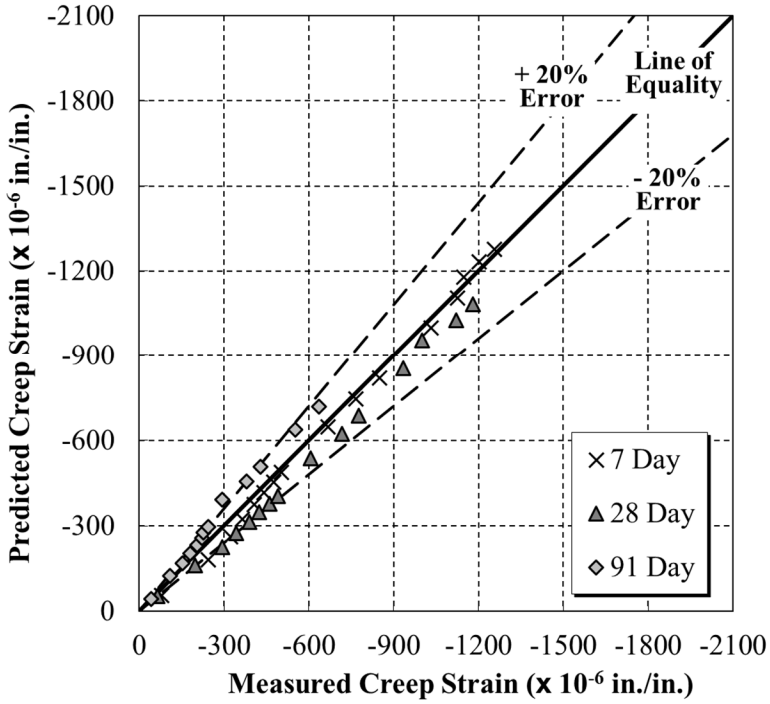

Figure 6-71: Measured versus predicted creep strains for the 04/10/2018-F field specimens using the Modified GL 2000 Model

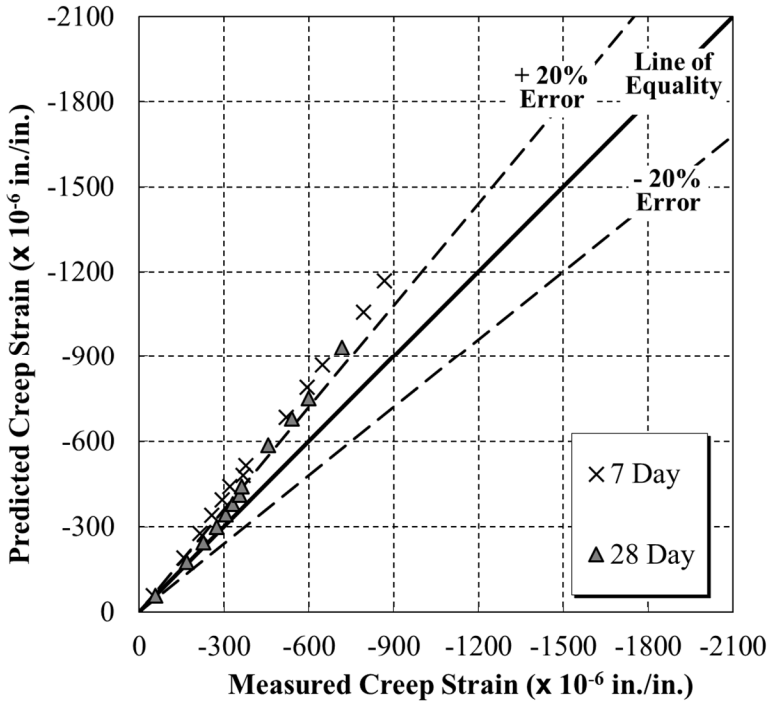

Figure 6-72: Measured versus predicted creep strains for the 07/09/2018-F field specimens using the Modified GL 2000 Model

Figures 6-72 and 6-73 show the predicted versus measured compliance values for the 04/10/2018-F and 07/09/2018-F test specimens using the Modified GL 2000 Model. The same loading ages that were discussed earlier for the predicted creep strains of the 04/10/2018-F and 07/09/2018-F samples are also presented for the predicted compliance values as well.

As seen in Figure 6-72, the Modified GL 2000 predicted compliance values for each of the loading ages for the 04/10/2018-F specimens increased in accuracy as the age of the concrete increased much like the Modified GL 2000 predicted creep strains. As seen in Figure 6-73, the Modified GL 2000 predicted compliance values for both the 7-day and 28-day loading ages of the 07/09/2018-F specimens were predicted with relatively good accuracy throughout the duration of testing.

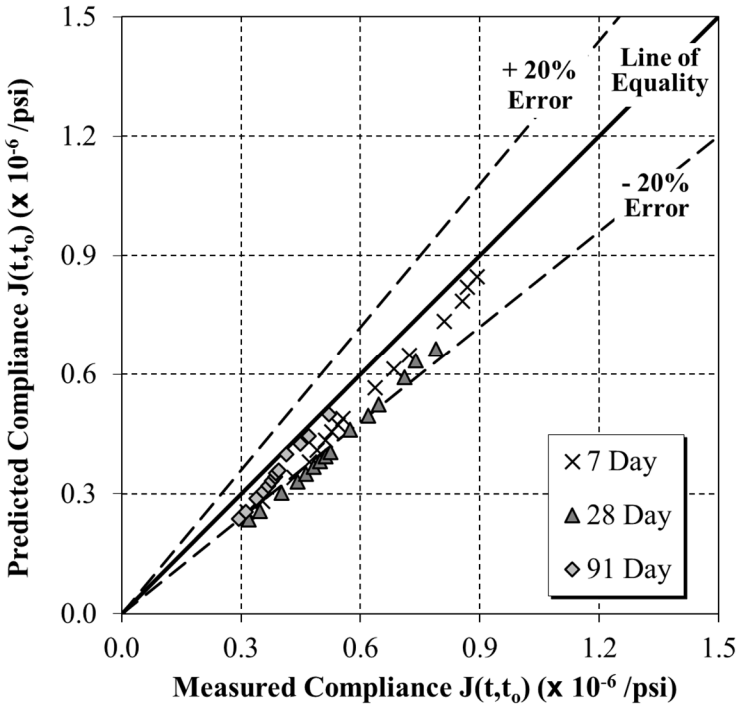

Figure 6-73: Measured versus predicted compliance for the 04/10/2018-F field specimens using the Modified GL 2000 Model

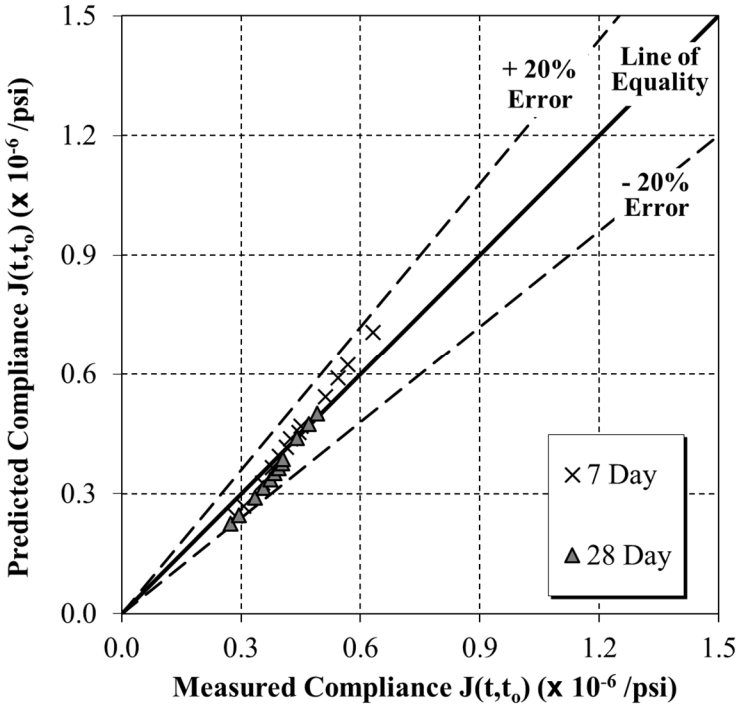

Figure 6-74: Measured versus predicted compliance for the 07/09/2018-F field specimens using the Modified GL 2000 Model

6.8.4 Predicted Shrinkage Values for Field Specimens

Figure 6-74 shows the Modified GL 2000 predicted versus measured shrinkage strains for the air-cured rectangular prisms that were cast in the field. When comparing Figure 6-74 to Figure 6-48, the Modified GL 2000 predicted shrinkage strains for the rectangular prisms greatly increased in accuracy as compared to the original GL 2000 predicted values. The predicted shrinkage values for each field mixture became more accurate as the age of drying increased as compared to the earlier ages of drying; however, even in the early ages of drying the predicted values are within the $\pm$ 20% target range, except for the 03/20/2018-F-Air specimens.

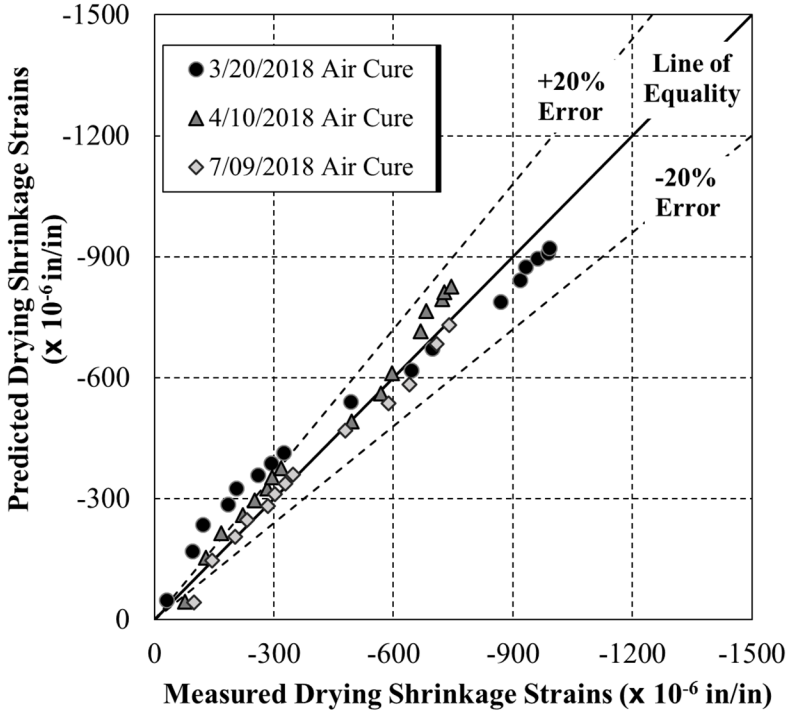

Figure 6-75: Measured versus predicted drying shrinkage strains for the air-cured field rectangular prisms using the Modified GL 2000 Model

Figure 6-75 shows the Modified GL 2000 Model's predicted versus measured shrinkage values for the cylindrical shrinkage specimens that were used during creep testing. As seen in Figure 6-75, the Modified GL 2000 predicted shrinkage values for both the 04/10/2018-F and 07/09/2018-F cylindrical test specimens are very accurate.

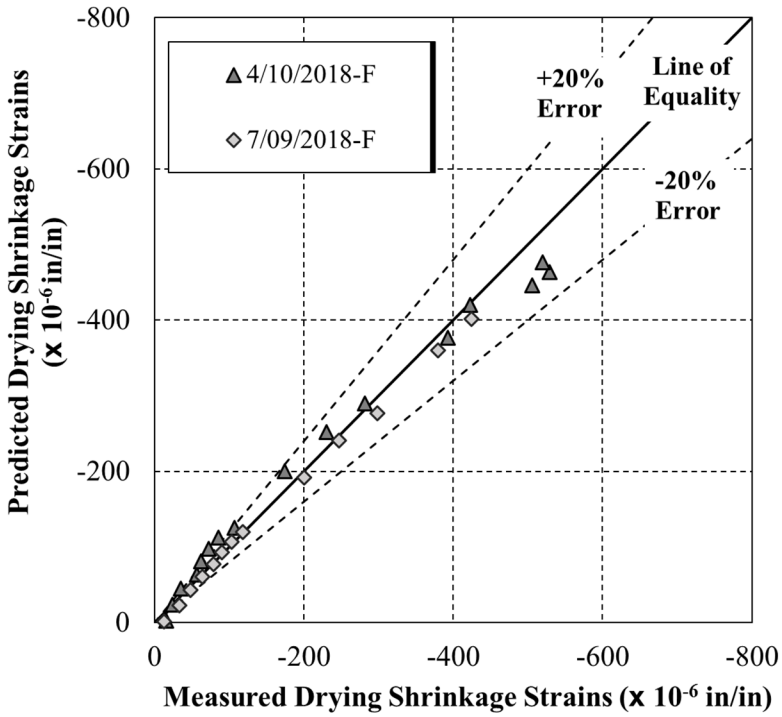

Figure 6-76: Measured versus predicted drying shrinkage strains for cylindrical field specimens using the Modified GL 2000 Model

6.8.5 Statistical Comparison of Calibrated Versus Original Predicted Values

This section covers the statistical analysis that was performed to compare the unbiased estimate of the standard deviation of the error of the measured creep, compliance, and shrinkage values when compared to the values predicted with the calibrated GL 2000 Model and the original version. Tables 6-24 through 6-27 show the S_j values for the predicted creep strains, compliance, and shrinkage strains, respectively.

Table 6-24: Comparison of S_j values for predicted creep strains for the Original GL 2000 Model versus Modified GL 2000 Model

Field Specimens	S_j values for creep strains for field test specimens (x 10^{-6} in./in.)	
	Original GL 2000 Model	**Calibrated GL 2000 Model**
04/10/2018-F	101	56
07/09/2018-F	101	134
All Specimens	101	92

Table 6-25: Comparison of S_j values for predicted compliance values for the Original GL 2000 Model versus Modified GL 2000 Model

Field Specimens	S_j values for compliance for field test specimens (x 10^{-6} /psi)	
	Original GL 2000 Model	**Calibrated GL 2000 Model**
04/10/2018-F	0.1186	0.0827
07/09/2018-F	0.0360	0.0384
All Specimens	0.0966	0.0696

Table 6-26: Comparison of S_j values for predicted rectangular prism shrinkage strains for the Original GL 2000 Model versus Modified GL 2000 Model

Field Specimens	S_j values for drying shrinkage strains for field test specimens (x 10^{-6} in./in.)	
	Rectangular Prism Shrinkage Specimens	
	Original GL 2000 Model	**Calibrated GL 2000 Model**
03/20/2018-F (Air)	168	79
04/10/2018-F (Air)	77	52
07/09/2018-F (Air)	110	28
All Specimens	123	58

Table 6-27: Comparison of S_j values for predicted cylindrical shrinkage strains for the Original GL 2000 Model versus Modified GL 2000 Model

Field Specimens	S_j values for drying shrinkage strains for field test specimens (x 10^{-6} in./in.)	
	Cylindrical Shrinkage Specimens	
	Original GL 2000 Model	**Calibrated GL 2000 Model**
04/10/2018-F	78	29
07/09/2018-F	53	12
All Specimens	67	23

According to Table 6-24, the Modified GL 2000 S_j values for the 04/10/2018-F and 07/09/2018-F predicted creep strains were calculated to be 56 microstrain and 134 microstrain, respectively. These S_j values indicate that the accuracy of the predicted creep strains for the

07/09/2018-F decrease slightly. However, the S_j value when both sets of field specimens are considered together was 92 microstrain, which is a decrease from the original value of 100 microstrain. According to Table 6-25, the S_j values for the Modified GL 2000 predicted compliance values for the 04/10/2018-F and 07/09/2018-F test specimens were calculated to be 0.0827 10^{-6}/psi and 0.0384 10^{-6}/psi, respectively. When the results from both sets of field specimens were combined, the S_j value was calculated to be 0.0696 10^{-6}/psi which is a decrease from the original value of 0.0966 10^{-6}/psi indicating that the Modified GL 2000 Model improves the overall prediction accuracy.

As can be seen in Table 6-26, the Modified GL 2000 Model's S_j values for the 03/20/2018-F-Air, 04/10/2018-F-Air, and 07/09/2018-F-Air test specimens were 79 microstrain, 52 microstrain, and 28 microstrain, respectively. In addition to the individual S_j values for each set of rectangular prisms, the Modified GL 2000 Model's S_j value for when all samples were considered together was 58 microstrain. This is a significant improvement from the Original GL 2000 Model's S_j value of 123 microstrain. According to Table 6-28, the Modified GL 2000 Model's S_j values for the 04/10/2018-F and 07/09/2018-F cylindrical specimens are 29 microstrain and 12 microstrain, respectively. In a similar manner to the creep specimens and the rectangular shrinkage specimens, the overall Modified GL 2000 Model's S_j value for all cylindrical specimens was also calculated to be 23 microstrain, which is a significant decrease from the Original GL 2000 Model's S_j value of 67 microstrain. This is a clear indication that the Modified GL 2000 Model produced a much higher accuracy for the predicted shrinkage values as compared to the Original GL 2000 Model's predicted values.

6.9 SUMMARY OF CONCLUSIONS

6.9.1 Conclusions in Relation to the Creep Prediction Methods

From the results that were obtained through the analysis outlined in this chapter, the following conclusions can be drawn for the creep prediction models that were considered during this study:

1. The GL 2000 Model performed the best in predicting the measured creep strains for both the 04/10/2018-F and 07/09/2018-F test specimens.
2. For the laboratory test specimens, the CEB MC 2010 and ACI 209 performed the best in the predicting the measured creep strains.

3. In general, the B3 Model and the GL 2000 Model performed the best in predicting the measured compliance values for the field test specimens.
4. In general, the GL 2000 Model and the CEB MC 2010 were the most accurate in the prediction of the measured compliance values for 05/03/2018-L-Q and 05/09/2018-L-L test specimens, respectively.
5. Overall, the GL 2000 Model was found to provide the most accurate predictions of the measured creep of the field-mixed concretes. After calibration of this model, a Modified GL 2000 Model was obtained as presented in Equations 6.5 and 6.8.

6.9.2 Conclusions in Relation to the Shrinkage Prediction Methods

From the results that were obtained through the analysis outlined in this chapter, the following conclusions can be drawn for the shrinkage prediction models that were considered during this study:

1. In general, the B3 Model and the GL 2000 Model performed the best in predicting the measured shrinkage strains for both the air-cured and moist-cured rectangular prisms for all field-mixed concrete.
2. The GL 2000 Model performed the best in the prediction of the measured shrinkage strains for both the 05/03/2018-L-Q and 05/09/2018-L-L rectangular prisms.
3. In general, AASHTO 2017 was the most accurate in the prediction of the measured cylindrical shrinkage strains for the 04/10/2018-F and 07/09/2018-F test specimens.
4. In general, AASHTO 2017 and the GL 2000 Model performed the best in the prediction of the measured cylindrical shrinkage strains for the 05/03/2018-L-Q and 05/09/2018-L-L test specimens.
5. Overall, the GL 2000 Model was found to provide the most accurate predictions of the measured shrinkage of the field-mixed concretes. After calibration of this model, a Modified GL 2000 Model was obtained as presented in Equation 6.11.

CHAPTER 7: SUMMARY, CONCLUSIONS, AND RECOMMENDATIONS

7.1 SUMMARY OF WORK PERFORMED

7.1.1 Collection of Field Specimens

For this study, 24- 6 in. ×12 in. concrete cylinders and 6- 3 in. × 3 in. × 11.25 in. concrete rectangular prisms were collected both on April 10, 2018 and July 09, 2018, and 6- 3 in. × 3 in. × 11.25 in. concrete rectangular prisms were collected on March 20, 2018 to accurately monitor and test the creep and shrinkage behavior of concrete that was being used in the casting of concrete segments for the I-59/I-20 segmental bridge located in Birmingham, Alabama. Each set of concrete produced by the contractor was mixed according to ALDOT's approved mixture design and was tested by quality control technicians to ensure that all concrete mixtures met the fresh property specifications required by ALDOT. All testing specimens were cured in the same manner as the concrete segments in which their concrete was sampled from by placing all test samples in the segmental formwork before being enclosed and the application of radiant heat. Once curing was complete, the test samples were transported back to Auburn University where creep and shrinkage testing commenced.

7.1.2 Laboratory Work

For this study, it was also concluded that it would be beneficial to mix two batches of concrete at Auburn University using the same ALDOT approved mixture design but varying the coarse aggregate content. This portion consisted of two concrete mixtures: one was mixed using the quartzite coarse aggregate, which was used in all concrete mixtures collected from the field, and the second was mixed using a limestone coarse aggregate. Each set of test specimens mixed in the laboratory consisted of eighteen, 6 in. × 12 in. concrete cylinders and three, 3 in. × 3 in. × 11.25 in. concrete rectangular prisms. After casting was complete, the 6 in. × 12 in. cylinders were accelerated-cured at elevated temperatures similar to those that were experienced by the field specimens during their curing duration. Once curing was complete, the cylinders were demolded and placed in the creep-testing room until creep testing commenced, and the drying

shrinkage prisms were exposed to lime-bath for a duration of 7-days before being subjected to drying.

7.1.3 Testing of Field and Laboratory Specimens

For both the field and laboratory test specimens, all fresh properties of concrete were either collected in the field or were tested in the laboratory during the mixing procedure. The fresh properties that were monitored during the duration of this project included the slump, air content, unit weight, and temperature.

Also, the compressive strength and modulus of elasticity of each loading age were determined prior to creep testing in accordance with AASHTO T 22 (2015) and ASTM C 469 (2018), respectively. After the compressive strength and modulus of elasticity were determined, creep and drying shrinkage testing were performed in accordance with ASTM C 512 (2018) and AASHTO T 160 (2015), respectively. Both the field and laboratory collected samples were loaded at four distinct loading ages to determine the creep response of each mixture while the rectangular prisms of each set of samples were used to monitor the drying shrinkage response. In creep testing, all specimens were loaded to 40 percent of their compressive strength at their desired loading age.

7.2 CONCLUSIONS

7.2.1 Fresh Properties

From this research, the following conclusions can be made in relation to the fresh properties of both the field and laboratory conventional-slump mixtures:

1. Both the field and laboratory mixtures used during testing met all fresh property requirements that were specified by ALDOT during the construction of the segmental bridge replacement.

2. In the laboratory testing phase, the substitution of the limestone coarse aggregate for the quartzite did not have any significant impacts during the fresh property testing.

7.2.2 Hardened Properties

From this research, the following conclusions can be made in relation to the hardened properties for the field and laboratory conventional-slump mixtures:

1. For the field specimens, the 04/10/2018-F samples tested with a lower compressive strength and modulus of elasticity at each loading age as compared to the 07/09/2018-F samples.

2. For the laboratory specimens, the mixture containing the quartzite coarse aggregate tested with a higher compressive strength at each loading age when compared to the mixture containing the limestone coarse aggregate. However, the mixture containing the limestone coarse aggregate tested with a higher modulus of elasticity at each loading age as compared to the mixture containing the quartzite.

3. For the field specimens subjected to creep testing, the 07/09/2018-F samples experienced lower creep values as compared to the 04/10/2018-F samples for each respected loading age.

4. The 07/09/2018-F-Air and 04/10/2018-F-Air rectangular prisms experienced lower and similar shrinkage values as compared to the 03/20/2018-F-Air samples.

5. The 07/09/2018-F-Moist and 04/10/2018-F-Moist samples experienced lower and similar shrinkage values as compared to the 03/20/2018-F-Moist samples.

6. For the laboratory specimens that were used in creep testing, the quartzite and limestone coarse aggregate mixtures experienced similar creep values at each of their respected loading ages through the duration of testing.

7. For the laboratory drying shrinkage prisms, both the quartzite and limestone mixtures experienced similar drying shrinkage values during the duration of testing.

7.2.3 Creep Prediction Methods

Based on the research performed during the duration of this project, the following conclusions can be drawn in relation to the creep prediction methods used:

1. The GL 2000 Model and ACI 209 provided accurate results in the prediction of the measured creep strains for both the field-mixed and laboratory-mixed concrete.
2. The B3 Model and the CEB MC 2010 provided accurate results in the prediction of the measured compliance values for both the field-mixed and laboratory-mixed concrete.
3. Of the creep prediction models considered in this study, the GL 2000 Model presented the most accurate results in creep predictions for both the field and laboratory specimens.
4. The Modified GL 2000 Model improved the overall accuracy of the predicted creep and compliance values for the field specimens.

7.2.4 Shrinkage Prediction Methods

Based on the research performed during the duration of this project, the following conclusions can be drawn in relation to the shrinkage prediction methods used:

1. GL 2000, the B3 Model, and the CEB MC 2010 all provided accurate results in the prediction of the measured shrinkage values.
2. Of the shrinkage prediction models considered, the GL 2000 Model provided the most accurate results in shrinkage predictions for both the field and laboratory specimens.
3. Overall, the Modified GL 2000 Model improved the accuracy of the shrinkage predictions for the cylindrical and rectangular prisms for both sets of field specimens.

7.3 RECOMMENDATIONS FOR FUTURE WORK

To improve the creep and shrinkage prediction models that were considered in this study, some recommendations include:

1. Continue to monitor the creep and shrinkage behavior of both the field and laboratory specimens that are undergoing testing in this research study.
2. Collect more field specimens from the I-59/I-20 segmental bridge located in Birmingham, AL to continue creep and shrinkage testing of concrete used in segmental bridge construction.
3. After a duration of 18 months, revaluate all data and recalibrate the GL 2000 Model or calibrate the method that provides the best overall results.

REFERENCES

AASHTO. 2017. *AASHTO LRFD Bridge Design Specifications: Customary U.S. Units.* 8th ed. Washington D.C.: American Association of State Highway and Transportation Officials (AASHTO).

AASHTO T 22. 2015. Compressive Strength of Cylindrical Concrete Specimens. In *Standard Specifications for Transportation Materials and Methods of Sampling and Testing.* Washington, D.C: American Association of State Highway and Transportation Officials.

AASHTO T 23. 2015. Making and Curing Concrete Test Specimens in the Field. In *Standard Specifications for Transportation Materials and Methods of Sampling and Testing.* Washington, D.C: American Association of State Highway and Transportation Officials.

AASHTO T 119. 2015. Standard Method of Test for Slump of Hydraulic Cement Concrete. In *Standard Specifications for Transportation Materials and Methods of Sampling and Testing.* Washington, D.C: American Association of State Highway and Transportation Officials.

AASHTO T 121. 2015. Method of Test for Density (Unit Weight), Yield, and Air Content (Gravimetric) of Concrete. In *Standard Specifications for Transportation Materials and Methods of Sampling and Testing.* Washington, D.C: American Association of State Highway and Transportation Officials.

AASHTO T 126. 2015. Making and Curing Concrete Test Specimens in the Laboratory. In *Standard Specifications for Transportation Materials and Methods of Sampling and Testing.* Washington, D.C: American Association of State Highway and Transportation Officials.

AASHTO T 160. 2015. Length Change of Hardened Hydraulic Cement Mortar and Concrete. In *Standard Specifications for Transportation Materials and Methods of Sampling and Testing.* Washington, D.C: American Association of State Highway and Transportation Officials.

AASHTO T 309. 2015. Temperature of Freshly Mixed Portland Cement Concrete. In *Standard Specifications for Transportation Materials and Methods of Sampling and Testing.* Washington, D.C: American Association of State Highway and Transportation Officials.

ASTM C157. 2008. Standard Test Method for Length Change of Hardened Hydraulic-Cement Mortar and Concrete. ASTM International. West Conshohocken, PA.

ASTM C 469. 2018. Standard Test Method for Static Modulus of Elasticity and Poisson's Ratio of Concrete in Compression. *ASTM International.* West Conshohocken, Pennsylvania.

ASTM C 512 (2018). 2018. Standard Test for Creep in Concrete. *ASTM International.* West Conshohocken, Pennsylvania.

ASTM C 1074 (2018). 2018. Standard Practice for Estimating Concrete Strength by the Maturity Method. *ASTM International.* West Conshohocken, Pennsylvania.

ASTM D 2216. 2018. Standard Test Methods for laboratory Determination of Moisture Content of Soil and Rock by Mass. *ASTM International*. West Conshohocken, Pennsylvania.

ACI Committee 209. 1992. Prediction of Creep, Shrinkage, and Temperature Effects in Concrete Structures (ACI 209R). In *ACI Manual of Concrete Practice 2001: Part 1.* Farmington Hills, Michigan: American Concrete Institute, 209R-1-209R-47.

ACI Committee 209. 2008. Guide for Modeling and Calculating Shrinkage and Creep of Concrete (ACI 209.2R-08). Farmington Hills, MI: American Concrete Institute.

Bazant, Z. P. and Baweja, S. 2000. Description of Model B3 and Prediction Procedure. In *The Adam Neville Symposium: Creep and Shrinkage – Structural Design Effects*, ed. A. Al-Manaseer. Farmington Hills, Michigan: American Concrete Institute, 3-34.

Bazant, Z. P., and Ignacio, C. 1993. *Creep and Shrinkage of Concrete*. E & FN Spon,

Bazant, Z. P. 2001. Prediction of concrete creep and shrinkage: past, present and future. *Nuclear Engineering and Design* 203, no. 1: 27-38.

CEB. 1990. "Creep and Shrinkage". In *CEB-FIP Model Code 1990.* Lausanne, Switzerland: Comite Euro-International du Beton (CEB), 53-65.

Cross, B. "Our Beautiful Roosevelt Bridge in Stuart Florida." ActiveRain. September 18, 2012. Accessed October 24, 2018. https://activerain.com/blogsview/2486704/our-beautiful-roosevelt-bridge-in-stuart-florida.

fib. 2012. “Creep and Shrinkage”. In *fib Model Code 2012: Final Draft.* Lausanne, Switzerland: fédération internationale du béton (*fib*), 124-149.

Gallaway, T. M. 1975. "Precasting of Segmental Bridges." In *Journal Proceedings*, Vol. 72, no. 10: 566-572.

Gardner, N. J., and Zhao, J. W. 1993. Creep and Shrinkage Revisited. *ACI Materials Journal* 90, no. 3: 236-246.

Gardner, N. J. and Lockman, M.J. 2001. Design Provisions for Drying Shrinkage and Creep of Normal-Strength Concrete. *ACI Materials Journal* 98, no. 2: 159-167

Holt, E. 2005. "Contribution of Mixture Design to Chemical and Autogenous Shrinkage of Concrete at Early Ages." *Cement and concrete research* 35, no. 3: 464-472.

Kavanaugh, B.P. 2008. Creep Behavior of Self-Consolidating Concrete. MS Thesis, Auburn, AL: Auburn University

Kim, J. K., and Lee, C. S. 1998. "Prediction of differential drying shrinkage in concrete." *Cement and Concrete Research* 28, no. 7: 985-994.

Libby, J. R. 1976. "Segmental Box Girder Bridge Superstructure Design." In *Journal Proceedings*, Vol. 73, no. 5: 279-290

Neville, A. M. 2011. *Properties of Concrete*, 5th. New York, New York: John Wiley & Sons, Inc.

Malm, R., and Sundquist, H. 2010. "Time-dependent analyses of segmentally constructed balanced-cantilever bridges." *Engineering Structures,* Vol. 32, no. 4: 1038-1045.

Mante, D. M. 2016. Improving Camber Predictions for Precast, Prestressed Concrete Bridge Girders. Ph.D. Dissertation, Auburn University

McCuen, R. H. 1985. *Statistical Methods for Engineers*. Lebanon, IN. Prentice Hall, Inc. pp. 439

Mehta, P., and Monteiro, J.M. 2014. *CONCRETE Microstructure, Properties and Materials,* 4th. New York, New York: McGraw-Hill Education.

Muller, J. M. 1969. "Long-span Precast Prestressed Concrete Bridges built in Cantilever." *Special Publication* 23: 705-740.

Podolny, W., and Muller, J. M. 1994. *Construction and Design of Prestressed Concrete Segmental Bridges*. New York, New York: John Wiley & Sons, Inc.

Raphael, W., Zgheib, E., and Chateauneuf, A. 2018. Experimental Investigations and Sensitivity Analysis to Explain the Large Creep of Concrete Deformations in the Bridge of Cheviré. *Case Studies in Construction Materials*, Vol. 9

Rizkalla, S., Mirmiran, A., Zia P., Russell, H., and Mast, R. 2007. *Application of the LRFD Bridge Design Specifications to High-Strength Structural Concrete: Flexure and Compression Provisions,* NCHRP Report 595. Transportation Research Board, National Research Council, Washington, DC.

Roberts, C. L., Breen, J. E., and Kreger, M. E. 1993. Measurement Based Revisions for Segmental Bridge Design and Construction Criteria. Center for Transportation Research, University of Texas at Austin.

Schindler, A.K., Barnes, R. W., Kamgang, J. K., and Kavanaugh, B. P. 2017. Compliance of Self-Consolidating Concrete for Prestressed Applications. *ACI Materials Journal* 114, no. 2: 273-283.

Shushkewich, K. W. 1986. Time-dependent Analysis of Segmental Bridges. *Computers & Structures*, Vol. 23, no. 1: 95-118.

Tadros, M. K., Al-Omaishi, N., Seguirant, S. P. and Gallt, J. G. 2003. *Prestress Losses in Pretensioned High-Strength Concrete Bridge Girders,* NCHRP Report 496. Transportation Research Board, National Research Council, Washington, DC.

Tazawa, E. 1999. *Autogenous Shrinkage of Concrete.* New York, New York: Routledge.

Wang, S., and Chung, C. F. 2014. Simplification of Creep and Shrinkage Analysis of Segmental Bridges. *Journal of Bridge Engineering*, Vol. 20 no. 8: 1-5.

APPENDIX A: RAW TEST DATA

A.1 COLLECTED CREEP TESTING DATA

Tables A-1 through A-11 contain all creep test data that were collected during the duration of this study. Tables A-1 through A-5 are represent the data that was collected for each set of field specimens and Tables A-6 through A-11 represent collected data for the laboratory test specimens. Each table contains the total strain, drying shrinkage strain, strain due to load, and the creep strains associated with the loading age of the indicated set of test specimens located on the top line. Also, each table contains the compressive strength and modulus of elasticity that was measured prior to creep testing as well as the target applied load level.

Table A-1: Raw collected data for 04/10/2018-F field specimens loaded at 7-days

Mixture ID			04/10/2018-F			
Loading Age			7-Days			
Compressive Strength (psi)			5,100			
Modulus of Elasticity (ksi)			3,800			
Target Applied Load (kips)			58.8			
	Reading Interval	Total Strain (με)	Shrinkage Strain (με)	Total Strain due to Load (με)	Creep Strain (με)	Total Force (kips)
Day One	Pre-Load	---	---	---	---	---
	Post-Load	-664	-8	-656	0	58.8
	2 to 6 Hour	-752	-16	-736	-80	58.7
Week One	1	-925	-24	-901	-245	57.3
	2	-1016	-36	-980	-325	58.7
	3	-1078	-57	-1021	-365	57.3
	4	-1126	-62	-1063	-407	58.7
	5	-1170	-72	-1097	-442	58.0
	6	-1218	-86	-1133	-477	58.1
	7	-1265	-107	-1158	-502	57.3
Month One	2	-1497	-174	-1322	-667	58.1
	3	-1652	-230	-1422	-766	57.7
	4	-1787	-282	-1505	-849	56.7
Months of Year One	2	-2080	-393	-1687	-1031	58.1
	3	-2204	-423	-1780	-1125	56.9
	4	-2311	-506	-1805	-1150	56.9
	5	-2387	-529	-1859	-1203	57.3
	6	-2482	-520	-1911	-1256	56.7

Table A-2: Raw collected data for 04/10/2018-F field specimens loaded at 28-days

Mixture ID			04/10/2018-F			
Loading Age			28-Days			
Compressive Strength (psi)			6,100			
Modulus of Elasticity (ksi)			4,050			
Target Applied Load (kips)			70.4			
	Reading Interval	Total Strain (με)	Shrinkage Strain (με)	Total Strain due to Load (με)	Creep Strain (με)	Total Force (kips)
Day One	Pre-Load	---	---	---	---	---
	Post-Load	-778	-13	-765	0	67.6
	2 to 6 Hour	-839	-9	-830	-65	70.3
Week One	1	-978	-16	-962	-197	69.6
	2	-1076	-18	-1058	-293	68.9
	3	-1125	-16	-1109	-344	69.9
	4	-1187	-33	-1154	-389	69.4
	5	-1235	-45	-1191	-426	68.5
	6	-1277	-52	-1226	-461	69.7
	7	-1320	-64	-1256	-491	67.9
Month One	2	-1475	-103	-1373	-608	69.4
	3	-1602	-120	-1482	-717	69.6
	4	-1686	-144	-1542	-777	70.0
Months of Year One	2	-1891	-193	-1698	-933	69.9
	3	-2042	-277	-1765	-1000	70.3
	4	-2196	-310	-1886	-1121	70.3
	5	-2260	-314	-1945	-1180	70.4
	6*	---	---	---	---	---

Note: * indicates that reading has not yet been recorded

Table A-3: Raw collected data for 04/10/2018-F field specimens loaded at 91-days

Mixture ID		04/10/2018-F				
Loading Age		91-Days				
Compressive Strength (psi)		6,000				
Modulus of Elasticity (ksi)		3,850				
Target Applied Load (kips)		69.22				
	Reading Interval	Total Strain (με)	Shrinkage Strain (με)	Total Strain due to Load (με)	Creep Strain (με)	Total Force (kips)
Day One	Pre-Load	---	---	---	---	---
	Post-Load	-714	0	-714	0	68.7
	2 to 6 Hour	-756	1	-758	-44	67.9
Week One	1	-836	-13	-823	-109	67.9
	2	-885	-18	-868	-154	68.4
	3	-913	-18	-895	-181	66.6
	4	-940	-22	-918	-204	66.6
	5	-960	-23	-936	-223	66.9
	6	-976	-34	-942	-228	67.3
	7	-993	-34	-959	-245	67.2
Month One	2	-1069	-62	-1007	-293	68.0
	3	-1167	-74	-1093	-379	66.6
	4	-1224	-82	-1143	-429	67.9
Months of Year One	2	-1370	-104	-1266	-552	68.4
	3	-1447	-96	-1351	-638	67.4
	4*	---	---	---	---	---
	5*	---	---	---	---	---
	6*	---	---	---	---	---

Note: * indicates that reading has not yet been recorded

Table A-4: Raw collected data for 07/09/2018-F field specimens loaded at 7-days

Mixture ID			07/09/2018-F			
Loading Age			7-Days			
Compressive Strength (psi)			5,600			
Modulus of Elasticity (ksi)			4,250			
Target Applied Load (kips)			64.6			
	Reading Interval	Total Strain (με)	Shrinkage Strain (με)	Total Strain due to Load (με)	Creep Strain (με)	Total Force (kips)
Day One	Pre-Load	---	---	---	---	---
	Post-Load	-661	-8	-653	0	64.7
	2 to 6 Hour	-716	-13	-703	-51	64.4
Week One	1	-845	-34	-811	-158	63.6
	2	-915	-49	-866	-214	64.3
	3	-972	-64	-908	-255	64.3
	4	-1027	-79	-947	-294	64.3
	5	-1063	-91	-972	-319	64.3
	6	-1123	-103	-1019	-367	63.6
	7	-1150	-119	-1031	-378	63.4
Month One	2	-1373	-200	-1173	-520	62.6
	3	-1493	-247	-1246	-593	63.3
	4	-1598	-298	-1300	-647	62.9
Months of Year One	2	-1826	-380	-1445	-793	64.3
	3	-1945	-425	-1521	-868	62.9
	4*	---	---	---	---	---
	5*	---	---	---	---	---
	6*	---	---	---	---	---

Note: * indicates that reading has not yet been recorded

Table A-5: Raw collected data for 07/09/2018-F field specimens loaded at 28-days

Mixture ID			07/09/2018-F			
Loading Age			28-Days			
Compressive Strength (psi)			6,700			
Modulus of Elasticity (ksi)			4,250			
Target Applied Load (kips)			77.3			
	Reading Interval	Total Strain (με)	Shrinkage Strain (με)	Total Strain due to Load (με)	Creep Strain (με)	Total Force (kips)
Day One	Pre-Load	---	---	---	---	---
	Post-Load	-749	-3	-746	0	77.3
	2 to 6 Hour	-810	-6	-804	-57	77.3
Week One	1	-930	-15	-916	-169	76.6
	2	-994	-20	-974	-228	77.0
	3	-1045	-25	-1020	-274	76.8
	4	-1078	-27	-1051	-305	77.2
	5	-1111	-33	-1078	-332	77.0
	6	-1140	-39	-1101	-355	77.2
	7	-1162	-54	-1108	-362	77.0
Month One	2	-1290	-88	-1202	-456	77.2
	3	-1398	-111	-1287	-541	75.6
	4	-1469	-124	-1345	-599	77.2
Months of Year One	2	-1612	-149	-1463	-716	77.2
	3*	---	---	---	---	---
	4*	---	---	---	---	---
	5*	---	---	---	---	---
	6*	---	---	---	---	---

Note: * indicates that reading has not yet been recorded

Table A-6: Raw collected data for 05/03/2018-L-Q laboratory specimens loaded at 7-days

Mixture ID			05/03/2018-L-Q			
Loading Age			7-Days			
Compressive Strength (psi)			7,200			
Modulus of Elasticity (ksi)			4,700			
Target Applied Load (kips)			83.1			
	Reading Interval	Total Strain (με)	Shrinkage Strain (με)	Total Strain due to Load (με)	Creep Strain (με)	Total Force (kips)
Day One	Pre-Load	---	---	---	---	---
	Post-Load	-725	-7	-718	0	81.7
	2 to 6 Hour	-795	-12	-784	-66	82.6
Week One	1	-938	-25	-912	-194	82.3
	2	-1000	-39	-961	-243	82.7
	3	-1067	-58	-1009	-291	81.0
	4	-1095	-62	-1032	-315	81.6
	5	-1121	-72	-1049	-331	83.0
	6	-1166	-90	-1076	-358	81.6
	7	-1198	-96	-1101	-384	80.5
Month One	2	-1364	-148	-1216	-498	81.0
	3	-1497	-212	-1285	-567	80.3
	4	-1565	-265	-1300	-582	82.9
Months of Year One	2	-1759	-341	-1419	-701	81.0
	3	-1866	-399	-1468	-750	81.5
	4	-1946	-469	-1477	-760	80.9
	5	-1997	-478	-1519	-801	81.6
	6*	---	---	---	---	---

Note: * indicates that reading has not yet been recorded

Table A-7: Raw collected data for 05/03/2018-L-Q laboratory specimens loaded at 28-days

Mixture ID			05/03/2018-L-Q			
Loading Age			28-Days			
Compressive Strength (psi)			8,500			
Modulus of Elasticity (ksi)			4,700			
Target Applied Load (kips)			98.06			
	Reading Interval	Total Strain (με)	Shrinkage Strain (με)	Total Strain due to Load (με)	Creep Strain (με)	Total Force (kips)
Day One	Pre-Load	---	---	---	---	---
	Post-Load	-876	-8	-868	0	94.8
	2 to 6 Hour	-920	-9	-910	-42	97.7
Week One	1	-1040	-22	-1018	-149	97.8
	2	-1109	-31	-1078	-210	97.3
	3	-1158	-33	-1124	-256	97.7
	4	-1190	-38	-1151	-283	97.3
	5	-1233	-48	-1185	-317	97.8
	6	-1268	-57	-1211	-343	97.3
	7	-1285	-61	-1224	-356	97.7
Month One	2	-1395	-73	-1322	-453	94.6
	3	-1475	-86	-1389	-520	95.0
	4	-1541	-102	-1440	-571	94.6
Months of Year One	2	-1740	-200	-1540	-671	97.5
	3	-1887	-261	-1626	-757	97.8
	4	-1964	-276	-1688	-820	97.6
	5*	---	---	---	---	---
	6*	---	---	---	---	---

Note: * indicates that reading has not yet been recorded

Table A-8: Raw collected data for 05/03/2018-L-Q laboratory specimens loaded at 91-days

Mixture ID			05/03/2018-L-Q			
Loading Age			91-Days			
Compressive Strength (psi)			8,800			
Modulus of Elasticity (ksi)			4,700			
Target Applied Load (kips)			101.5			
	Reading Interval	Total Strain (με)	Shrinkage Strain (με)	Total Strain due to Load (με)	Creep Strain (με)	Total Force (kips)
Day One	Pre-Load	---	---	---	---	---
	Post-Load	-868	-2	-866	0	97.6
	2 to 6 Hour	-918	-5	-913	-47	99.3
Week One	1	-1008	-12	-996	-130	99.0
	2	-1054	-18	-1036	-170	99.0
	3	-1090	-37	-1054	-187	99.2
	4	-1117	-44	-1073	-207	98.9
	5	-1141	-57	-1084	-218	97.8
	6	-1153	-44	-1109	-243	99.6
	7	-1172	-52	-1119	-253	99.6
Month One	2	-1243	-51	-1191	-325	99.4
	3	-1309	-53	-1256	-389	97.6
	4	-1350	-72	-1278	-412	97.9
Months of Year One	2	-1465	-82	-1384	-517	98.0
	3*	---	---	---	---	---
	4*	---	---	---	---	---
	5*	---	---	---	---	---
	6*	---	---	---	---	---

Note: * indicates that reading has not yet been recorded

Table A-9: Raw collected data for 05/09/2018-L-L laboratory specimens loaded at 7-days

Mixture ID			05/09/2018-L-L			
Loading Age			7-Days			
Compressive Strength (psi)			6,000			
Modulus of Elasticity (ksi)			5,300			
Target Applied Load (kips)			69.2			
	Reading Interval	Total Strain (με)	Shrinkage Strain (με)	Total Strain due to Load (με)	Creep Strain (με)	Total Force (kips)
Day One	Pre-Load	---	---	---	---	---
	Post-Load	-538	-5	-532	0	67.0
	2 to 6 Hour	-593	-2	-591	-58	68.8
Week One	1	-707	-18	-689	-157	69.1
	2	-768	-32	-736	-204	67.3
	3	-823	-42	-781	-249	67.1
	4	-879	-54	-825	-293	66.6
	5	-917	-66	-850	-318	69.0
	6	-938	-77	-861	-329	67.2
	7	-964	-96	-868	-336	68.0
Month One	2	-1124	-130	-994	-461	67.9
	3	-1240	-181	-1058	-526	67.4
	4	-1321	-222	-1099	-567	68.1
Months of Year One	2	-1515	-296	-1219	-687	66.6
	3	-1628	-340	-1289	-756	68.7
	4	-1719	-380	-1339	-807	68.9
	5	-1773	-387	-1386	-854	68.4
	6*	---	---	---	---	---

Note: * indicates that reading has not yet been recorded

Table A-10: Raw collected data for 05/09/2018-L-L laboratory specimens loaded at 28-days

Mixture ID			05/09/2018-L-L			
Loading Age			28-Days			
Compressive Strength (psi)			6,800			
Modulus of Elasticity (ksi)			5,350			
Target Applied Load (kips)			78.4			
	Reading Interval	Total Strain (με)	Shrinkage Strain (με)	Total Strain due to Load (με)	Creep Strain (με)	Total Force (kips)
Day One	Pre-Load	---	---	---	---	---
	Post-Load	-671	-10	-662	0	77.3
	2 to 6 Hour	-732	-9	-723	-61	77.9
Week One	1	-849	-17	-832	-170	78.1
	2	-897	-18	-879	-217	77.9
	3	-935	-23	-912	-251	78.0
	4	-970	-28	-943	-281	78.0
	5	-996	-33	-963	-301	77.9
	6	-1027	-45	-983	-321	78.1
	7	-1055	-49	-1005	-344	77.4
Month One	2	-1168	-74	-1094	-432	78.4
	3	-1228	-85	-1143	-482	76.0
	4	-1305	-107	-1198	-537	77.6
Months of Year One	2	-1475	-153	-1322	-660	76.7
	3	-1597	-200	-1397	-736	75.8
	4	-1656	-208	-1448	-787	76.2
	5*	---	---	---	---	---
	6*	---	---	---	---	---

Note: * indicates that reading has not yet been recorded

Table A-11: Raw collected data for 05/09/2018-L-L laboratory specimens loaded at 91-days

Mixture ID			05/09/2018-L-L			
Loading Age			91-Days			
Compressive Strength (psi)			7,200			
Modulus of Elasticity (ksi)			5,200			
Target Applied Load (kips)			83.1			
	Reading Interval	Total Strain (με)	Shrinkage Strain (με)	Total Strain due to Load (με)	Creep Strain (με)	Total Force (kips)
Day One	Pre-Load	---	---	---	---	---
	Post-Load	-623	-7	-616	0	82.7
	2 to 6 Hour	-668	-7	-661	-45	82.6
Week One	1	-733	-7	-726	-110	82.7
	2	-778	-8	-770	-154	82.6
	3	-803	-8	-794	-178	83.0
	4	-826	-8	-818	-202	82.9
	5	-846	-14	-832	-216	82.7
	6	-871	-15	-856	-240	82.5
	7	-879	-11	-868	-252	82.7
Month One	2	-962	-27	-934	-319	81.3
	3	-1016	-32	-984	-368	80.5
	4	-1049	-41	-1009	-393	82.9
Months of Year One	2	-1142	-47	-1095	-479	81.2
	3*	---	---	---	---	---
	4*	---	---	---	---	---
	5*	---	---	---	---	---
	6*	---	---	---	---	---

Note: * indicates that reading has not yet been recorded

A.2 COLLECTED SHRINKAGE TESTING DATA

Tables A-12 through A-14 contain the drying shrinkage data that were collected over the duration of this study. Tables A-12 and A-13 contain the collected data for the air- and moist-cured field specimens, respectively, while Table A-14 contains the collected data for the both the quartzite and limestone laboratory test specimens that were mixed at Auburn University.

Table A-12: Raw collected data for the drying shrinkage prisms for the air-cured field specimens

Mixture ID		03/20/2018-F (Air)	04/10/2018-F (Air)	07/09/2018-F (Air)
	Reading Interval	Drying Shrinkage Strain (με)	Drying Shrinkage Strain (με)	Drying Shrinkage Strain (με)
Day One	Initial Reading	---	---	---
	2 to 6 Hour	-30	-77	-100
Week One	1	-95	-130	-145
	2	-122	-168	-202
	3	-185	-222	-233
	4	-205	-252	-285
	5	-260	-283	-302
	6	-293	-295	-328
	7	-325	-318	-348
Month One	2	-492	-495	-480
	3	-645	-568	-587
	4	-698	-597	-640
Months of Year One	2	-868	-668	-708
	3	-917	-683	-740
	4*	-932	-723	---
	5*	-962	-728	---
	6*	-988	-745	---
	7*	-992	---	---

Note: * indicates that data not available for the indicated time interval for some specimens

Table A-13: Raw collected data for the drying shrinkage prisms for the moist-cured field specimens

Mixture ID		**03/20/2018-F (Moist)**	**04/10/2018-F (Moist)**	**07/09/2018-F (Moist)**
	Reading Interval	Drying Shrinkage Strain (με)	Drying Shrinkage Strain (με)	Drying Shrinkage Strain (με)
Day One	Initial Reading	---	---	---
	2 to 6 Hour	-67	-53	-25
Week One	1	-195	-152	-62
	2	-277	-225	-142
	3	-313	-270	-175
	4	-387	-300	-220
	5	-403	-342	-258
	6	-433	-375	-278
	7	-463	-398	-302
Month One	2	-668	-525	-425
	3	-757	-583	-520
	4	-873	-622	-553
Months of Year One	2	-1023	-693	-620
	3	-1063	-715	-657
	4*	-1070	-758	---
	5*	-1120	-778	---
	6*	-1150	-783	---
	7*	-1150	---	---

Note: * indicates that data not available for the indicated time interval for some specimens

Table A-14: Raw collected data for the drying shrinkage prisms for the quartzite and limestone coarse aggregate laboratory mixtures

Mixture ID		**05/03/2018-L-Q**	**05/09/2018-L-L**
	Reading Interval	Drying Shrinkage Strain (με)	Drying Shrinkage Strain (με)
Day One	Initial Reading	---	---
	2 to 6 Hour	-32	-32
Week One	1	-60	-125
	2	-122	-175
	3	-163	-215
	4	-205	-255
	5	-222	-262
	6	-230	-283
	7	-272	-297
Month One	2	-385	-382
	3	-425	-422
	4	-475	-462
Months of Year One	2	-545	-522
	3	-600	-572
	4	-623	-602
	5	-642	-612
	6*	---	---

Note: * indicates that data not available for the indicated time interval for some specimens